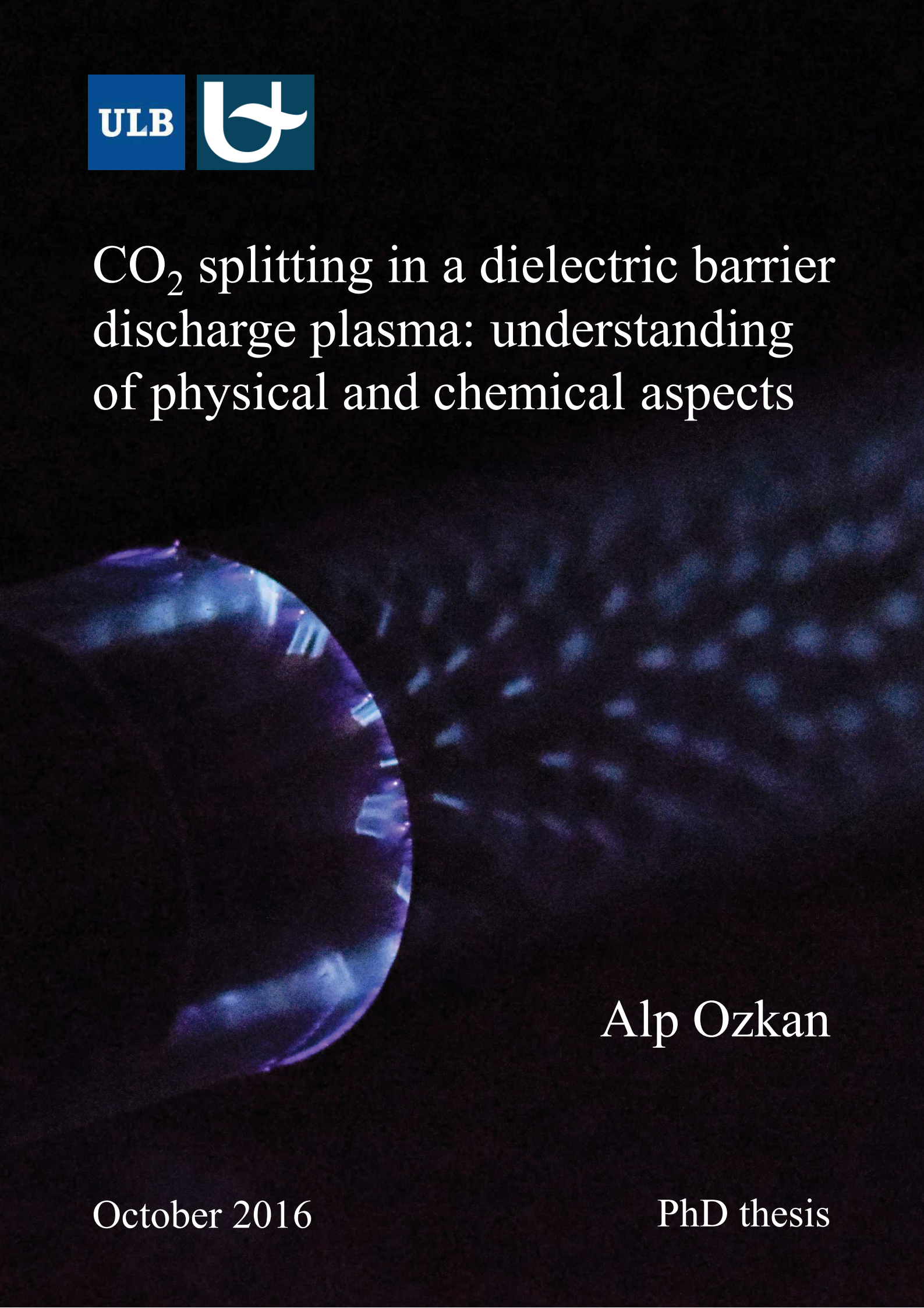




# CO<sub>2</sub> splitting in a dielectric barrier discharge plasma: understanding of physical and chemical aspects

A photograph of a dielectric barrier discharge (DBD) plasma. The image shows a dark, circular, glowing object on the left side, which is the plasma. It has a bright blue and purple hue. The background is dark, and there are some faint, blurry light spots scattered across it, possibly representing the plasma's interaction with the surrounding environment.

Alp Ozkan

October 2016

PhD thesis



UNIVERSITÉ LIBRE DE BRUXELLES

Universiteit Antwerpen



# CO<sub>2</sub> splitting in a dielectric barrier discharge plasma: understanding of physical and chemical aspects

by Alp Ozkan

Supervisors

Professor François Reniers

Professor Annemie Bogaerts

Université Libre de Bruxelles

Universiteit Antwerpen

CHANI

PLASMANT

Faculté des Sciences

Faculteit Wetenschappen

Département de Chimie

Departement Chemie

*A THESIS SUBMITTED FOR THE DEGREE OF PHILOSOPHIÆ DOCTOR IN SCIENCES*

**October, 2016**



## Acknowledgements

Je tiens avant tout à remercier le Professeur Claudine Buess-Herman de m'avoir accueilli au sein de son service de Chimie Analytique et Chimie des Interfaces et de m'avoir suivi tout au long de mon parcours.

Je voudrais aussi remercier mon promoteur de thèse, François Reniers, de m'avoir accepté dans son laboratoire et de m'avoir fait confiance. Tu m'as donné l'opportunité de travailler en collaboration avec un autre laboratoire et j'apprécie vraiment ce geste. Tu m'as sans cesse soutenu, même dans les moments « difficiles ». En tout cas, c'est là que je me rends compte que j'ai fait un très bon choix, il y a 4 ans, en choisissant de faire d'abord un mémoire et puis une thèse dans ton laboratoire de plasma. Ce fut un réel plaisir et j'espère que tu ne te rappelleras pas de moi comme celui qui te harcèle toutes les heures, celui qui te remplit ta boîte email sans arrêt et surtout celui qui joue le rôle d'Alpem\*\*.

Ik wil ook mijn andere promotor, Annemie Bogaerts, hartelijk bedanken om me in haar PLASMANT groep te accepteren. Simulatie was een helemaal nieuwe benadering voor mij en ik moet zeggen dat het een heel goede ervaring was. Je was altijd geduldig, glimlachend, goed gezind, je had een constant belang voor al mijn onderzoek, je verbeterde mijn rapporten altijd snel. Ik waardeer het echt en het was een plezier om in Antwerpen te werken.

Merci aussi aux professeurs de mon comité d'accompagnement Laurence Rongy et Thierry Visart pour leur suivi et leur intérêt pour l'ensemble de mon travail de recherche.

Je tiens à remercier Yannick pour ton aide, ta disponibilité, ta gentillesse ainsi que tes précieux conseils.

Je tiens à remercier tous les membres du CHANI (Thomas, Delphine, Jeremy, Caroline, Stéphanie C., Joffrey, Roman, Quentin, Alexandra, Qianqian, Qirong, Liis, Phuong, Magdalena) et les anciens (Thierry, Nicolas V., Bernard, Anne, Julie, Francis, Jennifer, Grégory, Eléonore, Jerika, Stéphanie V., Perrine, Aurore). Ce furent 4 agréables années de travail à vos côtés. Je voudrais remercier également les mémorants qui ont beaucoup participé à ce bon environnement de travail (Nicolas M., Luc, Alexia, Jessica, Julien, Berlin, Sofia). Merci également à Sandhya pour ton travail administratif, Philippe pour le travail technique et

Eric S. pour ta sympathie, ta bonne humeur, ton aide et ta disponibilité à chercher le matériel que je voulais.

Titi, c'était un réel plaisir de travailler avec toi, et tu m'as réorienté dans mon travail quand il le fallait et quand j'y pense, il s'agit de la meilleure collaboration que j'ai eue dans ma jeune carrière de chimiste, avec un travail fructueux à la clef. En plus avec un physicien français ! Il faudra aussi réécrire une nouvelle bible de plasma au passage ! Dédé, la plus expérimentée du labo (de loin), tu as toujours été disponible en cas d'aide, merci pour ta générosité et gentillesse. Bernard, c'était vraiment amusant de t'avoir dans ce labo de par ta bonne humeur et tes cadeaux matinaux ! Nico, un grand merci pour ton aide et ta disponibilité ! Bedankt ook voor je hulp, Francis ! Julie, merci également, tu as toujours été disponible en temps voulu ! Quant aux plus jeunes, je voudrais souligner la toute bonne ambiance qui règne au labo notamment grâce au trio SuperPotes (Jofke, Quentin et Jerem), Roman, Caro & Steph, Qianqian & Qirong, mais aussi Nathalia, Sylwia, Sten & Eric du CPMCT.

J'ai beaucoup apprécié les conférences avec le groupe plasma (ISPC, IVC et j'espère AVS), mais aussi les événements et sorties organisées par vous. Jofke, qui prendra la relève du selfiesleep ? Comment ça avance avec Alpe\*\* ? Jerem, il faut que tu diminues la fréquence de tes cours particuliers, demande de l'aide à ton turc préféré au cas où. Solvayboy, j'aime bien quand tu te défoules uniquement sur moi et Dédé lorsque tes manips ne marchent pas, et aussi tes nombreuses brusques interruptions dans le bureau (ultra-pote ?) et tes histoires du midi. I am also thankful for the best food made in China we had, thanks to Qianqian and Qirong. Thanks also for the funny moments we shared together. Ayant travaillé sur le même sujet en électrochimie et commencé plus au moins en même temps, je tiens à remercier Roman. Qui sait, peut-être qu'on aura un article en commun ! Merci à Caro pour les bijoux et vêtements fancy. Thank you to Liis for organizing some cool events ! Merci à Mario pour les discussions NBA, Luke pour les artichauts, Jess pour les crêpes et Alexia pour le yogurt.

Ook hartelijk bedankt aan mijn Antwerpse collega's. Ik heb me goed geamuseerd op events en ook op de Bad Honnef Plasma Summer School. Ik wil Ramses en Robby bedanken voor hun hulp en toelichtingen in simulaties maar ook in experimenten. Ik zou ook graag Inne willen bedanken voor haar vriendelijkheid en beschikbaarheid om in sommige bestelling te helpen. Ik bedank ook Stijn, Marleen, Johan voor hun hulp. I also thank Maryam for the organization of some nice events and her good mood. Je tiens à remercier Antonin, toujours chaleureux, toujours disponible pour aider de manière enthousiaste, merci aussi pour les

évènements organisés. Ik moet ook Luc hartelijk bedanken voor de sympathie en de hulp wanneer ik in Antwerpen ben gestart.

I acknowledge financial support from the IAP-VII/12, P7/34 (Inter-university Attraction Pole) program ‘PSI-Physical Chemistry of Plasma-Surface Interactions’, financially supported by the Belgian Federal Office for Science Policy (BELSPO), and also the collaboration I had throughout IAP project, with Tiago, Guoxing... Tiago, thank you for the advices and helps. I would like also to thank the financial support given by ‘Fonds David et Alice Van Buuren’.

Merci enfin à ma mère Ayten, mon père Soner, ma grande sœur Sibel, mon beau-frère Yannick et mon petit neveu Deniz, ainsi que le reste de ma famille, mon entourage et mes ami(e)s pour m’avoir supporté et aidé dans les moments les plus difficiles, pour m’avoir perpétuellement encouragé, pour avoir cru en mes capacités et projets futurs, et ce depuis toujours. Si je suis arrivé jusqu’ici dans mon parcours académique et mes études, c’est en grande partie grâce à vous.

## Abstract

Carbon dioxide appears as one of the most problematic gases for the environment, mostly because it is responsible for global warming. This is why its increasing concentration into the atmosphere, mainly due to anthropogenic activities, is a real concern for planet Earth. In order to prevent the release of large amounts of CO<sub>2</sub>, its conversion into value-added products is of great interest. In this context, plasma-based treatments using dielectric barrier discharges (DBDs) are nowadays more and more used for the conversion of this gas.

In this thesis, we investigated the CO<sub>2</sub> splitting process into CO and O<sub>2</sub> via a flowing cylindrical DBD and we studied its conversion and energy efficiency by means of several diagnostic methods, such as mass spectrometry to determine the conversion and energy efficiency of the process, optical emission spectroscopy for gas temperature measurements, and an oscilloscope for electrical characterization, in order to obtain a better understanding of the CO<sub>2</sub> discharge itself.

First, we focused on an extensive experimental study of a pure CO<sub>2</sub> plasma where different parameters were varied, such as the gas residence time, the operating frequency, the applied power, the pulsation of the AC signal, the thickness and the nature of the dielectric. CO<sub>2</sub> discharges typically exhibit a filamentary behavior, consisting of many microdischarges, which act as the main source of reactivity in a DBD. A detailed insight in the physical aspects was achieved by means of an in-depth electrical characterization, allowing more insight in the electrical properties of the discharge and more specifically in the microdischarges, which are spread out throughout the active zone of the plasma. It was found throughout this work that the plasma voltage, which reflects the electric field and thus determines how the charged particles are accelerated, the plasma current, which reflects the electron density, but also the number of microdischarges and their average lifetime, play an important role in the efficiency of the CO<sub>2</sub> dissociation process. It was revealed that the microdischarge number is important as it represents the repartition of the locations of reactivity. Indeed, as the microfilaments are more spread out in the same discharge volume, the probability for the CO<sub>2</sub> molecules to pass through the reactor and interact with at least one microdischarge filament becomes more important at a larger number of microfilaments.

The second part of the thesis was dedicated to discharges combining CO<sub>2</sub> and H<sub>2</sub>O or CH<sub>4</sub>, both being hydrogen source molecules. The combined CO<sub>2</sub>/H<sub>2</sub>O or CO<sub>2</sub>/CH<sub>4</sub> conversion allows forming value-added products like syngas (CO and H<sub>2</sub>), but also hydrocarbons (C<sub>2</sub>H<sub>6</sub>, C<sub>2</sub>H<sub>4</sub>, C<sub>2</sub>H<sub>2</sub> and CH<sub>2</sub>O), at least in the presence of methane. Throughout this study, we tried to obtain a better knowledge of the chemistry and physic behind these conversion processes.

## Résumé

Le dioxyde de carbone, principal gaz à effet de serre lié aux activités humaines, est considéré comme l'un des gaz les plus problématiques pour notre environnement ces dernières années, principalement à cause du réchauffement climatique qu'il engendre. C'est pour cette raison que l'augmentation de sa teneur dans l'atmosphère nous concerne tous quant aux conséquences futures pour notre planète. Afin de limiter l'émission de CO<sub>2</sub>, sa conversion en composés à valeur ajoutée présente un grand intérêt et est possible notamment via des procédés plasmas. Plus particulièrement, les décharges à barrière diélectrique (DBD) sont utilisées depuis quelques années pour générer des plasmas froids opérant à pression atmosphérique, principalement pour des applications en traitement de surface, mais également pour le traitement d'effluents gazeux.

Lors de cette thèse, nous nous sommes focalisés sur le processus de dissociation du CO<sub>2</sub> en CO et O<sub>2</sub> via un réacteur DBD à flux continu et avons analysé sa conversion et son efficacité énergétique via différentes études. Celles-ci ont été réalisées grâce à plusieurs méthodes de diagnostic, comme par exemple la spectrométrie de masse utilisée pour déterminer la conversion et l'efficacité du processus, la spectroscopie d'émission optique, l'oscilloscope pour une caractérisation électrique, etc. afin d'avoir une meilleure compréhension du comportement des décharges CO<sub>2</sub>.

Dans un premier temps, nous avons réalisé une étude détaillée d'un plasma CO<sub>2</sub> pur où nous avons fait varier différents paramètres, tels que le temps de résidence, la fréquence, la puissance, la pulsation de la haute tension et l'épaisseur et la nature du diélectrique. Le CO<sub>2</sub> donne lieu généralement à une décharge filamentaire, consistant en de nombreuses microdécharges réparties au niveau de la zone du plasma. Celles-ci constituent la principale source de réactivité dans une DBD. Un aperçu détaillé de l'aspect physique de ces microdécharges a été réalisé grâce à la caractérisation électrique, permettant de mieux comprendre les propriétés électriques de la décharge et des microdécharges. En effet, nous avons pu déterminer l'importance de la tension présente au niveau du plasma, de l'intensité du courant plasma, du nombre de microdécharges et de leur temps de vie sur l'efficacité du processus de dissociation de CO<sub>2</sub>.

Ensuite, nous avons conclu ce travail avec des études combinant le CO<sub>2</sub> en phase plasma avec de l'eau ou du méthane afin de produire des molécules à valeur ajoutée telles que les syngas (CO et H<sub>2</sub>), mais aussi des hydrocarbures (C<sub>2</sub>H<sub>6</sub>, C<sub>2</sub>H<sub>4</sub>, C<sub>2</sub>H<sub>2</sub> et CH<sub>2</sub>O) dans le cas de l'ajout du méthane. A travers ces études, nous avons obtenu une meilleure connaissance de la chimie et de la physique qui ont lieu dans ce type de plasma.

## Samenvatting

Koolstofdioxide wordt beschouwd als één van de meest problematische gassen voor onze omgeving, voornamelijk omdat het verantwoordelijk is voor het broeikas-effect. De concentratie van CO<sub>2</sub> neemt nog steeds toe, vooral door menselijke en industriële activiteiten, en dit heeft serieuze gevolgen voor onze planeet Aarde. Om de grote CO<sub>2</sub>-uitstoot te verminderen, is de omzetting naar producten met toegevoegde waarde van groot belang, en het is mogelijk om dit via plasma processen te doen. Diëlektrische barrière ontladingen (DBD), die gebruikt worden om koude plasma's te genereren, zijn hiervoor zeer interessant.

In dit proefschrift hebben wij ons gericht op het CO<sub>2</sub> dissociatieproces naar CO en O<sub>2</sub> via een cilindrische DBD reactor bij atmosferische druk. De conversie en energie-efficiëntie werden bestudeerd via diverse studies. Deze werden uitgevoerd met behulp van verschillende diagnostische methoden, zoals massaspectrometrie om de conversie en energie-efficiëntie van het proces te bepalen, optische emissie spectroscopie, en een oscilloscoop voor elektrische karakterisering, teneinde een beter inzicht te verkrijgen in CO<sub>2</sub> ontladingen.

Eerst voerden wij een gedetailleerde studie uit van een zuiver CO<sub>2</sub> plasma, waarbij diverse parameters werden veranderd, zoals verblijftijd, frequentie, vermogen, pulserende hoogspanning, de dikte en de aard van het diëlektricum. In het algemeen geeft CO<sub>2</sub> aanleiding tot een draadvormige ontlading. Een gedetailleerd overzicht van het fysische aspect werd bereikt door een diepgaande elektrische karakterisering, voor meer informatie over de elektrische eigenschappen van de ontladingen en meer in het bijzonder van de micro-ontladingen die verspreid zijn over de ontladingszone. De micro-ontladingen vormen de belangrijkste bron van reactiviteit in een DBD. In dit proefschrift hebben wij het belang bepaald van de spanning aangelegd over het plasma, de stroomsterkte, het aantal micro-ontladingen en hun levensduur, op de efficiëntie van het CO<sub>2</sub> dissociatieproces.

Vervolgens hebben wij ook CO<sub>2</sub> ontladingen bestudeerd, gecombineerd ofwel met water of met methaan, om moleculen met toegevoegde waarde te produceren, zoals synthesegas (CO en H<sub>2</sub>), maar ook koolwaterstoffen (C<sub>2</sub>H<sub>6</sub>, C<sub>2</sub>H<sub>4</sub>, C<sub>2</sub>H<sub>2</sub> en CH<sub>2</sub>O) bij de toevoeging van methaan in de ontlading. Door middel van deze studies hebben wij een beter begrip gekregen van de chemie en fysica die plaatsvindt in deze plasma's van CO<sub>2</sub>/H<sub>2</sub>O of CO<sub>2</sub>/CH<sub>4</sub>.

## Contents

List of abbreviations and symbols .....	14
Chapter I - Introduction.....	17
1.    CO <sub>2</sub> and global warming .....	18
2.    Challenges of CO <sub>2</sub> treatment .....	19
3.    Methods to convert CO <sub>2</sub> into added-value products .....	21
4.    Plasma methods for the conversion of CO <sub>2</sub> .....	22
5.    Thermodynamic analysis.....	23
5.1. Introduction .....	23
5.2. Carbon dioxide reforming .....	24
5.3. Thermal processes of CO <sub>2</sub> reforming.....	27
5.4. Plasma process.....	30
6.    Aim of the research.....	31
7.    Thesis outline.....	32
Chapter II - State of the art of plasma-based CO <sub>2</sub> conversion.....	34
1.    General information on plasmas .....	35
1.1. Introduction .....	35
1.2. Glow discharge .....	37
1.3. Dielectric barrier discharge .....	39
1.4. Paschen's Law .....	41
1.5. Two regimes and electrical circuit of a dielectric barrier discharge .....	42
2.    Properties of CO <sub>2</sub> plasmas.....	49
2.1. Reactivity of the plasma .....	49
2.2. Different types of plasma for CO <sub>2</sub> treatment .....	53
3.    Utilization of CO <sub>2</sub> plasmas for syngas production.....	57
3.1. Introduction .....	57
3.2. CO <sub>2</sub> /CH <sub>4</sub> mixture .....	58
3.3. CO <sub>2</sub> /H <sub>2</sub> O mixture .....	58
4.    Application of CO <sub>2</sub> plasma for surface treatment .....	59
Chapter III - Description of the experiments.....	61
1.    Experimental setup.....	62
1.1. Generator .....	62

---

1.2. Tubular DBD with 2 electrodes .....	62
1.3. Tubular DBD with multi-electrodes.....	64
2. Experimental diagnostics .....	66
2.1. Mass spectrometry .....	66
2.2. Gas chromatography .....	68
2.3. Optical emission spectroscopy.....	70
2.4. Electrical characterization .....	73
2.5. Infrared imaging .....	78
2.6. Profilometry.....	78
3. Simulation .....	79
3.1. Description of the model .....	79
3.2. Application of the 0D model to a DBD reactor .....	80
Chapter IV - CO <sub>2</sub> discharge - an extensive study of its conversion.....	83
1. Introduction .....	84
2. Influence of residence time and electrical parameters .....	86
2.1. Introduction .....	86
2.2. Effect of the flow rate .....	87
2.3. Effect of the frequency .....	90
2.4. Effect of the power.....	98
2.5. Effect of the multi-pulsed AC voltage (so-called burst mode) .....	102
2.6. Conclusion.....	114
3. Influence of the dielectric barrier.....	117
3.1. Introduction .....	117
3.2. Effect of the dielectric barrier thickness.....	118
3.3. Effect of the dielectric barrier material .....	124
3.4. Conclusion.....	132
Chapter V - CO <sub>2</sub> discharge with water addition .....	135
1. Introduction .....	136
2. Mass spectrometry results .....	137
2.1. Experimental details.....	137
2.2. CO <sub>2</sub> and H <sub>2</sub> O conversion.....	139
2.3. Product formation .....	141
3. Optical emission spectroscopy results.....	145
4. Electrical characterization .....	149

---

5. Conclusion.....	153
Chapter VI - CO <sub>2</sub> discharge with methane addition .....	157
1. Introduction .....	158
2. Influence of electrical parameters .....	158
2.1. Effect of the CO <sub>2</sub> and CH <sub>4</sub> flow rates on the reactivity and reaction products formed in the CO <sub>2</sub> /CH <sub>4</sub> conversion process .....	159
2.2. Effect of the power.....	165
2.3. Effect of the carrier gas .....	167
3. Conversion, specific energy input and energy efficiency: comparison with literature .....	170
4. Conclusion.....	175
Chapter VII - Conclusions and perspectives .....	176
1. Conclusions .....	177
2. Perspectives and future works .....	180
List of publications and conference contributions .....	182
1. Publications related to this PhD dissertation .....	182
2. Publications not related to this PhD dissertation .....	182
3. Conference contributions.....	183
Bibliography.....	185

## List of abbreviations and symbols

$\varepsilon$	Relative permittivity
$\Phi(\text{CO}_2) \text{ mL}_n \cdot \text{min}^{-1}$	Flow rate of $\text{CO}_2$ at standard conditions, 293 K and 1 atm
$\tau_{\text{anal}}$	Analysis time
$\chi_i$	Conversion of $i$ in the dissociation process of $i$
$\eta_i$	Energy efficiency of the dissociation process of $i$
AC	Alternative current
AFM	Atomic-force microscopy
BDE	Bond dissociation energy
BET	Brunauer–Emmett–Teller (theory)
CCD	Charge-coupled device (camera)
$C_{\text{DBD}}$	DBD capacitance
$C_{\text{diel}}$	Dielectric capacitance
CEM	Controlled evaporator mixer
$C_g$	Gas capacitance
$C_{\text{pl}}$	Plasma capacitance
DBD	Dielectric barrier discharge
DC	Direct current
$D_{\text{cycle}}$	Duty cycle
DRM	Dry reforming of methane
$E$	Electric field
$E/n_0$	Reduced electric field
$E_d$	Energy density
EDX	Energy-dispersive X-ray spectroscopy
EEDF or $f(\varepsilon)$	Electron energy distribution function
$f$	Frequency
FID	Flame ionization detector
FPS	First positive system
$f_{\text{repetition}}$	Repetition frequency of the burst mode
$f_{\text{signal}}$	Signal frequency
$f_v$	Volumetric fractions

FWHM	Full width at half maximum
GC	Gas chromatography
H-source	Source of hydrogen
HV	High voltage
$i_{\text{DBD}}$ or $i_{\text{tot}}$	Total current
$i_{\text{diel}}$	Dielectric current / displacement current in the dielectric barrier
$i_{\text{pl}}$	Discharge current
IR	Infrared
$L_{\text{md}}$	Lifetime of microdischarges
LTE	Local thermodynamic equilibrium
MID	Multiple ion detection mode
MS	Mass spectrometry
$n_e$	Electron density
$N_{\text{md}}$	Number of microdischarges
OES	Optical emission spectroscopy
P	Power
$P_{\text{abs}}$	Discharge power / power absorbed by the plasma
$P_{\text{applied}}$	Applied power
PECVD	Plasma-enhanced chemical vapor deposition
$p_i$	Partial pressure
$p_i$	Partial pressure
ppb	Part per billion
$P_{\text{plasma}}$	Power during the plasma ignition (used for the burst mode)
ppm	Part per million
$Q_{\text{DBD}}$ or $Q_{\text{tot}}$	Total electric charge of the DBD reactor for a certain time
$Q_{\text{DBD}}^{120\mu\text{s}}$	Total electric charge accumulation in the DBD reactor during 120 $\mu\text{s}$
$Q_{\text{diel}}$	Electric charges of the dielectric barrier
$Q_{\text{md}}$	Electric charge accumulated per microdischarge
$Q_{\text{pl}} / Q_{\text{pl}}^+$ or $Q_{\text{pl}}^-$	Electrical charge of the plasma for a certain time / for positive or negative half period
$R_{\text{disch}}$	Resistance of the plasma
RF	Radio frequency
RMS	Root mean square

$R_{\text{RMS}}$	Parameter for the roughness of a surface (root mean square value)
sccm	Standard cubic centimeters per minute
SEI	Specific energy input
SEM	Secondary electron multiplier or Scanning electron microscope
$S_i$	Selectivity of product i
$T_0$	Neutral species temperature
TCD	Thermal conductivity detector
$T_e$	Electron temperature
$T_{\text{electrode}}$	Electrode temperature
$T_{\text{gas}}$	Gas temperature
$T_i$	Ion temperature
$T_{\text{OFF}}$	Time when no power is applied to the reactor in the burst mode
$T_{\text{ON}}$	Time of plasma ignition in the burst mode
$T_{\text{rot}}$	Rotational temperature
UV	Ultraviolet
$V_{\text{DBD}}$	Applied voltage
$V_{\text{diel}}$	Voltage across the dielectric material
$V_{\text{diel}}(0)$	Memory voltage
$V_{\text{pl}}$	Voltage across the gap
$V_{\text{pl,eff}}$	Effective plasma voltage (used for filamentary discharge)
VV	Vibrational-vibrational (relaxation)
XPS	X-ray photoelectron spectroscopy
$\gamma$	Parameter of the emission of secondary electrons
$\Delta G^0$	Standard Gibbs free energy of reaction
$\Delta H^0$	Standard enthalpy of reaction

# **Chapter I - Introduction**

## 1. CO<sub>2</sub> and global warming

Carbon dioxide (CO<sub>2</sub>) is considered to be the major cause of climate change, because of its greenhouse properties and its continuous accumulation in the atmosphere. Every year, a new record in the concentrations of greenhouse gases is recorded. CO<sub>2</sub> is an unavoidable reaction product of human activity and it is probably one of the most problematic gases for our atmosphere because of the global warming it causes [1-5]. Almost 72% of the total greenhouse effect is attributed to water vapor and clouds, the remainder being mainly the result of CO<sub>2</sub>. Indeed, the CO<sub>2</sub> absorption wavelengths play a critical role on this global warming. In order to interact with IR radiation, a molecule must have a dipole moment ( $\mu \neq 0$ ). In this context, all molecules have positive (nuclei) and negative (electron clouds) regions. A molecule is polar and has a permanent dipole moment, if the averaged centers of its positively and negatively charged regions do not coincide. However in the ground state, CO<sub>2</sub> is linearly symmetrical and hence, does not have a permanent dipole moment. Due to its vibrational motion, the dipole moment of CO<sub>2</sub> can however change [6], i.e. the vibrations in its bonds are able to create an imbalance in the electric field. This is why it is known for being able to absorb the lower thermal infrared frequencies emitted by the Earth's surface. It is also important to stress that CO<sub>2</sub> has different vibrational modes, which differently contribute to the global warming scenario. CO<sub>2</sub> exhibits vibrations in three different main modes: the symmetric stretching, the bending and asymmetric stretching [7]. In the first vibration mode, the oxygen atom on one side pulls the electrons just as strongly as the other oxygen on the other side and hence, the molecule does not present greenhouse properties. The other two CO<sub>2</sub> vibrational modes indeed generate an asymmetry in the electric field, which makes the CO<sub>2</sub> molecule IR active. Among these two vibrational modes, the CO<sub>2</sub> bending vibration is the most relevant since it vibrates and absorbs IR light exactly at the peak of Earth's surface emission spectrum. Basically, all molecules with three or more atoms, such as CO<sub>2</sub>, H<sub>2</sub>O, CH<sub>4</sub>, N<sub>2</sub>O, and O<sub>3</sub>, meet the criterion of  $\mu \neq 0$  and are therefore IR absorbers. The Earth's atmosphere is predominantly composed of non-IR absorbers, not contributing to the climate change, i.e., N<sub>2</sub> (78%), O<sub>2</sub> (21%) (both are symmetrical molecules, made of two identical atoms whose electric fields cancel each other), and Ar (~0.9%), but the 0.1% of remaining trace gases contains many species that absorb IR.

Natural greenhouse gases are responsible for bringing the average temperature of the Earth to +15°C (instead of -18°C), which is essential for life, by absorbing part of its infrared

radiation. However, the excess presence of CO<sub>2</sub> constitutes of a real threat and real concern for planet Earth. Indeed, the anthropogenic activities lead to an increase of the CO<sub>2</sub> concentration in the atmosphere over the last 150 years from 280 ppm (recorded during the preindustrial era) to a current level of almost 400 ppm (recorded in 2014) [8].

The origin of this massive emission of CO<sub>2</sub>, and of its steady accumulation in the atmosphere, is the use of carbon-based fossil fuels in human activities. Numerous industries still employ combustion processes from fossil fuels (natural gas, petroleum products, oil, coal, lignite, etc.) in particular in the automotive and aerospace sectors, causing large emission of polluting and greenhouse gases [1, 9-11]. Moreover, as carbon-based fossil fuels currently represent 80-85% of the world's energy sources, and will continue to play an important role at least in the short to medium term, a major increase of CO<sub>2</sub> emissions is to be expected. Today, the robust growth of emerging economies such as China and India is driving worldwide energy demand and usage at a rate never experienced before; in fact, a further expansion in greenhouse gases emission of 50-100% is envisaged by the year 2030 [12].

Inevitably, these changes in the energy balance of the atmosphere are causing the temperature of the planet's waters to rise and their volume to increase, to a point where the rising sea levels on the Earth's surface are seen as a major problem, especially in coastal areas. A higher global temperature also leads to unwanted phenomena, like ocean acidity or more extreme ones affecting the weather such as heat waves, floods and melting ice [13-18].

Driven by worries on climate change, the European Commission has implemented increasingly stricter limits on CO<sub>2</sub> emissions and has run the H2020 work program with a societal challenge, clearly identified as *climate action and environment*. More generally, an increasing number of countries become aware of these issues: as an illustration, the COP-21 (Conference of the Parties) in 2015 has gathered almost 200 countries around a project agreement on the climate. This conference in Paris aimed at taking strong measures to limit the phenomenon of global warming.

## **2. Challenges of CO<sub>2</sub> treatment**

CO<sub>2</sub> emission due to anthropogenic activities represents 29 gigatons per year (much more than other potential greenhouse gases) and it is expected to increase to 36-43 gigatons/year, depending on the energy world policies, i.e. on how we will use existing and new energy

sources [2, 3, 19]. For this reason, the remediation of CO<sub>2</sub> (CO<sub>2</sub> abatement) has received increasing attention in recent years. Moreover, unlike other greenhouse gases that can be recycled and easily removed in the atmosphere by natural processes (for example H<sub>2</sub>O through condensation, or CH<sub>4</sub> through chemical reactions with OH radicals [20]), CO<sub>2</sub> can remain in the air for a while, despite the fact that the global warming potential of methane is even 21 times higher than for carbon dioxide [21].

The time required to stabilize the effects of increasing CO<sub>2</sub> concentration in the atmosphere will be very long. Any response by the Earth to measures that we might take today will not be effective tomorrow, nor the day after tomorrow – it will take centuries. All these extra greenhouse gas emissions released today will therefore affect the climate of the next generations. So, with such a long time-scale, the ability to forecast scenarios will be affected by any major error that might emerge as a result of any, often unpredictable, change that might occur. During the past twenty years, there have been major changes in the social, political, and economical structures of a large part of society. Clearly, under such conditions the variability and uncertainty of any scenario is very large, and it will inevitably become essential that responsible measures are taken in order to avoid reaching a “point of no return”. Nowadays, political authorities want to limit the CO<sub>2</sub> footprint. Five approaches can be promoted: (i) using renewable energies (and enhancing their energy efficiency), (ii) non-carbon energy resources, (iii) CO<sub>2</sub> capture/geological storage in deep underground [22-24], (iv) taxing tons of the CO<sub>2</sub> produced and (v) the reuse of CO<sub>2</sub> (CO<sub>2</sub> valorization). The latter approach aims at using carbon dioxide as a feedstock and transforming it into value-added products such as carbon monoxide and oxygen. Therefore, the purpose is not only to tackle climate change, but also to provide an answer to the issue of our dependence on fossil fuels.

To prevent the release of large quantities of CO<sub>2</sub> into the atmosphere [25], carbon capture and storage in geological reservoirs is one of the solutions considered over the last decades. However, this approach presents several disadvantages, including its cost, environmental assessment and long-term risks. Moreover, it barely matches with the principles of sustainable development since CO<sub>2</sub> is still considered as a waste for long term storage. However in a "cradle to cradle" approach, waste of all types is increasingly recycled [26]. Carbon dioxide, which is itself the product of the combustion of carbon compounds, could also be reused. However, it has the major disadvantage of being particularly stable and therefore its reuse is energetically demanding.

### 3. Methods to convert CO<sub>2</sub> into added-value products

Nowadays, a more eco-friendly approach has emerged: CO<sub>2</sub> can be considered as a feedstock to be converted into value-added products such as syngas (carbon monoxide CO and hydrogen gas H<sub>2</sub>), when mixing it with a gas acting as a source of hydrogen. This would result in a significant step towards the production of chemicals and energy, with a close to zero carbon-emission level. In that respect, conventional organic reactions [12], electrochemical reduction [27] and photochemical CO<sub>2</sub> reduction processes have already been successfully applied, either to obtain CO, formic acid, formaldehyde, methanol and methane using electrical energy, or to obtain CO and formate using light [12, 27, 28].

Moreover, the direct splitting of pure CO<sub>2</sub> into CO and O<sub>2</sub> is also of great interest. Despite its toxicity, carbon monoxide is indeed interesting since many well-known methods exist to synthesize specific organic molecules from it via heterogeneous catalysis. Therefore, the CO extracted from CO<sub>2</sub> becomes a useful product that can be fed back into other industrial processes as a reactant. It can for instance be utilized in various catalytic processes such as the Monsanto process (combined with methanol to produce acetic acid) [29, 30] and the Fischer-Tropsch process [31]. For the latter process, carbon monoxide reacts with hydrogen (H<sub>2</sub>) over a catalyst leading to the production of a wide variety of products (mainly liquid hydrocarbons) depending on the nature of the catalyst. Various products which can be obtained from synthesis gas (CO and H<sub>2</sub>; syngas) are shown in Figure 1.

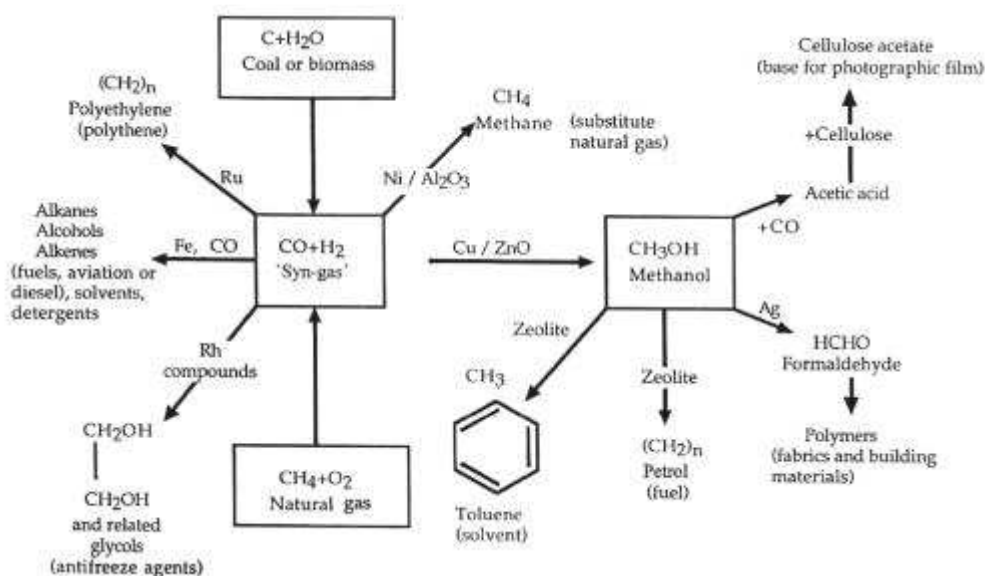


Figure 1 : General scheme of conversion of synthesis gas. The various products obtained are related to the nature of the metal catalyst [32].

#### 4. Plasma methods for the conversion of CO<sub>2</sub>

In recent years, cold (or non-thermal) plasmas have been pointed out in the literature as a new approach for the valorization of CO<sub>2</sub> [33, 34]. The plasma technique appears very promising, as it can directly operate in the gaseous phase as CO<sub>2</sub> is gaseous at ambient temperature and pressure, while electrochemistry techniques (electrochemical reduction), for example, must be carried out in liquid phase. As in electrochemical techniques, plasma technologies use electricity as an energy source. Non-thermal plasmas operate far from thermodynamic equilibrium, i.e. the electrons are mostly heated by the applied electric power and can activate the gas by electron impact excitation, ionization and dissociation. New reactive species can therefore be created and converted more easily into new molecules, while the gas can remain at (or near) room temperature. Moreover, plasmas can also allow for the synthesis of specific organic molecules when combined with heterogeneous catalysis [35, 36]. For instance, CO<sub>2</sub>-CH<sub>4</sub> treatments using Ni catalysts have already been used for the production of syngas and small amounts of organic molecules [37, 38]. Furthermore, plasmas allow storing peak currents from sustainable energy (renewable sources, e.g. solar and wind) into new fuels, since plasma can easily be switched on and off. Plasma can be considered hence as green technology. Finally, the capture, transport and storage of CO<sub>2</sub> might become no more necessary, as dedicated plasma sources could allow their direct and online implementation on industrial smokestack outputs.

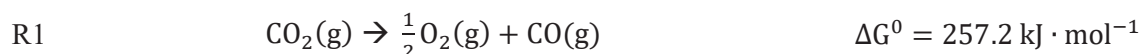
The reactions of greatest interest are the conversion of CO<sub>2</sub> to syngas, hydrocarbons (ethylene, etc.) and oxygenated products (i.e. methanol [39, 40], formaldehyde, formic acid, hydrogen peroxide used for sterilization [41-43], etc.) when combining this gas with an H-source, as mentioned above. Hydrocarbons and oxygenated products would be obviously preferable to syngas for many applications. For instance, hydrocarbons like ethylene and related C<sub>2</sub> species, obtainable from CO<sub>2</sub> mixed with a H-source plasma, are of great interest as they are the foundation of the petrochemical industry that has shaped the modern world. Indeed, ethylene is the basis for a several molecules in the chemical industry. With its immediate derivatives, it is the source of a large number of polymers and plastics (vinyl chloride, ethylbenzene, ethylene oxide, ethanol, polyethylene, etc.). Thus, C<sub>2</sub> hydrocarbons are one of the feedstock of our society and their production will increasingly make demands on energy resources to realize the potential of alternatives to traditional petroleum feedstock. Nevertheless, syngas can easily be converted to almost any commercial chemical or fuel

through the Fischer Tropsch synthesis, as mentioned above [44]. In order to obtain the desired products from this synthesis, it is important to have control of the H<sub>2</sub>/CO ratio [45].

## 5. Thermodynamic analysis

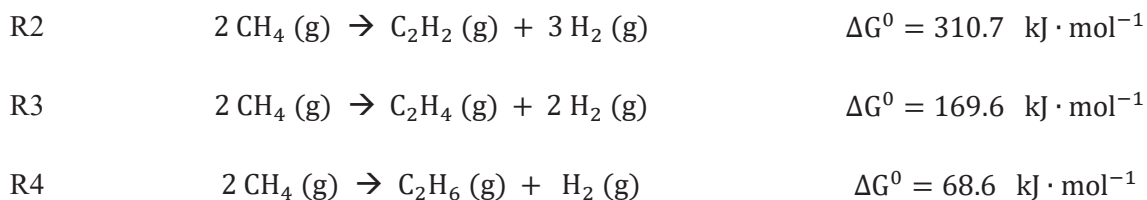
### 5.1. Introduction

The reduction of CO<sub>2</sub> is particularly energy intensive. Indeed, CO<sub>2</sub> is a very stable molecule that corresponds to the most oxidized state of carbon. As an example, the conversion of CO<sub>2</sub> into CO and O<sub>2</sub> (R1) is not spontaneous under standard conditions at 298 K, mainly because of the highly endothermic character of this reaction.



According to Le Chatelier's principle, a higher reaction temperature and a higher CO<sub>2</sub> partial pressure are required to achieve a high conversion [12, 46, 47]. Because of this thermodynamic stability of the CO<sub>2</sub> molecule in standard conditions, its dissociation can only be achieved through the use of an external energy source. In that respect, conventional chemistry processes have already been used, such as the electroreduction of CO<sub>2</sub> [27].

The addition of a source of hydrogen atoms to this process is also interesting, since H could play two roles: one in the reduction of CO<sub>2</sub> into CO and another in the hydrogenation of CO<sub>2</sub> (or CO) in order to form, for instance, oxygenated organic molecules. Examples of molecules that can act as an H-source are hydrogen, methane and water. Methane is an abundant gaseous molecule already present in Nature. This is not the case for hydrogen, which needs to be produced. Furthermore, both methane and carbon dioxide are greenhouse gases. Therefore, the reaction of these combined gases is of particular interest in order to obtain useful end products (carbon monoxide, hydrogen, oxygenated organic molecules and hydrocarbons). From a thermodynamic point of view, the production of hydrocarbons from pure methane requires high temperatures (> 973 K). The dimerization of methane is endothermic and non-spontaneous under standard conditions at 298 K. In this condition, ethane is the easiest dimer that can be obtained directly from CH<sub>4</sub> (R4).



The number of possible reactions either in pure  $\text{CO}_2$  or in pure  $\text{CH}_4$  can be numerous, but when combining carbon dioxide and methane, it becomes much larger. The reaction between them can lead, apart from  $\text{CO}$  and  $\text{H}_2$ , to the formation of organic molecules as already mentioned (oxygenated organic molecules like methanol, acetic acid, formaldehyde, and also hydrocarbons like ethane, ethylene and acetylene). Unfortunately, their formation requires quite a lot of energy as the free enthalpy of these reactions are quasi always positive. Therefore, most of them are not spontaneous under standard conditions and in thermodynamic equilibrium. The fact that plasmas are in thermodynamic non-equilibrium permits the occurrence of some reactions near room temperature. The ideal goal would thus be to exploit the products of the reaction between  $\text{CO}_2$  and  $\text{CH}_4$  as intermediates to further reduce  $\text{CO}_2$  and hydrogenated carbon. In the next section, we discuss the  $\text{CO}_2$  reforming (by  $\text{CH}_4$ ) from the point of view of a thermodynamic analysis.

## 5.2. Carbon dioxide reforming

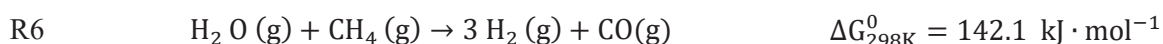
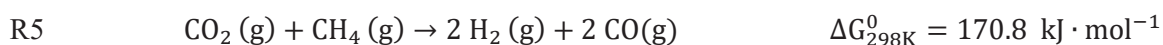
Carbon dioxide reforming (or dry reforming, represented in reaction R5) is a method of producing synthesis gas (mixture of hydrogen and carbon monoxide) from the reaction between carbon dioxide and methane. One of the disadvantages of such process is that this reaction has an endothermic character and is non-spontaneous [48, 49]. Apart from carbon monoxide and hydrogen, other products of interest can also be formed, such as oxygenated organic molecules and hydrocarbons [50, 51].

Synthesis gas is conventionally produced via the steam reforming reaction (reaction R6). In recent years, increased concerns on the contribution of greenhouse gases to global warming have increased interest in the replacement of steam by carbon dioxide [52]. Thus, two greenhouse gases are consumed and useful chemical building blocks, hydrogen and carbon monoxide, are produced. A challenge to the large-scale implementation of this process is that the hydrogen produced tends to react with the carbon dioxide to give water and carbon monoxide.

Typical catalysts for that process are noble metals (Pt, Rh, Ru, Pd), Ni or Ni alloys. In addition, a group of researchers investigated the use of activated carbon as an alternative catalyst [53-57].

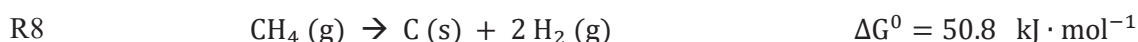
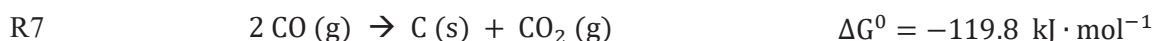
CO<sub>2</sub>-based reforming of methane has so far been much less successful than the steam reforming process, because the involved catalysts have a limited lifetime due to severe problems related to deposition of carbon on the catalyst surface, which consequently loses its activity.

Moreover, CO<sub>2</sub> reforming R5 ( $\Delta H^0 = 247.3 \text{ kJ} \cdot \text{mol}^{-1}$ ) is a more endothermic reaction as compared to steam reforming of methane R6 ( $\Delta H^0 = 206.3 \text{ kJ} \cdot \text{mol}^{-1}$ ), and requires a significant amount of energy input.



As mentioned earlier, an important reaction path of the combined CO<sub>2</sub>-CH<sub>4</sub> reaction is the formation of solid carbon deposits, which can poison the catalysts [58, 59].

In the CO<sub>2</sub> reforming reaction, the possible routes of carbon formation include methane decomposition (reaction R8,  $\Delta H^0 = 75 \text{ kJ} \cdot \text{mol}^{-1}$ ) and/or CO disproportionation (reaction R7,  $\Delta H^0 = -172 \text{ kJ} \cdot \text{mol}^{-1}$ ).



CH<sub>4</sub> decomposition is an endothermic reaction, with carbon formation being favored at higher temperatures. In contrast, CO disproportionation is an exothermic reaction, such that both equilibrium CO conversion and carbon formation decline as the reaction temperature is increased.

The clarification of this carbon deposition issue is necessary because it could help to understand the mechanism of carbon formation in this reaction. Such insight would also be beneficial not only for the design of reactors but also for the creation of stable and carbon - resistant catalysts.

Other important reactions such as the partial oxidation of methane (reaction R9), the complete oxidation of methane (reaction R10), the water gas shift reaction (reaction R11) and deoxygenation of CO (reaction R12) are also to be expected. It can be seen that an important amount of oxygen can have a negative effect (reaction R10) on the conversion of CO<sub>2</sub> and CH<sub>4</sub>.

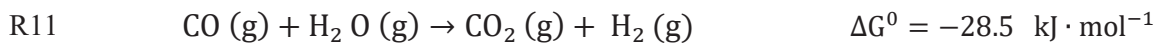
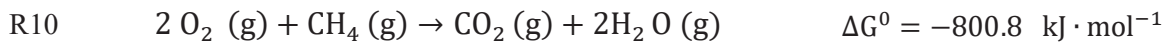
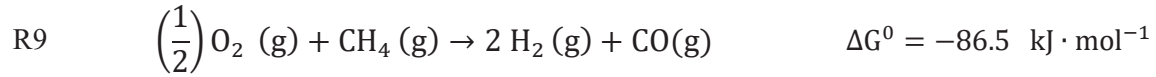


Figure 2 shows the theoretical equilibrium carbon formation during CO<sub>2</sub> reforming of methane, where all the mentioned reactions have been taken into account. In a real-world CO<sub>2</sub> reforming system, the CO<sub>2</sub>–CH<sub>4</sub> reforming reaction and side reactions, such as water gas shift reaction and carbon formation reactions, take place simultaneously. Hence, in order to obtain an equilibrium composition, the Gibbs energy minimization method [60] was employed and carried out using a commercial program by Rowlinson [12, 61].

Mainly six components can be found during CO<sub>2</sub>-based reforming, namely CO<sub>2</sub>, CH<sub>4</sub>, CO, H<sub>2</sub>, H<sub>2</sub>O, and C. Equations are established based on the mass balance of these three elements (C, H, and O). A higher carbon formation at low temperatures and a lower carbon formation at higher temperatures suggest that CO disproportionation probably dictates equilibrium carbon formation in the CO<sub>2</sub> reforming reaction since CO is the dominant source to produce carbon at lower temperatures. The CO disproportionation reaction has a large equilibrium constant at low temperatures, due to the highly exothermic character of this reaction. At higher temperatures, most of the CH<sub>4</sub> may react with CO<sub>2</sub> and form CO and, as a result, very little methane is left behind. Hence, CO will still largely determine the equilibrium carbon formation at higher temperatures in a CO<sub>2</sub> reforming reaction.

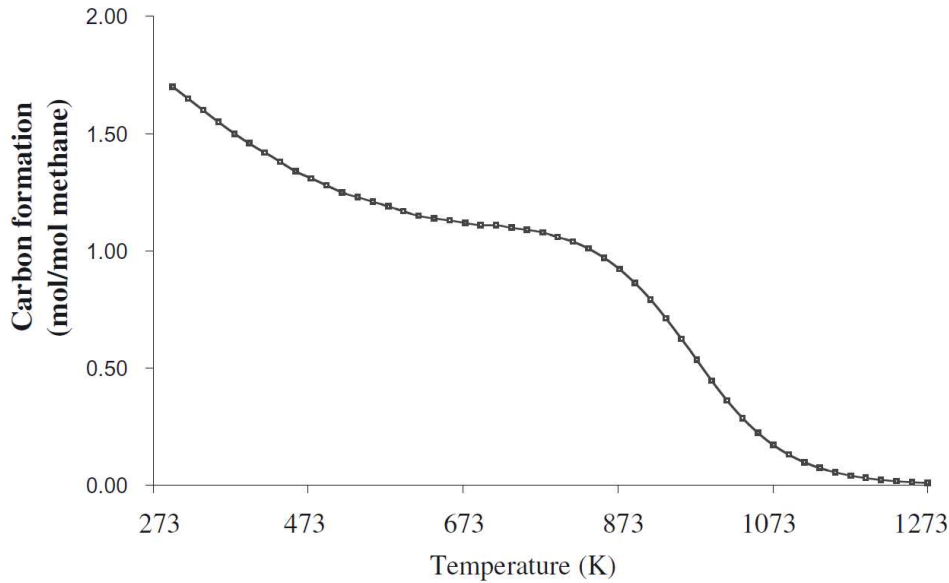


Figure 2 : Theoretical calculation of carbon formation in  $\text{CO}_2$  reforming of methane [12].

Thanks to the method of minimization of the Gibbs free energy, it is possible to determine the  $\text{CO}_2$  and  $\text{CH}_4$  conversion rates (see next section), as well as the composition balance of  $\text{CO}_2$  and  $\text{CO}$ , and to evaluate the quantity of carbon which can likely deposit on the catalyst. Nikoo et al. mention that other theoretical studies were also carried out without taking account of carbon deposit on the catalyst and that these results are closer to experimental data. In fact, it seems that the catalyst promotes the decomposition of  $\text{CO}_2$  to  $\text{CO}$  and  $\text{O}$  compared to the dissociation of methane into  $\text{C}$  and  $\text{H}_2$ , which would explain the formation of a smaller than expected amount of graphite [46]. Dry reforming of methane may also take place in a  $\text{CO}_2/\text{CH}_4$  plasma.

### 5.3. Thermal processes of $\text{CO}_2$ reforming

The main reactions that can take place in the thermal process of  $\text{CO}_2$  reforming are given below [48]. They were established by considering only  $\text{CH}_4$ ,  $\text{C}_2\text{H}_6$ ,  $\text{C}_2\text{H}_4$ ,  $\text{CO}$ ,  $\text{CO}_2$ ,  $\text{H}_2$ ,  $\text{CH}_3\text{OCH}_3$  (DME),  $\text{H}_2\text{O}$ ,  $\text{CH}_3\text{OH}$  and  $\text{C}(\text{s})$  species. The equilibrium constants, calculated for each reaction, allow discussing the influence of temperature on the conversion of  $\text{CO}_2$  and  $\text{CH}_4$ . As we can observe in Figure 3, the dry reforming reaction of methane (reaction (1)) is thermodynamically favorable only at temperatures larger than approximately 950 K.

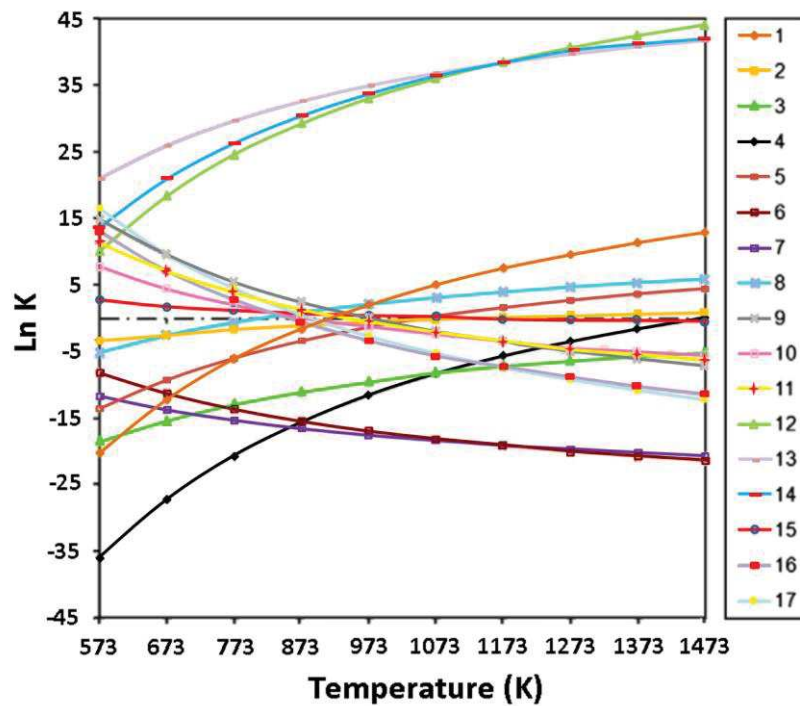
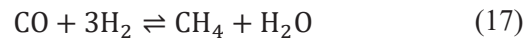
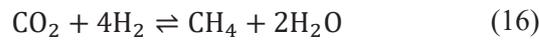
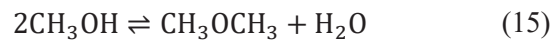
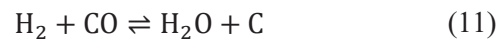
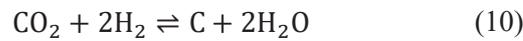
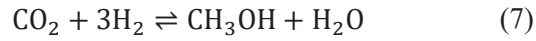
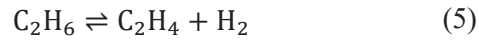
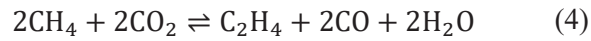
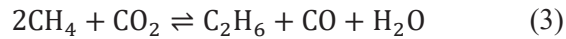
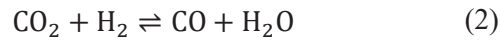
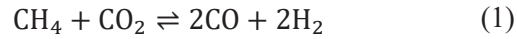


Figure 3 : Variation of equilibrium constants of reactions involved in a  $\text{CH}_4\text{-CO}_2$  mixture as a function of the temperature at atmospheric pressure [46].

CH<sub>4</sub> conversion increases with temperature regardless of the molar ratio of CO<sub>2</sub>/CH<sub>4</sub> (Figure 4a). For temperatures below 973 K, CO<sub>2</sub> appears to have a beneficial effect on methane conversion but methanation (reactions (16) and (17)) tends to compensate this effect and lowers the conversion rate. Above 973 K, the equilibrium constants associated to the methanation reactions become 1. On the other hand, as we have already noticed, the decomposition of methane becomes spontaneous and it increases the CH<sub>4</sub> conversion. Concerning the CO<sub>2</sub> conversion, CO<sub>2</sub> is mainly dissociated due to reactions (10) and (16), between 573 K and 823 K. These reactions are exothermic and their equilibrium constant decreases with increasing temperature, which explains the drop in conversion. When reaching temperatures above 873 K, reactions (1) and (2) become favorable and the conversion rate increases. The conversion decreases if the fraction of CO<sub>2</sub> in the initial mixture is increased. These trends are visible in Figure 4b.

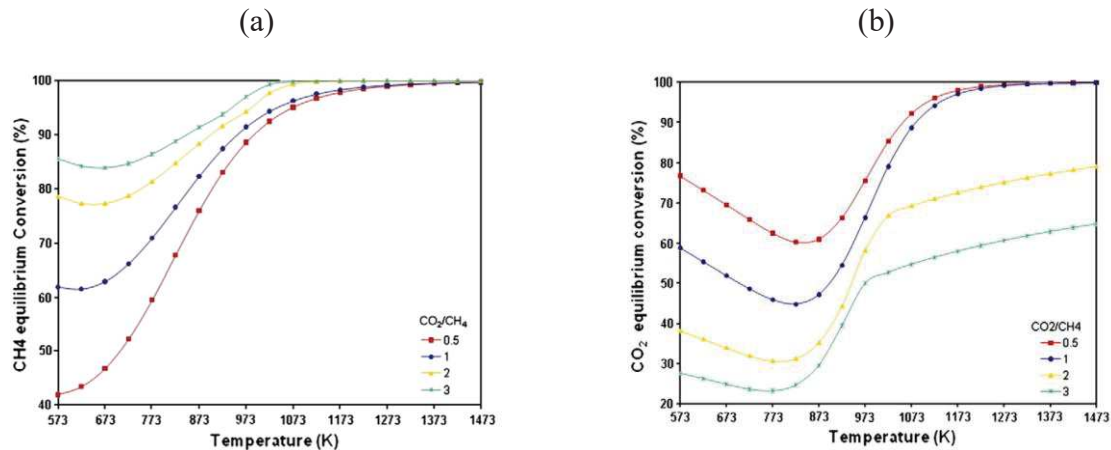


Figure 4 : (a) CH<sub>4</sub> equilibrium conversion as a function of temperature and CO<sub>2</sub>/CH<sub>4</sub> ratio at 1 atm for  $n_{\text{reactants}}=2$  mol, (b) CO<sub>2</sub> equilibrium conversion as a function of temperature and CO<sub>2</sub>/CH<sub>4</sub> ratio at 1 atm for  $n_{\text{reactants}}=2$  mol [46].

Considering a CO<sub>2</sub>/CH<sub>4</sub>=1 ratio and a temperature of 1173K, the CO<sub>2</sub> and CH<sub>4</sub> conversions are better at low pressures. This trend can be interpreted as a reaction of the system according to the Le Chatelier principle: when pressure increases, reactions that produce more gas molecules are disadvantaged. This is the case for the reforming reaction of methane (1), for the decomposition of methane (8) and for the disproportionation of CO (9). Moreover, the equilibrium of reactions (16) and (17) shifts in favor of the products. These displacements hence limit the CO<sub>2</sub> and CH<sub>4</sub> conversion. Other analyses were also made in the literature, considering a set of different chemical species. Zhu et al. carried out, for example, their analysis on a system containing CH<sub>4</sub>, O<sub>2</sub>, CO<sub>2</sub>, CO, H<sub>2</sub>O, H<sub>2</sub>, C, C<sub>2</sub>H<sub>2</sub>, C<sub>2</sub>H<sub>4</sub>, C<sub>2</sub>H<sub>6</sub>, CH<sub>3</sub>OH,

HCHO and HCOOH. [49]. They suggested that low pressure reforming is favorable whereas high temperatures can suppress the pressure effect.

#### 5.4. Plasma process

In a plasma, electrons provide the energy required for the dissociation of  $\text{CO}_2$  and  $\text{CH}_4$ . Thanks to these electrons, the mentioned reactions can take place at low temperature (around 350-400 K) while classical thermodynamic approaches predict that they should not take place at temperatures below 523 K (see above). In the temperature range between 353 and 523 K, Zhou et al. found that both the  $\text{CO}_2$ - $\text{CH}_4$  conversion and the amounts of formed products slightly increase with temperature as shown in Figure 5a and Figure 5b [48].

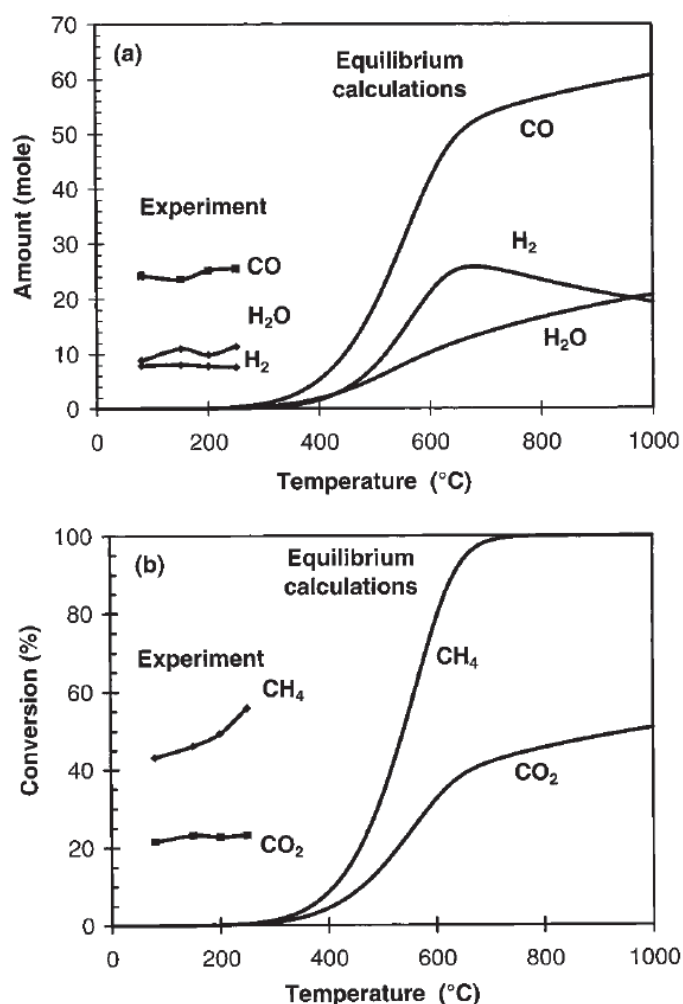


Figure 5 : (a) Product amount from 100 mol of feed gas and (b)  $\text{CH}_4$  and  $\text{CO}_2$  conversion; as a function of the temperature (dielectric barrier discharge (DBD)); power = 500 W; flow rate =  $0.5 \text{ L}_n \cdot \text{min}^{-1}$ ; pressure = 1 bar; feed  $\text{CH}_4:\text{CO}_2 = 20:80$  [48].

As in the thermal reaction, an increase in the  $\text{CO}_2/\text{CH}_4$  molar ratio yields an increase in the  $\text{CH}_4$  conversion but it decreases the  $\text{CO}_2$  conversion. In addition, the data processing (curve fitting to the experimental data) provides a relationship between the obtained  $\text{H}_2/\text{CO}$  molar ratio and the  $\text{CH}_4/\text{CO}_2$  molar ratio. A desired composition of synthesis gas can therefore be achieved in a dielectric barrier discharge from a given  $\text{CH}_4/\text{CO}_2$  ratio. We have to also note that low pressures promote  $\text{CO}_2$  and  $\text{CH}_4$  conversions. However, the  $\text{H}_2/\text{CO}$  molar ratio is not affected by the pressure in the studied range (between 0.34 bar and 2 bar), which means that the main reactions remain the same whatever the pressure.

## 6. Aim of the research

The introduction section clearly shows the increasing interest in the conversion of  $\text{CO}_2$  by means of plasma technology. Nowadays, the plasma scientific community is trying to improve the knowledge, both experimentally and theoretically (by means of simulation), concerning the  $\text{CO}_2$  splitting and how to maximize the efficiency of this process. The aim of this PhD work is to have a better insight in the physical and the chemical aspects of the  $\text{CO}_2$  dissociation in a Dielectric Barrier Discharge (DBD). In this context, the current work relies on the systematic investigation of key important points for the efficient decomposition of  $\text{CO}_2$  through studying the basic plasma parameters. These parameters play an important role in the  $\text{CO}_2$  conversion process in the physical aspect as well as the chemical aspect. From a physical point of view, the electrical diagnostics are revealed as an important topic of  $\text{CO}_2$  plasmas. Indeed, the understanding of the electrical characteristic of DBDs becomes of great interest for the plasma community dealing with gas conversion. For this purpose, a new approach and methodology is developed in order to investigate the electrical properties of the microdischarges, which are the real source of reactivity in a DBD, and understand their role in the process. The electrical characterization consists of using a numerical method to extract data in detail that are usually underestimated or poorly described in literature, in particular for filamentary  $\text{CO}_2$  discharges. A special attention is given to the investigation of tunable parameters in the DBD, which affect the  $\text{CO}_2$  splitting process and its efficiency, more specifically the residence time of the reactants in the reactor, the operating frequency, the applied power, the dielectric material and thickness, etc. Moreover, the understanding of the effect of other basic plasma parameters, such as gas temperature, wall reactor temperature, roughness of the dielectric barrier etc., is also achieved via some intrusive and non-intrusive

plasma diagnostics. All these diagnostics serve to have a better knowledge of CO<sub>2</sub> discharges and they are carried out simultaneously or successively during the experiments.

## 7. Thesis outline

The next chapter (Chapter II) is focused on the state of the art of plasma-based CO<sub>2</sub> conversion. First, a general introduction of the plasma phase is discussed to point out the interest of using a DBD system for the CO<sub>2</sub> conversion. A more specific aspect of the discharge is also present; the electrical characteristics of the DBD are described in general and also in a specific case, which is the CO<sub>2</sub> discharge. Moreover, the literature dealing with CO<sub>2</sub> conversion in non-thermal plasmas is reviewed and the differences between different characteristics of the different plasma technologies for non-thermal plasma are shown. First, the literature concerning pure CO<sub>2</sub> plasma is discussed. Afterwards, the state of the art for plasmas combining CO<sub>2</sub> with a hydrogen source is detailed. The two main reactants discussed here are methane and water. Finally, we also show other types of application of CO<sub>2</sub> plasma such as in surface treatment.

In Chapter III, the experimental setups as well as the different diagnostics are described. A description of the model used to simulate the plasma chemistry is also presented in this chapter.

Chapters IV, V and VI are dedicated to the results obtained in this PhD work. These studies are already published in the scientific literature as follows:

- A. Ozkan, T. Dufour, T. Silva, N. Britun, R. Snyders, A. Bogaerts and F. Reniers, The influence of power and frequency on the filamentary behavior of a flowing DBD—application to the splitting of CO<sub>2</sub>, *Plasma Sources Science and Technology*, 25(2) (2016) 025013
- A. Ozkan, T. Dufour, T. Silva, N. Britun, R. Snyders, F. Reniers and A. Bogaerts, DBD in burst mode: solution for more efficient CO<sub>2</sub> conversion?, *Plasma Sources Science and Technology*, 25 (2016) 055005
- A. Ozkan, T. Dufour, A. Bogaerts and F. Reniers, How do the barrier thickness and dielectric material influence the filamentary mode and CO<sub>2</sub> conversion in a flowing DBD?, *Plasma Sources Science and Technology*, 25(4) (2016) 045016

- R. Snoeckx, A. Ozkan, F. Reniers and A. Bogaerts, The quest for value-added products from CO<sub>2</sub> and H<sub>2</sub>O in a dielectric barrier discharge: a chemical kinetics study, *accepted in ChemSusChem*, (2016)
- A. Ozkan, T. Dufour, G. Arnoult, P. De Keyzer, A. Bogaerts and F. Reniers, CO<sub>2</sub>–CH<sub>4</sub> conversion and syngas formation at atmospheric pressure using a multi-electrode dielectric barrier discharge, *Journal of CO<sub>2</sub> utilization*, 9 (2015) 74-81

In Chapter IV, the splitting of CO<sub>2</sub> into O<sub>2</sub> and CO is investigated in a flowing cylindrical DBD operating at atmospheric pressure. For this purpose, the influence of electrical regimes and electrical configurations on the CO<sub>2</sub> conversion and energy efficiency of the process are studied in order to have a better understanding of the CO<sub>2</sub> discharge itself. The first section is dedicated to the variable parameters of the discharge, i.e., the gas residence time, the operating frequency, the HV discharge power and the pulsation in AC regime (so-called burst mode). The second section is focused on the change in DBD configuration, where we study the influence of the dielectric thickness and the dielectric material on the CO<sub>2</sub> splitting process.

Chapter V is dedicated to the CO<sub>2</sub> discharge ignited in the same reactor as the one used in the previous chapter, with water addition in the discharge. Both CO<sub>2</sub> and H<sub>2</sub>O conversion are discussed, and the main products formed are the syngas components CO and H<sub>2</sub>, as well as O<sub>2</sub> and H<sub>2</sub>O<sub>2</sub>. Furthermore, a comparison with simulation in the real time scale is also carried out. Indeed, the combination between experimental results and computer modeling efforts should further improve the insight related to the underlying plasma chemistry of combined CO<sub>2</sub>-H<sub>2</sub>O discharges. This understanding is fundamental for the desired industrial implementation of real plasma treatment for the massive CO<sub>2</sub> conversion into value added products.

Finally, in Chapter VI, we investigate the CO<sub>2</sub> discharge in presence of methane for the production of value added products such as CO, H<sub>2</sub>, C<sub>2</sub>H<sub>6</sub>, C<sub>2</sub>H<sub>4</sub>, C<sub>2</sub>H<sub>2</sub> and CH<sub>2</sub>O. Both the CO<sub>2</sub> and CH<sub>4</sub> conversion as well as the selectivities of different products are discussed. In this study, the influence of the carrier gas (so-called plasmagen gas) is also demonstrated on the conversions and efficiencies of the process.

Chapter VII is dedicated to the conclusion and perspectives.

# **Chapter II - State of the art of plasma-based CO<sub>2</sub> conversion**

## 1. General information on plasmas

### 1.1. Introduction

Often considered as the 4<sup>th</sup> state of the matter, plasma is defined as an ionized gas composed of electrons, ions and neutral particles [62]. It can be created when the energy supplied to the gas molecules and atoms is sufficient enough for an ejection of an electron during the collisions between particles. Although the plasma is composed of charged particles, it is characterized by overall electrical neutrality (but not locally):

$$n_{e^-} + \sum_A qn(A^{q^-}) = \sum_C pn(C^{p^+}) \quad \text{Eq. 2.1}$$

$n_{e^-}$  : electron density (m<sup>-3</sup>)  
 $n(A^{q^-})$  : negative ion density (m<sup>-3</sup>)  
 $n(C^{p^+})$  : positive ion density (m<sup>-3</sup>)

Locally, a charge is surrounded by charges with opposite sign. The charge of a particle is thus screened over a distance called Debye length ( $\lambda_D$ ). The latter represents how far these electrostatic effects persist for a charge. This critical distance characterizes the area of influence of a charged particle (electrons, positive and negative ions). Below this distance, electroneutrality is not valid due to the potential held by the charged particle. The Debye length is defined as follows:

$$\lambda_D \text{ (m)} = \sqrt{\frac{\epsilon_0 k_B T_e}{e^2 n_e}} \quad \text{Eq. 2.2}$$

$\epsilon_0$  : vacuum permittivity ( $8.85 \times 10^{-12} \text{ C}^2 \text{ J}^{-1} \text{ m}^{-1}$ )  
 $k_B$  : Boltzmann constant ( $1.38 \times 10^{-23} \text{ J K}^{-1}$ )  
 $e$  : electron charge ( $1.602 \times 10^{-19} \text{ C}$ )  
 $T_e$  : electron temperature (K)  
 $n_e$  : electron density (m<sup>-3</sup>)

Figure 6 shows the different types of plasma classified according to their electron density ( $n_e$ ) and electron energy ( $kT_e$ ). The Debye length increases when the electron energy rises. Plasmas used in laboratory contain charged species which have Debye lengths ranging between  $10^{-2}$  and  $10^{-4}$  cm.

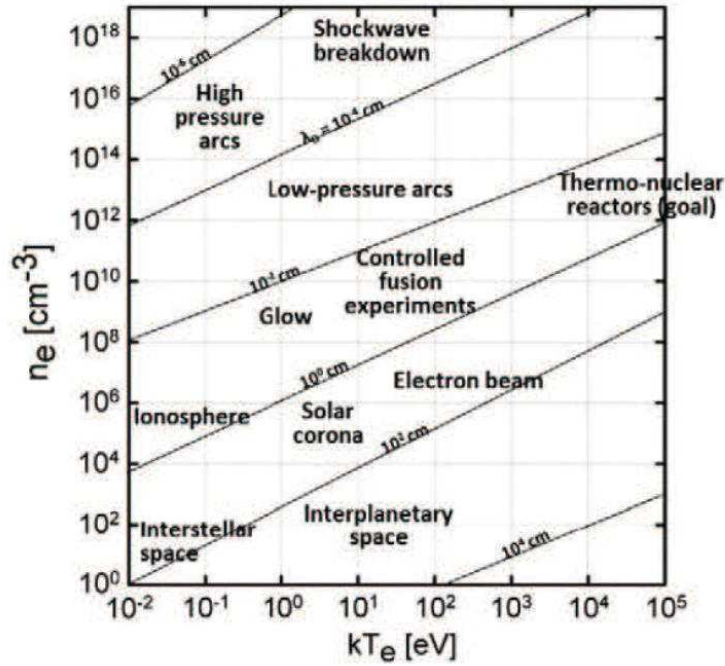


Figure 6 : Classification of plasmas in terms of their electron density and energy  $k_B T_e$  for different Debye lengths ( $\lambda_D$ ) [63].

The other parameters that are important to characterize the plasma are: the neutral species temperature ( $T_0$ ), ion temperature ( $T_i$ ) and the electron temperature ( $T_e$ ). These quantities characterize the average energy of thermal motion for particles in a system, which are defined by the kinetic theory of gases. Therefore, it is possible to distinguish plasmas in thermodynamic equilibrium ( $T_0 \approx T_i \approx T_e$ ), commonly called "hot plasmas", and plasmas in non-equilibrium ( $T_e \gg T_i$  and  $T_0$ ), commonly known as "cold plasmas". An example of a non-equilibrium plasma is the glow discharge, where  $T_e$  may vary between 1000 and 100,000 K while  $T_0$  ranges between 300 and 1000 K.

Plasmas can operate in a wide pressure range: from low pressure (few millitorrs – atmospheric pressure: laboratory use) to high pressure (hundreds of atmosphere). If the plasma is at low pressure, the electron temperature is considerably higher than the one of the heavy species due to their lower mass, which makes that they are more accelerated by the electric field in the plasma, and they lose less energy by collisions with heavy species (due to the large mass difference). By increasing the pressure, the number of neutral species and thus also the number of inelastic collisions increase. Therefore, the average kinetic energy of the electrons decreases. Their temperature also drops; one says that the system is "thermalized". Concerning gas molecules, they undergo more and more collisions, which generate an increase in temperature. In some cases, gas molecules can reach a temperature as high as

10000 K. There exist different ways to reduce these collisions, which are explained later in this chapter.

Characterizing a plasma by its temperature is possible if the distribution function (in velocity or energy) of the particles is Maxwellian. Since this condition is not verified in cold plasma, in addition to the average value of energy, we must specify the shape of the energy distribution function of the particles to know the exact characteristics of the plasma. Other types of distribution exist such as distributions of Druyvesteyn or Margenau [64]. The distribution function of the vector velocity of a particle is defined mathematically as follows:

$$f(\vec{v}) = n_e \left( \frac{m_e}{2\pi k T_e} \right)^{3/2} e^{-\frac{m_e}{2k T_e} |\vec{v}|^2} \quad \text{Eq. 2.3}$$

$n_e$  : electron density (m<sup>-3</sup>)  
 $m_e$  : electron weight (9.109 × 10<sup>-31</sup> kg)  
 $k$  : Boltzmann constant (1.38 × 10<sup>-23</sup> J K<sup>-1</sup>)  
 $T_e$  : electron temperature (K)

This function is more spread towards higher speeds when the temperature rises.

Finally, the plasma can also be characterized by its degree of ionization  $\alpha$ :

$$\alpha = \frac{n_e}{(n_e + n_0)} \quad \text{Eq. 2.4}$$

where  $n_e = n_i$  : electron density (number of particules per volume unit) (m<sup>-3</sup>)  
 $n_0$  : neutral species density (m<sup>-3</sup>)

The degree of ionization allows classifying plasmas in two main categories: the so-called weakly ionized plasmas where  $\alpha$  varies from 10<sup>-7</sup> to 10<sup>-4</sup> and the so-called strongly ionized plasmas where  $\alpha > 10^{-4}$  or close to 1.

## 1.2. Glow discharge

Plasma can be generated in several ways. The glow discharge is the simplest technique to generate in the laboratory and it also allows a good control of the plasma. A glow discharge is obtained by applying an electric current through a gas confined between two electrodes. The term "DC (direct current) discharge" corresponds to a diode discharge where the polarity of the electrodes does not change over time. One free electron must be at least present in the reactor to initiate the discharge. This electron can come from cosmic rays and has a short lifetime, therefore it is quickly consumed in normal cases. By applying a high potential

difference, the electron is accelerated and collides with atoms or molecules of the gas phase. These collisions will cause the release of other electrons which are also accelerated by the electric field, thereby allowing to have a chain-reaction (electron avalanche) that initiates the plasma. This potential difference is maintained in order to generate the plasma. The electrons are attracted towards the anode (positive electrode) and the positive ions toward the cathode, thereby establishing the electric current. A general profile of the evolution of the voltage versus current for a DC discharge is shown in Figure 7; it has three major regions: the Townsend discharge region, glow discharge region and arc discharge region.

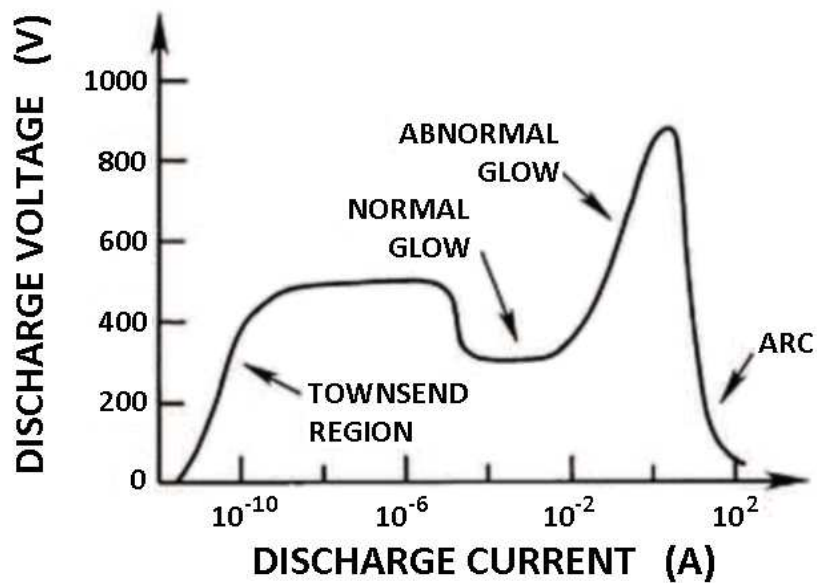


Figure 7 : Current-voltage characteristics and different schemes of DC discharge [65].

When the discharge is generated at low voltages and currents, free electrons and ions are created by cosmic radiation. The anode and the cathode collect the free electrons and ions, respectively. As the supplied current is very low, the discharge is not self-maintained: it is in a non-autonomous regime. When the current slightly increases, it gradually approaches the saturation value  $I_0$ . In this regime, the electrons do not have enough energy to create new ionization. At still larger values, electrons have enough energy to create new ionization. The multiplication of electrons results from electron impact ionization of the atoms and/or gas molecules, but also by the ion bombardment of the cathode. The current exponentially increases with the voltage until reaching the breakdown point (region called Townsend discharge).

Arriving at the glow discharge conditions, the discharge is called self-maintained and the plasma becomes bright and conducting. The current increases irrespective of the voltage. A

reduction in the resistance of the circuit leads to a growth of the current and plasma density, restructuring the electric field and leading to a decrease in the voltage and a transition from dark to glow discharge. Further resistance reduction involves the lower-voltage plateau corresponding to the normal glow discharge ( $10^{-4}$  to 0.1 A).

It is preferable to work in the abnormal region since the linearity between the voltage and the current allows to better control the plasma. A further increase in current leads to arc formation, usually taking place at currents of about 1 A.

The glow discharge is easily created at low pressures. To generate a glow discharge at atmospheric pressure, various constraints appear. Indeed at atmospheric pressure, the density of species is much higher than at reduced pressure. The mean free path ( $\lambda$ ) is drastically reduced.

$$\lambda \text{ (m)} = \frac{k_B T}{\sqrt{2\sigma p}}$$

$k_B$  : Boltzmann constant ( $1.38 \times 10^{-23} \text{ JK}^{-1}$ )

T : temperature (K)

$\sigma$  : collision cross section ( $\text{m}^2$ )

$\sigma = pd^2$  and d : diameter of the specie (considered as spherical)

p : pressure (Pa)

Eq. 2.5

Therefore, the collision frequency (molecule-molecule; electron-molecule) is much higher at atmospheric pressure compared to low pressure plasma.

The two major issues to face when increasing the pressure in the discharge are the arc formation and the increase of the voltage necessary to initiate the plasma (breakdown voltage). The first problem can be solved by placing a dielectric layer between two electrodes. The second issue is explained by the Paschen law. Both problems are described in the following paragraphs.

### 1.3. Dielectric barrier discharge

At atmospheric pressure, the density of species is high, i.e. the mean free path is small and the collision frequency is high. If the number of electrons in the discharge is not controlled, the number of ionizations can drastically increase and the plasma hence operates in arc regime (thermal equilibrium).

The transition to the arc regime is defined as a system in cascade where the electrons generated by collisions are so much accelerated that they ionize other species generating other electrons and so on. To limit the transition to the arc, covering at least one of the two electrodes by an insulating layer is necessary (Figure 8). This gives rise to a Dielectric Barrier Discharge (DBD), which is also called silent discharge. It corresponds to a non-equilibrium plasma.

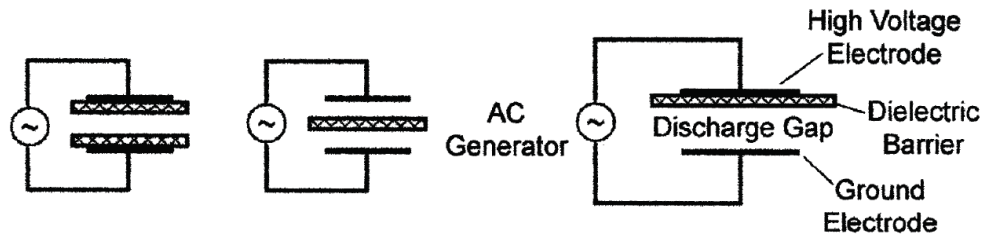


Figure 8 : Several configurations of planar DBD systems [66].

In a direct current DC discharge, if the dielectric material would cover the anode for example (positive electrode), the generated electrons are attracted to this electrode and reach the dielectric surface. At this time, the electrons cannot flow through the material and therefore accumulate on its surface. With the presence of an electric field, the dielectric barrier is polarized while remaining neutral overall. The negative charges which deposit on the dielectric generate an opposite local electric field in the plasma region near the dielectric. The latter affects the total electric field of the discharge. Therefore, the voltage affecting the electrons in the plasma bulk decreases. Once the steady state is reached, the charge on the dielectric induces an electric field equal to the one induced by the plasma voltage but in opposite direction. The electron acceleration decreases and the positive voltage tends to zero. Transition to the arc regime is hence avoided since the electrons are not accelerated quickly enough. However, the discharge tends to extinguish after a while. In order to maintain this discharge at the macroscopic level, an alternating voltage (AC discharge or pulsed voltage) is applied. Indeed, if one reverses the polarity of the electrodes over time, the induced charge on the dielectric dissipates periodically and the plasma is thus maintained.

### 1.4. Paschen's Law

The second limitation due to the atmospheric pressure is the increase of the voltage necessary to initiate the plasma. The breakdown voltage of a gas depends on the product of the gas pressure and the inter-electrode distance. This relationship is described by Paschen's law:

$$V_{bd} = Bp \frac{d}{(C + \ln pd)}$$

Eq. 2.6

$V_{bd}$  : breakdown voltage (V)

$p$  : pressure (Pa)

$d$  : inter-electrode distance (m)

B and C: constants depending on the gas

This theoretical relation is represented by the Paschen curve (Figure 9) and indicates that a minimum breakdown voltage for one configuration and for one gas exists. This value corresponds to "Paschen minimum".

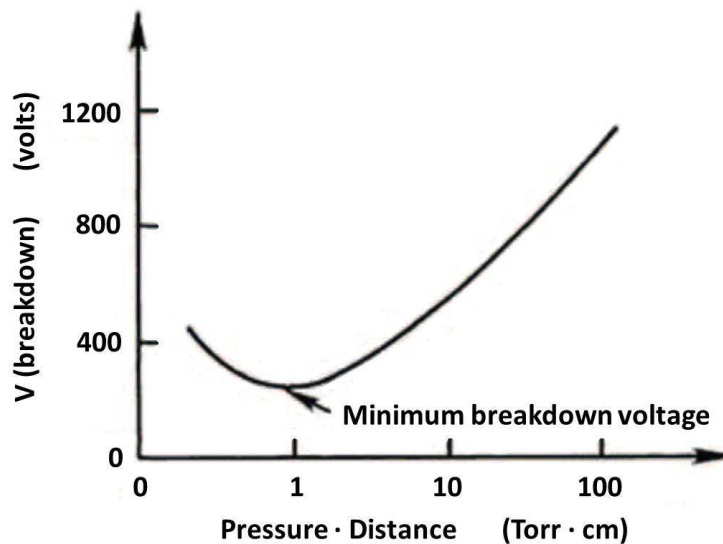


Figure 9 : Typical Paschen curve [65].

If the pressure becomes too high, the ionization by collisions becomes too low since the mean free path of the electrons is too small for them to acquire sufficient energy. This results in a higher minimum breakdown voltage. However, if the pressure is too low, the mean free path of the species is too high and hence, the number of collisions is not important enough to generate the plasma by electron avalanche. In this case too, a higher breakdown voltage is necessary. Considering a fixed pressure (atmospheric pressure), it is possible to reduce the inter-electrode spacing ( $d$ ) in order to avoid applying a too high voltage. Atmospheric plasmas are therefore operated in relatively small volumes.

## 1.5. Two regimes and electrical circuit of a dielectric barrier discharge

### 1.5.1. Two different regimes in a DBD

Two modes, either homogeneous or filamentary mode, may exist in a dielectric barrier discharge according to the nature of the gas, the nature of the electrodes, the pressure and the inter-electrode distance.

In the first case, the Townsend breakdown regime leads to a uniform and diffuse glow discharge. The latter consists of an equal distribution of the plasma species in the positive column (Figure 10) [67]. Such homogeneous mode is obtained when using rare gases, so-called plasmagen gases (helium, neon and argon, the latter can be homogeneous at reduced pressure, just below atmospheric pressure), but also nitrogen as discharge gas [68-71]. This is a desirable property for plasma treatments because it allows to treat uniformly a surface area during deposition (PECVD for example) or surface treatment [72]. It can also handle a larger volume during treatment of flowing waste gas. However, at atmospheric pressure, the realization of a diffuse discharge is restricted to particular conditions of geometry, electrical parameters, and gas composition [68-71]; thus, DBDs generally operate in a streamer/filamentary regime in which several narrow discharge filaments are typically formed.

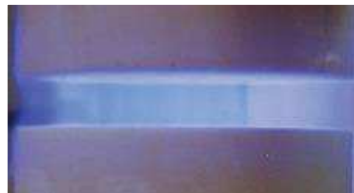


Figure 10 : Picture of a homogeneous discharge in a DBD [73].

In the case of the filamentary regime, electronic avalanches are initiated at several places over the dielectric and they spread via filaments called microdischarges when a sufficiently high voltage is applied between the electrodes. When the applied voltage exceeds the breakdown voltage the discharge is ignited and the total current increases. The breakdown voltage is the voltage needed to sustain the discharge, which is smaller than the ignition voltage due to residual charge carriers on the dielectrics [74]. A dielectric barrier is used to distribute the microdischarges uniformly over the electrode surface as shown in Figure 11. Plasmas can occur in such mode when they operate in O<sub>2</sub>, CO<sub>2</sub> or H<sub>2</sub>O for example.



Figure 11 : Picture of a filamentary discharge in a DBD [73].

Kogelschatz et al. [66] explain that, in a filamentary regime, each short-lived microdischarge has an almost cylindrical plasma channel - typically of about 100  $\mu\text{m}$  radius - a lifetime of a few nanoseconds, and spreads (in space and time) into a larger surface discharge at the dielectric surface(s). As schematically shown in Figure 12, there are four stages that characterize the evolution of a microdischarge: (i) electron avalanche formation (pre-breakdown phase), (ii) streamer growth, (iii) bridging of the gas gap between the electrodes and spreading on the surface (surface propagation), and (iv) finally decay of the filament. The radii of the microdischarge channels can be grouped in the following order according to the nature of gas: oxygen < carbon dioxide < air < nitrogen < xenon < helium. These features also depend on the device configuration [75-77]. On the other hand, diffuse or homogeneous discharges at breakdown lead to sufficient overlap of simultaneously propagating electron avalanches to cause smoothing of transverse field gradients. This condition is met most easily in helium with its relatively wide streamer channels.

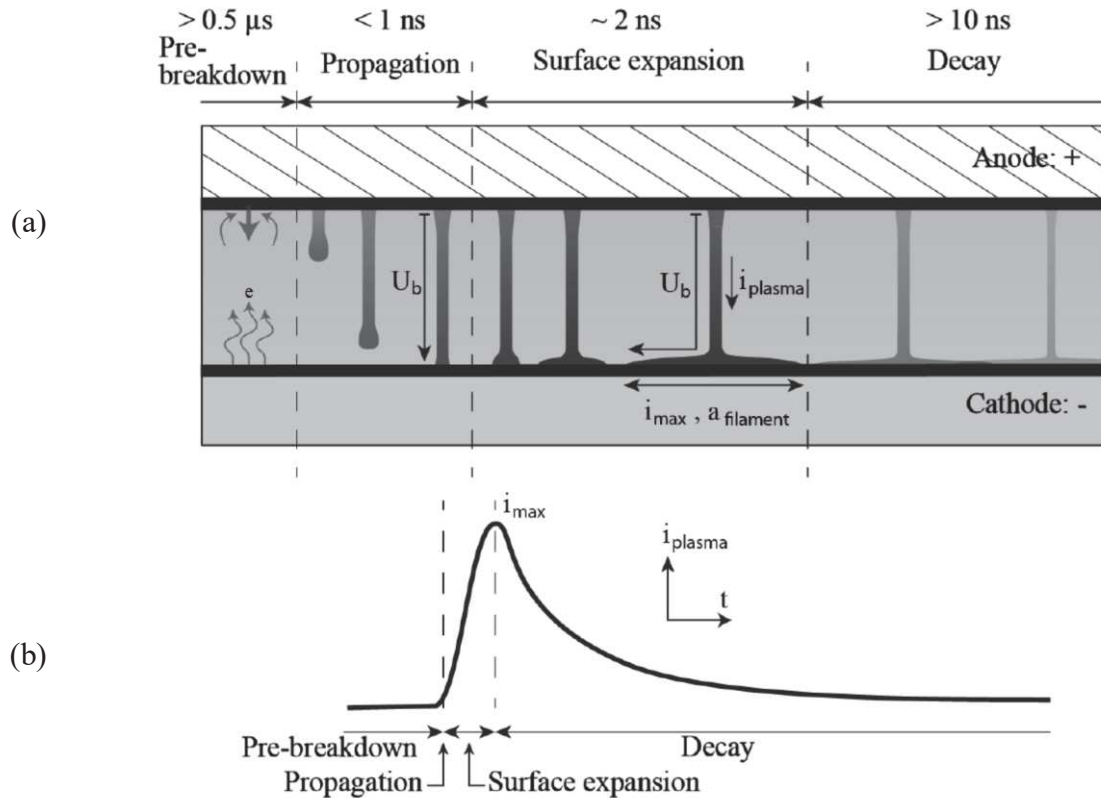


Figure 12 : Dynamics of one individual microdischarge; (a) spatial extent at different stages of a cathode directed filament development and (b) qualitative picture of the discharge current due to the filament during these stages [78].

### 1.5.2. Electrical circuit for a DBD

DBDs, both in planar or cylindrical geometry, can be represented by an equivalent electrical circuit, before and during a plasma ignition, as shown in Figure 13. It consists of two capacitors (or three if there are two dielectric barriers) in a serial connection: one for the gap with gas and the other one (or two) for the dielectric barrier(s) [66, 70, 72, 79-87]. Kogelschatz [66], Chiper et al. [80] and Naudé et al. [82] included a variable resistor which represents the microdischarge channel.

Indeed, by applying an electric field larger than the breakdown, a local field breakdown in the gap is initiated. In the equivalent circuit, this is symbolized by closing a switch and forcing some of the current through the plasma filament, whose resistance  $R(t)$  rapidly changes with time. The total charge  $Q$  transferred in a microdischarge depends on the gas properties and can be influenced by the gap spacing and by the properties of the dielectric.  $Q$  is proportional

to the width of the discharge gap  $d$ , to the relative permittivity  $\epsilon$  and to the thickness of dielectric. However, contrary to what one might expect,  $Q$  does not depend on the gas density [88]. Both the gas capacitance value  $C_g$  and the equivalent resistance  $R_{\text{disch}}$  depend on the applied gas composition [89].

In this model, the applied voltage ( $V_{\text{DBD}}$ ) is the sum of two voltages: the voltage across the gap ( $V_{\text{pl}}$ ) and the voltage across the dielectric material ( $V_{\text{diel}}$ ).

$$V_{\text{DBD}}(t) = V_{\text{pl}}(t) + V_{\text{diel}}(t) \quad \text{Eq. 2.7}$$

According to Kirchhoff's laws, the total current of the reactor ( $i_{\text{DBD}}$  or  $i_{\text{tot}}$ ) is the sum of two currents: the discharge current ( $i_{\text{pl}}$  which represents the microdischarges) and the dielectric current ( $i_{\text{diel}}$ ; displacement current in the dielectric barrier). Figure 14 shows a typical oscillogram of the voltage and the current. The orange curve represents the total current profile while the several current short peaks, present at each half period, represent the active current  $i_{\text{pl}}$ . In-between two subsequent discharge cycles the current is not equal to zero, which is caused by residual charges in the gas gap and on the dielectrics. The displacement current of the total capacity is seen as the sinusoidal trend of the current profile. It can be directly determined on the oscillogram by fitting a sinusoidal function to the signal. The latter attains indeed a sinusoidal shape because the gas remains weakly ionized during the discharge process and the capacitance can be considered constant [67, 70]. By subtracting the displacement current from the total current, the active current can be calculated. In a glow discharge, only the charge and the current can be calculated, while in a streamer (filamentary) regime, a detailed statistical analysis can be carried out on the individual and the collective behavior of the microfilaments occurring at each half period (both positive and negative) [90]. The characteristics of these microdischarges are dictated by the gas pressure, the type of gas, the plasma power and the repetition frequency [71, 75].

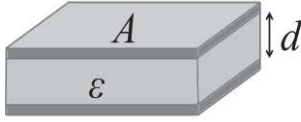
The current in each capacitor can be described mathematically as follows:

$$i_{\text{diel}}(t) = i_{\text{DBD}}(t) = C_{\text{diel}} \frac{dV_{\text{diel}}(t)}{dt} \quad \text{Eq. 2.8}$$

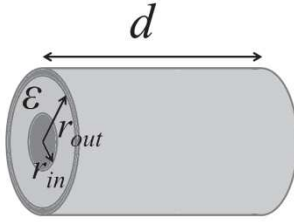
$$i_{\text{diel gap}}(t) = [i_{\text{DBD}}(t) - i_{\text{pl}}(t)] = C_{\text{g}} \frac{dV_{\text{pl}}(t)}{dt} \quad \text{Eq. 2.9}$$

with  $i_{\text{diel gap}}$  = the displacement current in the gap.

The first capacitor in the electrical circuit represents the capacitance of the dielectric barrier ( $C_{\text{diel}}$ ) and the second one represents the capacitance of the gap ( $C_{\text{g}}$ ). The equations below (2.10 and 2.11) can be used as an estimation of the capacitance values  $C_{\text{g}}$  and  $C_{\text{diel}}$ , in case of a parallel-plate capacitor and cylindrical tube capacitor. The order of magnitude of these capacitors in a DBD is in pF ( $1 \text{ F} = 1 \text{ s}^4 \cdot \text{A}^2 \cdot \text{m}^{-2} \cdot \text{kg}^{-1}$ ).



$$C_{\text{planar}} = \frac{\epsilon_0 \epsilon_r A}{d} \quad \text{Eq. 2.10}$$



$$C_{\text{cylindrical}} = \frac{2\pi\epsilon_0\epsilon_r L}{\ln\left(\frac{r_{\text{out}}}{r_{\text{in}}}\right)} \quad \text{Eq. 2.11}$$

with  $\epsilon_0$  = permittivity of vacuum ( $8.854 \cdot 10^{-12} \text{ F} \cdot \text{m}^{-1}$ ) →

$\epsilon_r$  = permittivity of the dielectric material or gas (1.000922 for gaseous CO<sub>2</sub>)

Differentiating equation 2.7 with respect to time, and replacing equation 2.8 and 2.9, we obtain:

$$\begin{aligned} V_{\text{DBD}}(t) = V_{\text{diel}}(t) + V_{\text{pl}}(t) &\rightarrow \frac{dV_{\text{DBD}}(t)}{dt} = \frac{dV_{\text{diel}}(t)}{dt} + \frac{dV_{\text{pl}}(t)}{dt} \\ &= \frac{i_{\text{DBD}}(t)}{C_{\text{diel}}} + \frac{[i_{\text{DBD}}(t) - i_{\text{pl}}(t)]}{C_{\text{g}}} \end{aligned} \quad \text{Eq. 2.12}$$

Finally, the current  $i_{\text{pl}}(t)$  can be calculated from equation 2.12 in terms of the external measurable parameters  $i_{\text{DBD}}(t)$  and  $V_{\text{DBD}}(t)$  ( $A \sin \omega t$ ) as:

$$i_{\text{pl}}(t) = \left(1 + \frac{C_{\text{g}}}{C_{\text{diel}}}\right) i_{\text{DBD}}(t) - C_{\text{g}} \frac{dV_{\text{DBD}}(t)}{dt} \quad \text{Eq. 2.13}$$

In order to determine the voltage components, the dielectric voltage is obtained by integrating equation 2.8 as follows:

$$V_{\text{diel}}(t) = \frac{1}{C_{\text{diel}}} \int_0^t i_{\text{DBD}}(\tau) d\tau + V_{\text{diel}}(0) \quad \text{Eq. 2.14}$$

And the gap voltage can be obtained by substituting equation 2.14 into equation 2.7.

$$V_{\text{pl}}(t) = V_{\text{DBD}}(t) - \frac{1}{C_{\text{diel}}} \int_0^t i_{\text{DBD}}(\tau) d\tau - V_{\text{diel}}(0) \quad \text{Eq. 2.15}$$

$V_{\text{diel}}(0)$  corresponds to the memory voltage that is a consequence of the charge accumulated in the previous half period. Depending on the applied voltage waveform, the value of  $V_{\text{diel}}(0)$  acquires different values. One has to know that the phenomenon called “memory effect” is a dominant feature in DBDs [75, 91]. In discharges ignited with continuous AC high-voltage, this effect can be described as the localization of filaments in space and in time. The origin of the memory effect can be explained in terms of volume mechanisms or more importantly in terms of charge accumulation on the dielectrics [75]. From the point of view of volume mechanisms, residual ions or metastables produced from one filament are present in higher concentrations in the location where the filament occurred in previous voltage cycle. These active species can help reignite the filament again at the same location and for the same applied voltage (i.e., time in a voltage cycle). The residual plasma conductivity can hence help in re-igniting the plasma again at the same spot because of the slow diffusion of charges left in the gap [92], and the driving voltage is thus locally modified. Moreover, the charge transported by the microdischarges to the dielectric cannot reach the conducting electrode as it accumulates near the insulator surface until the decrease in the local electric field extinguishes the current filament. The low mobility of charges on the dielectric also limits the lateral dimension of the modified field permitting the formation of other streamers in the proximity [90].

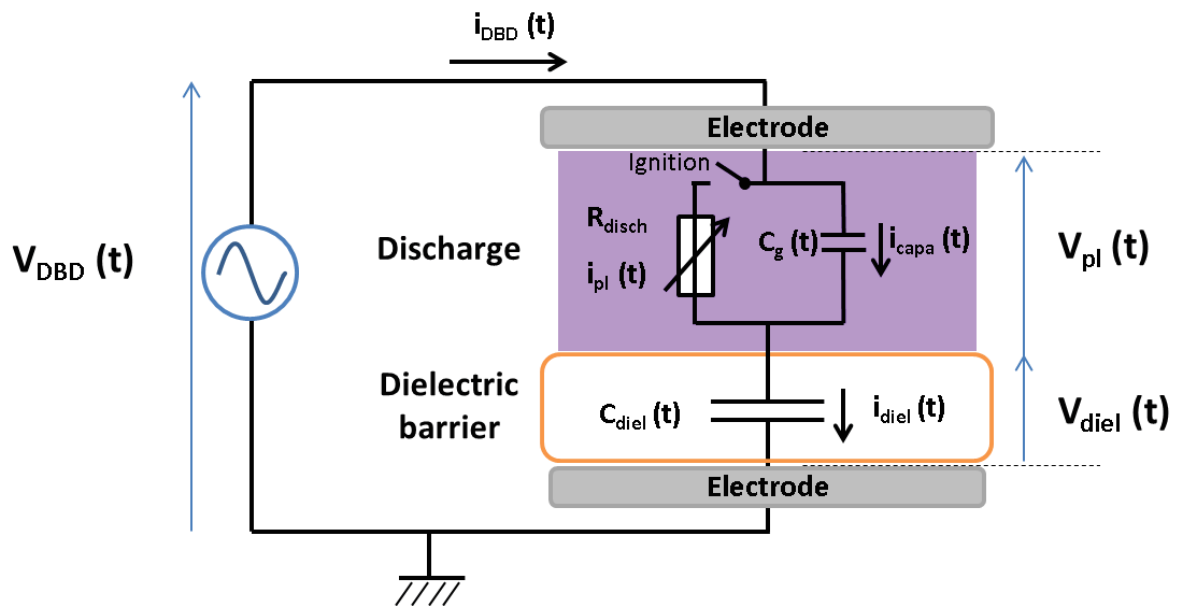


Figure 13 : Simple equivalent circuit of a DBD.

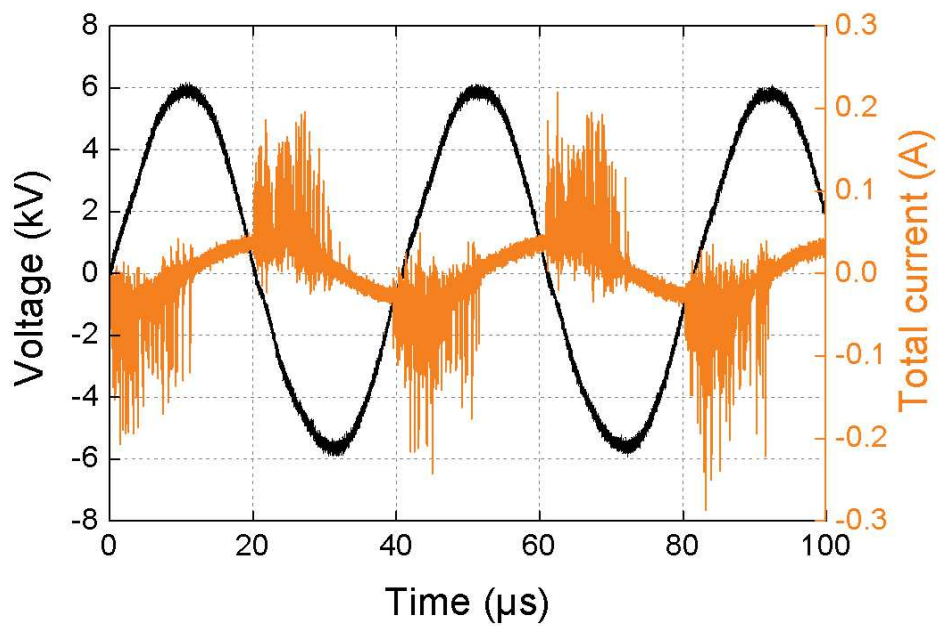


Figure 14 : Typical current-voltage waveforms for a filamentary DBD.

## 2. Properties of CO<sub>2</sub> plasmas

### 2.1. Reactivity of the plasma

The plasmas used in our laboratory are out of equilibrium, in which electrons contain an important part of the energy, much more than the heavy particles. A large fraction of the total plasma energy is also due to the emitted UV light (with photons reaching energy up to 40 eV [93]). The fact to have highly energetic electrons ( $10^4$ – $10^5$  K or 1–10 eV) allows the realization of endothermic chemical processes (such as the decomposition of CO<sub>2</sub>) in the discharge, while maintaining an ambient temperature into the reactor (near room temperature). Indeed, the heat capacity of these electrons is very low and the temperature related to the agitation of the gas molecules as well. These convenient temperatures thus prevent energy losses observed in conventional chemical processes that take place at high temperatures. It is the high electron temperature that determines the chemistry of non-thermal plasmas. Apart from the electrons, another important source of reactivity in the plasma are the metastable species, obtained with gases like helium, argon or nitrogen. These inert gases have already been used in combination with CO<sub>2</sub> in literature [94-99].

In a plasma, the most frequent reactions can be grouped into three categories: (i) reactions by electron impact, (ii) reactions by inelastic collisions between heavy particles and (iii) reactions between the plasma and the solid surfaces (walls of the reactor, electrodes, catalysts ...).

The plasma phase can be used in order to reduce CO<sub>2</sub> into CO and O<sub>2</sub> due to the energetic electrons [28]. When there are inelastic collisions between electrons and heavy particles in the gas phase, there is excitation, ionization, fragmentation/dissociation of the molecules or also formation of radicals. The excitation reactions are most likely because the energy threshold is lower than in the case of ionization for instance. In collisions involving electron impact processes, the reaction rate coefficients are described by means of the electron energy distribution function (EEDF)  $f(\epsilon)$ , which can be interpreted as the probability density for an electron to have energy  $\epsilon$ . In many practical cases, this function follows the well-known Maxwellian distribution in the first approximation for a non-thermal plasma. This function is characterized by the electron temperature  $T_e$ , thus depending on the electric field and gas composition [100]. The EEDF is generally calculated via the numerical solution of the Boltzmann equation [101]. A correlation between the EEDF and the cross section of some

specific reactions that could occur in the plasma phase can be made. An example in the case of CO<sub>2</sub> cross sections is represented in Figure 15a. The overlap between the EEDF and the cross section of a reaction gives an area which represents the efficiency and the speed of the reaction occurring in the plasma. On the other hand, the area of the EEDF which is not covered by the reaction cross sections, i.e. the major part, corresponds to the inefficiency of the process and thus, the energy which is not useful for the reaction progress. The electron energy received from the electric field in a non-thermal plasma is distributed between elastic energy losses and different channels of excitation and ionization. In terms of excitation energy in a molecule, there are four major channels into which energy can be transferred: the vibrational, electronic, rotational and translational (kinetic) channels. Each of these channels has different chemical pathways for dissociation with different energy efficiency.

Figure 15b depicts the fraction of electron energy that is typically transferred to the different channels for CO<sub>2</sub> as a function of the reduced electric field  $E/n_0$ . This figure shows some general features, which are similar also for the other gases. For example, the contribution of rotational excitation of molecules and elastic energy losses are essential only at low  $E/n_0$ , corresponding to low electron energy (less than 1 eV) since these two parameters are linked to each other. At electron temperatures of about 1 eV, which is conventional for non-thermal discharges, most of the electron energy and, therefore, most of the discharge power goes into vibrational excitation of molecules. It makes the process of vibrational excitation very important and special in the non-equilibrium plasma chemistry of molecular gases. CO<sub>2</sub> has different vibrational modes despite its linearity and its symmetry in the ground state. Indeed, the CO<sub>2</sub> exhibits vibrations in three different main modes: the symmetric stretching, the bending and asymmetric stretching [7]. These vibrationally excited molecules can help overcome the activation energy barrier of many reactions related to the CO<sub>2</sub> decomposition [102, 103]. The kinetics based on CO<sub>2</sub> vibrations, such as the vibrational-vibrational (VV) relaxation, is important to understand its splitting process. Indeed in CO<sub>2</sub> plasmas, vibrational excitations are considered as the species which are the most efficient to stimulate the endothermic CO<sub>2</sub> dissociation because it requires, compared to other processes, the least amount of energy input [64]. The CO<sub>2</sub> decomposition predominantly proceeds by electron impact vibrational excitation of the lowest vibrational levels, followed by VV collisions, which populate the higher vibrational levels. Fridman has suggested that the asymmetric stretch mode is the most efficient mode for CO<sub>2</sub> dissociation [64]. On the other hand, electronic excitation by electron impact occurs via highly energetic electrons, which

correspond generally to the tail of the EEDF in a typical non-thermal plasma. Note that rotational (energy is transferred to the rotation of the molecule around its axis) and translational (energy transferred to the motion of the molecules) excitations do not initiate pathways for CO<sub>2</sub> dissociation. Although high kinetic energy leading to collisions can cause CO<sub>2</sub> dissociation, it is not considered as an important dissociation pathway since all the kinetic energy is easily transferred to other energy states when colliding between other heavy particles. This process becomes less inefficient at very low pressures.

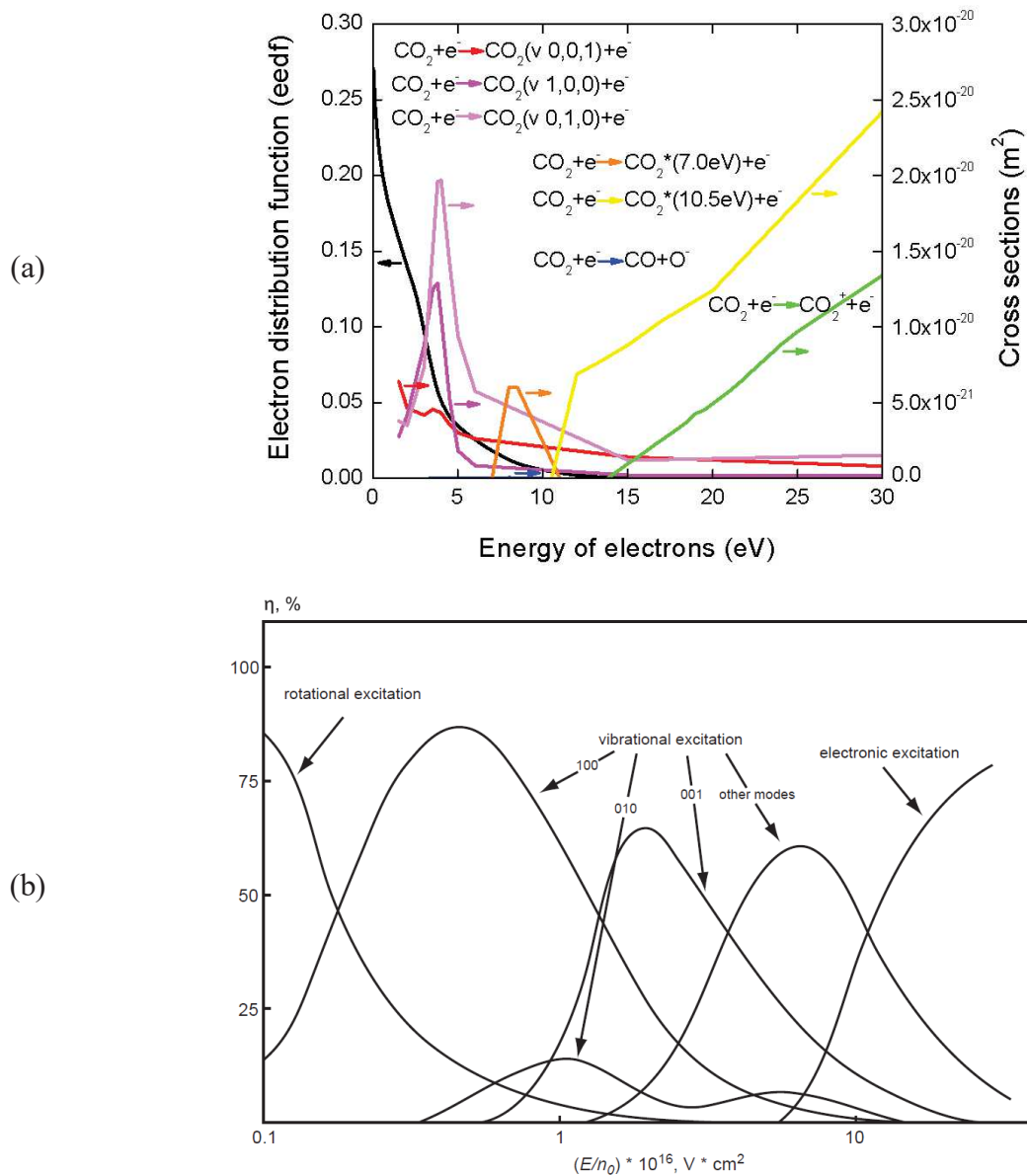


Figure 15 : (a) Representation of the electron energy distribution function (EEDF) for a typical CO<sub>2</sub> discharge and CO<sub>2</sub>-based cross sections of excitation, dissociation and ionization (values adopted from LXCat.net) and (b) fraction of electron energy transferred to different excitation channels in CO<sub>2</sub> [64].

To summarize, cold plasma can be applied to flowing gas treatment, and it is considered to show much promise for processes requiring energy, like organic syntheses or CO<sub>2</sub> dissociation, on the basis of its non-equilibrium properties, low power requirements, and its capacity to induce physical and chemical reactions within gases at relatively low temperatures. Therefore, these cold atmospheric plasma processes appear as a convenient and innovative method, since most of the energy is supplied by electrons, avoiding excessive

energy losses in gas heating. At the same time, since the electrons are significantly hotter than the bulk gas, the degree of non-equilibrium in the plasma is enhanced [64]. Therefore, and contrary to the case of thermal plasmas, there is less amount of energy dissipated by heating, which is particularly useful to avoid reverse reactions that form back CO<sub>2</sub> (CO<sub>2</sub> formation is favored at high temperature like in the thermal process).

## **2.2. Different types of plasma for CO<sub>2</sub> treatment**

Plasma technology is attracting a lot of attention because of several advantages over conventional gas conversion techniques as mentioned in the introduction. In recent years, many publications report on CO<sub>2</sub> recycling following reduction in plasma phase [64]. Based on the mechanisms by which plasma is generated, the pressure applied and the electrode geometry, non-thermal plasmas can exist as several very different types, including glow discharge, corona discharge, gliding arc discharge, dielectric barrier discharge, microwave discharge and radiofrequency discharge [104]. These different kinds of devices are used for CO<sub>2</sub> conversion and described below. Among these sources, most of the energy required for the dissociation of CO<sub>2</sub> depends on the EEDF as previously mentioned. The average electron energy is typically between 1 and 5 eV [105-109], depending on power, frequency (and dielectric barrier characteristics in case of DBDs). Moreover, every gas behaves differently in a discharge since the reactions with electrons and their energy dependence are different. Ar, He and N<sub>2</sub> are already known to change the CO<sub>2</sub> discharge behavior by changing for example the density and energy of electrons [94, 97, 110, 111].

### ***2.2.1. Dielectric barrier discharge***

Various types of plasma sources have already been employed for CO<sub>2</sub> conversion but the dielectric barrier discharge is the most widely used [112-118]. Most of the time, a DBD is investigated in a tubular configuration. The main advantage is the treatment of the quasi entire gas flow, since all the gas passes through the active discharge region (although not all molecules will pass through all the filaments), in contrast to coronas and gliding arcs where there can be “dead volumes”. Moreover, a DBD reactor has a simple design that can easily be up-scaled for industrial applications and for combination with catalysis, it is easy-to-handle with relatively cheap equipment, it operates at atmospheric pressure, and it has already been

demonstrated for the ozone synthesis as a commercial gas treatment application [66, 119-121]. It has been shown that a flowing DBD setup presents a good compromise between a reasonable energy efficiency and a high CO<sub>2</sub> conversion for low specific energy input [94]. Using a tubular DBD offers a promising and innovative solution since the transformation of CO<sub>2</sub> can be performed "on line", i.e. directly at the output of industrial chimneys instead of releasing the CO<sub>2</sub> into the atmosphere and hence increase the greenhouse effect. Therefore, it does not require capture, transport or storage of CO<sub>2</sub> and, for instance, could partially close the carbon loop if coupled to green electricity. It is also possible to further improve the efficiency of the DBD (basically around 10-15%) by combining it with catalysts in packed bed configuration [122, 123].

In the latter case, the gap between the two electrodes is packed with dielectric pellets (or full/porous beads) which aim to concentrate the electrostatic lines of flux leading to enhanced electric fields at the contact points between the beads. Moreover, catalysts can be introduced in such configuration to exploit the synergistic effect between plasma and surface [115]. In such a case, it could allow the selective production of value-added chemicals but also improve the energy efficiency of CO<sub>2</sub> splitting [114, 124-126].

Since the C=O bond dissociation energy of the CO<sub>2</sub> molecule is 5.52 eV, electrons must have energies larger than this value to directly dissociate CO<sub>2</sub>. Typically this corresponds to the tail of the electron energy distribution function (EEDF) and only a small fraction of electrons has such high energies. Most electrons have energies around 2-3 eV [127], which is also somewhat too high for exciting the vibrational states of CO<sub>2</sub> in a DBD. Indeed, Aerts et al. [127] and Kozák et al. [103] have shown that these vibrationally excited states have a minor influence on the CO<sub>2</sub> splitting in a DBD. As vibration-induced dissociation is considered the most energy-efficient process for CO<sub>2</sub> splitting, this explains the current limited energy efficiency (around 10-15%) of a DBD for CO<sub>2</sub> splitting. When not all energy is transferred to vibrational excitation, electronic excitation is the next best dissociative process. Electronic excitation will induce dissociation pathways of CO<sub>2</sub>, such as dissociative attachment, direct electron impact dissociation, and dissociative ionization. Only this discharge is investigated in this PhD work.

### 2.2.2. Corona discharge

The corona discharge is an inhomogeneous discharge, initiated at atmospheric pressure using inhomogeneous electrode geometries. The high voltage electrode is a pointed shape wire and the grounded electrode is a conductive plate, which causes arcs of conical shapes in a confined space when the discharge is ignited as shown in Figure 16. It is the small radius of curvature at the top of the wire electrode that leads to the high non-uniform electric field required to ionize the neutral molecules. Initially, the corona discharge was considered to be the most effective technique for producing CO from CO<sub>2</sub> [128]. Typical gas flow rates used in this technology are in the order of a few to a hundred mL·min<sup>-1</sup>.



Figure 16 : Pictures of CO<sub>2</sub> plasma generated by corona [129].

### 2.2.3. Gliding arc discharge

The gliding arc discharge occurs between two electrodes in "V" shape. The flowing gas and thus, the formed arcs move very fast in the increasing inter-electrode distance direction. This technology permits to treat higher gas flow rates at atmospheric pressure, in the order of several L·min<sup>-1</sup>. The experimental design of a classical gliding arc reactor is shown in **Figure 17**. This type of plasma generates very powerful arcs and it is suitable for gas treatment [130-132]. It has also been reported to be used for the conversion of CO<sub>2</sub> [133-136]. Nunnally et al. [134] has reported energy efficiencies reaching 43% for the decomposition of CO<sub>2</sub> in a reverse vortex flow gliding arc, which is quite high compared to the efficiency obtained with DBDs. The high energy efficiency is attributed to the: (i) high degree of non-equilibrium obtained, (ii) reverse vortex flow configuration (also known as tornado effect), (iii) high

residence time of the species in the plasma, (iv) minor role of reverse reactions and (v) uniform gas treatment.

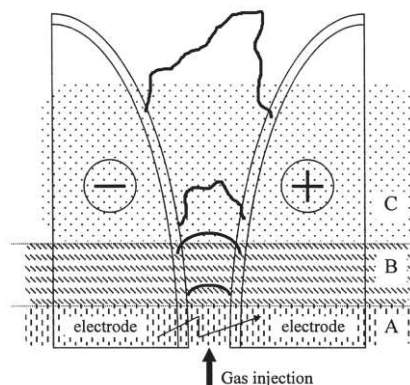


Figure 17 : Schematic configuration of a classical gliding arc. Phases of gliding arc evolution: (A) reagent gas break-down; (B) equilibrium heating phase and (C) non-equilibrium reaction phase [133].

#### 2.2.4. Microwave plasma

The microwave discharge operates at a frequency of 2.45 GHz. The plasma is created in a quartz tube which undergoes perpendicular microwave radiation (electromagnetic waves), while the gas flow passes through the dielectric tube. This discharge is far from local thermodynamic equilibrium at low pressure. It can be operated over a wide pressure range (from few mTorr to near atmospheric pressure) and the microwave discharges operating at atmospheric pressure are close to local thermodynamic equilibrium (LTE). The performance of a microwave discharge and the efficiency of CO<sub>2</sub> dissociation process depend heavily on the type of microwave power and the operating pressure [137-140]. The representation of a microwave plasma is depicted in Figure 18. Until today, microwave sources have been stated to provide the highest efficiencies as high as 85% of CO<sub>2</sub> decomposition, albeit at reduced pressure and in a supersonic flow configuration. As explained by Fridman [64], the ability to create a strong non-equilibrium environment in microwave discharges leads to the formation of vibrationally excited states of CO<sub>2</sub> via VV exchange reactions, which favors an efficient dissociation. On the other hand, as stated above, these high energy efficiencies in CO<sub>2</sub> decomposition are usually achieved at reduced pressures (between 100 and 200 Torr), which is not desirable in industrial applications. Moreover, microwave discharges operating at atmospheric pressure lead to a clear reduction in energy efficiency (20%) as recently reported

by Spencer et al. [138]. This can be explained because microwave plasmas tend to become more thermal at higher pressures, whereas the discharge remains largely at non-equilibrium at lower pressures. Microwave plasmas are typically characterized by low electron energy, typically 1 eV. In this temperature range, it has been estimated that about 95% of all the discharge energy is transferred from the plasma electrons to the CO<sub>2</sub> molecules, mostly to their asymmetric vibrational mode [64].

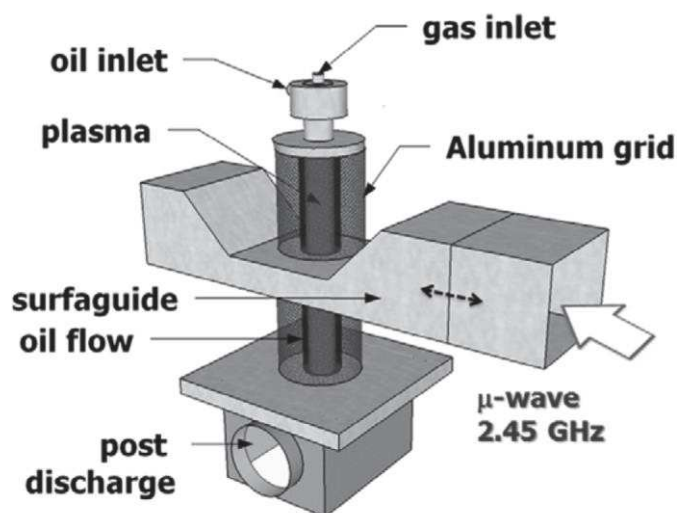


Figure 18 : Schematic representation of a microwave plasma [140].

### 3. Utilization of CO<sub>2</sub> plasmas for syngas production

#### 3.1. Introduction

The main products resulting from a pure CO<sub>2</sub> plasma are carbon monoxide (CO) and oxygen (O<sub>2</sub>). In order to exploit further products in plasma, CO<sub>2</sub> can be mixed with H-source reactants. Hydrogen (H<sub>2</sub>), methane (CH<sub>4</sub>) and water (H<sub>2</sub>O) are the most logical reactants which could be used to further reduce and hydrogenate CO<sub>2</sub>. In theory, a “Hydrogen Economy” would be very attractive [141]. In reality, however, hydrogen has a number of serious drawbacks due to its physicochemical properties [142]. Furthermore, the infrastructure needed to safely transport, store and dispense hydrogen would be very expensive to roll out [143, 144]. For this reason, methane and water are more suitable to use as H-source. Indeed combining CO<sub>2</sub> with methane is very interesting as the latter is also a greenhouse gas and thus, the synthesis of value added compounds from CO<sub>2</sub> considered as a "raw material" is a

very interesting concept for the industrial sector. On the other hand, combining water and carbon dioxide to obtain value-added compounds is also a very innovative and attractive solution since water is abundant. However, in the same manner as carbon dioxide, water is known to destabilize the plasma due to its ability to capture free electrons of the plasma.

### 3.2. CO<sub>2</sub>/CH<sub>4</sub> mixture

Methane is the principal component (between 70 and 90%) of most natural gas reserves [145]. The composition of natural gas varies significantly depending on the geographical source, time of year, and treatments applied during production or transportation [146]. Methane is therefore an abundant gaseous molecule already present in nature, which is not the case for hydrogen that needs to be produced. From a combination of methane and carbon dioxide (both greenhouse gases) in plasma phase, it is possible to obtain useful end products such as hydrocarbons and oxygenated organic molecules. The conversion into value added chemicals and liquid fuels is considered as one of the main challenges for the 21<sup>st</sup> century [147].

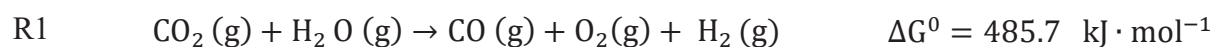
The type of plasma which is currently most often used for DRM (and gas conversion in general) is the dielectric barrier discharge (DBD).

A pure CH<sub>4</sub> plasma leads mainly to H<sub>2</sub> production, followed by C<sub>2</sub> products (ethane, ethylene and acetylene) [94, 111, 148]. The combined reforming of both CH<sub>4</sub> and CO<sub>2</sub> plasma makes such systems industrially relevant for fuel conversion and syngas (hydrogen and carbon monoxide) production applications, and permits to produce high value products from low value feedstock (CO<sub>2</sub> and CH<sub>4</sub>). Several types of plasmas have already been used for the conversion of methane [149-151], including dielectric barrier discharges (DBD) [38, 96, 123, 152-159], microwave discharge [160-162], glow discharges [163-165], coronas [164, 166, 167], plasma torch [168, 169], sparks [170], gliding arc plasma-jets [171-177], radio-frequency (RF) plasmas [178, 179] and thermal plasmas [180]. *Chapter VI* is dedicated to the CO<sub>2</sub> dry reforming of CH<sub>4</sub> in DBD operating at atmospheric pressure.

### 3.3. CO<sub>2</sub>/H<sub>2</sub>O mixture

Another interesting co-reactant for CO<sub>2</sub> to produce syngas is water. The latter is present in a very large quantity in our planet and it consists of a cheaper hydrogen source compared to CH<sub>4</sub> and H<sub>2</sub>. Furthermore, water is always present in industrial effluent gas streams (fumes).

As such, technologies that aim to convert CO<sub>2</sub> immediately at the exit of industrial installations, could take advantage of this major and unavoidable “contaminant”. Several routes for the combined conversion of CO<sub>2</sub> and H<sub>2</sub>O have already reported promising results, e.g. thermochemical, electrochemical, and photochemical, either with or without catalysts, and all their possible combinations [39, 40, 181-185]. In recent years, non-thermal plasma is also used [99, 122, 148, 186, 187]. H<sub>2</sub>O plasmas for the production of hydrogen have been extensively studied before [64, 188-192]. The research regarding the simultaneous conversion of CO<sub>2</sub> and H<sub>2</sub>O into syngas or oxygenated products by plasma, on the other hand, is very limited.



The reaction between CO<sub>2</sub> and H<sub>2</sub>O (R1) is indeed not spontaneous from the point of view of thermodynamic equilibrium at room temperature, so as for the pure CO<sub>2</sub> splitting, it requires a lot of energy. Nevertheless, some groups have already investigated on this topic via microwave plasmas [193-195], packed-bed DBD [196-199] and DC corona discharge [200].

In general, it is observed that the presence of water considerably affects the CO<sub>2</sub> discharge as such that the CO<sub>2</sub> conversion decreases with increasing water content. The main products observed are syngas (CO and H<sub>2</sub>) and O<sub>2</sub> whereas methanol (CH<sub>3</sub>OH) and hydrogen peroxide (H<sub>2</sub>O<sub>2</sub>) can be produced in minor quantity. On the other hand, it is possible to control the H<sub>2</sub>/CO ratio. Indeed, the latter increases with increasing water content.

#### 4. Application of CO<sub>2</sub> plasma for surface treatment

Besides gas treatment, CO<sub>2</sub> can also be used in surface treatment applications. It makes it possible to graft for example carboxylic functions, allowing the functionalization of the surface. Surface modifications by CO<sub>2</sub> plasma have already been tested on polymer like polytetrafluoroethylene (PTFE) [201, 202], polyethylene [203], polypropylene [204-206], polyethylene terephthalate [207] and polysulfone [208, 209]. Sarani et al. have modified the surface properties by a plasma jet fed by Ar/CO<sub>2</sub> [201]. They found that such discharge contains radicals containing CO groups, inducing changes in the chemical and physical aspects of the treated surface. They have analyzed the surface by contact angle measurements, SEM, AFM and XPS. The morphology does not change significantly but the surface tension

considerably increases, promoting subsequent capability to graft polymerization with acrylic acid for example [202]. Médard et al. have tried to treat a polyethylene surface both with CO<sub>2</sub> and combined CO<sub>2</sub>/H<sub>2</sub>O plasma [203]. Such plasma for the treatment of polyethylene can lead to many reactions like degradation, functionalization and cross-linking. It has been shown that CO<sub>2</sub> plasma is less degrading than O<sub>2</sub> plasma for polymeric surfaces [206]. CO<sub>2</sub> plasma leads to carboxylic acid function fixation onto polyethylene surface whereas the concentration of these last functions can be controlled when adding water into the discharge (CO + OH or CO<sub>2</sub> + H). On the other hand, the degradation mechanisms are mostly due to the presence of highly reactive atomic oxygen species (O<sup>3</sup>P and/or O<sup>1</sup>D) coming from the dissociation of CO<sub>2</sub> in the discharge. It has been shown that the degradation reactions are quite slow compared to the functionalization, which is a much faster phenomenon [205]. The functionalization corresponds to an increase of the surface energy and to an oxidation with the appearance of not only acid functions (carbonyl, carboxyl, and carbonate-like moieties) but also of alcohol (hydroxyl moieties) and ketone [205, 210]. Cross-linking also takes place during this type of treatment and will reinforce the stability of the modified surface. Yu et al. have demonstrated that the water contact angle, which reflects the hydrophilicity of the membrane surface, was reduced when treating the surface and thus, it is possible to obtain a hydrophilic surface (introduction of oxygen containing polar groups on the membrane surface) from a hydrophobic surface [204], and this high hydrophilicity of the membrane can last for a while [208]. Finally, Le et al. have also shown that, according to the plasma conditions, one can favor either functionalization or degradation phenomena [207]. Under rather mild treatment conditions (i.e. low plasma power combined with short treatment time), the formation of C-O bonds was found to be dominant, whereas the formation of highly oxidized carbon or double-bonded oxygen-containing groups required a high plasma power or a relatively long treatment time. Moreover, the treatments performed under excessive conditions frequently led to degradation at the polymer surface.

# **Chapter III - Description of the experiments**

## 1. Experimental setup

### 1.1. Generator

The power applied to the high-voltage electrode is provided by an AFS generator G10S-V with a maximum power of 1000 W. This generator is coupled to a transformer with the ability to tune the frequency in a range between 1 and 30 kHz and amplify the sinusoidal signal of the alternating voltage. The generator also allows pulsing the voltage in a controlled manner to obtain a multi-pulsed discharge (discharge ignited in so-called burst mode). Figure 19, Figure 20 and Figure 21 represent the experimental setups used for different chapters with all the diagnostic devices described in the following paragraphs.

### 1.2. Tubular DBD with 2 electrodes

#### 1.2.1. Reactor used for the CO<sub>2</sub> discharge

This experimental setup is used for the results presented in *Chapter IV*. A tubular DBD reactor dedicated to the treatment of CO<sub>2</sub> was designed, as shown in Figure 19. It consists of an alumina tube, with inner and outer diameter of 26 and 30 mm, respectively, a concentric inner electrode powered by an AC high voltage, and an outer electrode, surrounding the alumina tube, which is grounded. The inner electrode is a copper rod with a diameter of 22 mm and a length of 120 mm, while the outer electrode is a stainless steel mesh that can easily be rolled around the alumina tube, which acts as dielectric barrier. The gap, i.e. the distance separating the inner electrode from the dielectric barrier, is 2 mm, while the length of the outer electrode is 100 mm, which defines the length of the plasma zone, giving rise to a discharge volume of 15.1 cm<sup>3</sup>. This length is sufficient to ensure a long enough residence time. CO<sub>2</sub> is inserted in the reactor using a mass flow controller (MFC Bronkhorst El-Flow), where the flow rate can be varied in a range from 10 to 3000 mL<sub>n</sub>.min<sup>-1</sup> (in most of our study, the CO<sub>2</sub> flow rate is fixed at 200 mL<sub>n</sub>.min<sup>-1</sup>). The gas enters via several inlets (16 in total) of 0.75 mm diameter, arranged into a circular pattern, then travels through the tubular reactor and finally flows out of the reactor via several outlets (with the same configuration as the inlet, i.e. 16).

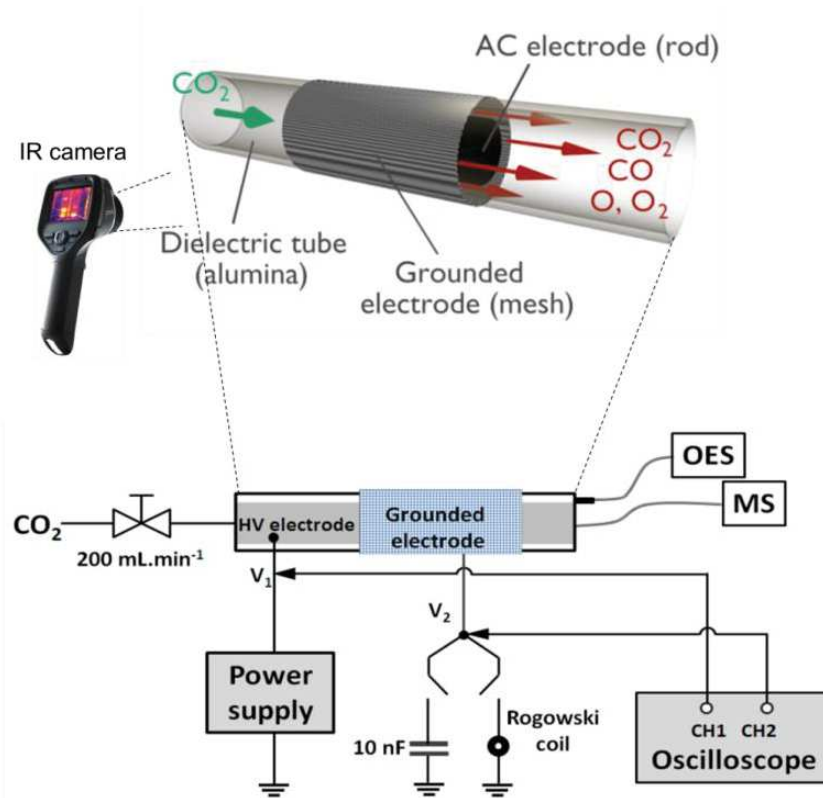


Figure 19 : Schematic diagram of the experimental set-up used in *Chapter IV*.

### 1.2.2. Reactor used for $\text{CO}_2 - \text{H}_2\text{O}$ discharge

The experiments in the  $\text{CO}_2\text{-H}_2\text{O}$  discharge (*Chapter V*) are carried out in the same coaxial DBD reactor as in the pure  $\text{CO}_2$  discharge (*Chapter IV*), as shown in Figure 20. However, for the  $\text{CO}_2\text{-H}_2\text{O}$  plasma study, borosilicate glass (pyrex) tube is used as dielectric material with the same dimensions as the tube used in *Chapter IV* (i.e. an inner and outer diameter of 26 and 30 mm for a thickness of 2 mm).  $\text{CO}_2$  and water vapor are used as feed gases with a continuous total flow rate of  $600 \text{ mL}\cdot\text{min}^{-1}$  at  $50^\circ\text{C}$ , varying the  $\text{H}_2\text{O}$  content in the mixture between 0 and 8%. The  $\text{CO}_2$  and water flow rates are controlled via a mass flow controller (MFC Bronkhorst EI-Flow) and a liquid flow controller (Bronkhorst Liqui-Flowtm), respectively. Both flows are mixed using a controlled evaporator mixer (CEM Bronkhorst), where the liquid and the carrier gas ( $\text{CO}_2$ ) are heated up in a controlled manner for total evaporation. Finally, this liquid delivery system with vapor control is then connected to the DBD reactor. Additionally, the entire system (tubing and reactor) is heated up to  $50^\circ\text{C}$  to avoid condensation and to promote total evaporation of the water throughout the discharge, as much as possible.

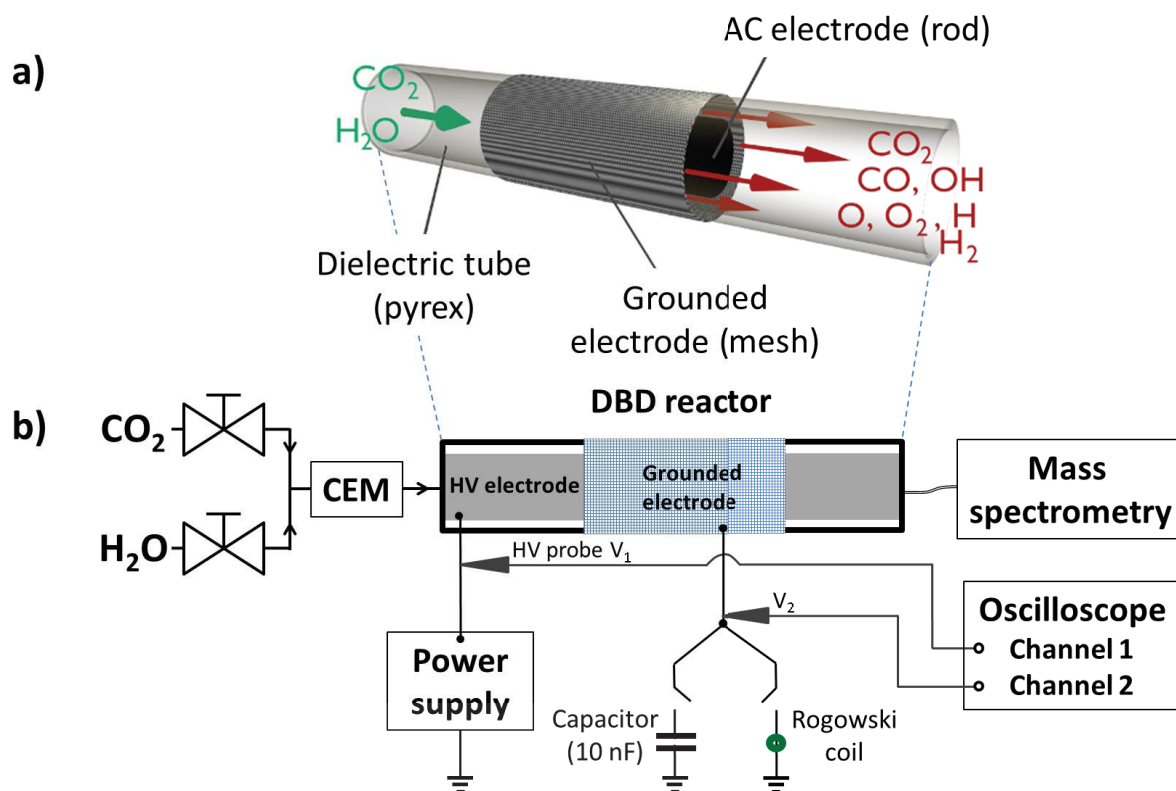


Figure 20 : Schematic of (a) the experimental DBD reactor and (b) the experimental setup used in *Chapter V*.

### 1.3. Tubular DBD with multi-electrodes

#### 1.3.1. Reactor used for the CO<sub>2</sub> - CH<sub>4</sub> discharge

The experimental setup presented here is used for the results of *Chapter VI*. A cylindrical multi-electrode DBD reactor dedicated to the treatment of elevated gas flow rates has been designed as shown in Figure 21a. It consists of a 2 mm thick tube made of quartz with an external diameter of 34 mm and a length of 100 mm (so as to ensure a long residence time with a corresponding plasma volume of 10.5 cm<sup>3</sup>). The gas enters via 16 inlets of 0.75 mm in diameter arranged into a circular pattern, then travels longitudinally through the tubular reactor and finally flows out of the reactor via 16 outlets (same configuration as the inlet). The discharge is generated between six AC high-voltage tubular electrodes set at equal distance from a central tubular electrode which is grounded. The distance between the grounded electrode and each high-voltage electrode is the same as the distance between two high-

voltage electrodes, namely 3 mm. The grounded electrode is a copper rod with a diameter of 5 mm and a length of 100 mm, while the high-voltage electrodes are copper wires approximately 1 mm in diameter and with the same length of 100 mm. The high-voltage electrodes are encompassed into alumina dielectric tubes with 0.75 mm thickness, as depicted in Figure 21a. A schematic of the entire experimental setup is shown in Figure 21b. Argon, carbon dioxide and methane are introduced into the reactor via Aalborg volumetric flow meters able to measure flow rates as high as 1800, 120 and 120 mL.min<sup>-1</sup>, respectively. Argon (or helium) is used as the carrier gas to initiate and maintain the discharge. The total flow rate of the gas mixture supplying the DBD reactor remains fixed at 1920 mL.min<sup>-1</sup> while the CO<sub>2</sub> and CH<sub>4</sub> flow rates are both varied from 0 to 120 mL.min<sup>-1</sup>.

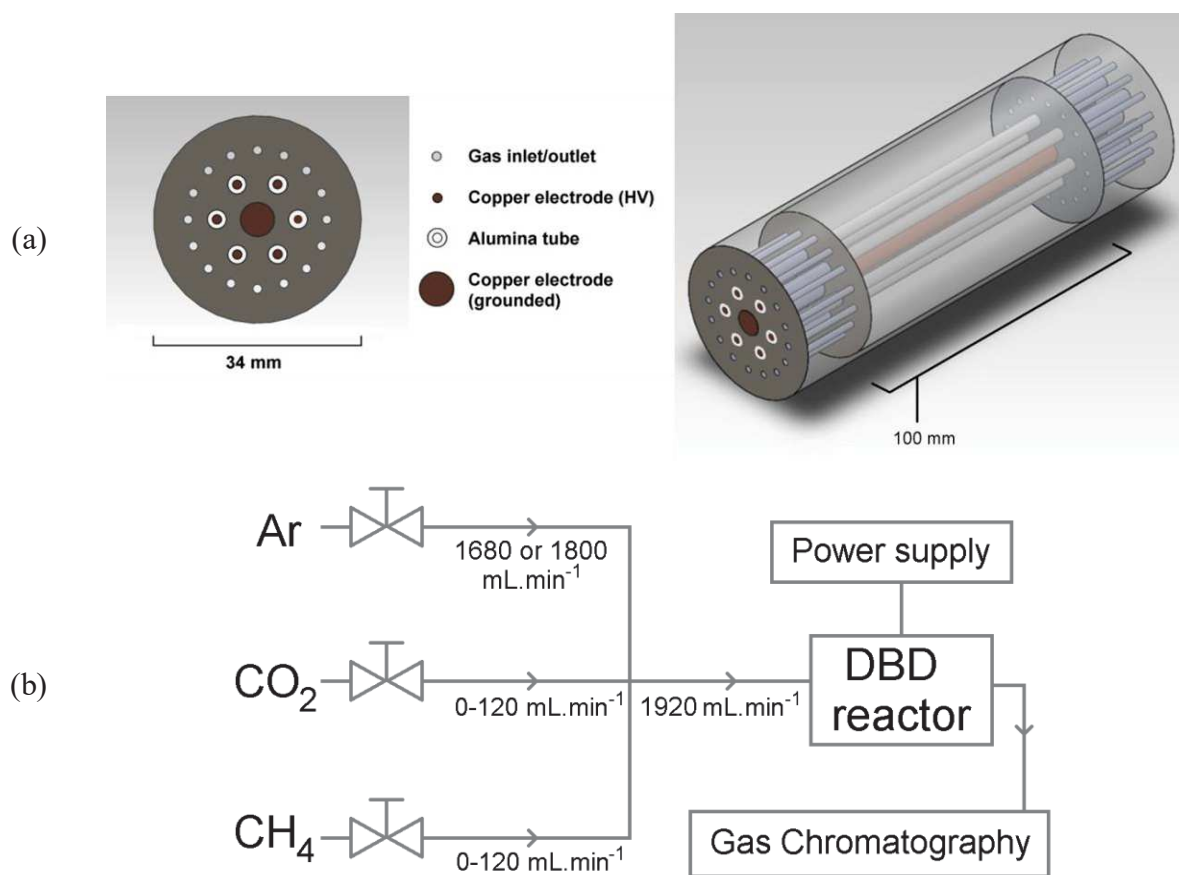


Figure 21 : (a) Representative picture of the DBD reactor and (b) schematic diagram of the entire experimental set up used in *Chapter VI*.

## 2. Experimental diagnostics

### 2.1. Mass spectrometry

#### 2.1.1. Principle

The mass spectrometry (MS) analysis defines the nature and structure of chemical compounds. A gas phase sample is ionized by electron impact:



This molecular ion will undergo fragmentation and each primary product ion can, in turn, undergo fragmentation, and so on. All these ions are then separated in the mass spectrometer based on their mass-to-charge ratio ( $m/z$ ) and are detected in proportion to their abundance. The mass spectrum obtained represents the partial pressure of different gas compounds, converted from a current intensity, as a function of the  $m/z$  ratio.

#### 2.1.2. The pumping system

The mass spectrometry technique requires a high vacuum so that the ions have a sufficient mean free path to reach the detector and to avoid collisions. The vacuum is obtained by the use of a turbomolecular pump assisted by a membrane pump which allows going from atmospheric pressure down to low pressure ( $\approx 10^{-6}$  Torr) in the spectrometer.

#### 2.1.3. The electron beam

Positive ions are created in the ionization chamber by collision with the electron beam. These electrons are formed by heating a tungsten filament (Joule effect) and their energy will play a role in the fragmentation. The typical energy is 70 eV but lower energies might be selected to reduce the fragmentation of the analyzed molecules. The ions are then accelerated towards the analyzer.

#### 2.1.4. *The quadrupole analyzer*

The quadrupole analyzer is based on the stability of the ion trajectories in oscillating electric fields to separate the ions based on their  $m/z$  ratios. The quadrupole analyzer is made up of four circular or ideally hyperbolic rods parallel in pairs.

Each opposing rod pair is connected to a potential  $\pm \Phi_0$  composed of a fixed DC ( $U$ ) and a RF alternating voltage ( $V \cos \omega t$ ):

$$\Phi_0 = U - V \cos \omega t$$

By varying the DC and RF components by maintaining a constant  $U/V$  ratio, the resultant field produced by the rods can be varied. At each interval on the RF scan, only the ions having the adequate  $m/z$  ratio are in a stable trajectory and reach the detector with an oscillating path described by the Mathieu equations [211, 212]. All the other species are deflected (unstable trajectories) and neutralized by impact upon the rods of the quadrupole.

#### 2.1.5. *The detectors*

The ions passing through the mass analyzer are detected and an ion current is measured by a sensitive amplifier. Two detectors are commonly used: the Faraday cup and the secondary electron multiplier (SEM). In the Faraday cup, the ions reach the inside of the metal cylinder and are neutralized by striking the walls. This leads to a current through the resistor connected to the ground. In the secondary electron multiplier, the positive ions are accelerated and collide with the conversion dynode which causes the emission of several secondary electrons. These secondary electrons are amplified by a cascade effect in the electron multiplier to produce a current.

#### 2.1.6. *Analysis of the flowing gases*

After passing through the reactor, the composition of the gas is analyzed by a mass spectrometer operating at atmospheric pressure with a quadrupole gas analyzer (Hiden Analytical QGA – Quantitative Gas Analyzer, Warrington, UK). These outlet gases arrive at the exit of the DBD reactor and are collected by a flexible 2 m capillary inlet (Hiden QIC - Quartz Inert Capillary), placed in post-discharge as shown in Figure 19. This capillary can sample from 100 mbar to 2 bar (atmospheric pressure in our case) and is heated up to 200°C

so that any molecule that enters in the analyzer is in gaseous phase. Since the capillary is very thin, it provides a fast response time of less than 300 ms for most common gases and vapors, including water and organic vapors with a gas consumption (sample flow) rate tunable from 0.8 to 16 sccm. The QGA system has a mass range up to 300 amu and with a real time detection capability in a wide dynamic range from 100% to less than 100 ppb. Its fast data acquisition up to 500 measurements per second allows achieving a multi-species analysis.

The high-vacuum in the ionization chamber is obtained via a UHV foreline pumping assisted by an external bypass dry scroll primary pump (Edwards XDS 5). Thanks to the turbomolecular pump installed just before the detector, a residual pressure of  $10^{-7}$  mbar is reached in the mass spectrometer.

A multi-level software package (called MASsoft7 Professional) allows having a simple control of mass spectrometer parameters. Three modes of recording data are available: profile, bar (gas composition at a certain time; partial pressure vs m/z ratio) and multiple ion detection (MID) modes. We mainly use the latter mode, which is used to monitor simultaneously the partial pressure variations with specific m/z ratios as a function of time. This software also permits to set the electron energy in the ionization chamber at 70 eV or lower for soft ionization in case of complex mixtures, in order to have a reduced spectral fragmentation and simplified data interpretation (for example in case of the presence of more than one reactive component in the discharge). We can also select the detectors, which are either a Dual Faraday detector and/or a Channeltron Secondary Electron Multiplier. The latter is used as it has a higher sensitivity.

Mass spectrometer measurements allow us to determine conversions and energy efficiencies of the plasma processes and these analyses are carried out in the studies present in *Chapter IV* and *Chapter V*.

## **2.2. Gas chromatography**

### ***2.2.1. Principle***

Chromatographic methods are generally used to separate components of a mixture based on their equilibrium between a mobile phase (carrier gas) and a stationary phase (liquid immobilized on a solid support) according to their interaction with both phases. In gas chromatography (GC), only interactions between the components and the stationary phase occur. The mobile phase aims to drive/carry the components through the column without

reacting between them. For this reason, an inert gas such as argon, helium or nitrogen, is used. By injecting a sample into the column, different gas species pass through the column at different rates, depending on the strength of electrostatic interactions with the walls of the column. As a consequence, the gas mixture becomes separated into individual components that reach the end of the column and are detected at different times. By measuring the retention time of each species in the column, the component gases can be identified by comparison with chromatograms for known standards. In general, the retention times are affected by the type of column, the gas concentration, pressure and the temperature; therefore, a selection of the appropriate column materials and operating conditions is critical for the resolution of the gas mixture [213]. The products are detected either by a Flame Ionization Detector (FID), or by a Thermal Conductivity Detector (TCD), or both. A signal is produced by each specific component when it reaches the detector, which results in a peak on the chromatogram. The relation between the peak area and the gas concentration allows a quantitative measurement. The detection of the FID is based on organic compounds pyrolysis. Indeed, the gas is electrically burned via hydrogen and dry air. This process produces ions and electrons collected by an amplifier. The detected amount is proportional to the number of carbon atoms (methylenic) present in the molecule to analyze. Methane, hydrocarbons and oxygenated organic molecules are detectable by this detector. The FID detection is very sensitive but has the disadvantage of being destructive. On the other hand, the detection of the TCD is based on measurements of gas thermal conductivity variations. Gas molecules to analyze have low thermal conductivities compared to the ones of the carrier gas, which provokes a decrease in thermal conductivity of the gas stream. Although this detector is less sensitive than the FID, it is capable to detect the unburned molecules (such as CO<sub>2</sub>, N<sub>2</sub>, O<sub>2</sub>, CO ...) and has the advantage of being a non-destructive detection.

### ***2.2.2. Analysis of the flowing gases***

The products resulting from the plasma phase reactions are analyzed downstream of the reactor with an online gas chromatograph (Agilent 6890N) equipped with a 60/80 Carboxen 1000 column (Supelco 1-2390-U). The products are analyzed with TCD and FID at the exit of the column. The injection of the gas coming from the plasma reactor is carried out via an antechamber heated in order to evaporate possible liquid oxygenated organic molecules (liquid at 20°C). To separate well the components with a good peak resolution, it is necessary to find the adequate conditions for separation in chromatographic analysis. The carrier gas

flow (constant at 30 mL.min<sup>-1</sup>) and oven temperature (keeping 35°C during 5 min; rise in temperature of 20°C.min<sup>-1</sup>; reaching a constant temperature of 225°C) in which the column is placed are the appropriate parameters. These are set via the GC ChemStation software.

GC measurements allow us to determine conversions and selectivities of the plasma processes, and this is carried out in the study presented in *Chapter VI*.

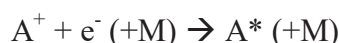
## 2.3. Optical emission spectroscopy

### 2.3.1. Principle

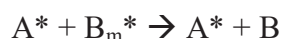
Optical emission spectroscopy analyses the radiation emitted by the plasma. The relaxation of the excited species to a lower energy state emits photons characteristics of the transition and can therefore allow the identification of emitting species present in the plasma. In plasmas, the creation of excited species can be due to excitation or dissociation by electron impact:



From recombination of ion and electron:



Or impact with metastable species:



These reactions generate excited species (A\*) at an energy level E<sub>j</sub> that emit a photon during their transition to a lower energy state E<sub>i</sub> (A\*\*) as illustrated in Figure 22.



In most cases, the most intense radiation is the transition from the first excited state to the ground state but A\*\* can also designate any other lower energy state compared to the excited state.



Figure 22 : Principle of the photon emission.

The energy of this photon  $E_{ij}$  is characteristic of the transition and is given by the following equation:

$$E_{ij} = E_j - E_i = \frac{hc}{\lambda} \quad \text{Eq. 3.1}$$

$h$  : Planck constant ( $6.626 \times 10^{-34}$  J.s)  
 $c$  : speed of light ( $3 \times 10^8$  m.s<sup>-1</sup>)  
 $\lambda$  : wavelength (m)

The spectral line has the following intensity:

$$I_{ij} = K_{ij} n_i A_{ij}$$

$K_{ij}$ : coefficient linked to the spectrometer (spectral response of the monochromator, the geometry of the optic, the energy of the emitted photon and the wavelength) Eq. 3.2  
 $n_i$ : density of the radiative state  
 $A_{ij}$ : radiative emission frequency (Einstein coefficient)

Optical emission spectroscopy is based on the measurement of the light intensity as a function of the wavelength. The measured spectra can be compared to tables from the literature (for instance the NIST database for atoms and [214] for molecules) in order to identify the species in the discharge or post-discharge.

The optical fibre collects the photons emitted by the plasma which are directed to a monochromator where the light is diffracted by a grating. The monochromator separates the light as a function of the wavelength and only the wavelength of interest is sent to the detector. Photons produce a current proportional to the intensity of the incident radiation. The emission spectrum of the plasma is obtained by turning the diffractive grating in order to scan all the wavelengths. A scheme of the setup is drawn in Figure 23.

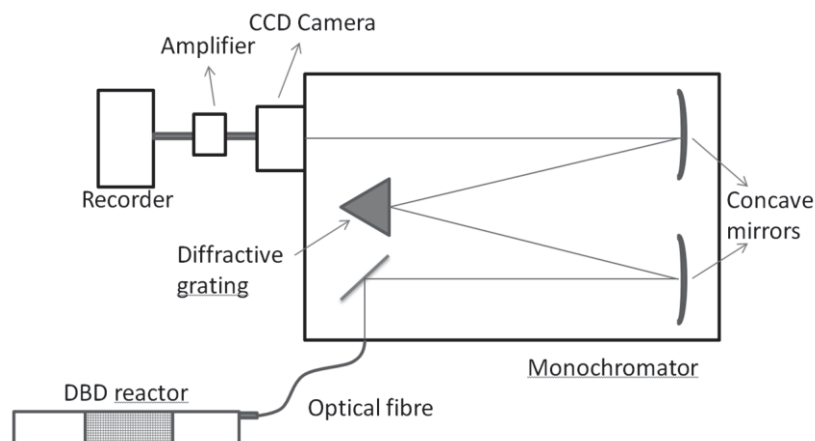


Figure 23 : Scheme of the OES setup.

### 2.3.2. *Analysis of the emitting species of the discharge*

The OES measurements are performed with an Andor Shamrock-500i spectrometer (0.500 meter focal length, triple grating imaging) including an Andor DU420A-OE CCD camera. The light emitted by the discharge in the gap is collected by an optical fibre and transmitted to the entrance slit (50  $\mu\text{m}$ ) of the monochromator. The optical fibre is thus placed at the exit of the reactor in parallel to the reactor and pointing to the gap. There, the light is collimated, diffracted, focused on the exit slit and finally captured by the CCD camera. Each optical emission spectrum is acquired with either the 1800 grooves/mm or the 2400 grooves/mm grating (blazed at 500 nm and 250 nm).

OES diagnostics allow to determine and evaluate some specific excited species in the plasma phase but also to have access to the gas temperature (and also electron temperature and electron density). The gas temperature ( $T_{\text{gas}}$ ) is a fundamental parameter in molecular gaseous discharges, defining the energy distribution of heavy particles. This temperature is one of the key parameters in technological applications because it strongly influences the plasma chemistry. In addition, many applications including for example gas treatment or the treatment of heat sensitive surfaces such as polymers and wounds require limited heat loads and thus an accurate measurement of the gas temperature or heat flux is needed. Following the corresponding literature [215-217], the rotational temperature ( $T_{\text{rot}}$ ) analysis is used in this study in order to determine the gas temperature, where these temperatures are assumed to be close for the considered molecules ( $\text{N}_2$  and  $\text{CO}$ ). It is generally known that  $T_{\text{gas}} \approx T_{\text{rot}}$  in the case of (i) a small energy gap between the rotational levels compared with that of the vibrational or electronic energy levels, and (ii) the presence of thermal equilibrium between the translational and rotational degrees of freedom [218]. These conditions are valid for a large variety of diatomic molecules including  $\text{CO}$ ,  $\text{OH}$  and  $\text{N}_2$  [219] but not for  $\text{CO}_2$  as its emission spectrum does not allow an evaluation of the rotational temperature, because its rotational levels cannot be distinguished in the emission spectra. In the general case, the rotational temperature can be measured based on the emission intensity of the rotational peaks between two energy levels with electronic, vibrational and rotational quantum numbers  $n$ ,  $v$  and  $J$ . However,  $\text{CO}$  emissions are always present in a  $\text{CO}_2$  discharge. Silva et al. have shown that in a  $\text{CO}_2$  microwave plasma at low pressure, the rotational temperature of the  $\text{CO}$  band is similar to the gas temperature [140]. This method is based on finding the best fit between the experimental and the simulated emission spectra of the  $\text{CO}$  Angstrom band and it is also

applied in our DBD study (see *Chapter IV* below). It is also possible to determine the gas temperature based on the first positive system of N<sub>2</sub>. By adding a small amount of nitrogen to a CO<sub>2</sub> discharge, the gas temperature is measured via a line-ratio peak formula, specific to this system [220, 221]. The peaks at 775.3 and at 773.9 nm are considered. This method is also applied to our DBD study (see *Chapter IV* below).

## 2.4. Electrical characterization

### 2.4.1. Power measurement in a DBD reactor

In order to determine the discharge power, the measurements of the high-voltage applied to the discharge ( $V_{DBD}$ ) and of the current passing through the discharge ( $i$ ) are required. The latter can be deduced from the voltage across a resistor ( $R$ ) or the voltage across a capacitor ( $C$ ). These two methods are explained below.

#### a. Current method

This is the simplest method to understand and it is based on the formalism of Feng and Castle [222]. The instantaneous power  $P^*(t)$  in the reactor is simply given by:

$$P^*(t) = V_{DBD}(t) \cdot i(t) \quad \text{Eq. 3.3}$$

where  $V(t)$  is the high voltage (HV) on the reactor and  $i(t)$  is the current flowing through the reactor (and resistor  $R$ ). The current  $i(t)$  is simply found from:

$$i(t) = \frac{V_R(t)}{R} \quad \text{Eq. 3.4}$$

where  $V_R(t)$  is the voltage across  $R$ . The average power over a single cycle of the high voltage, period  $T$ , is given by:

$$\begin{aligned} P &= \frac{1}{T} \int_{t_0-T/2}^{t_0+T/2} P^* dt = \frac{1}{T} \int_{t_0-T/2}^{t_0+T/2} V_{DBD}(t) \cdot i(t) dt \\ &= \frac{1}{T} \int_{t_0-T/2}^{t_0+T/2} \frac{V_{DBD}(t) \cdot V_R(t)}{R} dt \end{aligned} \quad \text{Eq. 3.5}$$

where  $t_0$  is the centre of the cycle.

DBDs can operate either in a homogeneous regime with only one current peak during each half period, or in a filamentary regime. In the second case, such as for a CO<sub>2</sub> discharge, the problem is that the plasma itself is a series of microdischarges of short duration in the current waveform (current peaks typically of a few ns). This indeed requires a very high bandwidth (and expensive) sampling oscilloscope, capturing all data very accurately [72]. In practice, even with such instrument, the overlap of current spikes makes the use of equation 3.5 very difficult to perform accurately.

### *b. Lissajous method*

This method is introduced by Manley [223] in 1943. In the absence of any way of accurately recording the microdischarge current spikes, the alternative is to replace the probe resistor by a probe capacitor. The capacitor accumulates a charge from the current flowing through the reactor and this can be determined by measuring the voltage on the capacitor  $V_C$ .

$$q(t) = C \cdot V_C(t) \quad \text{Eq. 3.6}$$

The advantage is that the charge is stored in the capacitor and does not require a fast transient digitizer to record it. Indeed, no charge is lost via a low bandwidth or overlapping peaks. The energy per cycle,  $W$ , can be found from equation 3.5 by multiplying by  $T$ .

$$W = \int_{t_0-T/2}^{t_0+T/2} V_{DBD}(t) \cdot i(t) dt \quad \text{Eq. 3.7}$$

The current flowing through the measuring capacitor,  $C$ , is given by:

$$i(t) = \frac{dq}{dt} = C \cdot \frac{dV_C}{dt} \quad \text{Eq. 3.8}$$

The energy per cycle becomes:

$$W = \int_{t_0-T/2}^{t_0+T/2} V_{DBD}(t) \cdot C \cdot V_C(t) dt = \int_{t_0-T/2}^{t_0+T/2} V_{DBD}(t) \cdot dq(t) \quad \text{Eq. 3.9}$$

If we record  $V_{DBD}(t)$  and  $q(t)$  as a series of  $n$  regularly sampled points over one cycle we can approximate equation 3.9 by a summation, using trapezoidal integration, as:

$$W \approx \sum_{k=1}^n \left( \frac{V_{k+1} + V_k}{2} \right) (q_{k+1} - q_k) \quad \text{Eq. 3.10}$$

Finally, we multiply the energy by the number of cycles per second in order to obtain the plasma power in the reactor. So, if the voltage  $V_{DBD}$  has a frequency,  $f$ , where  $f=1/T$ , we have:

$$P = W \cdot f = f \sum_{k=1}^n \left( \frac{V_{k+1} + V_k}{2} \right) (q_{k+1} - q_k) \quad \text{Eq. 3.11}$$

The integrals in equation 3.9 and equation 3.11 represent the area of a V-q Lissajous diagram with the charge  $q(t)$  on the Y-axis and the voltage  $V_{DBD}(t)$  on the X-axis, as shown in Figure 24.

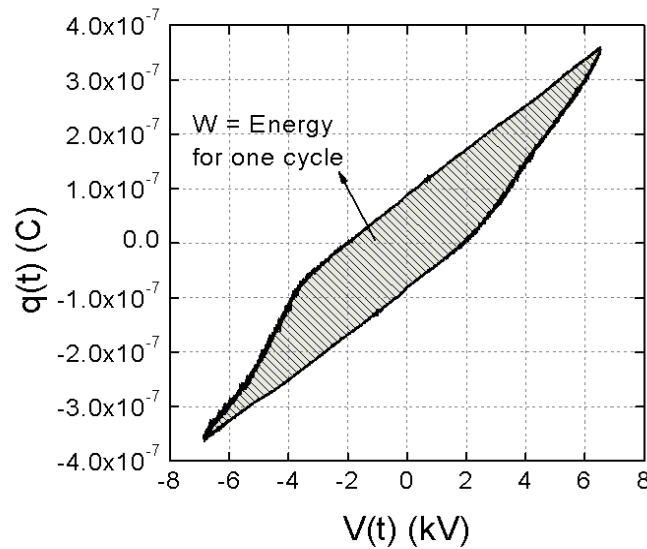


Figure 24 : Typical Lissajous figure.

#### 2.4.2. Electric analysis of the discharge

All the electrical measurements are performed using a two-channel digital oscilloscope (Tektronix DPO 3032). The applied voltage ( $V_1$ ) is measured with a high voltage probe (Tektronix P6015A) while the DBD voltage supplied by the generator ( $V_{DBD}$ ) is determined by subtracting  $V_2$  from  $V_1$ , as represented in Figure 19 and Figure 20.

$V_{DBD}$  is also expressed as the sum of two voltages: the dielectric voltage ( $V_{diel}$ ) and the effective plasma voltage ( $V_{pl,eff}$ ). In filamentary mode such as in a  $CO_2$  discharge, the plasma voltage is considered as the effective voltage, since the filamentary mode is responsible for an inhomogeneous electric field in the whole electrode-barrier gap, which is different from the

case of a diffuse and homogeneous glow discharge [87, 107, 224, 225]. Therefore,  $V_{pl,eff}$  should be considered as an average value and represents typically 70-80% of the DBD [118]. As indicated in Figure 19, the potential  $V_2$  is measured either through a capacitor or through a current probe (Pearson 2877 Rogowski coil), both placed in series with the DBD.

The external capacitor of 10 nF allows to evaluate first its electrical charge  $Q_{pl}(t)$  and subsequently the discharge power, also called absorbed power ( $P_{abs}$ ), by the plasma via the Lissajous method [37, 72, 97, 122, 223, 226-228], as described above. The absorbed power leading to the energy input is defined as the SEI (specific energy input) as the latter is equal to the ratio of the calculated plasma power to the gas flow rate.

The total current of the discharge ( $i_{DBD}$ ) is recorded using the Rogowski coil (instead of a resistance) presenting the ability to respond to fast changing currents due to its low inductance (rise time of 2 ns and drop rate of 0.2%/μs). The total current is the sum of the plasma or discharge current (i.e. conduction current) and the dielectric current (i.e. capacitive current):

$$i_{DBD}(t) = i_{pl}(t) + i_{diel}(t) \quad \text{Eq. 3.12}$$

### 2.4.3. *New methodology to analyze the microdischarges*

As previously mentioned, an atmospheric pressure DBD in CO<sub>2</sub> usually operates in the filamentary mode [112, 122, 127, 229]. The microdischarges can be individually or collectively characterized through their current peaks observed in the oscillograms (see Figure 25) and considering the dielectric current  $i_{diel}$  as the baseline (a sinusoidal-like signal; see Figure 25a) for determining the microdischarge properties. The plasma current  $i_{pl}$  consists of the peaks superposed to the previous signal and representing the microdischarges. An individual analysis for these microdischarges would have been too laborious to make visually. Indeed, several hundred microdischarges occur per half period. Therefore, a numerical method from the Origin software analyzer toolbox is applied to determine the number of microdischarges ( $N_{md}$ ), their peak intensity, electrical charge ( $Q_{pl}$ ) and lifetime ( $L_{md}$ ) for a given residence/analysis time. The intensity and lifetime of each microdischarge are evaluated considering the peak magnitude and FWHM, respectively. Its electric charge is determined by integrating the peak area from the baseline (see Figure 25c). In the case of  $N_{md}$ , the "filtering by height" method (including the local maximum option) is used. The accuracy of this numerical method is verified by comparing the provided  $N_{md}$  value with the one measured

from a visual counting. As the difference between the two approaches always remains lower than 5%, the numerical method is considered to be sufficiently accurate. This small intrinsic error of the discharge current is related to the fact that errors can be introduced by the sinusoidal fit when choosing the baseline of the displacement current in the electrical characterization of the current oscillogram profile. This method permits to have access to a statistical study for the thousands of microdischarges that are generated. This electrical investigation is important for the fundamental understanding of the physics behind CO<sub>2</sub> discharges operating in an atmospheric DBD but also helps for 0D simulations (described at the end of this chapter) by including the microdischarge features and the corresponding values as input data of the code. This type of modelling indeed simulates simultaneous microdischarges as a function of time.

The main electrical parameters of the DBD are calculated and reported in Table 1. Three different voltages have to be considered: the voltage over the entire DBD reactor ( $V_{DBD}$ ), the voltage over the dielectric barrier ( $V_{diel}$ ) calculated with  $\xi$  as a dummy variable, and the effective voltage of the plasma ( $V_{pl,eff}$ ). The electric charges of the DBD ( $Q_{DBD}$ ), the dielectric barrier ( $Q_{diel}$ ), the plasma ( $Q_{pl}$ ) and the charge per micro-discharge ( $Q_{md}$ ) are calculated from the current or voltage. Finally, the capacitances of the entire DBD ( $C_{DBD}$ ), the dielectric barrier ( $C_{diel}$ ) and the plasma ( $C_{pl}$ ) are given, considering for  $C_{diel}$  a dependence on the following parameters: the tubular barrier length ( $L$ ), its external and internal radius ( $R_{ext}$  and  $R_{int}$ , respectively) and the dielectric constant of the dielectric barrier ( $\epsilon_r$ ). In the present work, the expression of the DBD capacitance is adopted from the homogeneous model of Godyak & Lieberman based on the equivalent circuit model of a capacitive discharge [62].

Table 1 : Main electrical parameters of the discharge.

	Current	Voltage	Charge	Capacitance
Micro-discharge	-	-	$Q_{md} = \int_{microdischarge} i_{pl}(t).dt$	-
Plasma	$i_{pl}(t)$	$V_{pl,eff}(t) = V_{DBD}(t) - V_{diel}(t)$	$Q_{pl} = \int_{\tau} i_{pl}(t).dt$	$C_{pl}$
Dielectric barrier	$i_{diel}(t)$	$V_{diel}(t) = \frac{1}{C_{diel}} \int_0^t i_{DBD}(\xi).d\xi + V_{diel}(0)$	$Q_{diel} = C_{diel} \cdot V_{diel}$	$C_{diel} = \frac{2\pi\epsilon_0\epsilon_r.L}{\ln(R_{ext}/R_{int})}$
DBD	$i_{DBD}(t) = i_{pl}(t) + i_{diel}(t)$	$V_{DBD}(t) = V_1(t) - V_2(t)$	$Q_{DBD} = \int_{\tau} i_{DBD}(t).dt$	$\frac{1}{C_{DBD}} = \frac{1}{C_{pl}} + \frac{1}{C_{diel}}$

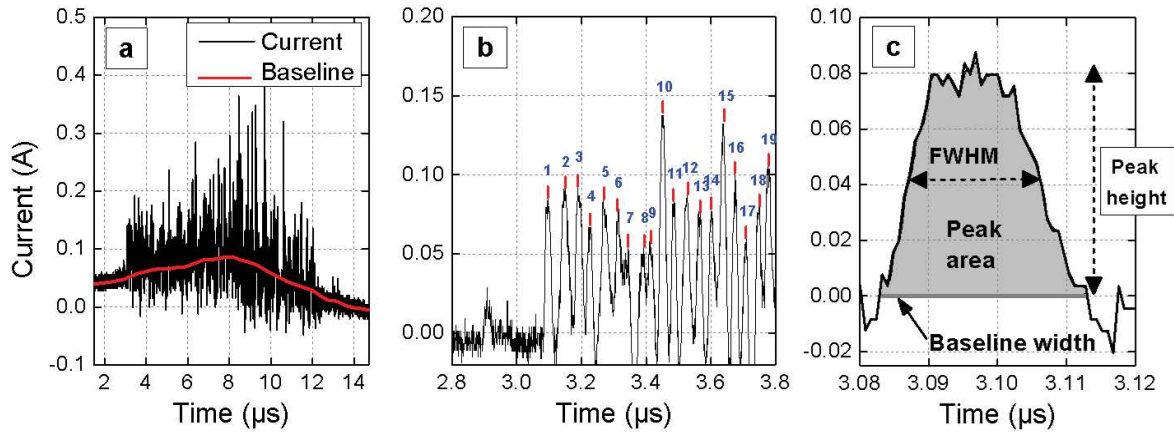


Figure 25 : (a) Oscillogram of the total current and determination of the baseline; (b) counting of the current peaks; (c) signal processing for the electrical characterization of the microdischarges.

## 2.5. Infrared imaging

2D temperature profiles of the grounded outer electrode and of the reactor wall of a cylindrical DBD are measured with an infrared camera (FLIR E40) with a resolution of 160x120 pixels and a thermal sensitivity lower than  $0.07^{\circ}\text{C}$  at  $30^{\circ}\text{C}$ . FLIR ResearchIR software is used to control, record and analyze the temperature profiles in a range from  $-20^{\circ}\text{C}$  to  $+650^{\circ}\text{C}$ . The emissivity coefficients of the different materials are introduced in the software. The temperature is calibrated at room temperature.

## 2.6. Profilometry

A profilometer is an instrument used to measure the surface's profile, in order to quantify its roughness. A stylus is vertically moved in contact with a sample and then moved laterally across the sample for a specified distance and specified contact force. A profilometer can measure small surface variations in vertical stylus displacement as a function of position. A typical profilometer can measure small vertical features ranging in height from 10 nanometres to 1 millimetre. The height position of the stylus generates an analog signal which is converted into a digital signal, stored, analyzed, and displayed. The horizontal resolution is controlled by the scan speed and data signal sampling rate. Profilometry measurements are performed on the dielectric surfaces (see *Chapter IV*) using a Brücker dektak XT stylus

profilometer (Brüker, Karlsruhe, Germany). The scanning stylus is 2  $\mu\text{m}$  in radius and is applied with a tracking force of 1 mg. The roughness, i.e.  $R_{\text{RMS}}$  parameter, is estimated using the Vision 64 software by summing 150 scans over a 0.9  $\text{mm}^2$  area.

### 3. Simulation

#### 3.1. Description of the model

##### 3.1.1. 0D chemical kinetics model

The computational model used to describe the underlying chemistry related to the  $\text{CO}_2\text{-H}_2\text{O}$  plasma (used in *Chapter V*) is a zero-dimensional (0D) kinetic model, called `Global_kin`, developed by Kushner and coworkers [230, 231]. The fact that the model has no dimension makes simulation simple and quick to run. The time-evolution of the species densities is calculated, based on production and loss processes, as defined by the chemical reactions. The rate coefficients of the heavy particle reactions depend on the gas temperature and are calculated by Arrhenius equations. All these reactions between heavy particles are grouped in the chemistry module. Note that no transport is included in this module and the assumption of uniformity of the plasma. Indeed, the plasma reactor is considered as a batch reactor, with a uniform concentration of species over the entire cylindrical reactor volume. The rate coefficients for the electron impact reactions are based on the collision cross sections and are a function of the electron temperature; they are calculated in the Boltzmann equation module. Subsequently, look-up tables with these rate coefficients as a function of electron energy (or electron temperature) are created. These coefficients are then used as input in the chemistry module to calculate the source terms for the electron impact gas phase reactions. Finally, the electron temperature is calculated with an energy balance equation. More details about this model can be found in the work of Kushner et al. [230, 231] and Snoeckx et al. [152].

##### 3.1.2. Plasma chemistry included in the model

The  $\text{CO}_2$  chemistry and the  $\text{H}_2\text{O}/\text{O}_2$  chemistry used in this study are adopted from Aerts et al. [127] and Van Gaens et al. [232], respectively, while the hydrocarbon chemistry, necessary to describe the reactions between  $\text{CO}_2$  and  $\text{H}_2\text{O}$  species, and thus for the product formation, is

taken from Snoeckx et al. [152]. The total chemistry set considers 75 different species (listed in Table 2), which react with each other in 187 electron impact reactions, 346 ion reactions and 369 neutral reactions. Their corresponding rate coefficients and the references where these data were adopted from are listed in [127, 152, 232] and can be found in [233]. The model results that will be shown in *Chapter V*, were obtained by Snoeckx [233].

In plasma, inclusion of different plasma species should be as close as possible to the reality. In this context, the knowledge of the main species formed in the plasma is fundamental to improve the theoretical works and to minimize the time consumption of calculations. As plasmas, in general, are very complex systems, simulations are very useful to describe the chemistry occurring in the plasma phase itself.

Table 2 : Species included in the model.

<b>C-O compounds</b>	$\text{CO}_2, \text{CO}, \text{C}_2\text{O}, \text{CO}_2^+, \text{CO}^+, \text{CO}_4^+, \text{CO}_4^-, \text{CO}_3^-, \text{C}_2\text{O}_4^+, \text{C}_2\text{O}_3^+, \text{C}_2\text{O}_2^+$
<b>C compounds</b>	$\text{C}, \text{C}_2, \text{C}_2^+, \text{C}^+$
<b>O compounds</b>	$\text{O}_3, \text{O}_2, \text{O}, \text{O}_4^-, \text{O}_3^-, \text{O}_2^-, \text{O}^-, \text{O}_4^+, \text{O}_2^+, \text{O}^+$
<b>C-H compounds</b>	$\text{CH}_4, \text{CH}_3, \text{CH}_2, \text{CH}, \text{CH}_5^+, \text{CH}_4^+, \text{CH}_3^+, \text{CH}_2^+, \text{CH}^+$
<b>C<sub>2</sub>-H compounds</b>	$\text{C}_2\text{H}_6, \text{C}_2\text{H}_5, \text{C}_2\text{H}_4, \text{C}_2\text{H}_3, \text{C}_2\text{H}_2, \text{C}_2\text{H}, \text{C}_2\text{H}_6^+, \text{C}_2\text{H}_5^+, \text{C}_2\text{H}_4^+, \text{C}_2\text{H}_3^+, \text{C}_2\text{H}_2^+$
<b>C<sub>3</sub>-H and C<sub>4</sub>-H compounds</b>	$\text{C}_3\text{H}_8, \text{C}_3\text{H}_7, \text{C}_3\text{H}_6, \text{C}_4\text{H}_2$
<b>H compounds</b>	$\text{H}_2, \text{H}, \text{H}_3^+, \text{H}_2^+, \text{H}^+, \text{H}^-$
<b>H-O compounds</b>	$\text{H}_2\text{O}, \text{OH}, \text{HO}_2, \text{H}_2\text{O}_2, \text{OH}^-, \text{H}_3\text{O}^+, \text{H}_2\text{O}^+, \text{OH}^+$
<b>C-H-O compounds</b>	$\text{CHO}, \text{CH}_2\text{O}, \text{CH}_3\text{O}, \text{CH}_2\text{OH}, \text{CH}_3\text{OH}, \text{CHCO}, \text{CH}_2\text{CO}, \text{CH}_3\text{CO}, \text{CH}_2\text{CHO}, \text{CH}_3\text{CHO}, \text{C}_2\text{H}_5\text{O}_2$
<b>Electrons</b>	$e^-$

### 3.2. Application of the 0D model to a DBD reactor

0D models can only calculate the species densities as a function of time, and thus they neglect spatial variations. Nevertheless, by using the gas flow rate, the time evolution can be translated into a spatial evolution (i.e. as a function of position in the DBD reactor). This spatial evolution is necessary to mimic the typical filamentary behavior found in DBDs used

for CO<sub>2</sub> conversion [118]. In this filamentary mode, one can be observed many short peaks in the electrical current waveform as shown in Figure 14. These filaments (streamers) are spread in volume and time, making it very difficult to model in a typical (continuum) plasma model. These microdischarges are also the real source of reactivity, where quasi all the initiation of chemical reactions (excitation, dissociation, ionization) occurs there.

On their way throughout the reactor, the gas molecules will pass through several micro-discharge filaments. This is mimicked in the model by applying a large number of consecutive triangular micro-discharge pulses of 10 ns (power deposition), as described in the work carried out by Snoeckx [152]. A large number of filaments occur per half cycle but in reality, an individual gas molecule will not pass all these filaments as they are spread in volume. Indeed, the actual plasma volume (i.e., sum of the filament volumes) is typically much smaller than the total volume of the plasma reactor. The exact number of filaments that a typical molecule will pass when flowing through the reactor is not known. Therefore, the model is fitted to the experiment in several steps. In the first step, an individual pulse is simulated with a certain specific energy input (SEI). In a second step, the SEI from the experiment is evaluated and fitted by repeating the individual pulse at a certain frequency until the SEI in the model is the same as in the experiment. In the last step, the accumulation effects are studied to study the conversions of the reactants, the selectivities of the products, the variation of the different plasma species densities, etc. Each model consists of repeating the pulses simulated for a certain frequency with the same residence time and energy input as in the experiment. This pulse duration and pulse frequency is slightly different from the procedure used in previous works of Snoeckx et al. [99, 111, 123, 152], but it is based on our electrical characterizations performed during the experiments for this specific gas mixture, in the same way as was done for pure CO<sub>2</sub> [118]. A block diagram of the model is depicted in Figure 26.

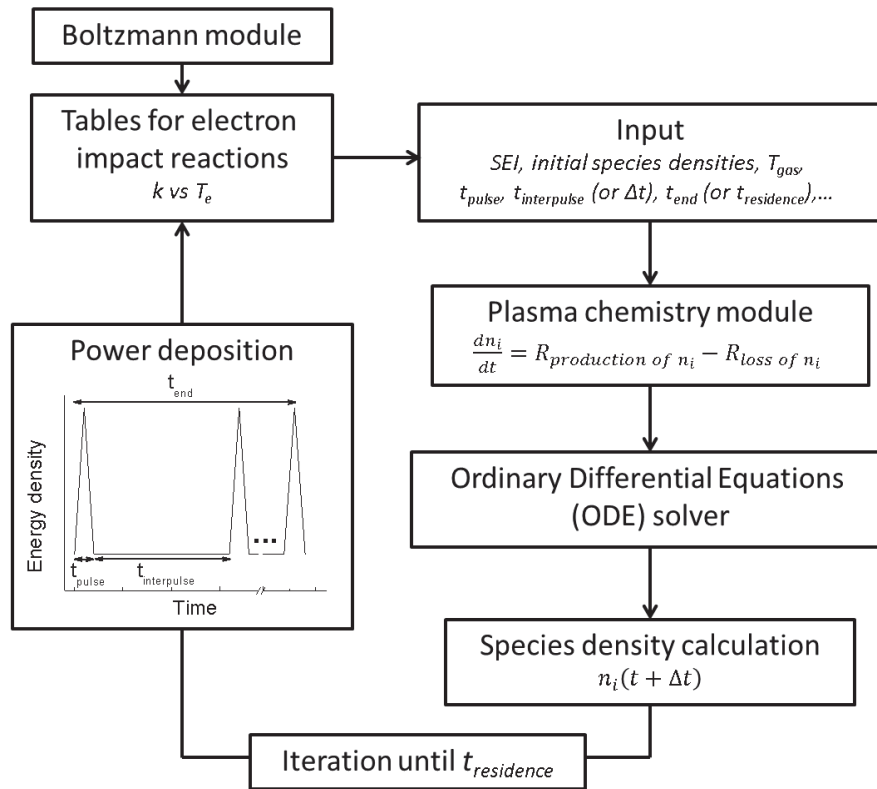


Figure 26 : Block diagram of the model.

The 0D model approach has already proven to be applicable for a variety of conditions, gas mixtures and different 0D simulation codes [99, 111, 123, 152, 234-236]. The experimental gas flow rate is used, i.e., 600 mL/min at 50°C and atmospheric pressure, with a DBD reactor volume of 15.1 cm<sup>3</sup> (see description of the DBD reactor), thus corresponding to a residence time of 1.66 s. In this simulation, we assume that each gas molecule passes through 475 micro-discharges for this given residence time, or in other words that the molecules pass through a micro-discharge every 3.4 ms. The average power consumed per microdischarge is equal to the power inserted in the plasma divided by the total number of microdischarges through which the molecules pass.

# Chapter IV - CO<sub>2</sub> discharge - an extensive study of its conversion

---

The results of this chapter were published in the following papers:

- **Ozkan A.**, Dufour T., Silva T., Britun N., Snyders R., Bogaerts A. and Reniers F., The influence of power and frequency on the filamentary behavior of a flowing DBD—application to the splitting of CO<sub>2</sub>, *Plasma Sources Science and Technology*, 25(2) (2016) 025013
- **Ozkan A.**, Dufour T., Bogaerts A. and Reniers F., How do the barrier thickness and dielectric material influence the filamentary mode and CO<sub>2</sub> conversion in a flowing DBD?, *Plasma Sources Science and Technology*, 25(4) (2016) 045016
- **Ozkan A.**, Dufour T., Silva T., Britun N., Snyders R., Reniers F. and Bogaerts A., DBD in burst mode: solution for more efficient CO<sub>2</sub> conversion?, *Plasma Sources Science and Technology*, 25 (2016) 055005

## 1. Introduction

In this chapter, the splitting of CO<sub>2</sub> into O<sub>2</sub> and CO is investigated in a flowing cylindrical DBD operating at atmospheric pressure. For this purpose, the influence of various electrical regimes and electrical configurations on the CO<sub>2</sub> conversion and energy efficiency of the process are studied in order to have a better understanding of the CO<sub>2</sub> discharge itself. The first section is dedicated to the operating parameters of the discharge, namely the gas residence time, the operating frequency, the HV discharge power (the latter two were published in the *PSST Journal* [118]) and the pulsation in the AC regime of the discharge (so-called burst mode, also published in *PSST* [237]). The second section is focused on the change in the DBD configuration, where we study the influence of the dielectric thickness and the dielectric material (published also in *PSST* [238]) on the CO<sub>2</sub> splitting process.

The present chapter is more focused on the physical aspects of a pure CO<sub>2</sub> discharge. A complete study of the chemical mechanisms is beyond the scope of this work, as the latter was already carried out by both experiments and computer simulations. Aerts et al. predicted reactions pathways for the CO<sub>2</sub> splitting in a DBD plasma. This process is mainly dictated by electron impact dissociation to form CO and O atoms [122]. More details about the chemical aspects of pure CO<sub>2</sub> discharges can be found in *Chapter II*. Furthermore, this aspect is also more discussed in the following chapters where CO<sub>2</sub> is mixed with either water (analyzed by means of simulations in *Chapter V*) or methane (*Chapter VI*).

If CO<sub>2</sub> is mixed with H<sub>2</sub>O or CH<sub>4</sub> to produce syngas (CO and H<sub>2</sub>) and also hydrocarbons, the chemical pathways become of course more complicated as many more species are produced in the plasma phase compared to a pure CO<sub>2</sub> discharge (see *Chapter V & VI*) [123, 152]. In some studies, CO<sub>2</sub> is also mixed with a rare gas such as argon or helium [94-97]. In this case, no extra products are obtained, but the chemistry can still be affected, leading to a higher absolute CO<sub>2</sub> conversion, but a lower effective conversion and energy efficiency [97]. Moreover, adding helium also affects the physical characteristics of the discharge, which becomes more homogeneous, whereas adding argon still results in a filamentary discharge [94, 97]. A study concerning the influence of the carrier gas is achieved and explained in *Chapter VI* (see our work published in *Journal of CO<sub>2</sub> Utilization* [94]). However in this entire chapter, the only reactant gas used is CO<sub>2</sub> without any use of carrier/plasmagen gas.

After passing longitudinally and being treated through the cylindrical reactor (see description in *Chapter III*), the gas is analyzed at the exit by mass spectrometry which leads to the calculation of conversion and energy efficiency. The CO<sub>2</sub> conversion ( $\chi_{\text{CO}_2}$ ) is calculated according to equation 4.1 in Table 3, where  $I$  corresponds to the intensity of the CO<sub>2</sub> signal in the mass spectrometer. The energy efficiency (equation 4.2) of the CO<sub>2</sub> conversion is calculated from  $\chi_{\text{CO}_2}$ , the enthalpy of the splitting reaction ( $\text{CO}_2 \rightarrow \text{CO} + \frac{1}{2} \text{O}_2$ ), namely  $\Delta H_{298\text{K}}^0 = 282.99 \text{ kJ}\cdot\text{mol}^{-1} = 2.94 \text{ eV}\cdot\text{molecule}^{-1}$ , and the specific energy input (SEI) (see Table 3). Note that the enthalpy of the reaction almost does not change in a temperature range from 298 to 473 K, which is a typical gas temperature inside the DBD plasma [239, 240]. The SEI corresponds to the energy density ( $E_d$  in  $\text{J}\cdot\text{cm}^{-3}$ ), converted into  $\text{eV}\cdot\text{molecule}^{-1}$ . The energy density depends on the power absorbed by the plasma ( $P_{\text{abs}}$ ) and the gas flow rate as presented in Table 3.

Table 3 : Formulas for conversion, energy efficiency, energy density and specific energy input.

Parameter	Formula	#
Conversion	$\chi_{\text{CO}_2} (\%) = \frac{I_{\text{CO}_2}^{\text{plasma OFF}} - I_{\text{CO}_2}^{\text{plasma ON}}}{I_{\text{CO}_2}^{\text{plasma OFF}}} \times 100\%$	Eq. 4.1
Energy efficiency	$\eta_{\text{CO}_2} (\%) = \chi_{\text{CO}_2} (\%) \cdot \frac{\Delta H_{298\text{K}}^0 (\text{eV}\cdot\text{molecule}^{-1})}{\text{SEI}_{(\text{eV}\cdot\text{molecule}^{-1})}}$	Eq. 4.2
Energy density	$E_d (\text{J}\cdot\text{cm}^{-3}) = \frac{\text{Absorbed power}_{(\text{J}\cdot\text{s}^{-1})}}{\text{Gas flow rate}_{(\text{cm}^3\cdot\text{s}^{-1})}}$	Eq. 4.3
Specific energy input	$\text{SEI}_{(\text{eV}\cdot\text{molecule}^{-1})} = \frac{E_d (\text{J}\cdot\text{cm}^{-3}) \times 6.24 \times 10^{18} (\text{eV}\cdot\text{J}^{-1}) \times 24500 (\text{cm}^3\cdot\text{mol}^{-1})}{6.022 \times 10^{23} (\text{molecule}\cdot\text{mol}^{-1})}$	Eq. 4.4

The conversion and energy efficiency of the CO<sub>2</sub> splitting process are discussed for different studies where we change the discharge parameters and we correlate them to other observations made by various diagnostics (oscilloscope, OES, IR imaging, etc.) in order to investigate the physical characteristics of the plasma. It is also important to stress that there are, in practice, system inefficiencies (e.g. reactions producing CO<sub>2</sub>) that contribute to a non-efficient CO<sub>2</sub> splitting.

Some important physical parameters are of interest in this chapter, in particular the evaluation of the electrical behavior of the CO<sub>2</sub> discharge by means of a detailed electrical characterization. The latter allows to evaluate the filamentary behavior and its influence on

the CO<sub>2</sub> conversion. In order to reach this goal, a new approach and methodology is developed in order to investigate the microdischarge properties and understand their role in the process. The electrical characterization consists of using a numerical method to extract data that are usually underestimated or poorly described in literature. Based on this numerical method validated in our work (see [118]), the microdischarges are investigated through their individual features, such as average lifetime ( $L_{md}$ ) and electrical charge, but also through their collective features, such as the plasma charge accumulation ( $Q_{pl}$ ) and their total number ( $N_{md}$ ) for a given analysis time. These data are collected for 20 periods – which corresponds to an analysis time of 700 ms – and then averaged over a single period in order to have statistically meaningful results. All this information is of great importance, for instance, for modeling CO<sub>2</sub> conversion in a DBD in filamentary mode [123, 127].

## **2. Influence of residence time and electrical parameters**

### **2.1. Introduction**

In this section, the influence of the flow rate of the inlet gas and the electrical parameters, such as the applied frequency and plasma power, on the filamentary behavior of the flowing DBD and the microdischarge properties will be presented. The understanding of their role on the CO<sub>2</sub> conversion is investigated. Electrical measurements are carried out to explain the conversion trends and to characterize the microdischarges through their number, their lifetime, their intensity and the induced electrical charge. In some studies, their influence on the gas and electrode temperatures is also evidenced through optical emission spectroscopy and infrared imaging.

It is shown that, in our configuration, the conversion depends mostly on the charge delivered in the plasma but also on the filamentation (number of microdischarges present throughout the discharge zone) and the voltage in the gap, representing the voltage of the plasma and thus the electric field in the plasma. These latter are critical parameters to take into account for the conversion of CO<sub>2</sub> and its efficiency. The following sub-chapters in this section gather different studies of the effect of various parameters to obtain a better understanding of the CO<sub>2</sub> splitting process.

## 2.2. Effect of the flow rate

### 2.2.1. CO<sub>2</sub> conversion and energy efficiency

The effect of the CO<sub>2</sub> flow rate on its conversion is carried out in a range from 50 to 3000 mL<sub>n</sub>.min<sup>-1</sup>. The controllable electrical parameters, i.e. applied power and operating frequency, are kept constant. The only varying parameter is the residence time, i.e. the average amount of time that particles spend in the discharge zone. The flow rate is inversely proportional to residence time as:

$$\tau_{\text{residence}}(\text{s}) = \frac{V_{\text{discharge zone}}(\text{cm}^3 \text{ or mL})}{\text{Flow rate}(\text{mL} \cdot \text{min}^{-1})} \times 60 (\text{s} \cdot \text{min}^{-1}) \quad \text{Eq. 4.5}$$

A low flow rate induces a long residence time, which is favorable for CO<sub>2</sub> splitting, as CO<sub>2</sub> spends more time in the discharge, and vice versa. Table 4 shows the residence times for their corresponding flow rate.

Table 4 : Residence time values for given flow rates in a discharge volume of 14.7 cm<sup>3</sup>.

Flow rate (mL <sub>n</sub> .min <sup>-1</sup> )	Residence time in the discharge zone (s)
50	17.64
75	11.76
100	8.82
200	4.41
300	2.94
500	1.76
1000	0.88
2000	0.44
3000	0.29

Figure 27 depicts the CO<sub>2</sub> conversion and energy efficiency versus the flow rate. The conversion can reach values as high as 35% at 50 mL<sub>n</sub>.min<sup>-1</sup> whereas the conversion barely reaches 1% at 3 L<sub>n</sub>.min<sup>-1</sup>. In this latter case, each molecule has an average residence time of 0.3 s, which seems to be too short for an appreciable conversion. A drop in energy efficiency is even observed at this flow rate. This shows how the residence time is an important parameter to take into account for the CO<sub>2</sub> splitting process. However, energy efficiencies are low at low flow rates and at very high (over 2.5 L<sub>n</sub>.min<sup>-1</sup>) flow rates. Indeed for a fixed applied power, the specific energy input is inversely related to the gas flow rate (equation

4.2). In the first window (I) of the graph (from 50 to 200 mL<sub>n</sub>.min<sup>-1</sup>), the variation in energy efficiency is considerable (from 6 to 11%) whereas this variation in energy efficiency is significantly lower in the second window (II), corresponding to a change of only 3% in a much bigger flow rate range. It is always important to find a good compromise for both conversion and energy efficiency at the same time. Therefore, in most of our experimental studies of CO<sub>2</sub> splitting (see next sections), a flow rate of 200 mL<sub>n</sub>.min<sup>-1</sup> is used.

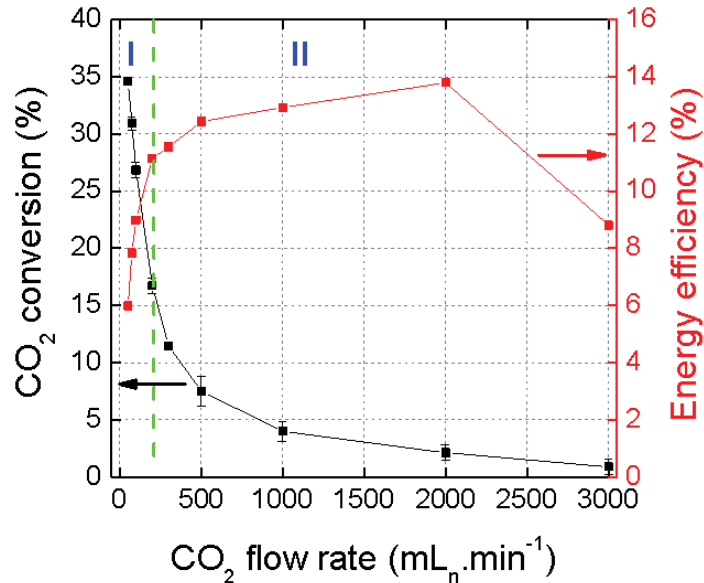


Figure 27 : CO<sub>2</sub> conversion and energy efficiency as a function of CO<sub>2</sub> flow rate, P<sub>abs</sub>=50-55W according to the flow rate, f=28.6 kHz.

### 2.2.2. Electrical characterization

An electrical characterization is carried out in detail to elucidate whether this conversion trend can be related to the voltages, the specific properties of the filaments or simply to the residence time.

As observed in Figure 28, the flow rate clearly affects the voltage present in the gap ( $V_{pl,eff}$ ) as the latter directly depends on the gas capacitance, while  $V_{diel}$  remains constant whatever the flow rate. A higher plasma voltage means that the electrons responsible for the CO<sub>2</sub> dissociation are more accelerated since the electric field is stronger. The electron temperature  $T_e$  is directly related to the electric field  $E$  (and thus to the reduced electric field  $E/n_0$ ) by the following equation [64]:

$$T_e = \frac{eE\lambda}{0.0548} \sqrt{\frac{\pi}{12}} \quad \text{Eq. 4.6}$$

where

$$e = \text{electron charge } (1.602 \times 10^{-19} \text{ C})$$

$$\lambda = 1/n_0\sigma_{en} \text{ electron mean free path (m)}$$

$$n_0 \text{ is the gas molecule density (m}^{-3}\text{)}$$

$$\sigma_{en} \text{ is the cross section of electron-neutral collisions at the same energy (m}^2\text{)}$$

This relation is based on the assumption of a Maxwellian EEDF. Therefore theoretically, when the EEDF is near Maxwellian, there exists a linear relation between  $T_e$  and  $E/n_0$  but it can be more complicated in reality, i.e. experimentally, even if the  $T_e(E/n_0)$  relation is quite linear for CO<sub>2</sub> [64]. In any case, this relation is a first good approximation to assume that the plasma voltage is directly proportional to the electron temperature.

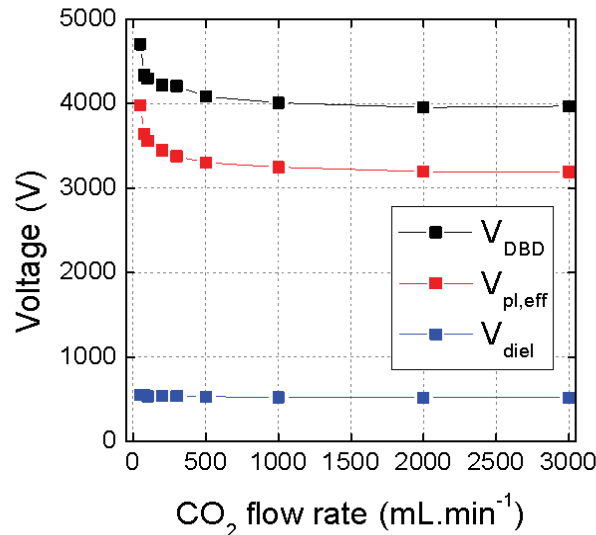


Figure 28 : RMS voltages as a function of the flow rate,  $P_{\text{abs}}=50\text{-}55\text{ W}$  according to the flow rate,  $f=28.6\text{ kHz}$ .

The specific properties of the microdischarges are also studied in detail. The number of microdischarges ( $N_{\text{md}}$ ) occurring during one half period versus the CO<sub>2</sub> flow rate is presented in Figure 29a. Over a flow rate of 1000 mL<sub>n</sub>.min<sup>-1</sup>, it is clear that the number of filaments drops from about 244 (*I*) to 222 (*II*) microdischarges during one half period, showing that the plasma becomes slightly less filamentary. On the other hand, increasing the inlet flow rate from 50 to 3000 mL<sub>n</sub>.min<sup>-1</sup> generates a clear rise in the mean lifetime of microdischarges from 14.3 to 15.6 ns, showing that the flowing gas might have an influence on the microdischarge properties. However, the plasma charge accumulation per half period is constant (0.22 μC). Therefore, the electron density remains constant whatever the flow rate since the plasma

current and the plasma charge accumulation for a given residence time are related to each other.

The electrical characterization shows that there is a small effect of the inlet gas flow rate on the discharge itself but the main cause of the drop in conversion (and thus increase in energy efficiency) is the decrease of the residence time.

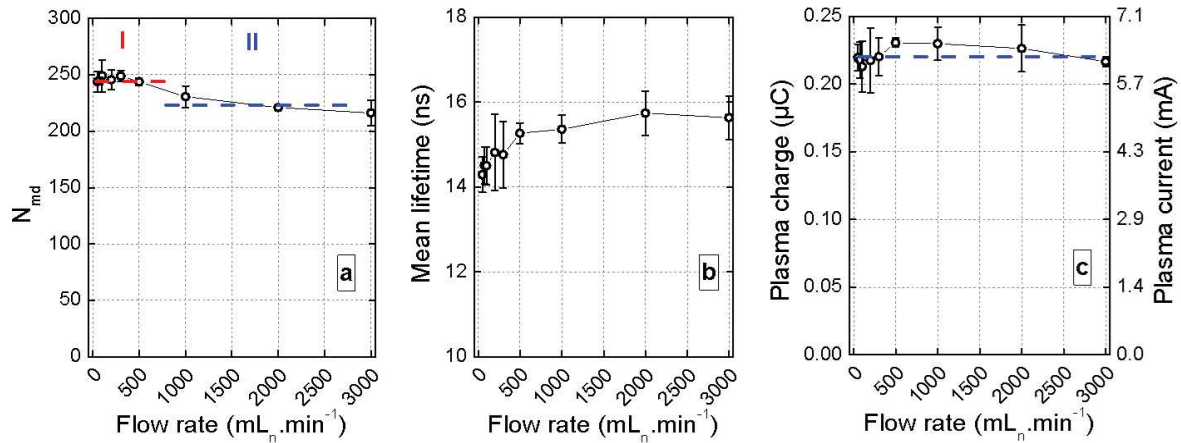


Figure 29 : (a) Number of microdischarges during one half period, (b) mean lifetime of the microdischarges and (c) Plasma charge accumulation during one half period, as a function of flow rate.  $P_{abs}=50-55W$ ,  $f=28.6$  kHz.

## 2.3. Effect of the frequency

### 2.3.1. CO<sub>2</sub> conversion and energy efficiency

The effect of the frequency on the CO<sub>2</sub> conversion ( $\chi_{CO_2}$ ) and on the CO<sub>2</sub> energy efficiency ( $\eta_{CO_2}$ ) is investigated for an absorbed power fixed at 55 W (determined by the Lissajous method; applied power = 60W). It is important to notice that the absorbed power always remains the same for a given applied power of 60 W, regardless of the used operating frequency.

As shown in Figure 30, an increase in the frequency from 16.2 to 28.6 kHz leads to a slight drop in the CO<sub>2</sub> conversion and energy efficiency. This is probably attributed to a drop in the density of electrons involved in the CO<sub>2</sub> splitting, although the total electron density in the whole discharge remains constant; see below. The reason why there is a drop in conversion may be related to the fact that the shape of the electron energy distribution function (EEDF) is

different when the plasma is in the filamentary regime (high frequency) or less filamentary regime-glow regime (low frequency) [241]. Depending on the shape of the tail of the EEDF, the number of electrons which can contribute to the breaking of the C=O bonds present in CO<sub>2</sub> might be higher for low frequency, i.e. electrons which are located on the right side of the EEDF over 5.52 eV (value of the C=O bond). Also,  $\chi_{\text{CO}_2} > \eta_{\text{CO}_2}$  in the whole frequency range because the SEI is in the order of  $\approx 4.2 \text{ eV}\cdot\text{molecule}^{-1}$ , and thus always higher than  $\Delta H_{298\text{K}}$ .

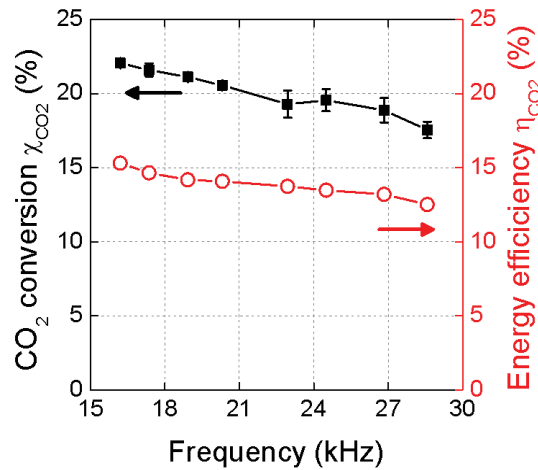


Figure 30 : CO<sub>2</sub> conversion and energy efficiency as a function of the frequency,  $P_{\text{abs}}=55 \text{ W}$ ,  $\Phi(\text{CO}_2)=200 \text{ mL}\cdot\text{min}^{-1}$ .

### 2.3.2. Electrical characterization

A complementary, electrical characterization is carried out to elucidate whether this trend in conversion and energy efficiency can be correlated with electrical measurements. As observed in Figure 31, the DBD voltage ( $V_{\text{DBD}}$ ) decreases as a function of the frequency (by almost 500 V in this frequency range).

For a DBD operating in glow mode, the DBD voltage is the sum of two components: the plasma voltage ( $V_{\text{pl}}$ ) and the dielectric voltage ( $V_{\text{diel}}$ ) [87, 107, 224, 225]. As in our case the DBD operates in the filamentary mode, the presence of micro-discharges and remnant surface charges from previous micro-discharges leads to a potentially inhomogeneous electric field distribution. Therefore, the measured voltage has to be considered as an effective plasma voltage ( $V_{\text{pl,eff}}$ ), i.e. a spatial average of the plasma voltage with potential local magnitude variations.

As the total electrical charge is conserved through the entire DBD source ( $Q_{pl}=Q_{diel}$ ) the relation  $C_{pl}\cdot V_{pl,eff}=C_{diel}\cdot V_{diel}$  leads to  $V_{pl,eff}/V_{diel}=C_{diel}/C_{pl}=11.2$ . This ratio is rather high and means that  $V_{pl,eff}$  represents almost 82% of  $V_{DBD}$ , as represented by the red curve in Figure 31. Similar values have also been reported in literature; for instance, in [229]  $V_{pl,eff}$  was stated to represent even 98% of  $V_{DBD}$ . It is clear that  $V_{DBD}$  and  $V_{pl,eff}$  also decrease upon increasing the frequency, and this can probably explain the drop in the CO<sub>2</sub> conversion and energy efficiency, shown in Figure 30 above, as a lower voltage leads to lower electron energies, and thus less efficient CO<sub>2</sub> conversion by electron impact excitation-dissociation. The dielectric voltage is obtained by subtracting  $V_{pl,eff}$  from  $V_{DBD}$ . It is almost constant in the entire frequency range with a value close to 450 V. To enhance the CO<sub>2</sub> conversion, one could increase  $V_{pl,eff}$  (hence the electric field in the gap) by decreasing  $V_{diel}$ , e.g. by changing the dielectric thickness or the nature of the dielectric (see section - effect of the dielectric barrier - below).

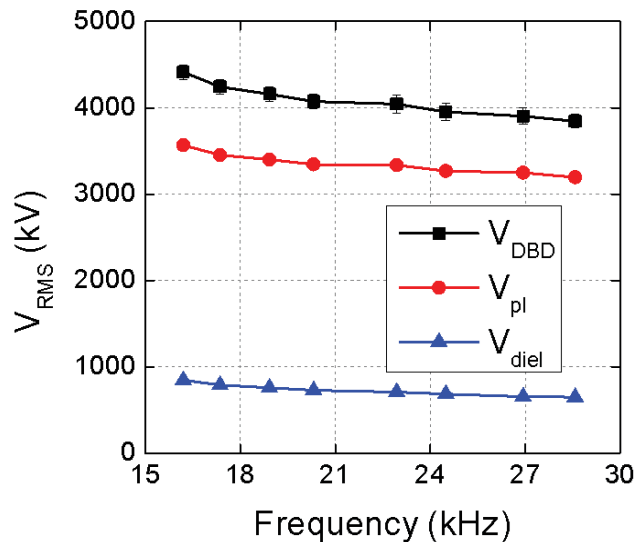


Figure 31 : RMS voltages as a function of frequency at  $P_{abs}=55$  W,  $\Phi(CO_2)=200$  mL<sub>n</sub>.min<sup>-1</sup>.

As the plasma current corresponds to a large number of individual peaks and not to a continuous periodic function, studying its variation versus frequency requires a dedicated analytical work. The number of peaks can be analyzed (i) per period or half period and (ii) for the entire CO<sub>2</sub> residence time or a given analysis time. In the present work, these variations are studied:

- (i) Per half period rather than per period since the current peak distributions can differ depending on their location on the positive or negative half periods.

- (ii) For an analysis time fixed at 120  $\mu\text{s}$  which is a more reasonable time window for this study than the residence time of CO<sub>2</sub>. The latter one is estimated to 4.5 s considering the geometrical characteristics of the tubular discharge reactor and the CO<sub>2</sub> flow rate fixed at 200 mL<sub>n</sub>.min<sup>-1</sup>.

The oscillograms of the total current ( $i_{\text{DBD}}=i_{\text{pl}}+i_{\text{diel}}$ ) are plotted in Figure 32 at 16.2 kHz, 22.9 kHz and 28.6 kHz. The comparison of these three oscillograms shows that increasing the frequency induces a decrease in the number of peaks per half period, which is not unlogical, as the time of a half period drops upon higher frequency. Also, for a given frequency, the peak distribution in the positive half periods appears different from that in the negative half periods, which might be attributed to the asymmetry of the tubular discharge, where only one electrode is covered by a dielectric [242]. These oscillograms are analyzed using the aforementioned numerical method to determine the microdischarge characteristics with higher accuracy.

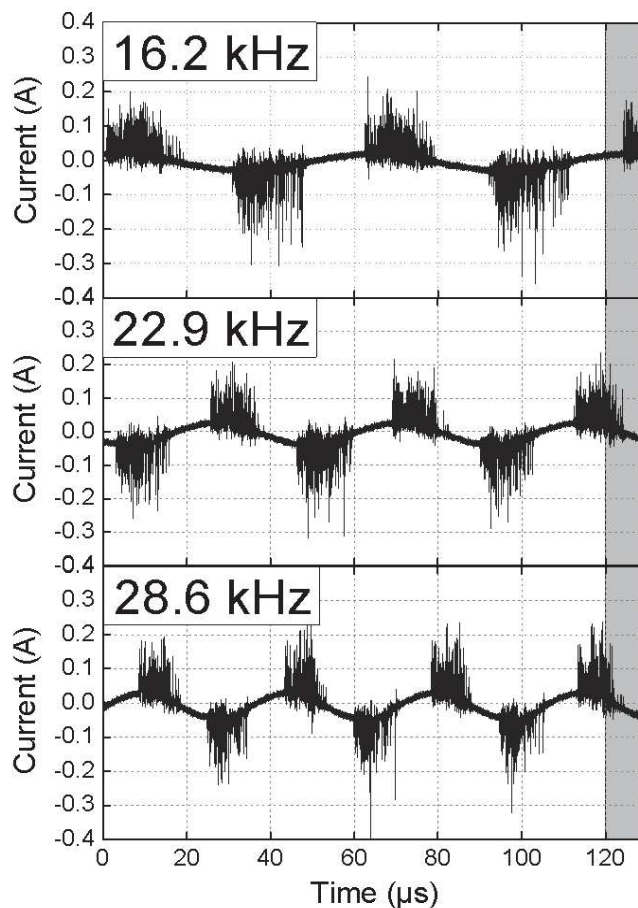


Figure 32 : Current profiles as a function of time for 3 different frequencies (16.2, 22.9 and 28.6 kHz) at  $P_{\text{abs}}=55$  W,  $\Phi(\text{CO}_2)=200$  mL<sub>n</sub>.min<sup>-1</sup>.

The effect of the frequency on the number of microdischarges ( $N_{md}$ ) is depicted in Figure 33a per half period and for  $\tau_{anal}=120 \mu s$ . As mentioned above, a higher frequency results in a lower number of microdischarges per half period (whatever the sign of the half period) but it remains unchanged for  $\tau_{anal}=120 \mu s$ . Therefore, the total number of microdischarges cannot explain the decrease in the CO<sub>2</sub> conversion. The same applies to the average lifetime of the microdischarges illustrated in Figure 33b as it remains close to 15 ns, regardless the operating frequency. As shown in Figure 33c, a rise in the frequency induces a slight drop in the plasma charge per half period (with  $Q_{pl}^+=Q_{pl}^-$ ). As the effect of the frequency on  $\chi_{CO_2}$  has to be explained based on the residence time, it is more relevant to consider  $Q_{DBD}^{120}$ , as plotted in Figure 33d. In this figure, the electrical charge of the DBD increases with frequency due to its dielectric component ( $Q_{diel}$ ) and not due to its plasma component ( $Q_{pl}$ ). In other words, the frequency does not seem to change the electrical properties of the plasma but the electric field distribution through the dielectric barrier.

Also,  $Q_{pl}^+$ ,  $Q_{pl}^-$  and  $Q_{pl}^{120}$  can be easily converted into conduction currents considering either the half period or the analysis time, as expressed in the following formulas:

$$i_{pl}^+(f) = \frac{Q_{pl}^+(f)}{T/2} = 2f \cdot Q_{pl}^+(f) \quad \text{Eq. 4.7}$$

$$i_{pl}^-(f) = \frac{Q_{pl}^-(f)}{T/2} = 2f \cdot Q_{pl}^-(f) \quad \text{Eq. 4.8}$$

$$i_{pl}^{120}(f) = \frac{Q_{pl}^{120}(f)}{\tau_{anal}} \quad \text{Eq. 4.9}$$

Plotting these currents in Figure 33e indicates that their variations versus the frequency are not that much significant: only a slight increase of 20% (from 11 mA to 14 mA) is observed for a half period. The discharge current also increases slightly for a given residence time. This is logical, as the voltage slightly drops upon rising frequency, so the current should slightly increase to keep the same power. Hence, it is clear that the microdischarge characteristics are not correlated to the CO<sub>2</sub> conversion.

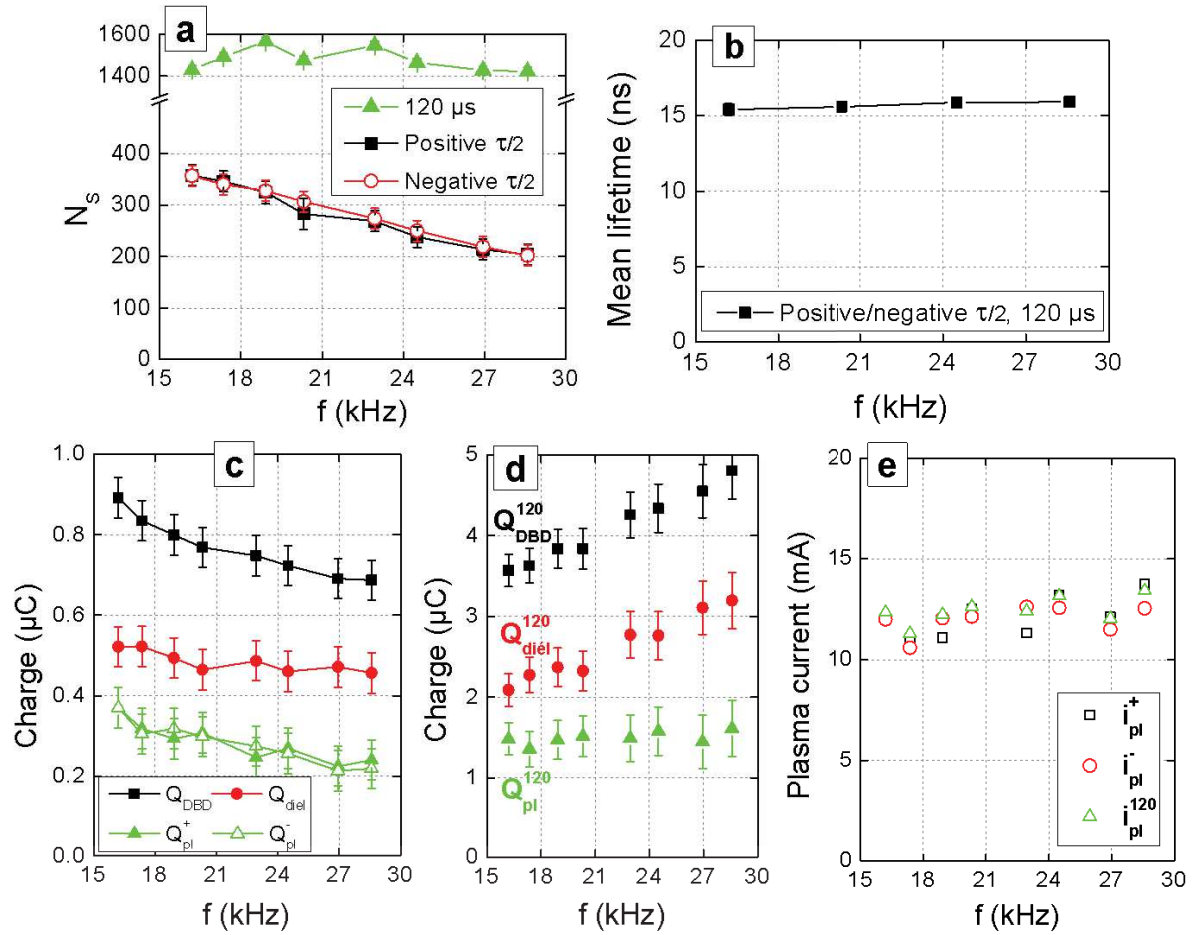


Figure 33 : (a) Number, (b) lifetime of the microdischarges per half period ( $T/2$ ) and for  $\tau_{\text{anal}} = 120 \mu\text{s}$ ; (c) charge per  $T/2$ , (d) charge for  $\tau_{\text{anal}} = 120 \mu\text{s}$  and (e) conduction current per  $T/2$  and for  $\tau_{\text{anal}} = 120 \mu\text{s}$ .

An alternative and convenient representation to evaluate how the frequency could change the microdischarge characteristics is to plot the distribution of their lifetimes versus their number ( $N_{\text{md}}$ ) for several frequencies, as presented in Figure 34. Most of the microdischarges ( $N_{\text{md}} \approx 1200$ ) exhibit a lifetime comprised between 7 and 25 ns. A small fraction of microdischarges exhibits a lifetime under 7 ns and above 25 ns. The drop in CO<sub>2</sub> conversion upon rising frequency may not be induced by the microdischarges. Only the drop of the discharge voltage seems to be responsible for the drop in CO<sub>2</sub> conversion.

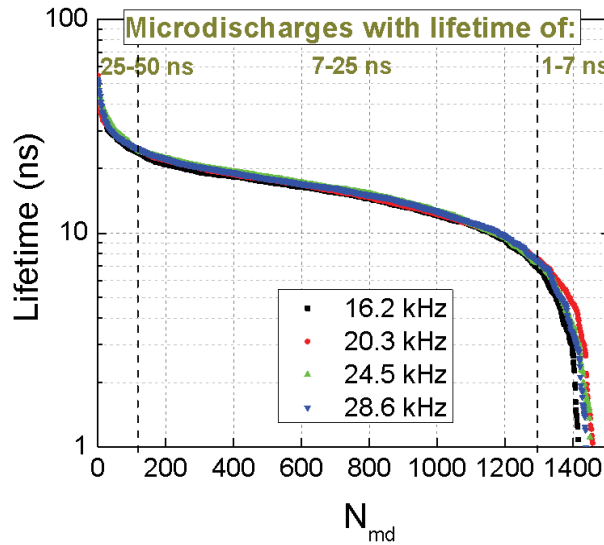


Figure 34 : Distribution of the microdischarge lifetime for  $\tau_{\text{anal}}=120 \mu\text{s}$  and  $P_{\text{abs}}=55 \text{ W}$ .

### 2.3.3. Gas temperature and electrode temperature

In OES measurements, each optical emission spectrum is acquired with either the 1800 grooves/mm or the 2400 grooves/mm grating (blazed at 500 nm and 250 nm) and recorded for an exposure time of 5 s and 7 accumulations. Silva et al. have shown that in a CO<sub>2</sub> microwave plasma at low pressure, the rotational temperature of the CO band is similar to the gas temperature [140]. However, as the CO Angstrom band is less suitable at atmospheric pressure for gas temperature measurements [243], we have analyzed the first positive system (FPS) of N<sub>2</sub> by adding 10% of nitrogen to CO<sub>2</sub>. Indeed, in the case of CO<sub>2</sub> atmospheric plasmas, the CO Angstrom band is less reliable since the lifetime of the CO excited molecules is too short to allow a sufficient number of collisions with the background gas to thermalize the rotational population [243]. At atmospheric pressure, the lifetime of excited N<sub>2</sub> (B) is 5000 ns, i.e. 200 times higher than the one of excited CO (Angstrom system), hence giving more robust gas temperatures [220, 221]. Moreover, adding 10% of N<sub>2</sub> to the CO<sub>2</sub> discharge does not affect that much its behavior as the current profile (electrical characterization) and the CO<sub>2</sub> conversion remain similar. The rotational temperature of N<sub>2</sub> is also found to be close to the gas temperature (see *Chapter III*). Then, the gas temperature has been measured via a line-ratio peak formula, specific to this system [220, 221]. The peaks at 775.3 and at 773.9 nm have been considered.

A slight increase in the conduction current as well as in the microdischarge lifetime may have an impact on the power dissipated by the discharge by the Joule effect since it is proportional to the square of  $i_{DBD}$ . This assumption has been verified by investigating the influence of the frequency on the gas temperature (obtained from OES measurements) as well as on the electrode temperature (obtained from IR imaging and calibrating the ambient temperature according to the emissivities of the different materials of the reactor). Figure 35a shows the 2D temperature profiles of the outer grounded electrode, obtained by placing the IR camera perpendicular to the gas flow. The electrode temperature appears rather uniform in the whole discharge region, regardless the frequency. As illustrated in Figure 35b, increasing the frequency from 16.2 kHz to 28.6 kHz induces an increase in the gas temperature (from 523 to 560 K) and a slight increase in the average temperature of the grounded electrode (from 375 K to 405 K). The difference  $T_{gas}-T_{electrode}$  can be considered as a representation of Joule losses. A rise in the frequency induces an increase of the gas temperature that can be linked with a decrease of the effective plasma voltage (see Figure 31). Indeed, a low frequency plasma gives rise to a higher effective plasma voltage, i.e. to a higher electric field where electrons can be more accelerated. The increase in gas temperature upon rising frequency may be correlated with the lower CO<sub>2</sub> conversion at high frequencies since more energy may be spent for heating and less to decompose CO<sub>2</sub>. The gas temperature values which are found with the OES spectra are in good agreement and in the same order of magnitude with temperature values determined by other methods (like by Raman scattering) for a CO<sub>2</sub> DBD in the same kind of conditions [244].

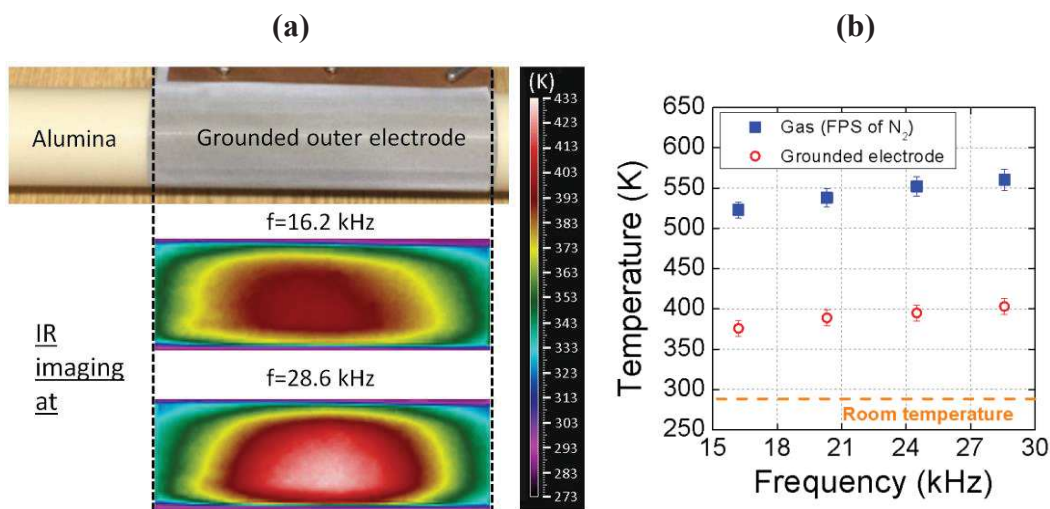


Figure 35 : (a) 2D temperature profiles of the grounded electrode; (b) Gas and grounded electrode temperature as a function of frequency.  $P_{abs}=55$  W, process time = 5 min.

### 2.3.4. *Electron temperature*

The electron temperature ( $T_e$ ) has been estimated by mixing 10% of argon with the CO<sub>2</sub> discharge, thus allowing the measurements of two specific Ar lines at 420.07 nm (3p<sub>9</sub>→1s<sub>5</sub> transition) and 419.83 nm (3p<sub>5</sub>→1s<sub>4</sub> transition). Based on the work of Boffard et al. [245], the line-ratio  $I_{3p9 \rightarrow 1s5}^{Ar} / I_{3p5 \rightarrow 1s4}^{Ar}$  can be used to extract the value of  $T_e$  in pure Ar discharges. However, it should be emphasized that this ratio depends on the Ar metastable up to energies of 4 eV. In the current work, the Ar metastable densities were not measured, so this method cannot provide accurate values of  $T_e$ . Nevertheless, the mentioned ratio is close to 1, which should result in  $T_e$  values in the order of 3 eV or higher.

## 2.4. Effect of the power

### 2.4.1. *CO<sub>2</sub> conversion and energy efficiency*

Figure 36 shows that the CO<sub>2</sub> conversion rises linearly with power, reaching a value as high as 28% at 100W. In the same power range, a slight decrease in the energy efficiency is measured from 12.5% to 11%. These trends are logical, because more energy is put into the system, leading to a higher electron density [246, 247], and to more CO<sub>2</sub> conversion. At the same time, the rise in CO<sub>2</sub> conversion is less pronounced than the rise in SEI, thus the energy efficiency drops slightly upon increasing power, as predicted by equation 4.2. An electrical characterization is carried out to elucidate whether this conversion trend can be related to specific properties of the filaments.

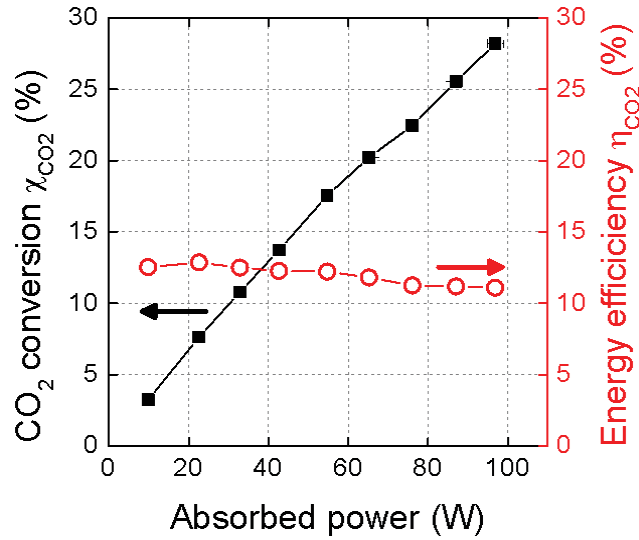


Figure 36 : CO<sub>2</sub> conversion and energy efficiency as a function of the absorbed power, for  $f=28.6$  kHz, and  $\Phi(\text{CO}_2)=200$  mL<sub>n</sub>.min<sup>-1</sup>.

#### 2.4.2. Electrical characterization

First, the influence of the absorbed power on the DBD voltage has been studied, as plotted in Figure 37, which shows a clear increase from 3.8 kV to 4.2 kV, as expected.  $V_{\text{pl,eff}}$  represents 89% of the DBD voltage at 3 W and it drops to 80% at 97 W. The effective plasma voltage is thus not really correlated with the increase in  $\chi_{\text{CO}_2}$  but the influence of the filaments has to be investigated as well for a complete interpretation of the behavior.

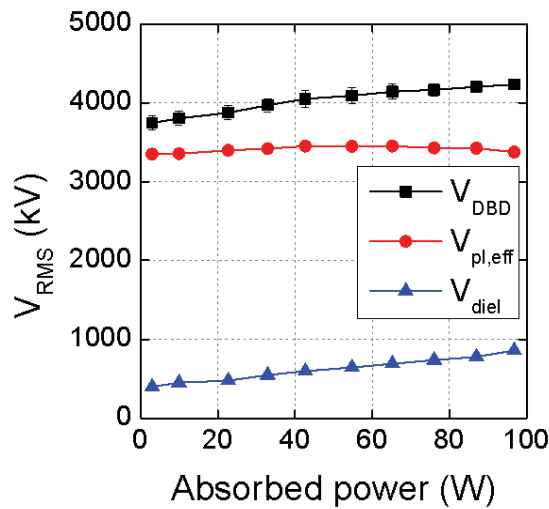


Figure 37 : RMS voltages as a function of the absorbed power, for  $f=28.6$  kHz and  $\Phi(\text{CO}_2)=200$  mL<sub>n</sub>.min<sup>-1</sup>.

As the oscillograms present a very symmetric signal for the positive and negative sign of  $\tau/2$ , we only focus our study on the filaments for a certain analysis time.

Figure 38a depicts the number of microdischarges within a fixed  $\tau_{\text{anal}}$ , as well as their mean lifetime, as a function of the absorbed power. Increasing the power leads to a rise in the number of peaks as well as their mean lifetime. The power effect is therefore very different from the frequency effect where no influence was observed both on  $N_{\text{md}}$  and the microdischarge lifetime (see Figure 33a and Figure 33b). Also, Figure 38b illustrates the electrical charge of the DBD versus the absorbed power: a clear increase is observed from 20W to 100W. It is attributed to the increase in the plasma charge (which corresponds therefore to an increase of the discharge current), even if the dielectric component remains always higher than the plasma component in the entire power range. The latter one, however, remains rather constant since the operating frequency is fixed. Thus, it is clear that the rise in number of microdischarges, in the microdischarge lifetime and in the total electric charge of the DBD are correlated with the rise in CO<sub>2</sub> conversion with higher power.

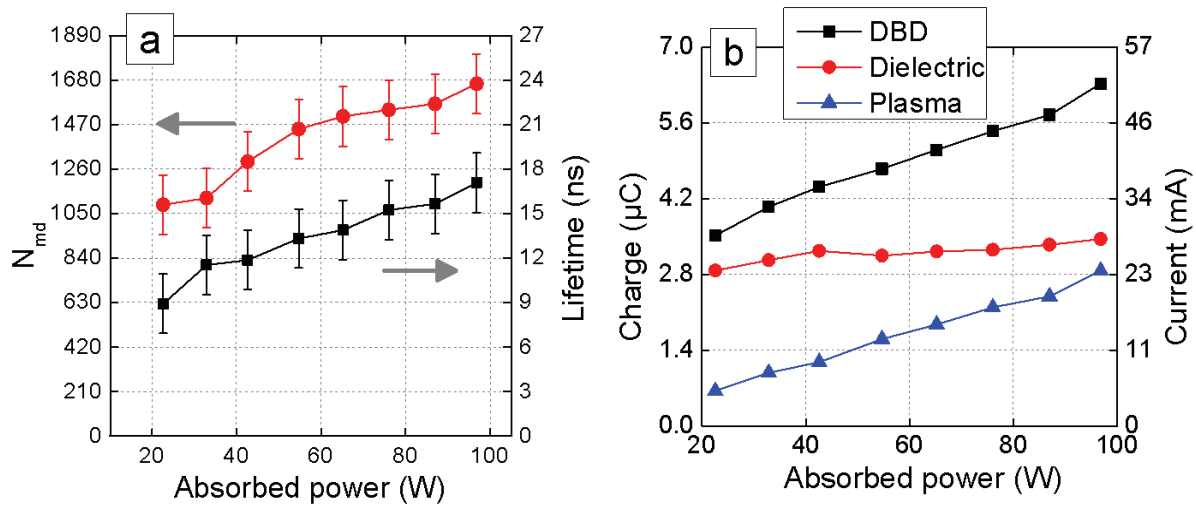


Figure 38 : Characteristics of the microdischarges as a function of the absorbed power: (a) number of current peaks and mean lifetime, (b) charge and current for  $\tau_{\text{anal}}=120\mu\text{s}$ .

The distribution of the microdischarge lifetimes versus their number ( $N_{\text{md}}$ ) is represented in Figure 39. It appears that decreasing the power leads mostly to the production of short-lifetime microdischarges (cf. line a). Indeed, the percentage of microdischarges which has less than 7 ns of lifetime is 31, 23 and 8% for a plasma power of 23, 65 and 97 W, respectively. However, increasing the power leads to a higher extent to the production of long-lifetime microdischarges (cf. line b). Indeed, the percentage of microdischarges which has more than

25 ns of lifetime is 3, 5 and 12% for a plasma power of 23, 65 and 97 W, respectively. This effect is not observed when tuning the frequency.

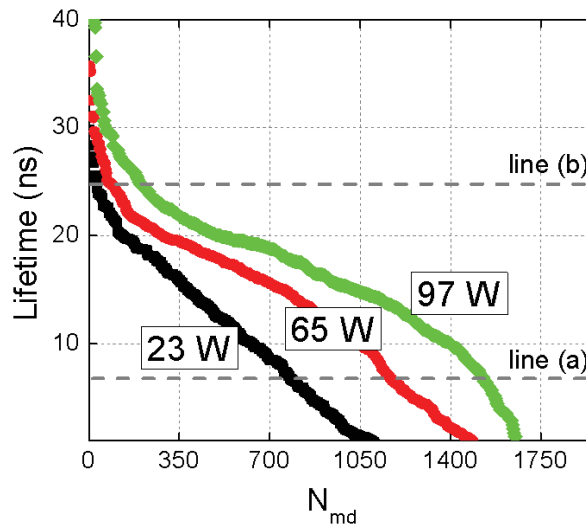


Figure 39 : Distribution of the microdischarge lifetime for  $f=28.6$  kHz,  $\tau_{\text{anal}}=120\mu\text{s}$ .

#### 2.4.3. Gas temperature and electrode temperature

Furthermore, we also check if the rising CO<sub>2</sub> conversion is correlated with the gas temperature (same spectra acquisition as in the previous section: exposure time of 5 s and 7 accumulations) and the temperature of the grounded electrode. In Figure 40a, the 2D profiles of the temperature at the outer grounded electrode are plotted for 20 W, 50 W, 80 W and 100 W. The electrode temperature appears not entirely uniform in the whole discharge region, and it is clearly correlated with power. As illustrated in Figure 40b, the temperature of the grounded electrode increases linearly with power and reaches a mean value as high as 430 K at 100 W after 5 min of process time. On the other hand, the gas temperature increases by almost 40 K as a function of the power as observed in Figure 40b. Increasing the plasma power generally enhances the electron impact processes and thus, could lead to gas heating. When the plasma is ignited, the gas heating is responsible for an increase of the wall temperature. The Joule losses are quite significant since both the alumina dielectric and the mesh stainless steel electrode have quite high thermal conductivities.

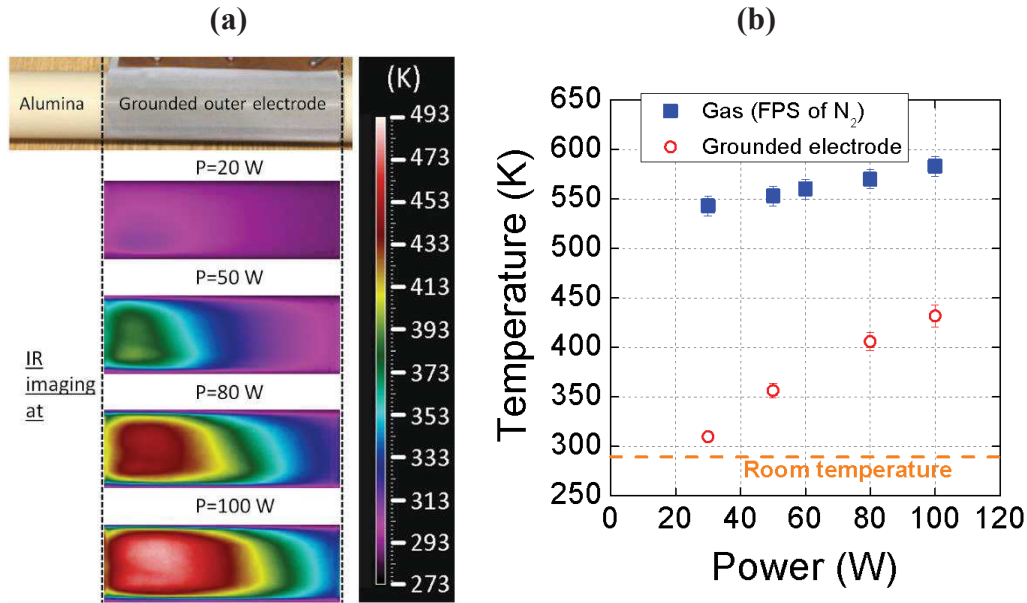


Figure 40 : (a) 2D profiles of the grounded electrode temperature for various powers; (b) Gas temperature and grounded electrode temperature as a function of power ( $f=28.6$  kHz, process time=5 min).

## 2.5. Effect of the multi-pulsed AC voltage (so-called burst mode)

### 2.5.1. Introduction

A DBD is commonly supplied with an AC voltage (pure AC mode) (e.g., [112, 117, 248]) and sometimes by high voltage nano or micro pulses [84, 167, 249-257] (pulsing mode). According to Jiang et al. [249], supplying a DBD with high voltage nanopulses enhances its stability over time, as well as its uniformity, since no irregular distribution of microdischarges is revealed. Such a power delivery presents great benefits for plasma polymerization, thin layer deposition and surface treatments since no significant texturization appears and it allows for instance an optimal deposition of a subsequent barrier layer [73, 108, 258]. This configuration is also of interest for gas treatment since a larger number of microdischarges is produced, increasing the probability for a single gas molecule to pass through the discharge and interact with a single microdischarge. Ndong et al. explain that positive voltage pulses create discrete discharge channels uniformly arranged on the dielectric surface in a streamer-like regime, while negative voltage pulses mostly tend to generate a uniform discharge along the active electrode such as a glow-like discharge [259, 260]. Song et al. investigated a bipolar pulsed discharge for the CO<sub>2</sub> reforming of methane where both the CO<sub>2</sub> and CH<sub>4</sub>

conversion are higher when applying a pulse mode compared to a classical sinusoidal AC mode [261]. Some other authors have also compared a unipolar and bipolar DC discharge [262-264] and showed that the CO<sub>2</sub> conversion slightly increases upon rising pulse frequency.

Besides the usual pure AC and pulsing modes, a DBD can also be supplied by an AC voltage that is switched off at regular times, at a frequency much lower than the AC frequency. This so-called burst mode is well known in manufacturer's manuals and also in the literature dedicated to power supplies [265-273]. Benard et al. [265] have demonstrated how the production of small perturbations to the classical alternative voltage (i.e. burst mode) can enhance the stability of the DBD. However, the literature dealing with cold atmospheric plasma sources operating in this so-called burst mode for gas conversion is very limited [274].

In this section, we investigate the splitting of CO<sub>2</sub> using a flowing DBD operating in burst mode and we compare its performance with the usual pure AC mode. This burst mode corresponds to a sinusoidal voltage which is switched on and off at several repetition frequencies. The applied power is provided by the AFS generator G10S-V and the transformer, which amplify the sinusoidal signal of the alternating voltage and which allow us to pulse the voltage in a controlled manner. The influence of this mode is investigated on the CO<sub>2</sub> conversion, the energy efficiency and the microdischarge features (i.e., number, lifetime and charge of the microdischarges) and we compare the results with the same DBD that is supplied with a pure AC voltage (duty cycle = 100%). Electrical characterization, mass spectrometry and optical emission spectroscopy are applied to understand how and why the CO<sub>2</sub> conversion is enhanced.

The signal frequency always remains fixed at  $f_{\text{signal}}=28.6$  kHz (period of 35.7  $\mu\text{s}$ ). Furthermore,  $T_{\text{ON}}$  and  $T_{\text{OFF}}$  are defined as the time of plasma ignition and the time when no power is applied to the reactor. Except for the analysis of  $T_{\text{ON}}$  and  $T_{\text{OFF}}$  at constant duty cycle, the main results described in this work are related to the influence of the duty cycle. In this latter case,  $T_{\text{ON}}$  remains fixed at 1 ms while  $T_{\text{OFF}}$  is changed between 0 and 1.5 ms, corresponding to a duty cycle ( $D_{\text{cycle}}$ ) between 100 and 40%. Therefore, the repetition frequency of the burst mode,  $f_{\text{repetition}}=1/(T_{\text{ON}}+T_{\text{OFF}})$ , is varied between 400 and 900 Hz. The voltage as a function of time is plotted in Figure 41 for high voltages delivered either in pure AC mode (a) and in burst mode (b). As the total power applied to the plasma ( $P_{\text{applied}}$ ) is fixed at 50 W in all cases, the power during the plasma ignition ( $P_{\text{plasma}}$ ) in burst mode is always

higher than in pure AC mode, since  $P_{\text{plasma}} \text{ (W)} = P_{\text{applied}} \text{ (W)} / D_{\text{cycle}} \text{ (\%)}$ . All electrical measurements are performed during  $T_{\text{ON}}$ .

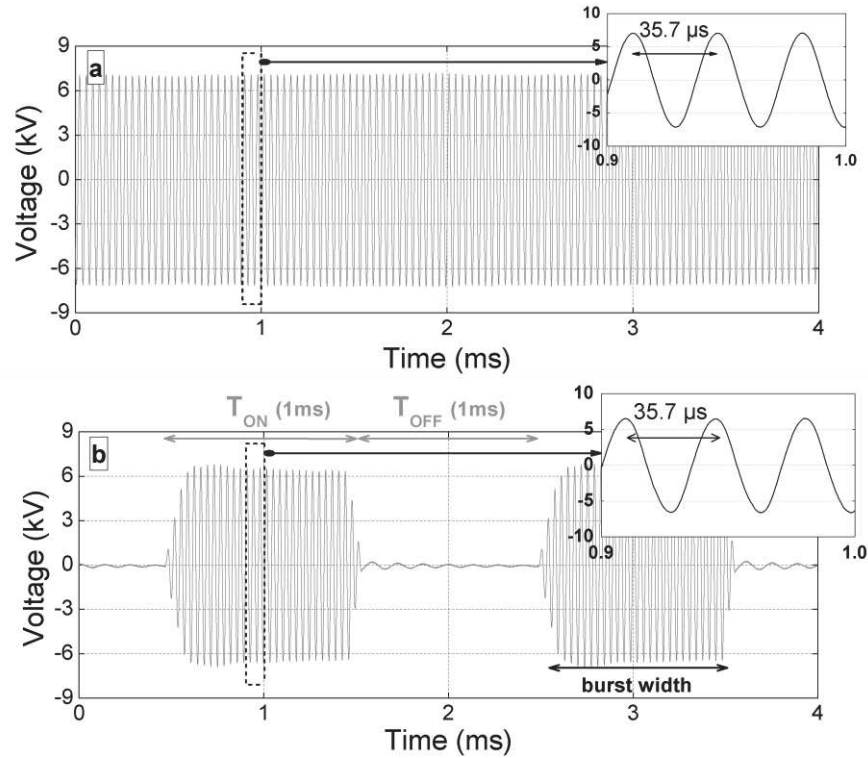


Figure 41 : High voltage signals applied to the discharge, with frequency of 28.6 kHz (or period of 35.7 μs), in (a) pure AC mode, and (b) burst mode, with a duty cycle of 50% ( $T_{\text{ON}} = T_{\text{OFF}} = 1 \text{ ms}$ ).

Moreover, each OES spectrum is acquired for an exposure time of 5 s and 7 accumulations. Here, of particular interest is the CO emission band headed at 483.3 nm from the CO Angstrom system ( $B^1 \Sigma^+ \rightarrow A^1 \Pi; v'=0 \rightarrow v''=1$ ) shown in Figure 42. Its ro-vibrational structure is calculated and fitted to the experimental spectra in order to determine the rotational temperature ( $T_{\text{rot}}$ ) and hence the gas temperature ( $T_{\text{gas}}$ ), assuming  $T_{\text{rot}} \approx T_{\text{gas}}$  [140, 275, 276]. For the sake of comparison, the gas temperature is also measured using another band: the first positive system (FPS) of N<sub>2</sub> is analyzed by adding 10% of nitrogen to CO<sub>2</sub>. In this case, the temperature is measured via a line-ratio peak formula, specific to this system [220, 221], using the peaks at 775.3 and at 773.9 nm.

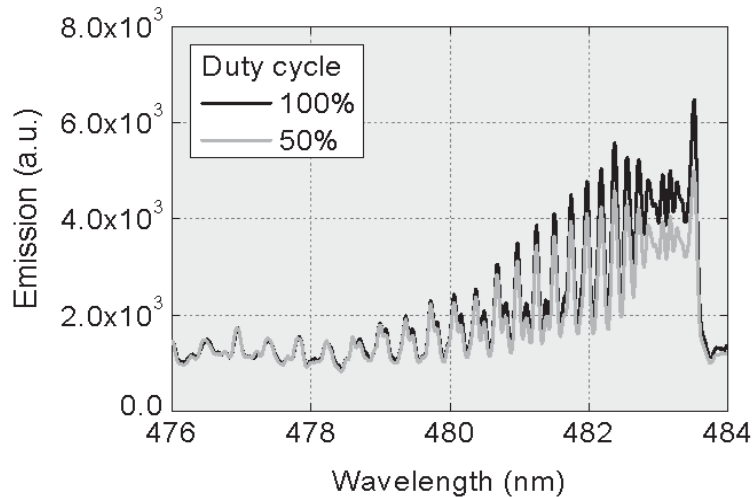


Figure 42 : CO band from the  $[B^1\Sigma^+ \rightarrow A^1\Pi; v'=0 \rightarrow v''=1]$  Angstrom System in the DBD supplied with pure CO<sub>2</sub>, at two different duty cycles.

### 2.5.2. CO<sub>2</sub> conversion and energy efficiency

The CO<sub>2</sub> conversion and energy efficiency as a function of the duty cycle of the burst mode are depicted in Figure 43a. The conversion obtained in the pure AC mode ( $D_{\text{cycle}}=100\%$ ) is 16.1%, which is significantly lower than in the burst mode at 40% duty cycle (i.e., 25.8%). Decreasing the duty cycle at constant applied power thus results in a higher CO<sub>2</sub> splitting. As evidenced in Figure 43b, smaller duty cycles yield higher peak powers, e.g. 100 W for  $D_{\text{cycle}}=50\%$  versus 50 W for  $D_{\text{cycle}}=100\%$ . These higher peak powers delivered within shorter times can explain the higher CO<sub>2</sub> conversion. However, we will also show at the end of this section that the enhancement of the burst mode is not only attributed to the higher peak power, but also to other effects (see below). The corresponding energy efficiency also increases upon decreasing duty cycle from 14.5% (at  $D_{\text{cycle}}=100\%$ ) to 23.1% (at  $D_{\text{cycle}}=40\%$ ).

On the other hand, keeping the duty cycle constant but increasing the burst width from 1 ms to more than 20 ms has no effect on the CO<sub>2</sub> conversion and energy efficiency, as illustrated in Figure 44. Therefore, in the next sections we will only investigate the influence of  $T_{\text{OFF}}$  (or duty cycle or repetition frequency) on the electrical properties of the discharge, and more specifically on the microdischarge features. First we will show the effect of the duty cycle on the evolution of the applied voltage with increasing process time, to check the time-stability of the discharge. Next, the influence of the duty cycle on the current oscillograms and on the microdischarge properties, as well as on the gas temperature will be studied. Finally, the burst

mode and the normal AC mode will be compared at the same delivered power, to illustrate that the enhancement of the burst mode is not only attributed to the higher peak power, but also due to the microdischarge properties.

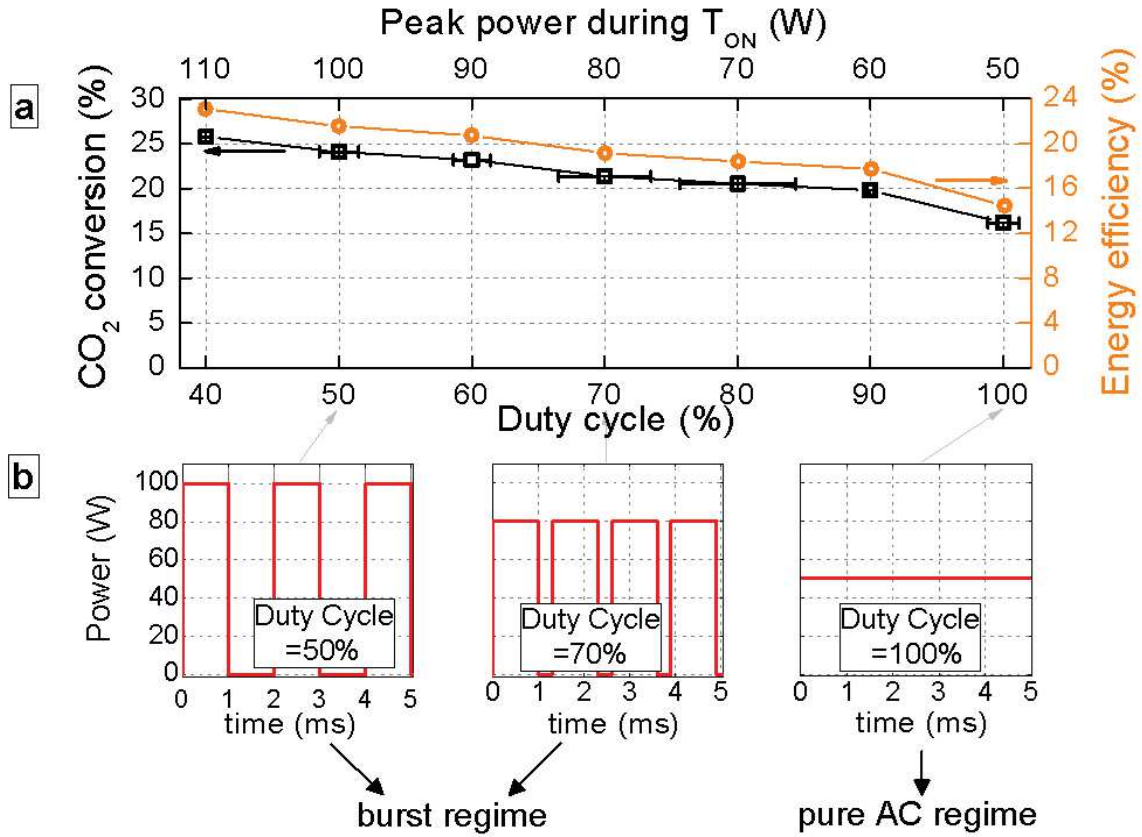


Figure 43 : (a) CO<sub>2</sub> conversion and energy efficiency as a function of the duty cycle –  $P_{\text{applied}}=50$  W,  $f_{\text{signal}}=28.6$  kHz,  $f_{\text{repetition}}=400 - 900$  Hz and  $\Phi(\text{CO}_2)=200$  mL<sub>n</sub>.min<sup>-1</sup> ; (b) Power versus time for  $D_{\text{cycle}}=50, 70$  and 100%.

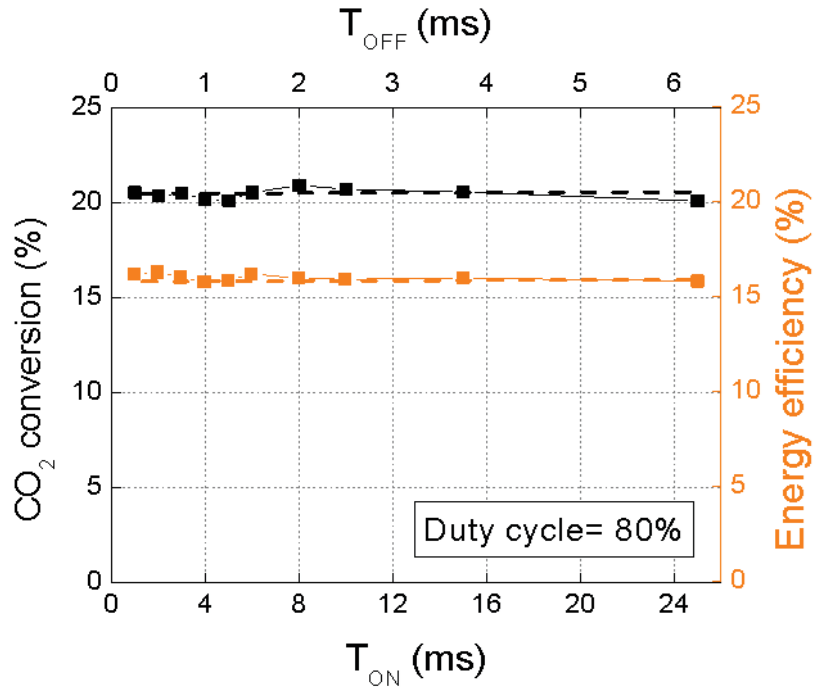


Figure 44 : CO<sub>2</sub> conversion and energy efficiency for a fixed duty cycle of 80%, as a function of T<sub>ON</sub>. P<sub>applied</sub>=50 W, f<sub>signal</sub>=28.6 kHz and Φ(CO<sub>2</sub>)=200 mL<sub>n</sub>.min<sup>-1</sup>.

### 2.5.3. Influence of the duty cycle on the discharge time-stability

Figure 45 shows the applied voltage as a function of the process time for several different duty cycles. The lower the duty cycle, the more stable and the higher is the voltage as a function of the process time. For  $D_{\text{cycle}} < 70\%$ , the voltage remains quite stable over time, e.g. at  $D_{\text{cycle}} = 50\%$  it is close to 4400 V for all process times investigated (with only a small variation within the first 60 s). Therefore, the discharge appears as very stable in time. However, this time-stability gradually vanishes upon increasing  $D_{\text{cycle}}$  and in the pure AC mode ( $D_{\text{cycle}}=100\%$ ) the time dependency is quite significant: a drop of approximately 500 V is reached in 90 s, from 4400 V to a plateau at 3900 V. This transient regime is clearly visible in pure AC mode and is due to the dielectric properties of the barrier: it behaves as a capacitor with a dielectric relaxation time that is much longer than the period associated with the applied voltage. The dielectric relaxation time of the barrier  $t_{\text{relax}}$  is defined as the product of its dielectric permittivity ( $\epsilon = \epsilon_0 \cdot \epsilon_r$ ) with its electrical resistivity ( $\rho$ ), i.e.,  $t_{\text{relax}} = \epsilon_0 \cdot \epsilon_r \cdot \rho$ , where  $\epsilon_0 = 8.854 \cdot 10^{-12}$  F.m<sup>-1</sup> and, in the case of alumina,  $\epsilon_r = 9$  and  $\rho \approx 10^{14}$  Ω.cm [277]. A rough estimation leads to  $t_{\text{relax}} \approx 0.8$  s. This value is much higher than the period of the applied voltage, which is 35.7 μs (since  $f_{\text{signal}} = 28.6$  kHz). In the first half period, the electrical charge deposited on the barrier cannot be entirely evacuated and partially remains in the second half

period. This charge accumulation is negligible at the very beginning of the discharge ignition, but becomes significant in less than 30 seconds of operation (see Figure 45 for  $D_{\text{cycle}}=100\%$ ). Once the DBD is ignited, the barrier potential gradually increases, hence inducing a gradual decrease in  $V_{\text{DBD}}$  observed in Figure 45. This phenomenon is clearly less pronounced in the burst mode, where the  $T_{\text{ON}}$  times are too short to induce significant charge accumulations on the barrier. Moreover, the  $T_{\text{OFF}}$  times are much longer so that the sustaining voltage can remain closer to the ignition voltage [229]. The applied voltage ( $V_{\text{DBD}}$ ) is expressed as the sum of two voltages,  $V_{\text{DBD}}=V_{\text{pl,eff}}+V_{\text{diel}}$ , where  $V_{\text{pl,eff}}$  is the effective plasma voltage (in the gap) and  $V_{\text{diel}}$  is the voltage through the dielectric barrier. In the previous section [118], we have demonstrated that varying  $V_{\text{DBD}}$  for a fixed power induces variations of  $V_{\text{pl,eff}}$  while  $V_{\text{diel}}$  remains almost unchanged. Here, decreasing the duty cycle at  $P_{\text{applied}}=50$  W only induces an increase in  $V_{\text{DBD}}$ , hence of  $V_{\text{pl,eff}}$ . As the gap is fixed, we can thus conclude that a stronger electric field is created as the plasma voltage is higher, and therefore there will be more energetic electrons. As a result, the burst mode can enhance the rates of electron impact excitation, ionization and dissociation of CO<sub>2</sub> and thus improve the conversion and energy efficiency of the CO<sub>2</sub> splitting process, as illustrated in Figure 43a. Hence, besides the higher peak power (due to the shorter duty cycle), this can also explain the higher CO<sub>2</sub> conversion in the burst mode.

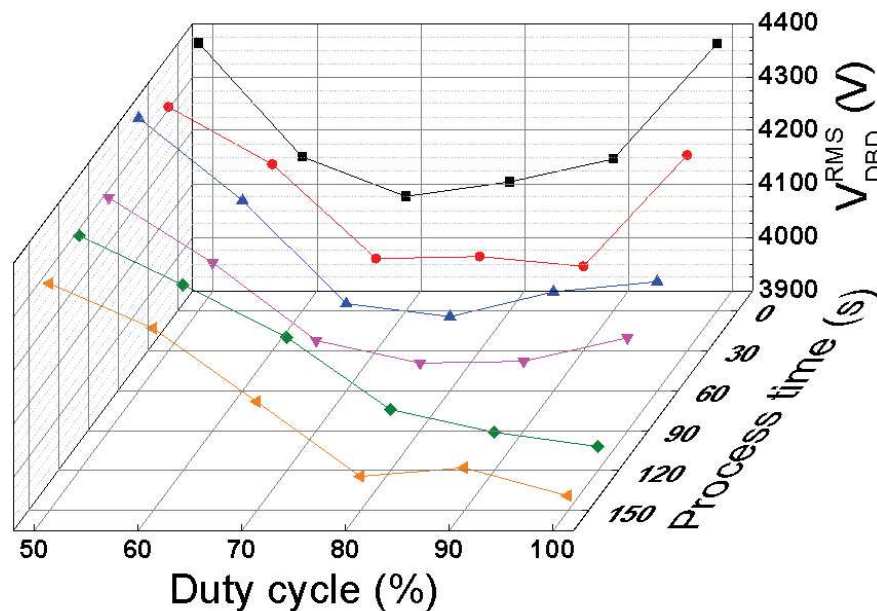


Figure 45 : RMS value of the DBD voltage as a function of the duty cycle and the process time.  $P_{\text{applied}}=50$  W,  $f_{\text{signal}}=28.6$  kHz,  $f_{\text{repetition}}=500 - 900$  Hz and  $\Phi(\text{CO}_2)=200$  mL<sub>n</sub>.min<sup>-1</sup>.

### 2.5.4. Influence of the duty cycle on the gas temperature

The influence of the duty cycle on the gas temperature is obtained from OES measurements. Ro-vibrational spectra of the Angstrom CO band are investigated, as well as the first positive system (FPS) of N<sub>2</sub>. In Figure 46, a linear decrease in gas temperature is observed when reducing the duty cycle, i.e. when increasing the T<sub>OFF</sub> times. This is logical because in the burst mode, the gas can cool down. In the pure AC mode, where the CO<sub>2</sub> conversion is the lowest (16.1%), the gas temperature is the most elevated, suggesting that in general, a larger fraction of the power is used for gas heating, while a smaller fraction of the power leads effectively to CO<sub>2</sub> splitting. It should be noted that the gas temperature as obtained from the FPS of N<sub>2</sub> is about 100 K higher than the gas temperature obtained from the Angstrom CO band, over the entire range of duty cycles investigated. At this point, it is rather difficult to explain this difference since no other independent method (e.g. Doppler broadening, thermocouple, etc.) was used for the gas temperature determination in the plasma phase. Besides this, it is also worth mentioning that the line-ratio and synthetic spectra calculation methods are prone to errors as they assume a Boltzmann distribution and the validity of this assumption cannot be directly checked. Nevertheless, despite the difference of about 100 K, the trend of decreasing gas temperature with decreasing duty cycle is obvious from both curves, as shown in Figure 46.

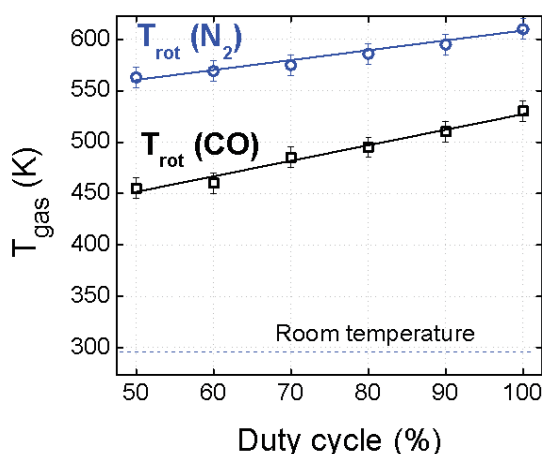


Figure 46 : Gas temperature as a function of duty cycle, as obtained from the FPS of N<sub>2</sub> and from the Angstrom CO band; P<sub>applied</sub>=50 W, f<sub>signal</sub>=28.6 kHz, f<sub>repetition</sub>=500 - 900 Hz and  $\Phi(\text{CO}_2)=200 \text{ mL}_n\cdot\text{min}^{-1}$ .

### 2.5.5. Influence of the duty cycle on the electrical characteristics

Figure 47a shows a picture of the filaments in the DBD for two different duty cycles (50 and 100%). For this purpose, the alumina dielectric barrier is replaced by (transparent) borosilicate glass in order to visually observe these filaments. The pictures reveal an apparent larger number of filaments at  $D_{\text{cycle}}=50\%$  than in pure AC mode ( $D_{\text{cycle}}=100\%$ ). To study this in more detail, these pictures are correlated with their corresponding current oscillograms in Figure 47b, illustrating the current peaks ( $I_{\text{DBD}}=I_{\text{pl}}+I_{\text{diel}}$ ) during one AC period, i.e. 35.7  $\mu\text{s}$ . Note that the oscillogram corresponding to  $D_{\text{cycle}}=50\%$  is a current profile related to  $P_{\text{plasma}}=100\text{ W}$ , as all these oscillograms are recorded only during  $T_{\text{ON}}$ . A visual observation of these oscillograms indicates that the number of microdischarge pulses, as well as their lifetime and the current amplitude all increase from  $D_{\text{cycle}}=100\%$  to  $D_{\text{cycle}}=50\%$ . Based on the numerical method explained in *Chapter III*, we can also obtain more quantitative information on these microdischarges, such as their number ( $N_{\text{md}}$ ), lifetime ( $L_{\text{md}}$ ), charge ( $Q_{\text{pl}}$ ) and conduction current ( $i_{\text{pl}}$ ), from these current peaks.

These parameters are plotted as a function of duty cycle in Figure 48, as obtained for one AC period of 35.7  $\mu\text{s}$ . These results refer to the same applied power, and thus the peak power is higher in the burst mode. All these parameters are given in terms of:

- (i) the same residence time (by taking into account  $T_{\text{OFF}}$  and thus, the electrical parameters are multiplied by  $D_{\text{cycle}}$ ; see solid lines in Figure 48);
- (ii) only the plasma ignition (without taking into account  $T_{\text{OFF}}$ ; see dotted lines in Figure 48).

As observed in the figures, all of them are clearly changed in the burst mode and upon decreasing duty cycle. For instance in terms of same residence time, a reduction of  $D_{\text{cycle}}$  from 100 to 50% induces a decrease in the  $N_{\text{md}}$  from 400 to 340 per period as well as a decrease in their mean lifetime ( $L_{\text{md}}$ ) from 12.9 to 7.4 ns. However, a drastic rise of the plasma current  $i_{\text{pl}}$  (from 9 to 14 mA) is observed when the duty cycle drops from 100 to 50%, which will result in a significant increase in electron density. The latter can be deduced from the rise in plasma charge  $Q_{\text{pl}}$  in terms of a given residence time (from 0.3 to 0.5  $\mu\text{C}/\tau$ ). As the oscillograms are recorded during  $T_{\text{ON}}$  and the peak power becomes higher in the burst mode, the values of  $N_{\text{md}}$ ,  $L_{\text{md}}$ ,  $Q_{\text{pl}}$  and  $i_{\text{pl}}$  will increase upon increasing plasma power  $P_{\text{plasma}}$  (cf. the study presented above on the effect of power - electrical characterization in *Chapter IV*). Therefore in the last

paragraph, we will also compare the electrical characteristics in burst mode and pure AC mode, at the same delivered power during  $T_{ON}$ .

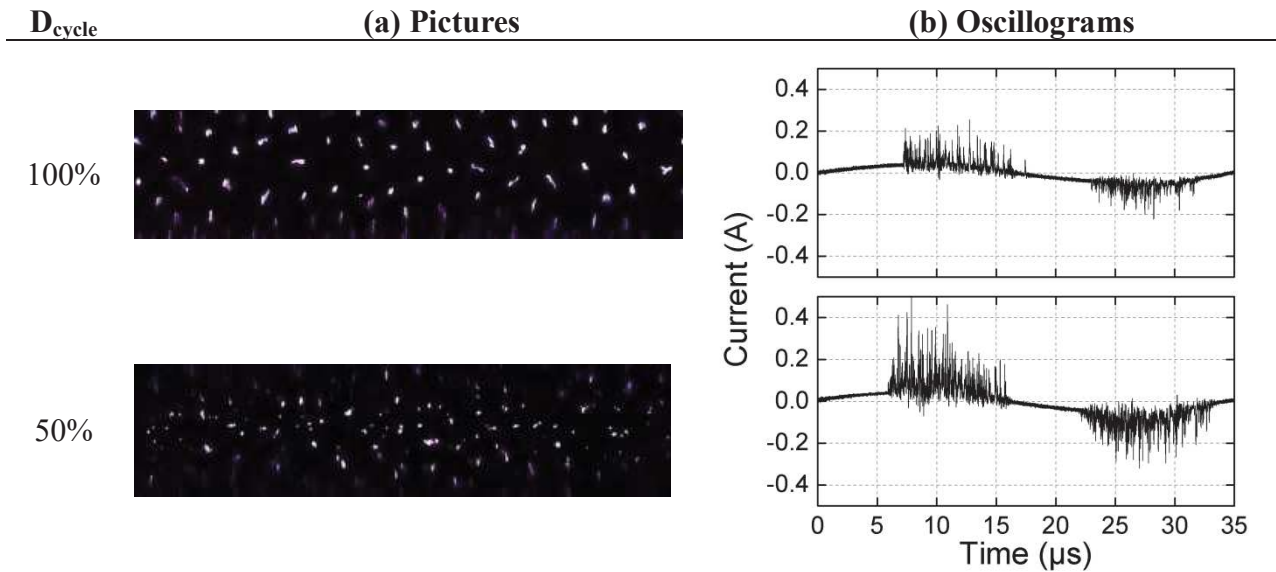


Figure 47 : (a) Pictures of the distribution of the microdischarges in the DBD, and (b) corresponding current oscillograms, for two different duty cycles (50 and 100%).  $P_{\text{applied}}=50$  W,  $f_{\text{signal}}=28.6$  kHz and  $\Phi(\text{CO}_2)=200$  mL<sub>n</sub>.min<sup>-1</sup>. Camera aperture is 1/100 s.

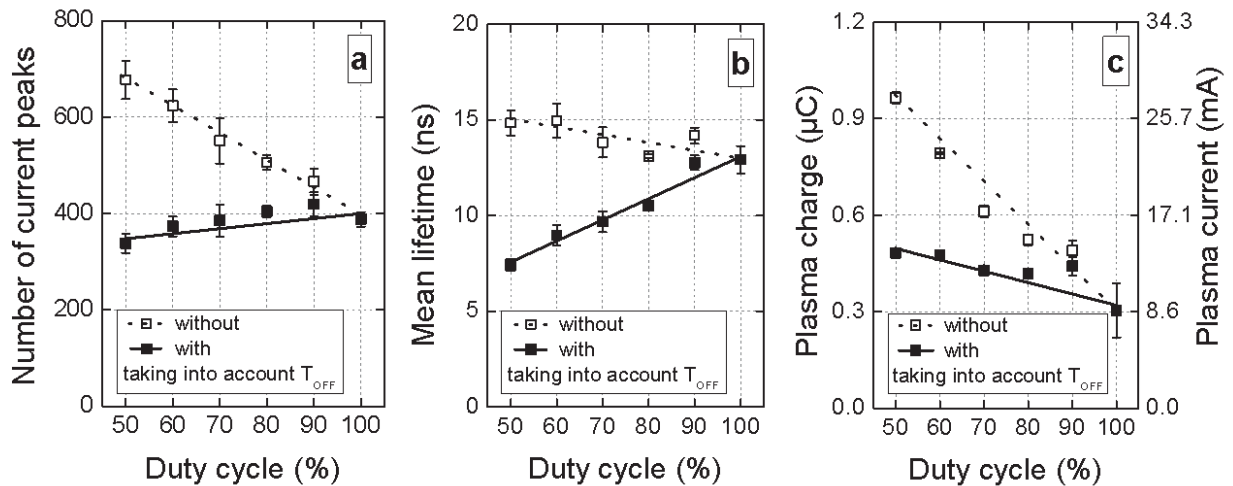


Figure 48 : (a) Number of microdischarges over one period, (b) their mean lifetime versus duty cycle, and (c) plasma charge accumulation over one period (left axis) and plasma current (right axis) versus duty cycle. All electrical parameters are given either considering a total residence time (solid lines) or  $T_{ON}$  (dotted lines).  $P_{\text{applied}}=50$  W,  $f_{\text{signal}}=28.6$  kHz,  $f_{\text{repetition}}=500 - 900$  Hz and  $\Phi(\text{CO}_2)=200$  mL<sub>n</sub>.min<sup>-1</sup>.

### 2.5.6. *Memory effect in the DBD ignited by pure AC or burst mode*

So far, the main consequences of the burst mode are that the plasma voltage is increased and the  $N_{md}$  is decreased. The electrical characterization allows to know that the  $N_{md}$ , in average, decreases in terms of residence time, which is indeed contradictory to the increase in CO<sub>2</sub> conversion in the burst mode, despite the higher plasma voltage and electric field in the gap. In order to further explain Figure 43 (i.e. CO<sub>2</sub> conversion increasing in the burst case), we also try to give an explanation based on how the microdischarges are spread out throughout the gap. The discharge ignited in burst mode looks more filamentary (see Figure 47a: picture below) compared to the discharge ignited with continuous pure AC voltage (see Figure 47a: picture above). Note that the pictures are taken in a macro-time scale (aperture time of 1/100 s).

In a DBD ignited with a classical AC high-voltage, a phenomenon called “memory effect” can occur. The latter can be described as the localization of filaments in space and in time. The origin of the memory effect can be explained in terms of volume mechanisms or more importantly in terms of charge accumulation on the dielectrics [75]. From the point of view of volume mechanisms, residual ions or metastables produced from one filament are present in higher concentrations at the place where the filament occurred during the previous voltage cycle. These active species, inducing the plasma conductivity, can help reignite the filament again at the same location because of the slow diffusion of charges in the gap [92] and for the same applied voltage (i.e time in a voltage cycle). The low mobility of charges on the dielectric also limits the lateral dimension of the modified field permitting the formation of other streamers in the proximity [90].

In the burst mode, the fact that the high-voltage is repeatedly switched off makes that the memory effect becomes less pronounced at lower duty cycle. Therefore, the microfilaments (less in number) occur at more different locations (see Figure 47a: picture below), meaning that the discharge is more diffuse and the microfilaments are more spread out. This is also why the plasma looks less intense in luminosity. As the microfilaments occur at more spots in the entire discharge zone, the probability that the CO<sub>2</sub> molecules pass at least through one microdischarge when travelling through the DBD reactor is enhanced. Indeed, the residence time of CO<sub>2</sub> is quite high in the reactor (4.5 s), whereas the occurrence of microdischarges at different spot is in order of the nano- or microsecond scale. The flowing CO<sub>2</sub> has thus more

chance to pass through a microdischarge and the efficiency of the CO<sub>2</sub> splitting process is improved.

### 2.5.7. *Correlation between microdischarge parameters and energy efficiency of burst and pure AC mode*

Figure 49 depicts the number of microdischarges, their mean lifetime and the plasma charge and current for pure AC (values from the previous study above, see section - effect of the power - electrical characterization) and burst mode, as a function of plasma power. Several observations are noteworthy:

- (i) In pure AC mode (i.e., all corresponding to  $D_{\text{cycle}}=100\%$ ), the plasma power corresponds to the applied power ( $P_{\text{plasma}}=P_{\text{applied}}$ ). Thus, the plasma power is increased by tuning the applied power.
- (ii) The plasma power in the burst mode corresponds to  $P_{\text{plasma}}=P_{\text{applied}}/D_{\text{cycle}}$  where  $P_{\text{applied}}$  is fixed (50 W). The plasma power (delivered during  $T_{\text{ON}}$ ) is increased by tuning the duty cycle. For example,  $P_{\text{plasma}}=50$  W at  $D_{\text{cycle}}=100\%$  and ca. 100 W at  $D_{\text{cycle}}=50\%$ . The corresponding duty cycles are indicated next to the black points in the figure.
- (iii) All the aforementioned results in this study can only be compared to the black curves in Figure 49, i.e. for  $P_{\text{applied}} = 50\text{W}$ .

In Figure 49a, the number of microdischarges ( $N_{\text{md}}$ ) is determined for  $T_{\text{ON}}=1\text{ms}$  and multiplied by the duty cycle to always consider the same residence time. Whatever the plasma power,  $N_{\text{md}}$  is higher in pure AC mode than in burst mode (as the discharge is constantly switched off in the latter case). For instance, at  $P_{\text{plasma}}=100$  W, the burst mode (for 50% duty cycle) allows the formation of 340 microdischarges per period at  $P_{\text{applied}}=50$  W, while 480 microdischarges are obtained at  $P_{\text{applied}}=100\text{W}$  in the pure AC mode. The burst mode presents a lower number of microdischarges, but the applied power is twice as low, which is thus more interesting in terms of energy efficiency. For the same plasma power, a lower  $N_{\text{md}}$  means a higher plasma voltage ( $V_{\text{pl,eff}}$ ), hence a higher electric field and thus higher electron temperatures. The filaments are generated in a higher electric field, leading to a higher efficiency of the CO<sub>2</sub> conversion.

Figure 49b and Figure 49c give information on the microdischarge lifetime as well as the electrical charge and current versus plasma power. Note that the errors in the electrical

parameter values are larger in the case of the burst mode, since it is laborious sometimes to record a clear oscillogram during  $T_{ON}$  in the presence of  $T_{OFF}$ . These electrical parameters increase with plasma power and the differences between pure AC mode and burst mode are noteworthy:  $Q_{pl}$  is indeed lowered in the burst mode. In terms of plasma ignition, the two modes result in a quite similar plasma charge accumulation and plasma current, when operating at the same delivered power, as observed in Figure 49c. As the plasma charge is directly related to the plasma current, the electron densities might be very similar in both modes during  $T_{ON}$ .

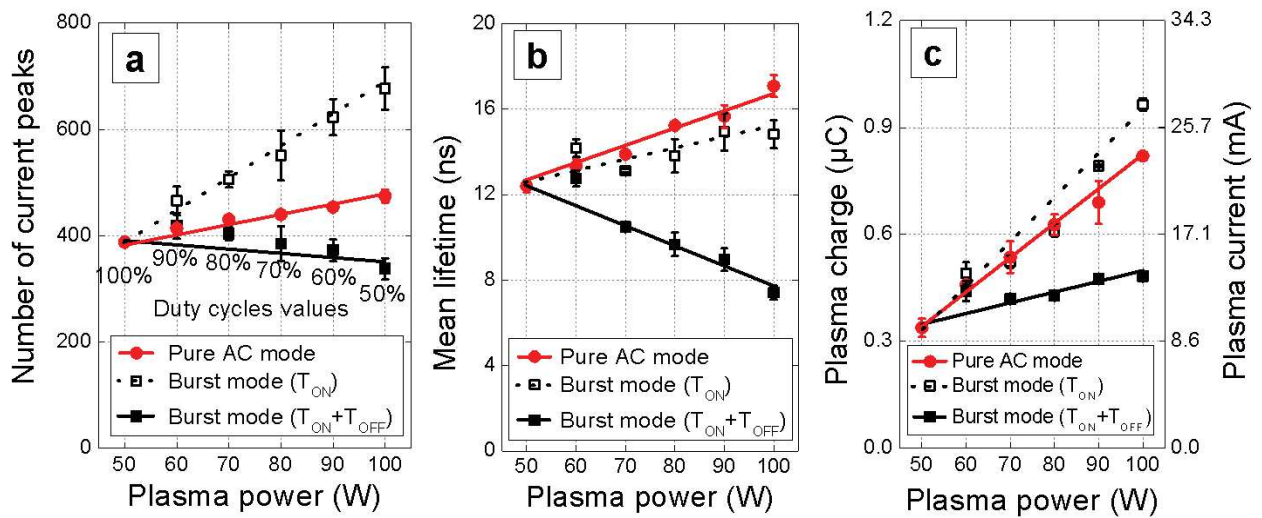


Figure 49 : (a) Number of microdischarges during one period, (b) mean lifetime of the microdischarges, and (c) plasma charge accumulation/plasma current during one period, as a function of the plasma power.  $P_{\text{applied}}$  is fixed in the burst mode while  $D_{\text{cycle}}$  is varied (the solid lines and the dotted lines for the parameters considering a total residence time and only the plasma ignition, respectively).  $P_{\text{applied}}$  is changed in the pure AC mode (electrical parameter values are adopted from the previous study presented above - effect of the power).  $f_{\text{signal}}=28.6$  kHz and  $\Phi(\text{CO}_2)=200 \text{ mL}_n \cdot \text{min}^{-1}$ .

## 2.6. Conclusion

The splitting of CO<sub>2</sub> into CO and O<sub>2</sub> is studied at atmospheric pressure in a tubular DBD operating in pure CO<sub>2</sub>.

First, the influence of the residence time, the operating frequency and the applied plasma power on the filamentary discharge behavior and on CO<sub>2</sub> conversion and energy efficiency is discussed. Table 5 summarizes the results of all the experiments to correlate the CO<sub>2</sub> conversion with the process parameters by increasing the flow rate, the frequency and the power. We can observe how the flow rate, the frequency and power affect the CO<sub>2</sub> conversion and energy efficiency, as well as other plasma parameters, for  $\tau_{anal}=120 \mu s$ . It is clear that these three experimental parameters, which can be easily controlled, have an important impact on the CO<sub>2</sub> splitting process. It is observed that all parameters (especially the power) strongly affect the charge delivered in the plasma, the number of microdischarges which occur for a certain time, the gas temperature, the effective plasma voltage (i.e. the electric field in the gap), the total number of electrons and also the number of electrons which have enough energy to split CO<sub>2</sub>, depending on the shape of the EEDF and thus, defining the energy efficiency of the splitting process.

Table 5: Summary of interpretation for the CO<sub>2</sub> splitting when changing the flow rate, the frequency and the power.

		Increasing the Flow rate (from 50 to 3000 mL <sub>n</sub> .min <sup>-1</sup> )	Increasing the Frequency (from 16.2 to 28.6 kHz)	Increasing the Power (from 3 to 97 W)
CO <sub>2</sub> conversion ( $\chi_{CO_2}$ )		↘ (34.6 - 0.9 %)	↘ (22 - 17.5 %)	↗ (3.2 – 28.2 %)
CO <sub>2</sub> energy efficiency ( $\eta_{CO_2}$ )		↗ (6.0 - 13.8 %)	↘ (15.3 - 12.5 %)	↘ (12.5 – 11.1 %)
Voltage	Plasma	↘ (3.97 - 3.19 kV)	↘ (3.57 – 3.20 kV)	≈ (3.34 – 3.37 kV)
	Dielectric	≈ (0.55 - 0.52 kV)	↘ (0.85 – 0.65 kV)	↗ (0.40 – 0.86 kV)
Current peaks	Number	↘	=	↗
	Lifetime	↗ (14.3 – 15.6 ns)	≈ (15.4 – 15.9 ns)	↗ (8.9 – 17.2 ns)
	Intensity	≈ (6.3 – 6.2 mA)	≈ (12.3 – 13.4 mA)	↗ (5.5 – 24.0 mA)
	Distribution	Unchanged	Unchanged	Changed
Charge	Plasma (Q <sub>pl</sub> )	-	≈	↗
	DBD (Q <sub>DBD</sub> )	-	↗	↗
Temperature	Gas (T <sub>g</sub> )	-	↗ (523 – 560 K)	↗ (543 – 583 K)
	Electrode	-	↗ (376 – 403 K)	↗ (309 – 432 K)

The flow rate mainly affects the residence time of the gas. If the gas remains in the discharge longer, the probability that the gas interacts with microdischarges becomes more important and improves the conversion.

It is shown that, in our configuration, the conversion depends mostly on the charge delivered in the plasma and not on the plasma voltage when the applied power is modified. Similarly, at constant total current, a better conversion is observed at low frequencies, where a less filamentary discharge regime with a higher plasma voltage than at higher frequency is obtained. Increasing the frequency may induce an increase in  $T_e$  (which is approximatively calculated when adding a small quantity of argon in the discharge), hence the measured increase of  $T_{\text{gas}}$ . Moreover, the gas heating also leads to a slight increase in the outer electrode temperature. As the microdischarge distribution, their average lifetime, their number, and electrical charge do not depend on the frequency, we consider that they do not affect the CO<sub>2</sub> conversion when varying the frequency. The most relevant parameter to explain the decrease in  $\chi_{\text{CO}_2}$  with rising frequency is the drop of the effective plasma voltage. The increase of the gas temperature with the power may result from a rise in the electron impact processes. This could explain the increase of the CO<sub>2</sub> conversion in close correlation with the electrical characterizations.

The other study in this subchapter is dedicated to a multi-pulsed discharge. A detailed comparison of this DBD ignited in the burst mode (i.e., where an AC voltage is applied during a limited amount of time) and pure AC mode is carried out to evaluate their effect on the conversion of CO<sub>2</sub> as well as on the energy efficiency. The AC voltage signal has a period of 35.7  $\mu\text{s}$  (corresponding to an applied frequency of 28.6 kHz) while the time width of the voltage burst (i.e.,  $T_{\text{ON}}$ ) is 1 ms and the  $T_{\text{OFF}}$  period varies between 0 and 1.5 ms (corresponding to duty cycles ( $D_{\text{cycle}}$ ) between 100 and 40%, respectively). Note that  $D_{\text{cycle}}=100\%$  corresponds to the AC mode. Comparing this usual AC mode with the burst mode leads us to conclude that the CO<sub>2</sub> conversion is significantly higher in the burst mode, and it increases from 16.1 to 25.8% upon decreasing  $D_{\text{cycle}}$  from 100 to 40%. Likewise, the corresponding energy efficiency of the CO<sub>2</sub> splitting rises from 14.5 to 23.1%. To explain the impact of the plasma electrical properties on the CO<sub>2</sub> conversion, a detailed electrical characterization is again carried out in the burst mode for various duty cycles. A comparison between the burst and pure AC mode at the same plasma powers reveals that the plasma currents and microdischarge mean lifetimes are quite similar, while the number of microdischarges appears lower in the burst mode. We have also investigated the time-variation of the applied DBD voltage in the two modes: it is much more stable and constant as a function of processing time at low duty cycle (burst mode), whereas the voltage always drops at duty cycles higher than 70%, or in the pure AC mode. Also, we have shown that for

the same plasma power, a lower  $N_{\text{md}}$  means a higher plasma voltage ( $V_{\text{pl,eff}}$ ), hence a higher electric field and thus higher electron temperatures. The filaments are generated in a higher electric field, leading to a higher efficiency of the CO<sub>2</sub> conversion. Moreover, because of the memory effect in a continuous DBD, the filaments have the tendency to always light up at the same location. As shown in the above pictures taken in aperture time of 1/100 s (Figure 47a), there are more “intense” filaments, located at the same position, in the continuous mode, whereas in the burst mode, the less intense filaments can light up everywhere, as there is no memory effect. As a consequence, the CO<sub>2</sub> molecule, whose travel time in the reactor is around 4.5 s has more chances to encounter filaments, which form the basis of the plasma reactivity, in the burst mode. Giving the fact that the electric field is higher and the fact that the microdischarges have a better repartition throughout the gap in the burst mode, the conversion rate is enhanced. Finally, OES measurements have shown that the burst mode leads to a lower gas temperature, indicating that a smaller fraction of the power is used for gas heating, so that a larger fraction can be dedicated to the CO<sub>2</sub> dissociation. Overall we can conclude that the so-called burst mode yields a significantly higher CO<sub>2</sub> conversion for the same applied power as in a usual AC mode, which is very promising in terms of applications.

### **3. Influence of the dielectric barrier**

#### **3.1. Introduction**

In a DBD, the presence of a dielectric barrier is mandatory to prevent too much charge build up in the plasma and the formation of a thermal arc. In this section, the role of the barrier thickness (2.0, 2.4 and 2.8 mm) and of the kind of dielectric material (alumina, mullite, pyrex, quartz) is investigated on the filamentary behavior in the plasma and on the CO<sub>2</sub> conversion in the tubular flowing DBD, by means of mass spectrometry measurements correlated with electrical characterization and IR imaging. The electrical diagnostics allow us to characterize the filamentary mode of the discharge and to elucidate the role played by the microdischarges on the CO<sub>2</sub> conversion. Increasing the barrier thickness decreases the capacitance, while preserving the electrical charge. As a result, the voltage over the dielectric increases and a larger number of microdischarges is generated, which enhances the CO<sub>2</sub> conversion. Furthermore, changing the dielectric material of the barrier, while keeping the same geometry and dimensions, also affects the CO<sub>2</sub> conversion. The highest CO<sub>2</sub> conversion and energy

efficiency are obtained for quartz and alumina, thus not following the trend of the relative permittivity. From the electrical characterization, we clearly demonstrate that the most important parameters are the higher effective plasma voltage (yielding a higher electric field and electron energy in the plasma) for quartz, as well as the higher plasma current (and thus larger electron density) and the larger number of microdischarge filaments (mainly for alumina, but also for quartz). The latter could be correlated to the higher surface roughness for alumina and to the higher voltage over the dielectric for quartz.

## **3.2. Effect of the dielectric barrier thickness**

### ***3.2.1. Experimental details***

Very few experimental papers explain how the barrier thickness of a DBD can influence the filamentary behavior of the DBD, especially on the topic of gas treatment [278-283]. To our knowledge, only Forte et al. [278] have studied this effect. They consider that reducing the thickness makes the discharge more unstable and large energetic filaments can appear and damage the barrier due to strong local heating.

In our experimental study, the barrier always has an inner diameter of 26 mm to fix the electrode-barrier gap at 2 mm in all experiments, and therefore keeping the same discharge volume of 15.0 cm<sup>3</sup>. Since the CO<sub>2</sub> flow rate is set at 200 mL<sub>n</sub>.min<sup>-1</sup> the residence time is estimated to 4.5 s. To study the effect of the dielectric thickness, we used pyrex as dielectric barrier (borosilicate glass 3.3) with 3 different thicknesses: 2.0, 2.4 and 2.8 mm (+/-0.02 mm). As mentioned above, the inner diameter is fixed while the outer diameter is changed.

### ***3.2.2. CO<sub>2</sub> conversion and energy efficiency***

Figure 50 presents the CO<sub>2</sub> conversion versus the absorbed power, for different barrier thicknesses. This figure clearly shows that increasing the absorbed power improves the CO<sub>2</sub> conversion. More electrons are indeed produced and likely to participate to the splitting process. Usually, this rise in conversion is correlated with a drop in the energy efficiency [122]. However, in our case this drop is very minor because the conversion rises almost proportionally with the absorbed power (see equations 4.2 to 4.4). The highest conversion (17%) and energy efficiency (9%) are obtained for an absorbed power of 75 W (i.e. specific

energy input of 5.75 eV.molecule<sup>-1</sup>) and the largest dielectric thickness (2.8 mm). These values are in agreement with typical values found in literature. Indeed, the maximum energy efficiency of a DBD in pure CO<sub>2</sub> is usually comprised between 3 and 9%, with maximum conversions reported between 13 and 35% [115, 122, 284].

Furthermore, Figure 50 indicates that for a fixed absorbed power, the conversion and energy efficiency always increase with rising thickness of the barrier. For instance, at 50 W, an enhancement of 50% is obtained when increasing the thickness from 2.0 mm to 2.8 mm. Also, for measurements performed at fixed applied power, the data points show a small horizontal shift because a larger barrier thickness induces a higher reflected power (and hence a slightly lower absorbed power). To understand how a thicker barrier improves the CO<sub>2</sub> conversion and energy efficiency, a detailed electrical characterization is presented in the next section.

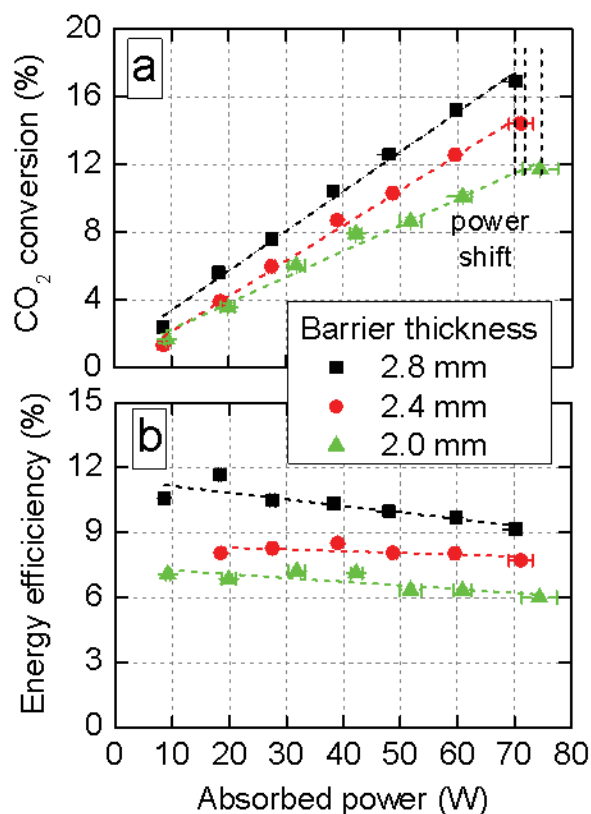


Figure 50 : (a) CO<sub>2</sub> conversion and (b) energy efficiency as a function of the absorbed (plasma) power for three different dielectric thicknesses of pyrex (2.0, 2.4 and 2.8 mm);  
 $f=28.6$  kHz;  $\Phi(\text{CO}_2)=200$  mL<sub>n</sub>.min<sup>-1</sup>.

### 3.2.3. Electrical characterization

As shown in Figure 51a, the voltage applied to the DBD reactor ( $V_{\text{DBD}}$ ) increases with the absorbed power. This was also reported in our previous work dealing with the effect of the power (see above or [118]). At fixed power, Figure 51b illustrates that  $V_{\text{DBD}}$  can significantly rise with the dielectric thickness, e.g. at 60 W it linearly increases from 5050 V to 5600 V (RMS values) for a barrier thickness ranging from 2.0 to 2.8 mm. As mentioned before,  $V_{\text{DBD}}$  consists of two components – averaged plasma voltage ( $V_{\text{pl,eff}}$ ) and dielectric voltage ( $V_{\text{diel}}$ ). It is clear from Figure 51b that the rise in  $V_{\text{DBD}}$  is attributed to  $V_{\text{diel}}$ , while the plasma voltage remains constant and close to 3800 V. This means that the electric field remains constant whatever the barrier thickness and therefore, this cannot explain the rise in CO<sub>2</sub> conversion.

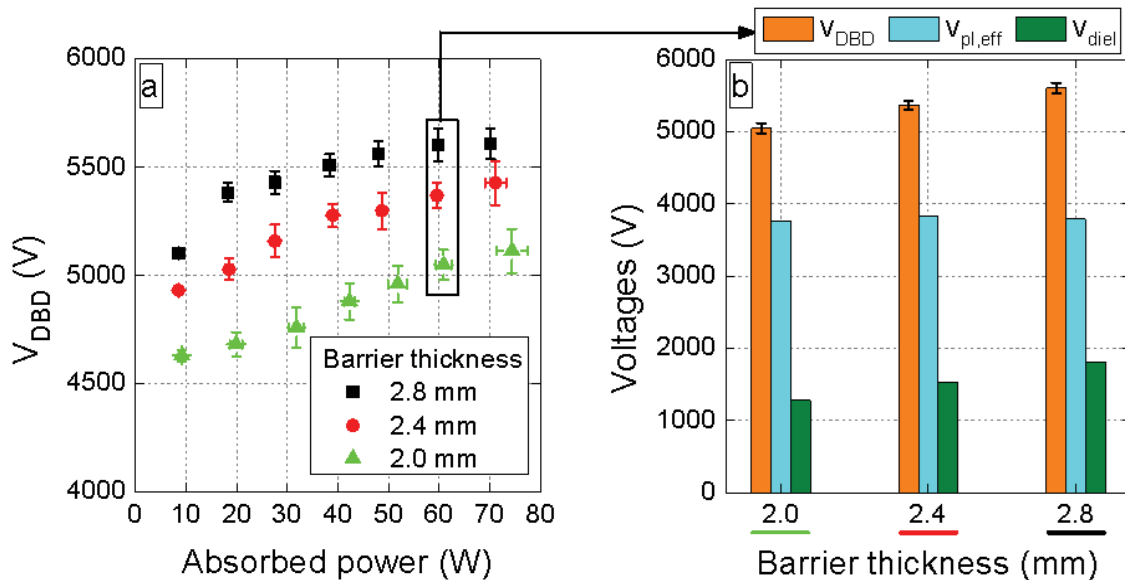


Figure 51 : (a) Applied voltage ( $V_{\text{DBD}}$ ) as a function of absorbed power for three different dielectric thicknesses, and (b) Voltage components as a function of the dielectric thickness at a given absorbed power  $P_{\text{abs}}=60$  W;  $f=28.6$  kHz;  $\Phi(\text{CO}_2)=200$  mL<sub>n</sub>.min<sup>-1</sup>.

However, the latter can be explained by performing a detailed analysis of the currents to extract information about the microdischarges, i.e. their individual features such as their average lifetime and electrical charge, but also their collective features such as the plasma charge accumulation and their total number for a given analysis time (e.g. period or residence time). Table 6 summarizes the average number ( $N_{\text{md}}$ ) and lifetime ( $L_{\text{md}}$ ) of the microdischarges for one period, as a function of the barrier thickness. Increasing the barrier from 2.0 to 2.8 mm leads to a significant increase of  $N_{\text{md}}$  (from 465 to 506) and a slight

decrease in  $L_{\text{md}}$  (from 13.3 ns to 12.3 ns). However, the electrical charge accumulated on the barrier remains unchanged and close to 1  $\mu\text{C}$  (see  $Q_{\text{diel}}$  in Table 6). The same applies to the charge accumulated in the plasma ( $Q_{\text{plasma}}$ ) and thus to the total charge ( $Q_{\text{total}}$ ). For the dielectric, the following equation can thus be written:

$$Q_{\text{diel}} = C_{\text{diel}} \cdot V_{\text{diel}} = \text{Constant}, \forall \text{ barrier thickness} \quad \text{Eq. 4.10}$$

Table 6 : Number of microdischarges during one period, mean lifetime of the microdischarges and charge accumulation as a function of the dielectric thickness;  $P_{\text{abs}} = 60 \text{ W}$ ;  $f = 28.6 \text{ kHz}$ ;  $\Phi(\text{CO}_2) = 200 \text{ mL}_n \cdot \text{min}^{-1}$ .

Parameters measured		Dielectric barrier thickness		
		2.0 mm	2.4 mm	2.8 mm
for 1 period				
$N_{\text{md}} (-)$		465 ( $\pm 20$ )	487 ( $\pm 23$ )	506 ( $\pm 7$ )
$L_{\text{md}} (\text{ns})$		13.3 ( $\pm 0.4$ )	12.9 ( $\pm 0.4$ )	12.3 ( $\pm 0.2$ )
Charge ( $\mu\text{C}$ )	$Q_{\text{total}}$	1.27 ( $\pm 0.01$ )	1.27 ( $\pm 0.02$ )	1.30 ( $\pm 0.02$ )
	$Q_{\text{plasma}}$	0.29 ( $\pm 0.01$ )	0.30 ( $\pm 0.04$ )	0.29 ( $\pm 0.01$ )
	$Q_{\text{diel}}$	0.98	0.97	1.01

According to equation 4.11 (see next section), increasing the barrier thickness corresponds to an increase of  $r_{\text{out}}$  and thus to a drop in the barrier capacitance. Since our measurements reveal that  $Q_{\text{diel}} (=C_{\text{diel}} \cdot V_{\text{diel}})$  is constant, an increase of  $V_{\text{diel}}$  is needed, as confirmed by our results presented in Figure 51b. In other words, the drop in barrier capacitance yields a higher voltage over the dielectric ( $V_{\text{diel}}$ ), and the latter causes clearly a larger number of microdischarges per period ( $N_{\text{md}}$ ), as reported in Table 6.

Figure 52 indeed illustrates a higher density of microdischarges upon rising the barrier thickness, always maintaining a uniform spatial distribution in the entire discharge region. This increase is about 9% for a barrier thickness increasing from 2.0 to 2.8 mm. As the reactor volume is the same, independent of the barrier thickness, the probability for a single CO<sub>2</sub> molecule to pass through the discharge and interact with at least one microdischarge therefore increases for the thicker barriers. As a result, a higher CO<sub>2</sub> conversion (and thus energy efficiency) is obtained. It should be mentioned that the average lifetime of the microdischarges slightly drops upon increasing barrier thickness, but this seems of lower importance for determining the CO<sub>2</sub> conversion.

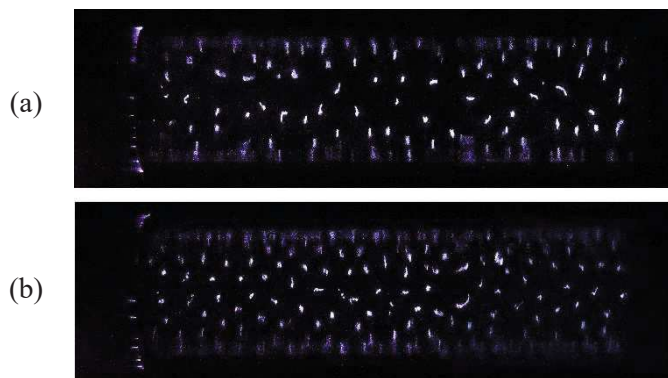


Figure 52 : Pictures of the microdischarges observed through the pyrex and the outer mesh electrode, at same power, frequency and flow rate (for a camera aperture of 1/100 s). The barrier thickness is (a) 2.0 mm, (b) 2.8 mm.

#### 3.2.4. *Wall reactor temperatures and influence of the inlet gas temperature*

Finally, when the plasma is ignited, the heat dissipation is much higher in thicker dielectric material, yielding a lower wall temperature in case of the 2.8 mm thickness of the barrier. In Figure 53, the average temperature of the mesh outer electrode is 169, 151 and 134°C for 2.0, 2.4 and 2.8 mm, respectively. Moreover, the wall temperature outside of the discharge zone is also getting lower from 51 to 46°C when increasing the thickness. Thus, the heat appears more confined in the discharge region for the thinner dielectric. The different surface temperature might affect the CO<sub>2</sub> conversion and the energy efficiency of the process. Indeed, as the gas temperature increases, the particle densities decrease in order to maintain a constant pressure, following the ideal gas law, and the gas velocity increases to maintain a constant mass flow (hence, a lower amount of gas will be treated). The effect of the ambient temperature on the conversion is depicted in Figure 54. The temperature is varied from 20 to 80°C in a controlled manner in the entire experimental set-up (flow meter, gas tubes, DBD reactor) in a heated chamber. Therefore, the flowing gas temperature inside the reactor is assumed to be close to the outside controlled temperature. The conversion clearly decreases when increasing the temperature of the system. This is due to the expansion of the gas volume upon increasing temperature (ideal gas law). Therefore, the gas flow is higher, corresponding to a lower residence time. The temperature also affects the applied voltage (and thus the plasma voltage since the power is kept constant, as seen previously) since the latter decreases from 4250 to 3950 V, respectively, when the temperature rises from 20 to 80°C.

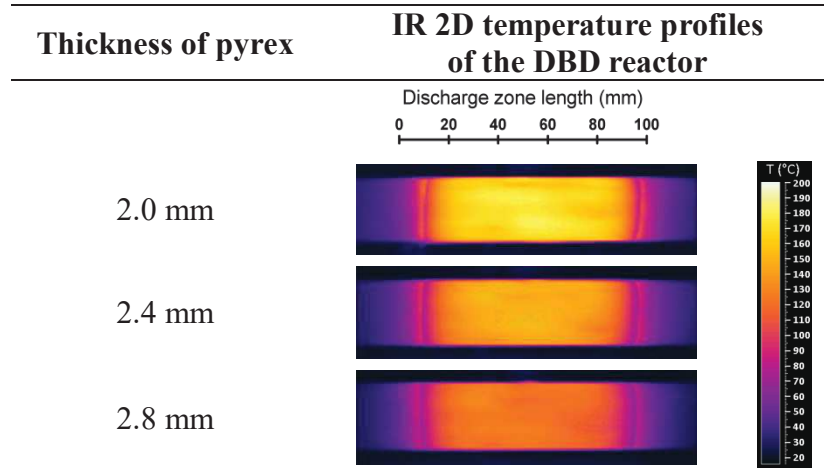


Figure 53 : 2D temperature profiles of the DBD reactors for the three different dielectric thickness materials, for  $P_{abs}=75$  W, process time = 4 min, dielectric material = pyrex. The black graded line indicates the length of the outer electrode, i.e. the discharge region.

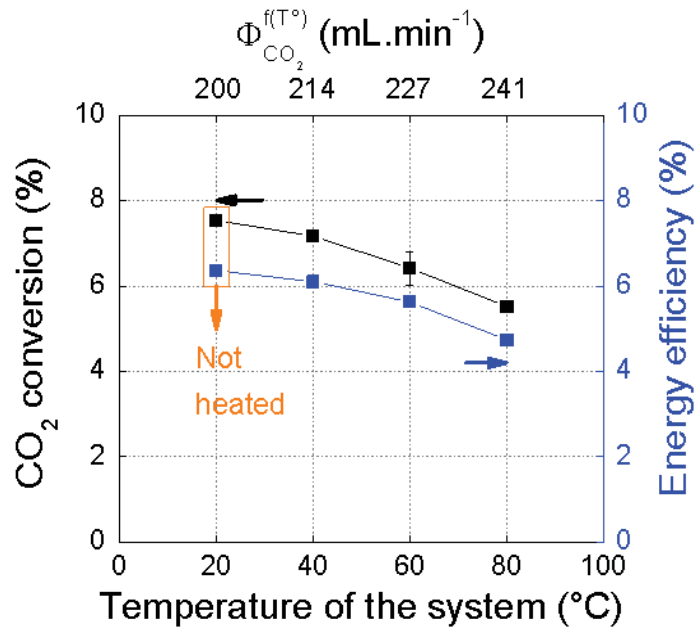


Figure 54 : (a) CO<sub>2</sub> conversion and (b) energy efficiency as a function of the ambient temperature of the entire experimental set-up (varied from 20 to 80°C). Dielectric thickness of pyrex = 2.0 mm;  $P_{abs} = 45$  W;  $f=28.6$  kHz and  $\Phi_{inlet}(CO_2)=200$  mL<sub>n</sub>.min<sup>-1</sup>.

### 3.3. Effect of the dielectric barrier material

#### 3.3.1. Experimental details

A packed bed DBD typically yields a higher conversion and energy efficiency [114, 115, 124-126]. For example, packing a DBD reactor with dielectric zirconia (ZrO<sub>2</sub>) beads enhances the CO<sub>2</sub> conversion and energy efficiency by a factor of 1.9 and 2.2, respectively, reaching a conversion up to 42% for a flow rate of 20 mL.min<sup>-1</sup>, and a maximum energy efficiency of 10% at a flow rate of 100 mL.min<sup>-1</sup> [35]. These improvements are attributed to polarization of the dielectric beads, enhancing the local electric field. Furthermore, the material of the dielectric barrier is also reported to be of great importance [115, 285-287].

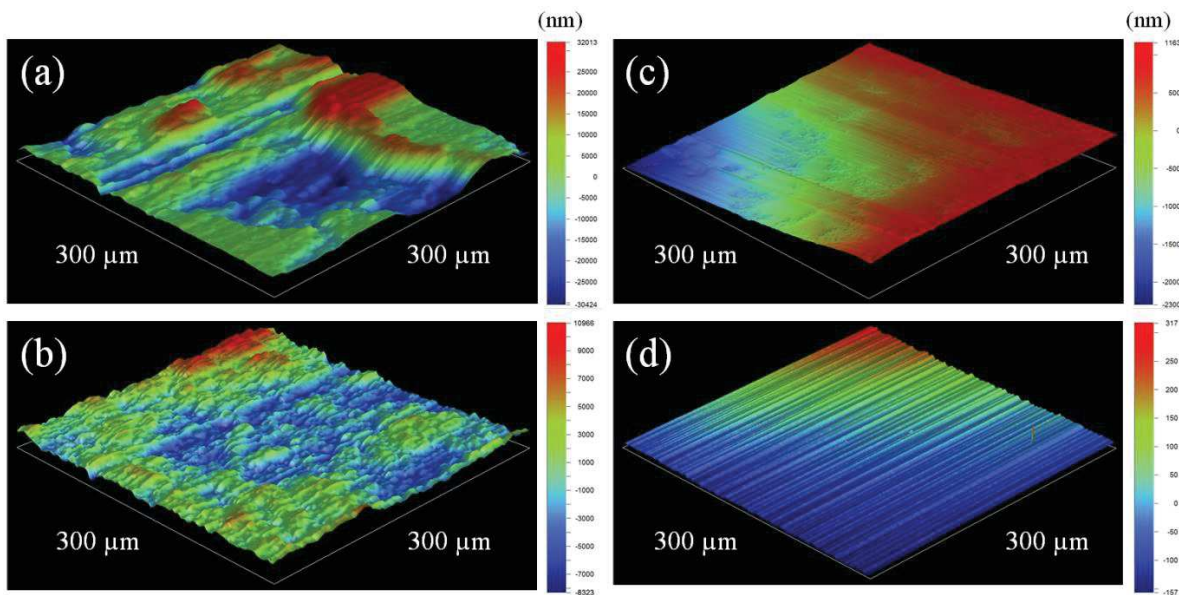
In our experimental study, the barrier always has an inner diameter of 26 mm to fix the electrode-barrier gap at 2 mm in all experiments, and therefore keeping the same discharge volume of 15.0 cm<sup>3</sup>. Since the CO<sub>2</sub> flow rate is set at 200 mL.n.min<sup>-1</sup> the residence time is estimated to 4.5 s.

Four different dielectric barriers with the same thickness (2mm) but different relative permittivities ( $\epsilon_r$ ) are compared: alumina ( $\epsilon_r = 9.6$ ), mullite ( $\epsilon_r = 6.0$ ), pyrex ( $\epsilon_r = 4.6$ ) and quartz ( $\epsilon_r = 3.8$ ). These  $\epsilon_r$  values remain constant for our conditions of frequency (between 1 kHz and 1 MHz) and temperature (from 300 K to 473 K for quartz and 573 K for alumina) [288, 289]. Additional properties of the barriers are indicated in Table 7, i.e. the chemical composition, the surface roughness measured by profilometry (images shown in Figure 55), the thermal conductivity and the capacitance. The last parameter is calculated considering the equation 4.11, where  $L$ ,  $r_{in}$  and  $r_{out}$  are the dielectric length, the inner and outer radius, respectively:

$$C = \frac{2\pi\epsilon_0\epsilon_r \cdot L}{\ln(r_{out}/r_{in})} \quad \text{Eq. 4.11}$$

Table 7 : Physical properties of the four different dielectric barriers tested, 2 mm in thickness.

Material	Chemical composition	Relative permittivity ( $\epsilon_r$ )	R <sub>RMS</sub> (nm)	Thermal conductivity (W.m <sup>-1</sup> .K <sup>-1</sup> ) at 20°C	Capacitance (pF)
Alumina (C799)	Al <sub>2</sub> O <sub>3</sub> 99.70% Na <sub>2</sub> O 0.15% SiO <sub>2</sub> 0.10%	9.6	6800	29	373.2
Mullite (C610)	Al <sub>2</sub> O <sub>3</sub> 62.60% SiO <sub>2</sub> 35.15% Fe <sub>2</sub> O <sub>3</sub> 0.82% TiO <sub>2</sub> 0.39% CaO 0.18%	6.0	3100	2	233.2
Pyrex (3.3 Duran)	SiO <sub>2</sub> 81% B <sub>2</sub> O <sub>3</sub> 13% Na <sub>2</sub> O + K <sub>2</sub> O 4% Al <sub>2</sub> O <sub>3</sub> 2%	4.6	780	1.1	178.8
Quartz	SiO <sub>2</sub> (high purity)	3.8	89	1.4	147.7

Figure 55 : Profilometry scan images of 0.9 mm<sup>2</sup> (a) alumina, (b) mullite, (c) pyrex and (d) quartz.

### 3.3.2. CO<sub>2</sub> conversion and energy efficiency

Figure 56 shows the CO<sub>2</sub> conversion and energy efficiency for different dielectric materials, but keeping the same operating conditions and configuration ( $f=27.1$  kHz;  $\Phi(\text{CO}_2)=200$  mL<sub>n</sub>.min<sup>-1</sup>). These materials are indicated on the X-axis, in decreasing order of their relative permittivities (see Table 7 above). Each barrier is 2 mm thick.

Surprisingly, the highest CO<sub>2</sub> conversions (e.g. 24.6% at 74 W) are obtained for dielectric barriers with the highest and lowest relative permittivities, i.e. alumina and quartz, respectively. Similar results, i.e., the same CO<sub>2</sub> conversion for alumina and quartz, were also obtained in [122]. The two other dielectric barriers with intermediate relative permittivities, i.e., mullite and pyrex, yield somewhat lower CO<sub>2</sub> conversion. The energy efficiency follows the same trend, and here the results are even somewhat higher for quartz (i.e., above 15% at 39 W).

At first sight, the results presented in Figure 56 seem counter-intuitive, if we only consider a change in the  $\epsilon_r$  parameter (i.e. capacitance). However, changing the nature of the dielectric material does not solely mean a change of its capacitance. Other relevant parameters of the barrier can also influence the CO<sub>2</sub> conversion in a DBD, such as its surface roughness and thermal conductivity, as will be explained below. However, first we present a detailed electrical characterization, as this will clarify the observed trends in CO<sub>2</sub> conversion and energy efficiency.

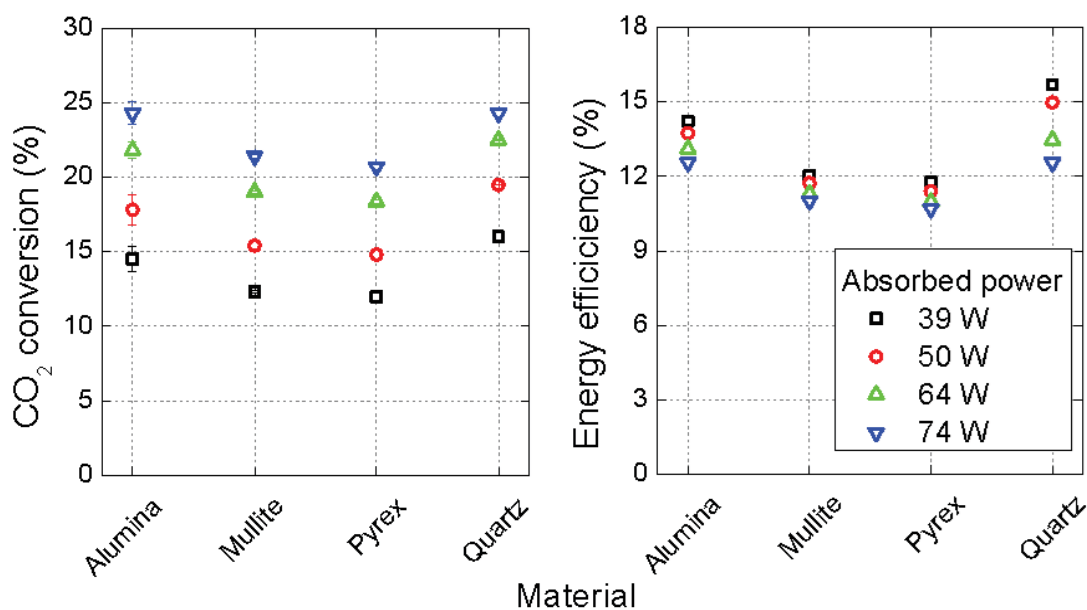


Figure 56 : (a) CO<sub>2</sub> conversion and (b) energy efficiency for different values of the absorbed power and for four different dielectric materials;  $f=27.1$  kHz;  $\Phi(\text{CO}_2)=200$  mL<sub>n</sub>.min<sup>-1</sup>.

### 3.3.3. Electrical characterization

$V_{\text{DBD}}$  is plotted as a function of the absorbed power in Figure 57a, for the four different dielectric materials.  $V_{\text{DBD}}$  clearly rises with increasing power, but also with decreasing

relative permittivity of the materials. The latter is also shown in Figure 57b, for a fixed power of 75 W. Moreover, both the average plasma voltage ( $V_{pl,eff}$ ) and the voltage over the dielectric ( $V_{diel}$ ) slightly rise upon decreasing relative permittivity, although pyrex is behaving somewhat differently. Hence, this behavior might partially explain the higher CO<sub>2</sub> conversion and energy efficiency in the case of quartz, as a higher average plasma voltage yields a higher electric field in the gap, which results in more electron heating and hence, in a higher CO<sub>2</sub> conversion by electron impact dissociation. However, this behavior does not explain the higher conversion and energy efficiency for alumina compared to mullite and pyrex. Therefore, there must be other effects coming into play as well. In order to explain this, the relation between the trend in CO<sub>2</sub> conversion and the specific properties of the microdischarges will be discussed in the next paragraph.

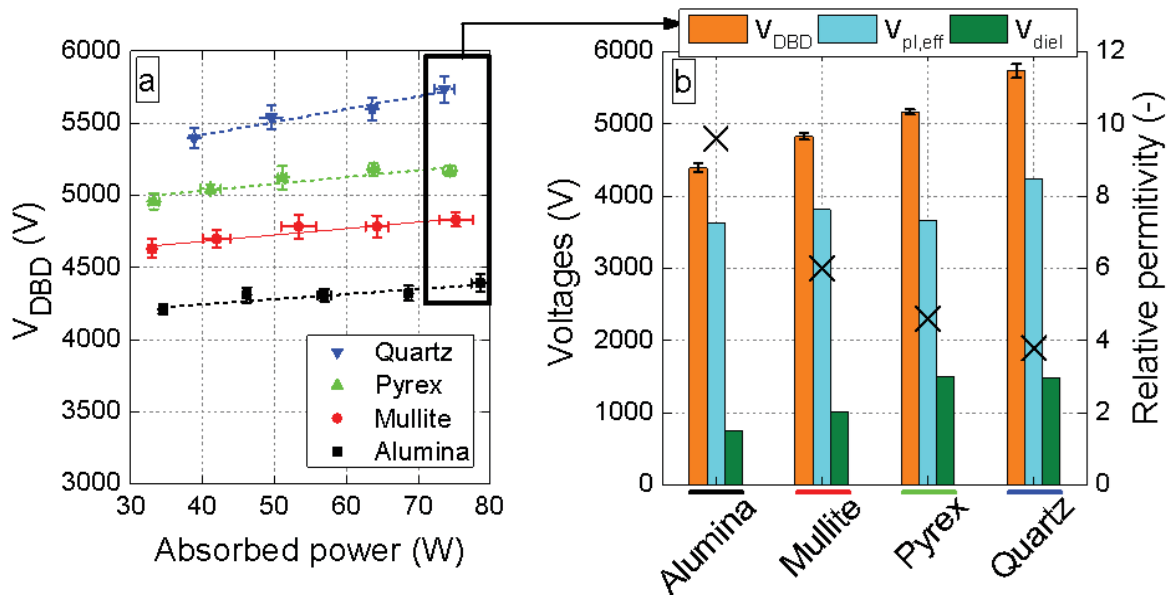


Figure 57 : (a) RMS applied voltage ( $V_{DBD}$ ) as a function of absorbed power for four different dielectric materials at  $f=27$  kHz, and (b) RMS voltage components as a function of the dielectric material at a given absorbed power  $P_{abs}=75$  W;  $\Phi(\text{CO}_2)=200$  mL<sub>n</sub>.min<sup>-1</sup>. The relative permittivities of the materials are indicated with crosses, referring to the right y-axis.

The oscillograms of the total current in a DBD with alumina, mullite, pyrex and quartz are plotted in Figure 58. By comparing these current profiles, one can observe that the discharge filamentation is different for the different dielectric materials, and the peak distribution in the positive and negative half cycle during one period is also different for the different materials.

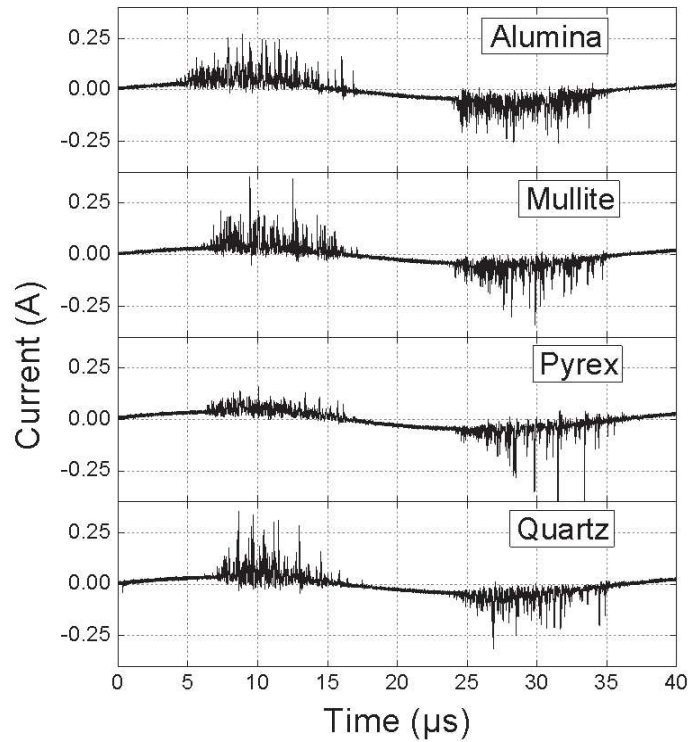


Figure 58 : Current profiles as a function of time for four different dielectric materials;  $P_{\text{abs}} = 75 \text{ W}$ ;  $\Phi(\text{CO}_2) = 200 \text{ mL}_n \cdot \text{min}^{-1}$ .

Usually – and as evidenced above for the effect of the barrier thickness – decreasing the capacitance leads to an increase in the voltage over the dielectric (see also Figure 57), so that the plasma charge remains unchanged. However, in the present comparison of the different dielectric materials, the plasma charge (or plasma current) is not constant: as shown in Figure 59a, it is much higher in the case of alumina than for the other dielectric materials. Likewise, the number of microdischarge filaments, as well as their average lifetime, is higher for alumina as well (see Figure 59b and Figure 59c). The alumina barrier gives rise to 430-570 microdischarges over one period (depending on the power), while this value varies between 350 and 490 for the other materials. Moreover, the mean lifetime of the microdischarges is also longer for alumina – between 11.5 and 15.3 ns, depending on power – while it is between 10.5 and 13.5 ns for the other materials.

Alumina thus gives rise to a filamentary discharge with more microfilaments, which are also broader compared to the other discharges. As the discharge zone is the same in all cases, the larger number of filaments (with longer average lifetime) means that a larger discharge volume is available for the CO<sub>2</sub> conversion, and the latter can explain why alumina yields a higher CO<sub>2</sub> conversion and energy efficiency. Furthermore, alumina gives a higher plasma

charge, and this implies a higher electron density, which might also explain the higher CO<sub>2</sub> conversion and energy efficiency, for the same power as for the other materials.

In summary, the trends of the plasma charge (Figure 59a) (which reflects the plasma current and hence, the number of electrons present in the discharge region), the number of microdischarge filaments (Figure 59b) and average lifetime (Figure 59c), in combination with the higher effective plasma voltage (and thus the higher electric field and electron energy in the plasma) for quartz (Figure 57b), can explain the trend of the CO<sub>2</sub> conversion and energy efficiency, as observed in Figure 56a and Figure 56b.

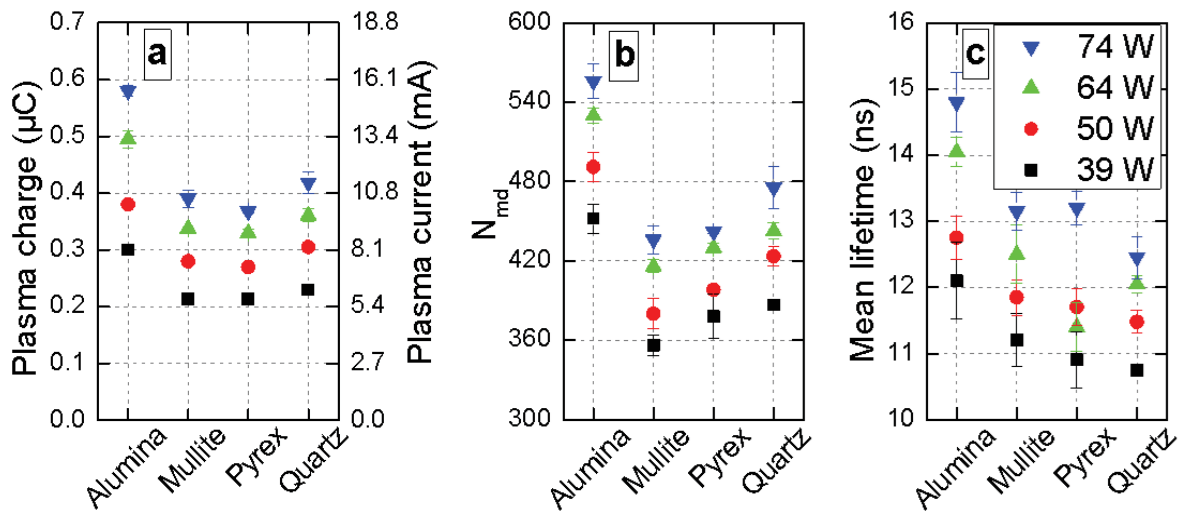


Figure 59 : (a) Plasma charge accumulation during one period, (b) number of microdischarges during one period and (c) mean lifetime of the microdischarges, for the four different dielectric materials and for different absorbed powers and  $\Phi(\text{CO}_2)=200 \text{ mL}_n\cdot\text{min}^{-1}$ .

### 3.3.4. Wall reactor temperatures and roughness analysis of the dielectric material

To explain why alumina yields a larger number of microdischarge filaments than the other materials, we have investigated the surface roughness of the dielectric materials. A higher surface roughness can indeed imply easier generation of filaments. The roughness was estimated through the  $R_{\text{RMS}}$  parameter and is reported in Table 7 above for each material. It is clear that alumina has by far the largest roughness (in average 6800 nm), and this could explain why alumina induces more microdischarges, as observed above (cf. Figure 59b). On the other hand, the surface roughness does not explain why quartz also induces a relatively large number of microdischarges, as it has a clearly lower surface roughness than mullite and

pyrex. In this case, it can be attributed to the higher voltage over the dielectric, as illustrated in Figure 57, exactly as for the effect of the barrier thickness (see previous section). In summary, the larger number of filaments can be attributed to the higher voltage over the dielectric (like in the case of quartz, and for the effect of the dielectric thickness – higher at 2.8 mm of thickness) and/or to the higher surface roughness (like in the case of alumina).

Finally, the last material property that we have investigated is the thermal conductivity. As indicated in Table 7, the thermal conductivity of alumina is (more than) ten times higher than for the three other materials. Hence, when the plasma is ignited, the heating dissipation through the alumina barrier is much faster, yielding a lower wall temperature as compared to the other materials. In Figure 60, the average temperature of the mesh outer electrode is 136°C in case of alumina, against 149°C, 157°C and 169°C in case of mullite, quartz and pyrex, respectively. Moreover, the wall temperature outside of the discharge zone is quite elevated for alumina (almost 80°C) while it is only 45°C for the three other materials. Thus in the latter cases, the heating appears clearly confined in the discharge region. The different surface temperature might also yield a different gas temperature (inside the discharge region, as well as before or after), and this may also affect the CO<sub>2</sub> conversion, due to changes in the chemical reaction rates at different temperature. The rate constants of the heavy particle reactions are indeed often a function of the gas temperature. The temperature-dependence of the rate constants of the neutral reactions and of some ion reactions in a CO<sub>2</sub> DBD plasma is presented in [102, 103, 122, 127]. Kozak et al. evaluated the effect of the gas temperature on the CO<sub>2</sub> conversion and energy efficiency by means of plasma chemistry modeling [102]. We expect that the temperature affects the CO<sub>2</sub> conversion much more in a microwave plasma [102] than in a DBD plasma [122], because of the important role of the vibrational kinetics in a MW plasma, and because the latter are very much temperature-dependent [102, 103]. Moreover, besides the effect of the gas temperature on the reaction rate constants, it also affects the particle densities through the ideal gas law, i.e., at constant pressure, a higher temperature yields a lower gas density. As a result, the reduced electric field ( $E/N$ ) will rise, and this will affect the electron energy distribution function (EEDF), which will in turn affect the electron impact reaction rates, and thus the CO<sub>2</sub> conversion. However, the exact reason why the changes in gas temperature might affect the CO<sub>2</sub> conversion is beyond the scope of this work.

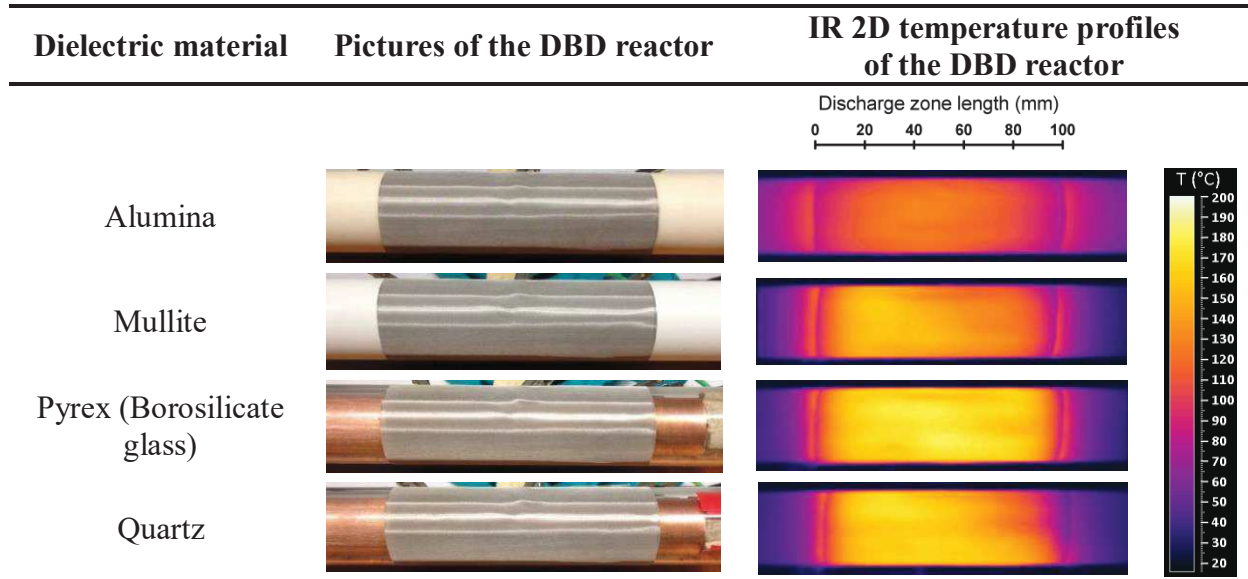


Figure 60 : 2D temperature profiles of the DBD reactors for the four different dielectric materials, for  $P_{\text{abs}}=75$  W, process time = 4 min. The black graded line indicates the length of the outer electrode, i.e. the discharge region.

### 3.3.5. Secondary emission

The emission of secondary electrons can be induced when primary incident electrons of sufficient energy hit a surface or pass through some material. This emission is defined and quantified by a parameter  $\gamma$ , which is called secondary electron emission coefficient. All four dielectric materials have obviously different  $\gamma$  values (see Table 8), depending also on the primary electron energy. The average electron energy in a DBD operating at atmospheric pressure is about 2-3 eV [105-109], and the  $\gamma$  values of the different materials are given for this primary electron energy. It appears that the  $\gamma$  value of alumina ( $\gamma_{\text{Al}_2\text{O}_3}=8$  for 2 eV and  $\gamma_{\text{Al}_2\text{O}_3}=6$  for 3 eV) is quite high compared to  $\gamma$  of the other materials [290, 291]. Silica (SiO<sub>2</sub>) leads to a lower secondary emission ( $\gamma_{\text{SiO}_2}=3$  for 2 eV and  $\gamma_{\text{SiO}_2}=2.5$  for 3 eV) [291]. Mullite is a material which consists of Al<sub>2</sub>O<sub>3</sub> (63 %) and SiO<sub>2</sub> (37 %). Therefore, its secondary electron emission is less intense than the one of alumina. Silica is even more present in the chemical composition of both borosilicate glass (81 %) and quartz (~99 %). However, the impurities (like boron trioxide B<sub>2</sub>O<sub>3</sub>) of borosilicate glass might have an impact on the magnitude of the secondary electron emission coefficient. Indeed, its emission is lowered ( $\gamma_{\text{borosilicate glass}}=2$  for 2 eV) [64, 292, 293]. Hence to summarize,  $\gamma_{\text{alumina}} > \gamma_{\text{mullite}} > \gamma_{\text{quartz}} > \gamma_{\text{borosilicate glass}}$ . The high

secondary electron emission coefficient of alumina might promote the CO<sub>2</sub> conversion since the electron density might be further improved with this material.

Table 8 : Secondary electron emission coefficient of four dielectric materials for a primary incident electron with energy of 2-3 eV.

Material	Energy of incident electron (eV)	$\gamma$
Alumina (Al <sub>2</sub> O <sub>3</sub> )	2	8
	3	6
Quartz (99%SiO <sub>2</sub> ) = Silica	2	3
	3	2.5
Mullite (63%Al <sub>2</sub> O <sub>3</sub> -37%SiO <sub>2</sub> )	3	5.2
Borosilicate glass (81%-SiO <sub>2</sub> )-19%B <sub>2</sub> O <sub>3</sub>	2	2

### 3.4. Conclusion

We have investigated how the thickness and the material of the dielectric barrier affect the CO<sub>2</sub> conversion in a DBD reactor operating at atmospheric pressure. Table 9 summarizes the results of all the experiments with arrows (for the effect of barrier thickness) and plus signs (for the different materials), to correlate the CO<sub>2</sub> conversion and energy efficiency with the other plasma characteristics (like the voltage, the microdischarge properties and the charges in the plasma) and with the material characteristics (like thermal conductivity and surface roughness). From this correlation, the trends in CO<sub>2</sub> conversion (and energy efficiency) can clearly be explained.

Table 9 : Summary of CO<sub>2</sub> conversion and energy efficiency as a function of the barrier thickness and kind of dielectric material, and correlation with the plasma and material characteristics.

		Increasing the dielectric barrier thickness (from 2 to 2.8 mm)	Dielectric materials			
			Quartz	Pyrex	Mullite	Alumina
CO <sub>2</sub> conversion ( $\chi_{\text{CO}_2}$ )		↗	++++	++	+	++++
Energy efficiency ( $\eta_{\text{CO}_2}$ )		↗	++++	++	+	++++
Voltage	Applied ( $V_{\text{DBD}}$ )	↗	++++	+++	++	+
	Plasma ( $V_{\text{pl,eff}}$ )	=	++++	+	++	+
	Dielectric ( $V_{\text{diel}}$ )	↗	++++	++++	++	+
Microdischarges	Number ( $N_{\text{md}}$ )	↗	++	+	+	++++
	Lifetime ( $L_{\text{md}}$ )	↘	+	++	++	++++
	Current ( $i_{\text{pl}}$ )	=	++	+	+	++++
Charge	Plasma ( $Q_{\text{pl}}$ )	=	++	+	+	++++
	DBD ( $Q_{\text{DBD}}$ )	=	/	/	/	/
Energy loss to Joule effect (thermal conductivity)		↘	++++	++++	+++	+
Roughness of dielectric material		=	+	+	+++	++++

By increasing the thickness of the barrier from 2.0 to 2.8 mm, the CO<sub>2</sub> conversion (and thus also the energy efficiency) clearly increases by about 50%. The best results, in terms of both conversion and energy efficiency, are obtained at an absorbed power of 70 W (corresponding to a SEI of 5.75 eV.molecule<sup>-1</sup>) and the largest dielectric thickness (2.8 mm), yielding a conversion of 17% and a corresponding energy efficiency of 9%. As indicated in Table 9, the charge and the average plasma voltage remain unchanged and therefore, they cannot explain the higher conversion. The reason for the higher CO<sub>2</sub> conversion is the larger number of microdischarges in a certain period. Indeed, the CO<sub>2</sub> gas flowing through the reactor will have a larger chance to pass through at least one microdischarge, explaining the higher conversion.

Among the four dielectric materials investigated, quartz and alumina lead to the highest CO<sub>2</sub> conversion (i.e., 24.6% at 74 W) and energy efficiency (i.e., above 15% at 39 W for quartz, and slightly lower for alumina). This can be explained from the plasma charge, the number of microdischarge filaments and their average lifetime, which are clearly the highest for alumina, and the second highest for quartz. In addition, the high values for quartz, which are a bit counter-intuitive because this material has the lowest relative permittivity, can be explained from the higher effective plasma voltage (and thus the somewhat higher electric field and electron energy in the plasma). In general, the relative permittivity of the materials

seems not to be important for determining the CO<sub>2</sub> conversion and energy efficiency, at least not in the range investigated in this study (i.e.,  $\epsilon_r$  between 3.8 and 9.6). On the other hand, the larger number of microdischarges in a certain period seems mostly responsible for the higher CO<sub>2</sub> conversion, just like in the case of the effect of barrier thickness. This larger number of microdischarges could be explained in the case of quartz by the higher voltage over the dielectric (again similar to the effect of the barrier thickness), and in the case of alumina by the higher surface roughness of the material.

# Chapter V - CO<sub>2</sub> discharge with water addition

---

The results of this chapter will be published soon:

- Snoeckx R., **Ozkan A.**, Reniers F. and Bogaerts A., The quest for value-added products from CO<sub>2</sub> and H<sub>2</sub>O in a dielectric barrier discharge: a chemical kinetics study, *accepted in ChemSusChem*, (2016)

## 1. Introduction

To date not much is known about the simultaneous conversion of CO<sub>2</sub> and H<sub>2</sub>O into value added products by means of a (DBD) plasma, and especially not about the underlying mechanisms. In this chapter, we study the combined plasma-based conversion of CO<sub>2</sub> and H<sub>2</sub>O in a DBD plasma reactor, by means of experiments, which will be compared to computer simulations, based on a zero-dimensional (0D) chemical kinetics model. The aim of this study is to identify the influence of the water content and the SEI on the conversion and product formation.

We investigate CO<sub>2</sub> discharges with water content in the same DBD configuration as the one used for the previous chapter (see more details in the description of the DBD in the experimental setup section). The first part of the results is dedicated to the experimental results obtained by MS, OES and an oscilloscope. MS permits to have access to conversions in CO<sub>2</sub> and H<sub>2</sub>O and yields of various products. Moreover, OES allows us to determine some specific species present in the plasma and observe how they vary versus the water content in the DBD reactor. Finally, the last experimental diagnostic is carried out via an oscilloscope to do a detailed electrical characterization (like in the previous chapter) and to obtain the power absorbed by the plasma. The latter is indeed important and related to the input value of the simulation.

In parallel to the experimental work, simulations were performed by Snoeckx in order to interpret the experimental results, more specifically the CO<sub>2</sub> and H<sub>2</sub>O conversions. The modeling part permits to elucidate the chemistry aspect of the plasma as it is based on chemical kinetics reactions. The plasma chemistry model, with the results presented below, shows reasonable agreement with the experimental conversions. This model is used to elucidate the mechanisms behind these trends, the critical reactions that are mostly responsible for the CO<sub>2</sub> conversion and allow us to obtain a better understanding of the mechanisms related to the reactivity of CO<sub>2</sub>/H<sub>2</sub>O plasmas, and to investigate which products are mainly formed in the plasma-based conversion of CO<sub>2</sub> with water and the formation pathways of value added products, as described in detail in [233].

## 2. Mass spectrometry results

### 2.1. Experimental details

Mass spectrometry measurements allow to have access to CO<sub>2</sub> and H<sub>2</sub>O conversion. To study the formation of H<sub>2</sub>, CO, O<sub>2</sub> and the decomposition of CO<sub>2</sub> and H<sub>2</sub>O, MS software is used to monitor simultaneously the partial pressure of these species, measured at specific  $m/z$  values as a function of time. For example, the CO<sub>2</sub> conversion (equation 5.1) is calculated based on the signal  $m/z=44$  before (plasma OFF) and during (plasma ON) the discharge. After the plasma ignition, the percentages of products and remaining reactants are calculated based on the proportion of the partial pressures of the concerning species to the total pressure, which is the sum of all partial pressures ( $p_{\text{tot}}=p_{\text{CO}_2}+p_{\text{H}_2\text{O}}+p_{\text{CO}}+p_{\text{O}_2}+p_{\text{H}_2}$ ). Figure 61 depicts a typical graph with the partial pressure of certain species, defined by their  $m/z$  values, as a function of time. In all experiments, the total flow rate is kept constant at  $\Phi_{323\text{ K}}(\text{CO}_2+\text{H}_2\text{O}) = 600$  mL/min to have the same residence time in each case, varying the H<sub>2</sub>O content in the mixture between 0 and 8 %, resulting in a CO<sub>2</sub> content between 100 and 92%. The inlet quantities at 20°C and 50°C for the CO<sub>2</sub>-H<sub>2</sub>O discharge are detailed in Table 10. The water percentage is converted from g/h (delivered by the water vapor generator) to mL/min via the ideal gas law (assuming that the working pressure is precisely 1 atm). It should be mentioned that all the system (reactor + gas tubes) is heated up in order to avoid the condensation and have quasi only water vapor (H<sub>2</sub>O (g) instead of H<sub>2</sub>O (l)). These percentages in water are based on the assumption that 100% of the water is in gaseous phase, which is not in every case evident especially at high water flow rates.

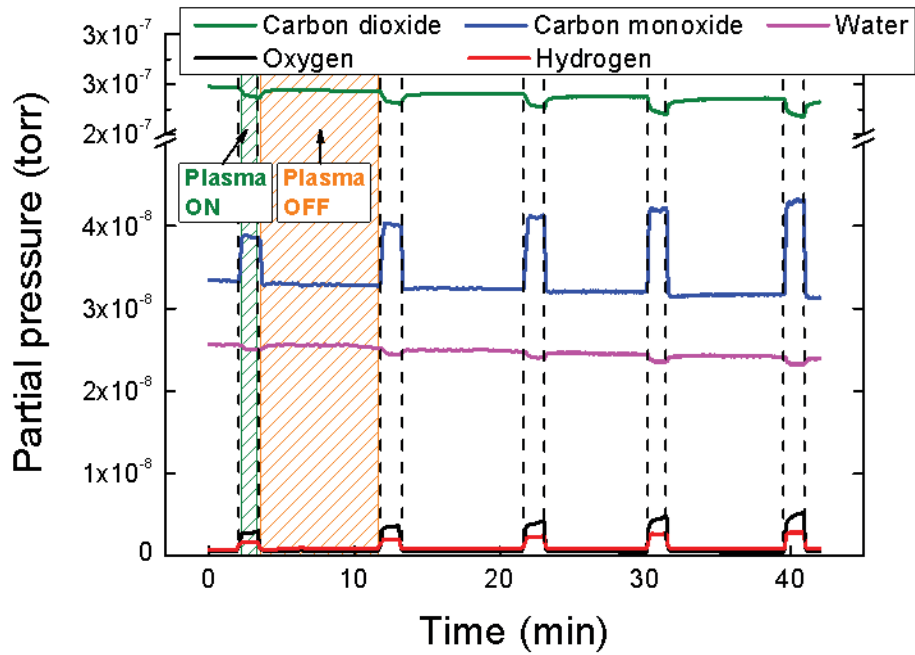


Figure 61 : Partial pressure versus time of the 5 different species indicated in the legend; absorbed power = 23, 32, 40, 48 and 58 W, respectively; operating frequency = 28.06 kHz;  $\Phi_{323\text{ K}}(\text{CO}_2) = 563\text{ mL/min}$  and  $\Phi_{323\text{ K}}(\text{H}_2\text{O}) = 37\text{ mL/min}$  (93.9 - 6.1% CO<sub>2</sub>/H<sub>2</sub>O mixture).

Table 10 : Inlet gas amount in the CO<sub>2</sub>-H<sub>2</sub>O mixture.

$\Phi_{\text{CO}_2}$ at 20°C (mL <sub>n</sub> /min)	$\Phi_{\text{CO}_2}$ at 50°C (mL/min)	$\Phi_{\text{H}_2\text{O}}$ at 20°C (g/h)	$\Phi_{\text{H}_2\text{O}}$ at 50°C (mL/min)	CO <sub>2</sub> (%)	H <sub>2</sub> O (%)
544	600	0.0	0.0	100.00	0.00
533	588	0.5	12.3	97.95	2.05
522	575	1.0	24.5	95.91	4.09
511	563	1.5	36.8	93.87	6.13
500	551	2.0	49.0	91.83	8.17

The conversion of CO<sub>2</sub> and H<sub>2</sub>O is calculated from the mass spectrometry response:

$$X_{\text{CO}_2} (\%) = \frac{\text{moles of CO}_2 \text{ converted}}{\text{moles of CO}_2 \text{ without plasma}} = \frac{I_{\text{CO}_2}^{\text{plasma OFF}} - I_{\text{CO}_2}^{\text{plasma ON}}}{I_{\text{CO}_2}^{\text{plasma OFF}}} \times 100\% \quad \text{Eq. 5.1}$$

$$X_{\text{H}_2\text{O}} (\%) = \frac{\text{moles of H}_2\text{O converted}}{\text{moles of H}_2\text{O without plasma}} = \frac{I_{\text{H}_2\text{O}}^{\text{plasma OFF}} - I_{\text{H}_2\text{O}}^{\text{plasma ON}}}{I_{\text{H}_2\text{O}}^{\text{plasma OFF}}} \times 100\% \quad \text{Eq. 5.2}$$

The absorbed power (and the SEI values in J/cm<sup>3</sup>) corresponding to the applied power is mentioned as follows in Table 11. Note that all measurements are performed at an applied frequency of 28.06 kHz. The measured absorbed power (obtained by Lissajous method) seems to be independent of the different water contents in the discharge (in the range of water content from 0 to 8.2%). These SEI values are used as input for the corresponding simulation. Only the experiments carried out at SEI of 3.2, 4.0 and 4.8 J/cm<sup>3</sup> are taken into consideration for the correlation with the simulation. We used the energy density (in J/cm<sup>3</sup>) as input values in the code of the simulation and not the power (in watt). The power per pulse in the code is thus based on experimental SEI.

Table 11 : Absorbed powers and corresponding specific energy inputs in CO<sub>2</sub>-H<sub>2</sub>O discharge.

<b>Applied power (W)</b>	<b>Absorbed power (W)</b>	<b>SEI (J/cm<sup>3</sup>)</b>
40	31.8	3.2
50	40.0	4.0
60	48.2	4.8

In the sections below, we compare the measured CO<sub>2</sub> and H<sub>2</sub>O conversion and the product formations with the model calculations. We try to explain the observed trends based on the model predictions, made by Snoeckx [233].

## 2.2. CO<sub>2</sub> and H<sub>2</sub>O conversion

In Figure 62a&b, the experimental and calculated CO<sub>2</sub> and H<sub>2</sub>O conversions (calculated via equations 5.1 and 5.2) are plotted as a function of water vapor content for three different SEI values, i.e., 3.2, 4.0 and 4.8 J/cm<sup>3</sup>. The CO<sub>2</sub> and H<sub>2</sub>O conversions increase when more energy is applied, i.e. at higher SEI values (as already explained in the previous chapter - effect of the power). Regardless of the SEI, the CO<sub>2</sub> conversion is the highest when no water vapor is

added to the discharge, i.e. for pure CO<sub>2</sub>. The presence of small amounts of vapor water (2%) is enough to affect the properties of the CO<sub>2</sub> discharge to the extent that CO<sub>2</sub> conversion is significantly lowered. We can observe in Figure 62a that the calculated conversions are quite similar to the experimental ones, whatever the SEI. The decrease in CO<sub>2</sub> conversion, observed with increasing water content, may result from the destabilization of the discharge induced by the presence of water. Indeed, the calculations reveal a ~40% drop of the maximum electron density with increasing water content from 0 to 8% [233]. The fact that the electron density is lowered leads to a lower rate of the electron impact dissociation reactions. This is the physical reason why the CO<sub>2</sub> conversion drops. For all SEI values investigated, adding only 2% of water vapor yields a drop in the CO<sub>2</sub> conversion by about 25%. Increasing further the water content does not lead to a significant drop as the one observed in the first 2% addition; the CO<sub>2</sub> conversion decreases slightly up to 8% (drop of 15-25% from 2 to 8% of water content). Furthermore, the chemical analysis pathway, presented in [233], also allows identifying a chemical reason for the drop in CO<sub>2</sub> conversion. One of the crucial reactions, explaining the limitation of CO<sub>2</sub> (and H<sub>2</sub>O) conversion upon water addition, is the reaction between CO and OH (with the corresponding kinetic rate constant).



This is a fast reaction (R3) and plays an important role in the ratio between the conversion of CO<sub>2</sub> and H<sub>2</sub>O (see details in [233]).

In Figure 62b, we observe that the H<sub>2</sub>O conversion shows a slightly decreasing trend of about 10%, much less compared to the drop in CO<sub>2</sub> conversion, upon increasing water content. We can notice that the calculated H<sub>2</sub>O conversions are generally overestimated (compared to the experimental conversions) in the entire range of water addition, for all SEI values. The fact that the simulation overestimates the water conversions might come from some more complex processes in experiments. Indeed, it is possible that the evaporation is not complete in reality, leading to nebulization (formation of small water droplets spread out in the discharge zone), even if the entire experimental setup is heated (from CEM to the exit of the reactor). As the 0D model describes only the plasma chemistry processes without taking account physical effects like condensation or nebulization, this is the reason why the experiments leads to lower water conversions (compared to the calculated results). We can even observe that the deviation between experimental and simulated conversion becomes less significant

upon increasing SEI. Indeed, when more energy is supplied, the reactor, and thus the gas, is locally more heated in the discharge zone (as observed in the previous chapter - see the study of the effect of the power). This might improve the probability of evaporation (or reduce the probability of condensation), leading to a lower deviation in conversion at higher SEI.

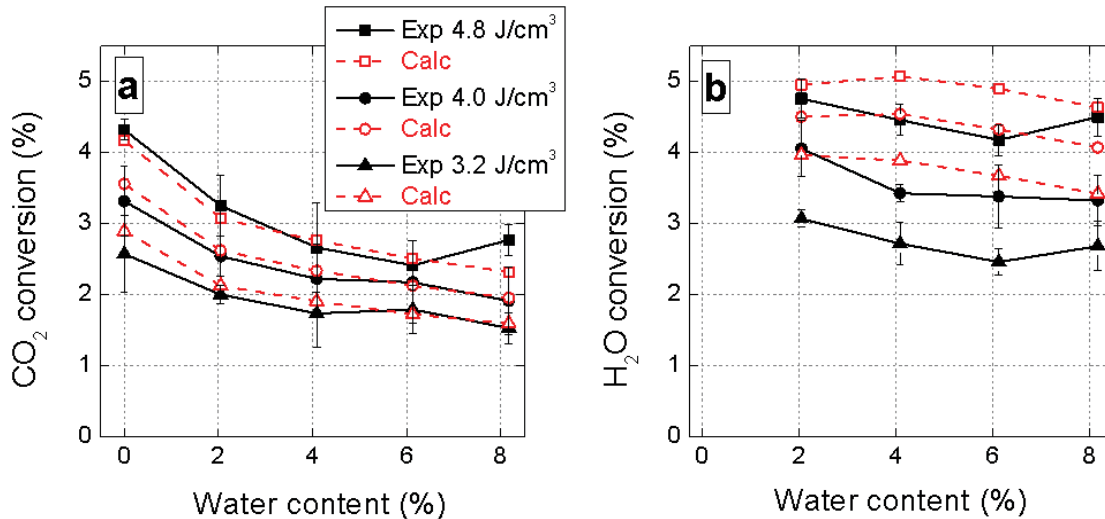


Figure 62 : Experimental and calculated values of (a) CO<sub>2</sub> and (b) H<sub>2</sub>O conversion as a function of water vapor content for the different values of SEI and a constant total flow rate of  $\Phi_{323\text{K}}(\text{CO}_2+\text{H}_2\text{O}) = 600 \text{ mL/min}$  at 50°C. Dielectric barrier: pyrex and  $f_{\text{signal}}=28.06 \text{ kHz}$ .

### 2.3. Product formation

The products formed experimentally are also analyzed for the three SEIs and compared to calculated results. Figure 63 represents the graphs with the product formation of CO, O<sub>2</sub> and H<sub>2</sub> (in %), after the plasma treatment ignited with 3.2, 4.0 and 4.8 J/cm<sup>3</sup>. Table 12 gives the same values presented in Figure 63 with their absolute error of the measured values. Moreover, this table also shows the calculated H<sub>2</sub>O<sub>2</sub> (in ppm), O<sub>3</sub> (in ppm) and CH<sub>3</sub>OH (in ppb) concentrations.

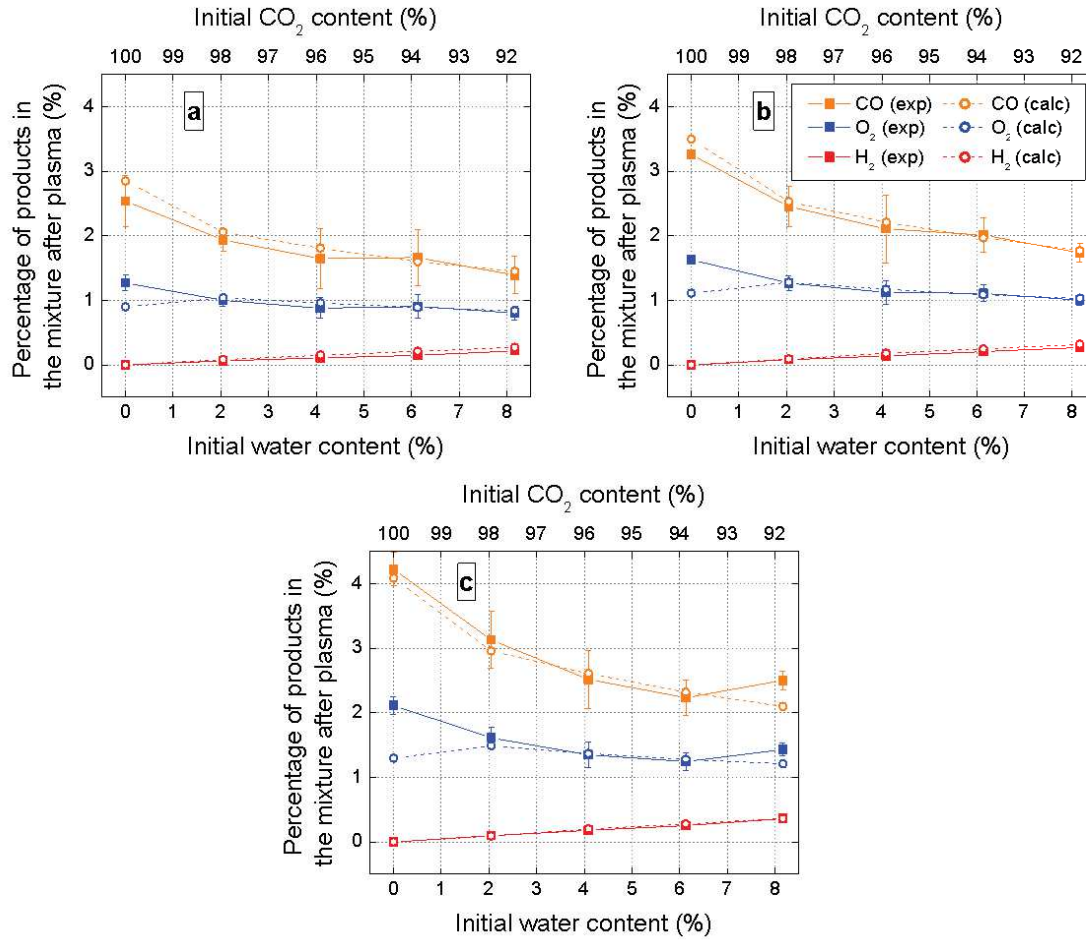


Figure 63 : Measured and calculated gas composition after plasma treatment for the different water vapor contents investigated (0 to 8.2%) and for an SEI of (a) 3.2 J/cm<sup>3</sup>, (b) 4.0 J/cm<sup>3</sup> and (c) 4.8 J/cm<sup>3</sup>, with the remainder being unconverted CO<sub>2</sub> and H<sub>2</sub>O.

Table 12 : Product analysis in different water content (from 0 to 8.2%) at 3 different specific energy input.

SEI 3.2 J/cm <sup>3</sup>								
CO <sub>2</sub> (%)	H <sub>2</sub> O (%)		O <sub>2</sub> (%)	CO (%)	H <sub>2</sub> (%)	H <sub>2</sub> O <sub>2</sub> (ppm)	O <sub>3</sub> (ppm)	CH <sub>3</sub> OH (ppb)
100.00	0.00	exp	1.27 ± 0.12	2.54 ± 0.40	-	-	ca. 500	-
		calc	0.90	2.85	-	-	3518	-
97.95	2.05	exp	1.00 ± 0.09	1.94 ± 0.18	0.062 ± 0.004	ca. 10-100	ca. 10	-
		calc	1.04	2.06	0.08	39	139	0.3
95.91	4.09	exp	0.88 ± 0.16	1.65 ± 0.47	0.110 ± 0.008	ca. 10-100	ca. 10	-
		calc	0.96	1.81	0.15	64	60	0.6
93.87	6.13	exp	0.91 ± 0.19	1.66 ± 0.43	0.149 ± 0.005	ca. 10-100	ca. 10	-
		calc	0.89	1.60	0.21	89	35	1.4
91.83	8.17	exp	0.80 ± 0.11	1.39 ± 0.29	0.217 ± 0.010	ca. 10-100	ca. 10	-
		calc	0.84	1.45	0.27	113	62	1.9
SEI 4.0 J/cm <sup>3</sup>								
CO <sub>2</sub> (%)	H <sub>2</sub> O (%)		O <sub>2</sub> (%)	CO (%)	H <sub>2</sub> (%)	H <sub>2</sub> O <sub>2</sub> (ppm)	O <sub>3</sub> (ppm)	CH <sub>3</sub> OH (ppb)
100.00	0.00	exp	1.63 ± 0.02	3.26 ± 0.03	-	-	ca. 500	-
		calc	1.11	3.50	-	-	4299	-
97.95	2.05	exp	1.27 ± 0.11	2.46 ± 0.32	0.081 ± 0.006	ca. 10-100	ca. 10	-
		calc	1.28	2.53	0.09	47	193	0.3
95.91	4.09	exp	1.12 ± 0.18	2.11 ± 0.53	0.138 ± 0.015	ca. 10-100	ca. 10	-
		calc	1.17	2.21	0.18	77	118	0.8
93.87	6.13	exp	1.11 ± 0.13	2.01 ± 0.27	0.205 ± 0.005	ca. 10-100	ca. 10	-
		calc	1.09	1.97	0.25	106	96	1.8
91.83	8.17	exp	1.00 ± 0.08	1.74 ± 0.14	0.269 ± 0.003	ca. 10-100	ca. 10	-
		calc	1.03	1.77	0.32	135	81	2.6

		SEI 4.8 J/cm <sup>3</sup>						
CO <sub>2</sub> (%)	H <sub>2</sub> O (%)		O <sub>2</sub> (%)	CO (%)	H <sub>2</sub> (%)	H <sub>2</sub> O <sub>2</sub> (ppm)	O <sub>3</sub> (ppm)	CH <sub>3</sub> OH (ppb)
100.00	0.00	exp	2.11 ± 0.14	4.23 ± 0.26	-	-	ca. 500	-
		calc	1.30	4.09	-	-	4971	-
97.95	2.05	exp	1.61 ± 0.17	3.13 ± 0.44	0.957 ± 0.014	ca. 10-100	ca. 10	-
		calc	1.49	2.96	0.09	55	229	0.22
95.91	4.09	exp	1.35 ± 0.20	2.52 ± 0.45	0.180 ± 0.010	ca. 10-100	ca. 10	-
		calc	1.37	2.61	0.20	89	152	0.97
93.87	6.13	exp	1.24 ± 0.13	2.23 ± 0.28	0.253 ± 0.009	ca. 10-100	ca. 10	-
		calc	1.28	2.32	0.28	120	120	2.1
91.83	8.17	exp	1.43 ± 0.10	2.50 ± 0.14	0.362 ± 0.012	ca. 10-100	ca. 10	-
		calc	1.21	2.10	0.36	156	103	3.2

The main products formed are O<sub>2</sub>, and the syngas components CO and H<sub>2</sub> in all the experiments and the calculations. With the presented results, we can also say that we form some hydrogen peroxide (H<sub>2</sub>O<sub>2</sub>) and trace amounts of ozone (O<sub>3</sub>). On the other hand, no oxygenated hydrocarbons were detected in the experiments whereas the calculated concentrations of methanol were only in the ppb range (hence far below the experimental detection level).

The agreement between measured and calculated gas composition is very good. CO is the main product (being formed out of CO<sub>2</sub>, mainly from electron impact dissociation towards CO and O), as expected (due to the higher CO<sub>2</sub> content in the mixture), but its fraction obviously drops upon increasing H<sub>2</sub>O content, as it is also the case for the O<sub>2</sub> and O<sub>3</sub> fraction. O<sub>3</sub> can be created but in little amount as it tends to react in the plasma and gives back O<sub>2</sub>. The fractions of H<sub>2</sub> and H<sub>2</sub>O<sub>2</sub> (being formed out of H<sub>2</sub>O, also mainly from electron impact dissociation into OH and H which react with each other), on the other hand, rise upon addition of more H<sub>2</sub>O. The O<sub>3</sub> and H<sub>2</sub>O<sub>2</sub> contents could not be accurately measured as their signal-to-noise ratio is too low to exactly quantify their effective amount. Therefore, only an order of magnitude is given in the experimental data of Table 12. If we take a look at the experimental and calculated H<sub>2</sub>/CO ratio (from 5<sup>th</sup> and 4<sup>rd</sup> column), also known as syngas ratio, we can conclude that this ratio increases with increasing water content. At a SEI of 4.0 J/cm<sup>3</sup>, the ratio values are 0.03, 0.07, 0.10, 0.16 and rise upon increasing water content. One also has to

notice that the SEI has only a minor effect on this ratio in the investigated range. This ratio is important, since several post-processes require a different syngas ratio depending on the targeted products [45]. Even if no detectable amounts of hydrocarbons are produced, the fact that the syngas ratio can be easily tuned just by changing the water content is of great interest.

### 3. Optical emission spectroscopy results

Optical emission spectroscopy measurements are also achieved in order to observe the absolute emission variations of some specific emitted species. Since the OES diagnostic takes place during the plasma ignition, a study of the emission versus the process time is carried out. The time required to perform a complete spectrum takes about 10 minutes, during which the plasma properties can change. The most intense emission in a CO<sub>2</sub>-H<sub>2</sub>O discharge is the emission related to the band of CO<sub>2</sub><sup>+</sup> ( $A^2 \Sigma^+ \rightarrow X^2 \Pi$ ). To this purpose, this band at 289 nm, which does not show any other band overlapping, is studied as a function of time. Figure 64 depicts the emission of the CO<sub>2</sub><sup>+</sup> band versus time. It is shown that the emission signal reaches a stable intensity only after 90 s of plasma operation, explaining the reach of the steady regime, as explained in the previous chapter (see section “Influence of the duty cycle on the discharge time-stability”). The FWHM of the second peak of CO<sub>2</sub><sup>+</sup> depends on several effects, including the Doppler effect related with the gas temperature and this is why this broadening reaches a plateau at the steady regime. OES diagnostics are therefore achieved only once this steady regime is reached, i.e. after 90 s of plasma ignition.

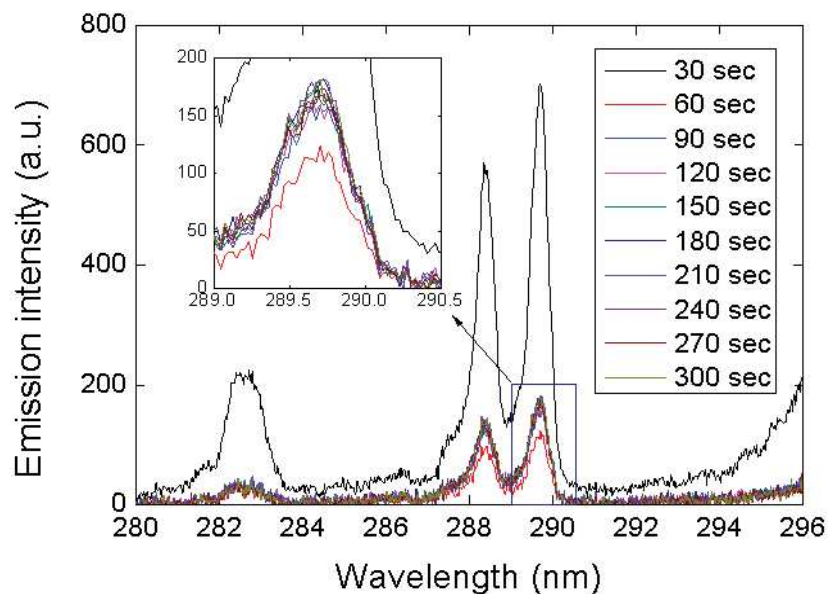


Figure 64 : Emission of the band of CO<sub>2</sub><sup>+</sup> ( $A^2 \Sigma^+ \rightarrow X^2 \Pi$ ) as a function of the plasma process time. Acquisitions of spectra are taken in kinetics series every 30 s.  $P_{\text{abs}}=56$  W;  $f=28.1$  kHz.

Grating 1800 lines/mm  $\rightarrow$  resolution of 22 pm; exposure time = 0.5 s.

Figure 65 depicts the emission spectra of a CO<sub>2</sub> discharge in the presence and absence of water vapor. The spectra are carried out over a complete spectral range from 200 to 900 nm, using the step-and-glue technique for automatic concatenation. Typical regions can be identified in this spectrum. Lines and bands related to emitted atoms or molecules can be found in literature (NIST for the atomic lines and the book of Pearse & Gaydon for the molecular bands [214]). When H<sub>2</sub>O is added, the overall intensity of the plasma emission is lowered whereas the OH band at 309 nm and H alpha line at 656 nm appear. Individual spectra related to specific emitted species are represented for increasing water content in Figure 66a-f. These different spectra of specific bands and peaks are recorded with a higher resolution (grating 2400 lines/mm  $\rightarrow$  resolution of 18 pm). Subsequently, the maximum values of the lines or band in intensity are plotted versus the water content from 0 to 12% in Figure 67. It is noticed that the OES spectra are quite reproducible as the error bars are not that high. These variations in intensity can give us an idea about how the water affects the production of OH or atomic H for example. Indeed, these highly reactive species are important in terms of the reactivity of the CO<sub>2</sub>-H<sub>2</sub>O plasma and for its chemistry, as discussed by Snoeckx [233].

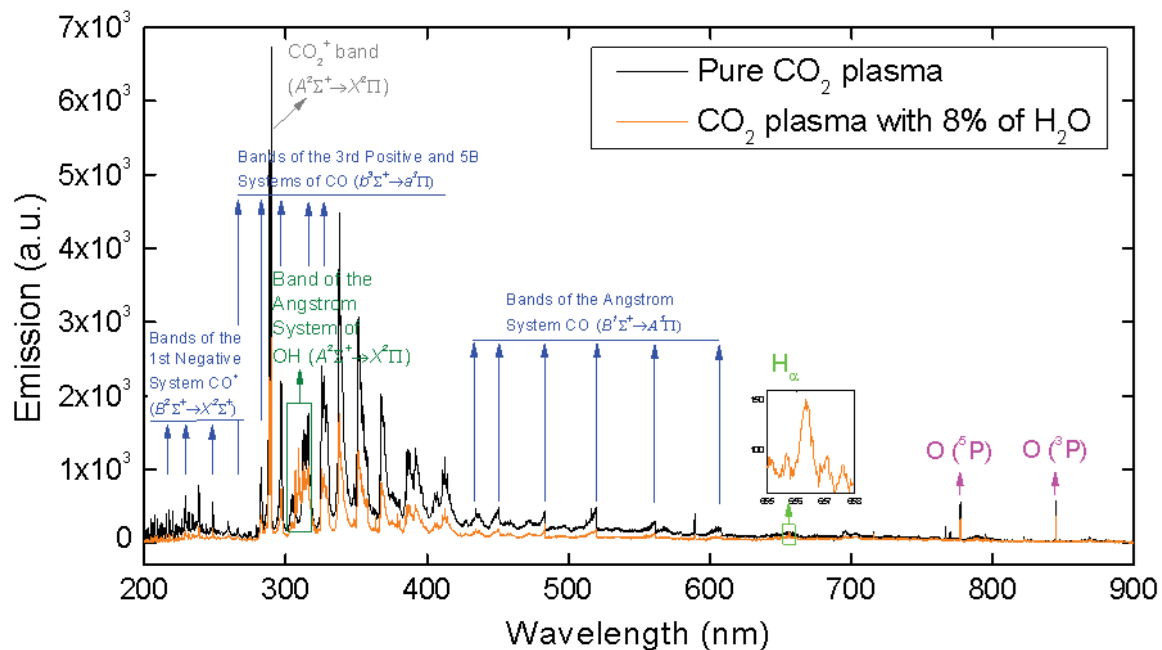


Figure 65 : Typical emission spectra of a CO<sub>2</sub> discharge with and without water vapor from 200 to 900 nm. Acquisitions of spectra are taken in 10 accumulations.  $P_{\text{abs}}=56$  W;  $f=28.1$  kHz.

Grating 1800 lines/mm; exposure time = 1 s.

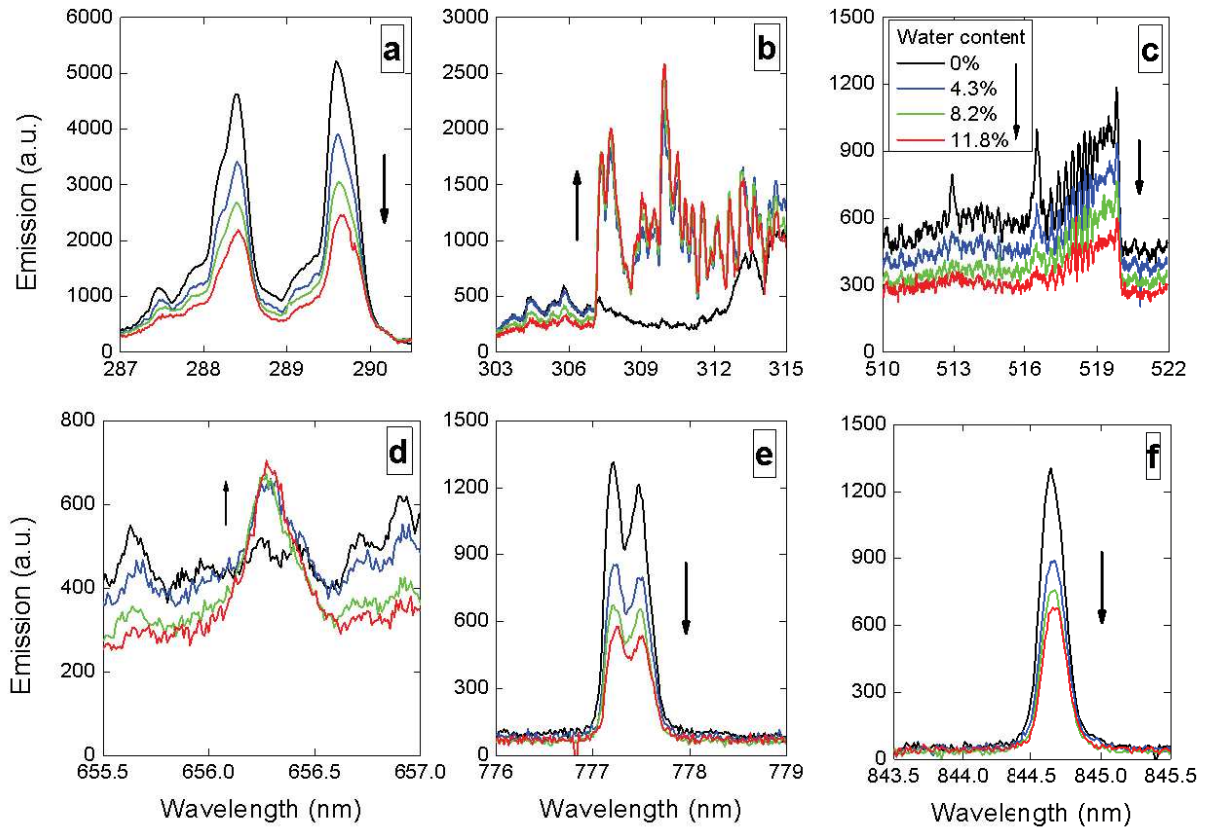


Figure 66 : High resolution emission spectra of (a) the band of CO<sub>2</sub><sup>+</sup> ( $A^2 \Sigma^+ \rightarrow X^2 \Pi$ ), (b) the Angstrom System of OH ( $A^2 \Sigma^+ \rightarrow X^2 \Pi$ ), (c) one of the Angstrom System bands of CO ( $B^1 \Sigma^+ \rightarrow A^1 \Pi$ ), (d) the H<sub>α</sub> peak, (e) the O(<sup>5</sup>P) peak (<sup>5</sup>P→<sup>5</sup>S transition) and (f) the O (<sup>3</sup>P) peak (<sup>3</sup>P→<sup>3</sup>S transition) - in a CO<sub>2</sub> discharge for an increasing water vapor content.  $P_{\text{abs}}=56 \text{ W}$ ;  $f=28.1 \text{ kHz}$ ;  $\Phi_{323 \text{ K}}(\text{CO}_2)=551 \text{ mL}\cdot\text{min}^{-1}$ ;  $\Phi_{323 \text{ K}}(\text{H}_2\text{O})=0, 24, 49 \text{ and } 73 \text{ mL}\cdot\text{min}^{-1}$  (from 0 to 11.8%). Acquisitions of spectra are taken in 5 accumulations. Grating 2400 lines/mm → resolution of 18 pm; exposure time = 2 s.

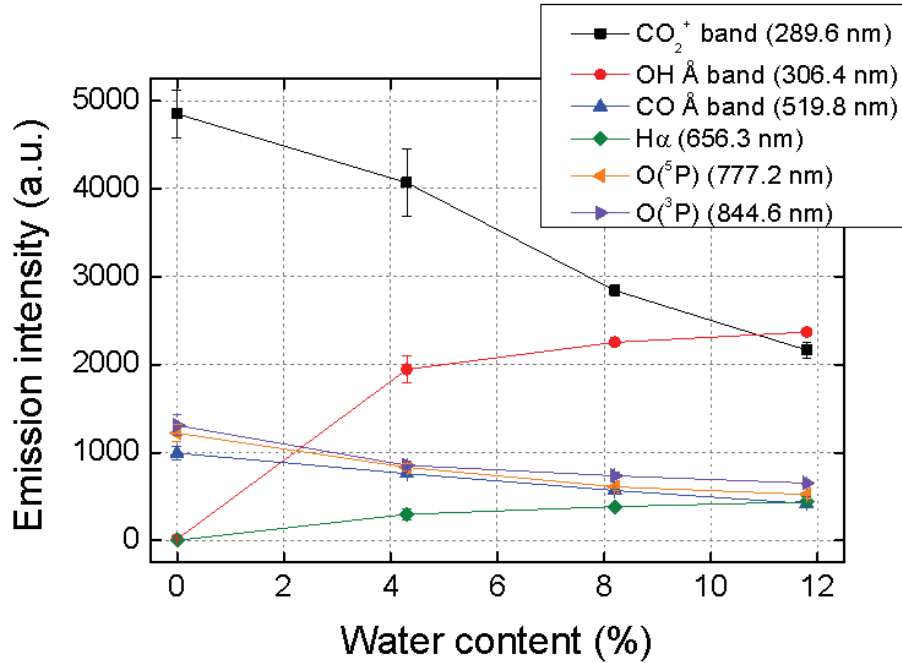


Figure 67 : Absolute intensities of specific bands and lines as a function of the water content.

#### 4. Electrical characterization

An electrical characterization study is also crucial for the interpretation of the plasma in the simulation (see [233]) as we need to have accurate information about the exact energy input but also about the characteristics of the microdischarges itself, such as the number of microdischarges and their lifetime. Indeed the simulation is based on the modelling of consecutive microdischarge pulses (see description of the model previously). The physical values (like specific energy input, the microdischarge characteristics, the total flow rate and thus the residence time, the operating frequency...) are included in the model as input values.

During each plasma ignition, the peak-to-peak voltage and absorbed power are recorded via an oscilloscope, precisely after 90 s of process time (i.e. when the steady regime is reached). In this regime, 3 consecutive measurements are recorded and the results shown below are thus the average of these 3 consecutive measurements. Here, the electrical characterization is achieved only at an applied power of 60 W, corresponding to an absorbed power of 48 W. The fraction of the absorbed power (and thus also the reflected power) does not change as a function of the water content as shown in Figure 68 (black curve). In the same figure, the root-mean-square (RMS) applied voltage ( $V_{\text{DBD}}$ ), as well as its two components (voltage of the gap  $V_{\text{pl,eff}}$  and voltage of the dielectric  $V_{\text{diel}}$ ) are plotted as a function of the water content.

From a water content of 0 to 8.2%,  $V_{\text{DBD}}$  and  $V_{\text{pl,eff}}$  slightly increase from 4950 to 5250 V and from 3450 to 3750 V, respectively. This increase in voltage (+300 V) is clearly related to the presence of water in the discharge as the water tends to trap the electron. Therefore, the electrons must be more accelerated with a higher electric field in a combined CO<sub>2</sub>-H<sub>2</sub>O discharge in order to have a self-sustained discharge [294]. On the other hand, the  $V_{\text{diel}}$  component does not vary as a function of the water content – it remains at 1500 V as the dielectric tube (pyrex) is still the same.

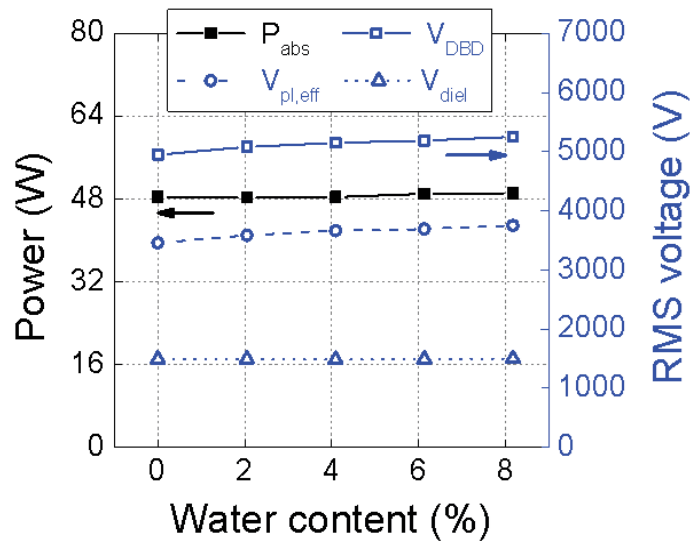


Figure 68 : Absorbed power (left axis) and RMS voltages (right axis) as a function of water content; dielectric material=pyrex, applied power=60 W,  $f=28.58$  kHz and  $\Phi_{323}$   
 $\kappa(\text{CO}_2+\text{H}_2\text{O})=600 \text{ mL}_n\cdot\text{min}^{-1}$ .

Based on the detailed electrical characterization (used also in the previous chapter [118]), the number of microfilaments for a given residence time (here one period) does not change upon increasing water content, as depicted in Figure 69 (black curve). The fact that the presence of water does not affect the number of the microdischarges (420 during  $\tau_{\text{anal}}=35 \mu\text{s}$ ) is important as this information is included in the model (number of pulse occurrence during the entire simulation, i.e. within the residence time 1.66 s, corresponding to the total gas flow rate of 600 mL/min passing through a discharge volume of 15.1 cm<sup>3</sup>). On the other hand, the mean lifetime of the microdischarges decreases significantly from 12.3 to 10.9 ns as a function of the water content from 0 to 8.2% as shown in the same figure (blue curve). That is also why the plasma is less intense in emission when water is added (as also shown by OES measurements above – cf. Figure 65).

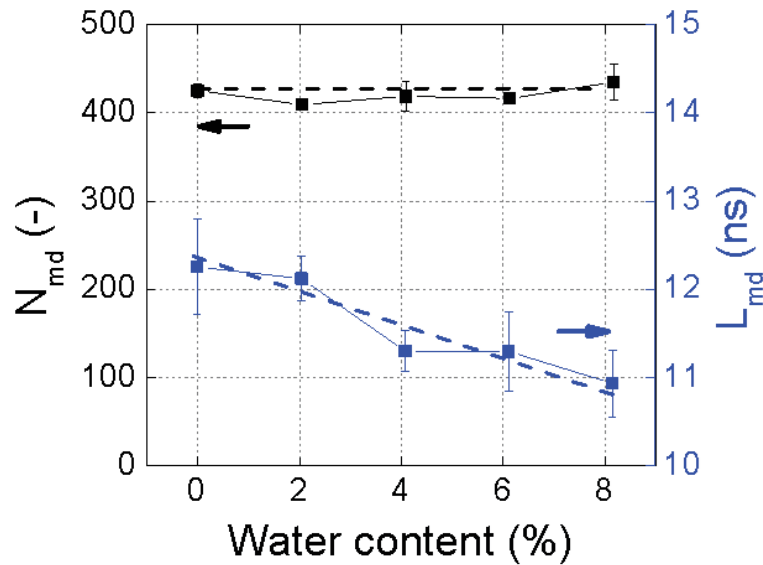


Figure 69 : (a) Number of microdischarges during one period (left axis) and mean lifetime of the microdischarges (right axis) as a function of the water content in the discharge. Dielectric material=pyrex,  $P_{abs}=48$  W,  $f_{signal}=28.6$  kHz and  $\Phi_{323\text{ K}}(\text{CO}_2+\text{H}_2\text{O})=600$  mL<sub>n</sub>.min<sup>-1</sup>.

Figure 70a shows the distribution of the microdischarge lifetime versus their number ( $N_{md}$ ) over 2 periods (71  $\mu$ s) of analysis time. This alternative representation allows to evaluate how the water could affect the microdischarge characteristics. We can observe that most of the microdischarges ( $\approx 72\%$ ) exhibit a lifetime comprised between 7 and 60 ns. On the other hand, a small fraction of microdischarges exhibits a lifetime under 7 ns. It is difficult to extract information from this, since these microdischarges are too small, and therefore the errors in their lifetime are a bit higher for the electrical characterization. The filaments which have  $\text{FWHM} < 3$  ns correspond to the noise of the current profile and those which have  $\text{FWHM} < 10$  ns corresponds to the “birth” and “death” microdischarges. Despite the error on the lower  $L_{md}$ , we can observe in Figure 70b that the lifetimes of the microdischarges are significantly lowered upon increasing water content in the discharge. Again, the information concerning the lifetimes of the microdischarges is directly inserted as input for the simulations.

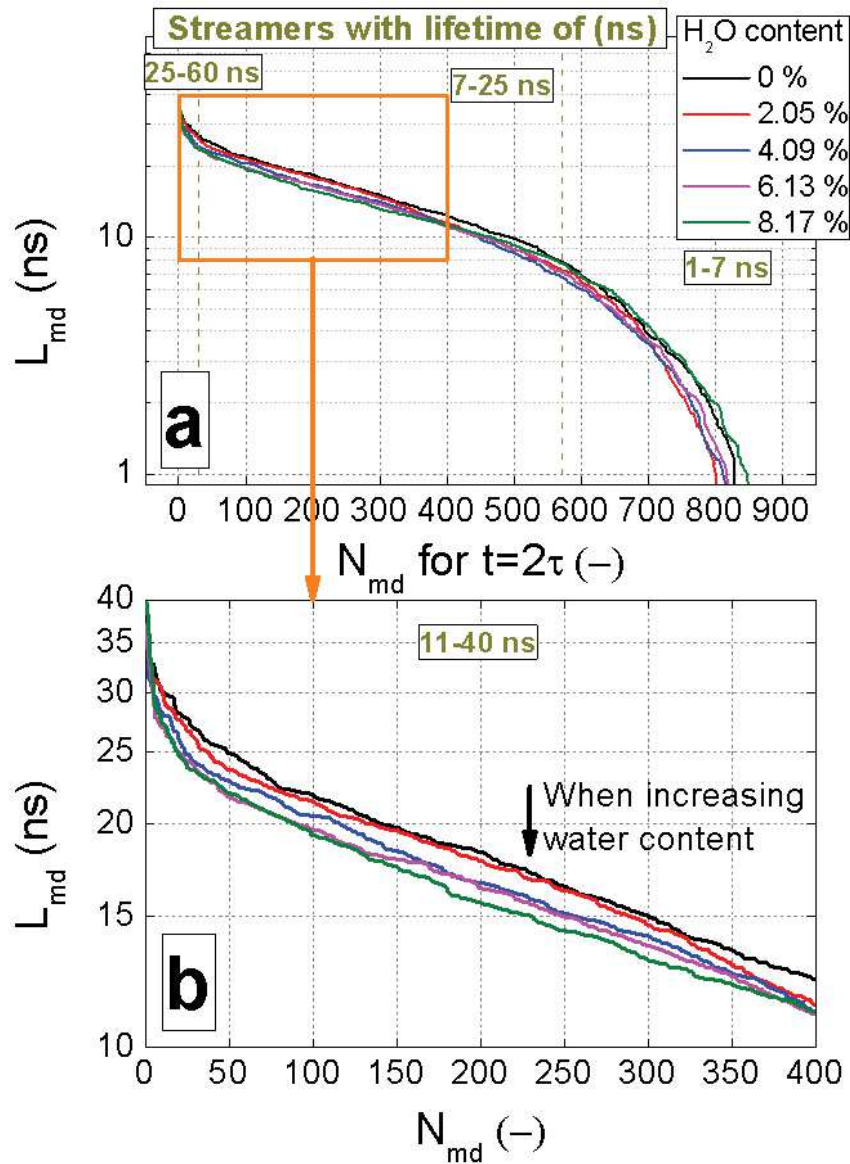


Figure 70 : Distribution of the microdischarge lifetime (a) over an analysis time of 2 periods, (b) for microdischarges which have lifetimes between 11 and 40 ns – for different water contents. Dielectric material=pyrex,  $P_{\text{abs}}=48$  W,  $f_{\text{signal}}=28.6$  kHz and  $\Phi_{323\text{ K}}(\text{CO}_2+\text{H}_2\text{O})=600$  mL<sub>n</sub>.min<sup>-1</sup>.

Furthermore, the plasma charge accumulation ( $Q_{\text{pl}}$ ) and the plasma current ( $i_{\text{pl}}$ ) versus the water content are also depicted in Figure 71. Both  $Q_{\text{pl}}$  and  $i_{\text{pl}}$  decrease as a function of the water content. As mentioned in the previous chapter,  $Q_{\text{pl}}$  can be easily converted into conduction currents considering the analysis time (one period here), as expressed in the following formulas:

$$i_{pl}^{\tau}(f) = Q_{pl}^{\tau}(f) / \tau = 2f \cdot Q_{pl}^{\tau}(f) \quad \text{Eq. 5.3}$$

A decrease in plasma current corresponds to a lower electron density in the combined CO<sub>2</sub>-H<sub>2</sub>O plasma as the water tends to trap the electrons present in the discharge. This is also why the plasma voltage (see Figure 68) slightly increases upon rising water content to keep the same plasma power.

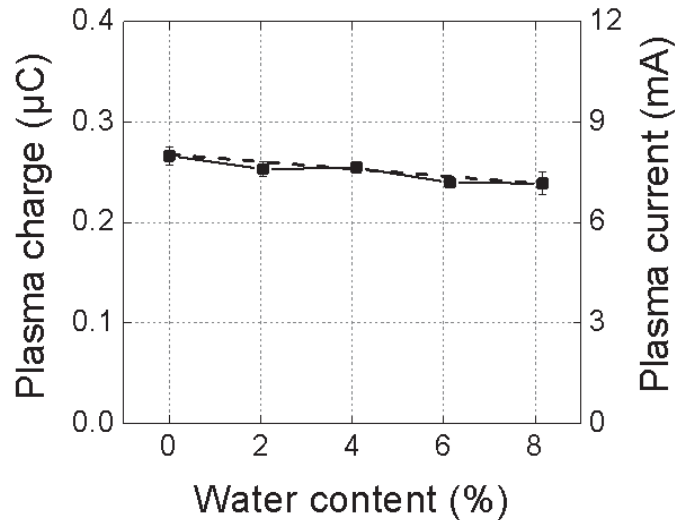


Figure 71 : (a) Plasma charge during one period (left axis) and plasma current (right axis) as a function of the water content in the discharge. Dielectric material=pyrex,  $P_{abs}=48$  W,

$$f_{signal}=28.6 \text{ kHz and } \Phi_{323 \text{ K}}(\text{CO}_2+\text{H}_2\text{O})=600 \text{ mL}_n \cdot \text{min}^{-1}.$$

To sum up, increasing the water content in the discharge leads to an increase of applied voltage, a constant number of peaks and a decrease of the mean lifetime of the streamers and plasma charge accumulation. However, the decrease in CO<sub>2</sub> conversion upon increasing water content is not only related to physical phenomena as described above, but it can also be explained based on the plasma chemistry, as explained in detail by Snoeckx [233].

## 5. Conclusion

We studied the combined CO<sub>2</sub>-H<sub>2</sub>O dissociation in a cylindrical pyrex DBD reactor operating at atmospheric pressure. The aim of this study is to identify the influence of the water content and the SEI (or the plasma power) on the conversion and product formation. This has been carried out based on MS, OES and an oscilloscope in order to determine the macroscopic

trends like CO<sub>2</sub> and H<sub>2</sub>O conversion, the yields of different formed products (i.e. mainly CO, O<sub>2</sub> and H<sub>2</sub> but also O<sub>3</sub> and H<sub>2</sub>O<sub>2</sub>). The reach of the steady state regime after plasma ignition is also evidenced here by OES, like in the previous chapter. OES also permits to determine some specific species present in the plasma and to observe how they vary versus the water content.

Simulations have been carried out by Snoeckx [233] in order to interpret the experimental results and the macroscopic observations, i.e. the conversions and products formation. To have the model the closest to the reality as possible, a detailed electrical characterization is achieved. Indeed, the real plasma power (measured by the Lissajous method) or the characteristics of the microdischarges (such as the number of pulses per time unit, the lifetime of these pulses) are of great interest as this information is included as input in the model.

Overall we can conclude that the experiments and computer simulations reveal the same trends for the conversion of CO<sub>2</sub> and H<sub>2</sub>O and for the yields of CO, H<sub>2</sub> and O<sub>2</sub>. In particular, the water addition in the discharge leads to a drop in CO<sub>2</sub> conversion as the water destabilizes the latter.

Table 13 summarizes the main experimental results to correlate the CO<sub>2</sub> (and H<sub>2</sub>O) conversion with the process parameters by increasing the water content. We can observe how this water content (at a fixed SEI or power) affects the CO<sub>2</sub> (and H<sub>2</sub>O) conversion and the products formation, as well as other plasma parameters.

Table 13 : Summary of CO<sub>2</sub> and H<sub>2</sub>O conversion and products yields as a function of the water content in the discharge, and correlation with the electrical plasma characteristics (at fixed SEI = 4.8 J/cm<sup>3</sup> and a total flow rate of 600 mL.min<sup>-1</sup>).

		Increasing water content (from 0 to 8.2%)
Conversion	CO <sub>2</sub> (%) ( $\chi_{\text{CO}_2}$ )	↘ (4.22 - 2.40)
	H <sub>2</sub> O (%) ( $\chi_{\text{H}_2\text{O}}$ )	↘ (4.81 - 4.12)
Product yields	CO (%)	↘ (4.2 - 2.5)
	O <sub>2</sub> (%)	↘ (2.1 - 1.4)
	H <sub>2</sub> (%)	↗ (0.0 - 0.4)
	O <sub>3</sub> (ppm)	↘ (1000 - 100)
	H <sub>2</sub> O <sub>2</sub> (ppm)	↗ (0 - 100)
Syngas ratio	H <sub>2</sub> /CO	↗ (0 - 0.15)
Plasma power		Unchanged
Voltage	Applied (V <sub>DBD</sub> )	↗ (4.95 - 5.25 kV)
	Plasma (V <sub>pl,eff</sub> )	↗ (3.45 - 3.75 kV)
	Dielectric (V <sub>diel</sub> )	≈ (1.49 - 1.50 kV)
Microdischarges	Number (N <sub>md</sub> )	≈ (421 for one $\tau$ )
	Lifetime (L <sub>md</sub> )	↘ (12.3 - 10.9 ns)
	Current (i <sub>pl</sub> )	↘ (8.0 - 7.2 mA)
	Distribution	Changed
Charge	Plasma ( Q <sub>pl</sub>  )	↘ (0.27 - 0.24 $\mu\text{C}$ for one $\tau$ )

It is clear that the water content, which can easily be controllable at the inlet, has an important impact on the CO<sub>2</sub> splitting process. It is observed that it lowers the charge delivered in the plasma, the plasma current and thus, the electron density. Moreover, this drop in electron density upon increasing water content is demonstrated via simulation, and it is the main physical reason why the CO<sub>2</sub> splitting is less efficient with water present in the discharge. This can also be related, experimentally, to the drop in the microdischarge lifetime and the fact that the global emission of the plasma (observed by OES) is lowered. At a fixed power, one can clearly see that the electrical parameters like the plasma voltage, and the microdischarges lifetime, are affected whereas the number of microdischarges remains constant.

Finally, via simulations and more precisely via chemical kinetics analysis, the reaction between CO and OH giving back CO<sub>2</sub> appears to be the pivotal reaction in terms of interactions between CO<sub>2</sub> and H<sub>2</sub>O. The latter plays an important role on the CO<sub>2</sub> splitting pathway. This reaction appears to be very fast and thus, this is also the reason in the drop of CO<sub>2</sub> conversion, from a chemical point of view.

# Chapter VI - CO<sub>2</sub> discharge with methane addition

---

The results of this chapter were published in the following paper:

- **Ozkan A.**, Dufour T., Arnoult G., De Keyzer P., Bogaerts A. and Reniers F., CO<sub>2</sub>-CH<sub>4</sub> conversion and syngas formation at atmospheric pressure using a multi-electrode dielectric barrier discharge, *Journal of CO<sub>2</sub> utilization*, 9 (2015) 74-81

## 1. Introduction

In this last chapter, the conversion of CO<sub>2</sub> and CH<sub>4</sub> into value-added chemicals is studied in a new geometry of a dielectric barrier discharge (DBD) with multi-electrodes, dedicated to the treatment of high gas flow rates (see description of the DBD in *Chapter III*). Gas chromatography is used to define the CO<sub>2</sub> and CH<sub>4</sub> conversion as well as the yields of the products of decomposition (CO, O<sub>2</sub> and H<sub>2</sub>) and of recombination (C<sub>2</sub>H<sub>6</sub>, C<sub>2</sub>H<sub>4</sub>, C<sub>2</sub>H<sub>2</sub> and CH<sub>2</sub>O). The influence of three parameters is investigated on the conversion: the CO<sub>2</sub> and CH<sub>4</sub> flow rates, the plasma power and the nature of the carrier gas (argon or helium). The energy efficiency of the CO<sub>2</sub> conversion is estimated and compared with those of similar atmospheric plasma sources presented in the literature. We will show that our DBD reactor shows a good compromise between a good energy efficiency and the treatment of a large CO<sub>2</sub> flow rate.

## 2. Influence of electrical parameters

The conversion of CO<sub>2</sub> and CH<sub>4</sub> is calculated according to equations 6.1 and 6.2, respectively, where A represents the peak area assigned to CO<sub>2</sub> or CH<sub>4</sub> in the chromatogram:

$$CO_2 \text{ Conversion}(\%) = \chi_{CO_2} = \frac{A_{CO_2 \text{ without plasma}} - A_{CO_2 \text{ with plasma}}}{A_{CO_2 \text{ without plasma}}} \times 100 \quad \text{Eq. 6.1}$$

$$CH_4 \text{ Conversion}(\%) = \chi_{CH_4} = \frac{A_{CH_4 \text{ without plasma}} - A_{CH_4 \text{ with plasma}}}{A_{CH_4 \text{ without plasma}}} \times 100 \quad \text{Eq. 6.2}$$

The selectivities of H<sub>2</sub>, O<sub>2</sub>, CO, C<sub>2</sub>H<sub>6</sub> and C<sub>2</sub>H<sub>4</sub> have been calculated as reported in Table 14, listed as H, O or C based selectivities, depending on the plasma composition (CH<sub>4</sub>, CO<sub>2</sub>, CO<sub>2</sub>/CH<sub>4</sub> respectively).

Table 14 : Formulas for the H, O or C based selectivities of H<sub>2</sub>, O<sub>2</sub>, CO, C<sub>2</sub>H<sub>6</sub> and C<sub>2</sub>H<sub>4</sub> (n is the number of moles).

	H-based selectivities (CH <sub>4</sub> plasma)	O-based selectivities (CO <sub>2</sub> plasma)	C-based selectivities (CH <sub>4</sub> /CO <sub>2</sub> plasma)
S <sub>H<sub>2</sub></sub> (%)	$\frac{n_{\text{H}_2}^{\text{produced}}}{2 \cdot n_{\text{CH}_4}^{\text{converted}}} \times 100$	-	-
S <sub>O<sub>2</sub></sub> (%)	-	$\frac{n_{\text{O}_2}^{\text{produced}}}{n_{\text{CO}_2}^{\text{converted}}} \times 100$	-
S <sub>CO</sub> (%)	-	$\frac{n_{\text{CO}}^{\text{produced}}}{2 \cdot n_{\text{CO}_2}^{\text{converted}}} \times 100$	$\frac{n_{\text{CO}}^{\text{produced}}}{n_{\text{CO}_2}^{\text{converted}} + n_{\text{CH}_4}^{\text{converted}}} \times 100$
S <sub>C<sub>2</sub>H<sub>4</sub></sub> (%)	$\frac{n_{\text{C}_2\text{H}_4}^{\text{produced}}}{n_{\text{CH}_4}^{\text{converted}}} \times 100$	-	$\frac{2 \cdot n_{\text{C}_2\text{H}_4}^{\text{produced}}}{n_{\text{CO}_2}^{\text{converted}} + n_{\text{CH}_4}^{\text{converted}}} \times 100$
S <sub>C<sub>2</sub>H<sub>6</sub></sub> (%)	$\frac{3 \cdot n_{\text{C}_2\text{H}_6}^{\text{produced}}}{2 \cdot n_{\text{CH}_4}^{\text{converted}}} \times 100$	-	$\frac{2 \cdot n_{\text{C}_2\text{H}_6}^{\text{produced}}}{n_{\text{CO}_2}^{\text{converted}} + n_{\text{CH}_4}^{\text{converted}}} \times 100$

### 2.1. Effect of the CO<sub>2</sub> and CH<sub>4</sub> flow rates on the reactivity and reaction products formed in the CO<sub>2</sub>/CH<sub>4</sub> conversion process

The plasma is generated in a mixture of CO<sub>2</sub>, CH<sub>4</sub> and Ar (or He) to investigate the effect of the reactive gas flow rates on their conversion. The Ar flow rate is set to 1800 mL.min<sup>-1</sup> while the CO<sub>2</sub> and CH<sub>4</sub> flow rates can be tuned between 0 and 120 mL.min<sup>-1</sup>, but the sum of both is always equal to 120 mL.min<sup>-1</sup>. Figure 72 represents the CO<sub>2</sub> and CH<sub>4</sub> conversions as a function of the CO<sub>2</sub> and CH<sub>4</sub> flow rates. Both for CO<sub>2</sub> and CH<sub>4</sub>, an increase in the flow rate is always correlated with a decrease in its conversion. Indeed, for CO<sub>2</sub> flow rates increasing from 20 to 120 mL.min<sup>-1</sup>,  $\chi_{\text{CO}_2}$  decreases from 8.3% to 6.1% while  $\chi_{\text{CH}_4}$  decreases from 21.5% to 10.9% when the CH<sub>4</sub> flow rates rises from 20 to 120 mL.min<sup>-1</sup>. This figure illustrates also that CH<sub>4</sub> is always converted to a larger extent than CO<sub>2</sub>, whatever the individual gas flow rates. Chemical reactions in the plasma lead to the dissociation of these molecules, thus generating products that can also recombine to form new species such as H<sub>2</sub>, O<sub>2</sub>, CO, C<sub>2</sub>H<sub>4</sub> and C<sub>2</sub>H<sub>6</sub> whose volumetric fractions ( $f_v$ ) are plotted in Figure 73a as a function of the CO<sub>2</sub> and CH<sub>4</sub> flow rates. Each  $f_v$  fraction is calculated as the ratio of the product flow rate to the CO<sub>2</sub>/CH<sub>4</sub> mixture flow rate, multiplied by 100. The main products are molecular hydrogen ( $f_{\text{V,H}_2}^{\text{max}} = 7.73\%$ ), carbon monoxide ( $f_{\text{V,CO}}^{\text{max}} = 8.13\%$ ) and molecular

oxygen ( $f_{V,O_2}^{\max} = 3.98\%$ ), the latter being detected only if no CH<sub>4</sub> is injected in the discharge. Other products such as ethylene and ethane are also formed but in smaller proportions ( $f_{V,C_2H_4}^{\max} = 0.52\%$  and  $f_{V,C_2H_6}^{\max} = 1.51\%$ ). The production of CO is more important with an increase in the CO<sub>2</sub> flow rate, reaching a plateau of approximately 8.10% for CO<sub>2</sub> flow rates higher than 80 mL.min<sup>-1</sup>. In the same way, the production of hydrogen, ethane and ethylene increases with the CH<sub>4</sub> flow rate. As the production of O<sub>2</sub> is only present for pure CO<sub>2</sub> plasma while it disappears after CH<sub>4</sub> addition, this probably means that the CH<sub>4</sub> reactive species interact with oxygen in the discharge. It is quite logical that the decomposition of CO<sub>2</sub> favors the production of CO and O<sub>2</sub> while the decomposition of CH<sub>4</sub> leads to the production of H<sub>2</sub>, C<sub>2</sub>H<sub>4</sub> and C<sub>2</sub>H<sub>6</sub> but also of carbon black powder (not detected by gas chromatography).

The selectivities of these products have also been calculated using the formulas from Table 14 and considering three cases:

- (i) When using CH<sub>4</sub> as unique reactive gas, the H-based selectivities are approximately 26% for H<sub>2</sub>, 32% for C<sub>2</sub>H<sub>6</sub> and 6% for C<sub>2</sub>H<sub>4</sub>. As  $S_{H_2}^{(H)} + S_{C_2H_6}^{(H)} + S_{C_2H_4}^{(H)} < 100\%$ , it means that also other products are formed, i.e., CH<sub>x</sub> non-gaseous products which are assumed to deposit on the inner walls of the reactor, especially on the surface of the high voltage central electrode.
- (ii) When using CO<sub>2</sub> as unique reactive gas, the O-based selectivities lead to  $S_{O_2}^{(O)} + S_{CO}^{(O)} = 48.2 + 49.2 = 97.4$ . This value is very close to 100% and if experimental errors are considered – in particular the uncertainties of the flowmeters (<3%) – then we can conclude that CO<sub>2</sub> is virtually only converted to molecular oxygen and carbon monoxide.
- (iii) When using a CH<sub>4</sub>/CO<sub>2</sub> mixture, the C-based selectivities of three gaseous carbonated products (namely CO, C<sub>2</sub>H<sub>6</sub> and C<sub>2</sub>H<sub>4</sub>) are plotted as a function of CO<sub>2</sub> flow rate in Figure 73b. As  $S_{CO}^{(C)} + S_{C_2H_6}^{(C)} + S_{C_2H_4}^{(C)}$  drops with rising CH<sub>4</sub> flow rate, it is clear that an increase of other product formation ( $S_{others}^{(C)} \uparrow$ ) occurs with a rise in the CH<sub>4</sub> flow rate. We believe that this can be due to solid carbon deposit, formation of acetylene and liquid/gaseous formaldehyde.

The case of solid carbon deposit on the central copper electrode area clearly appears after a few minutes of plasma treatment. The coke deposit on the copper electrode may influence the discharge electrical properties, leading to a more filamentary discharge. As a result, the CO<sub>2</sub>

conversion would change in case of prolonged use of the reactor. More worrying would be the plausible formation of arcs (since carbon black is an electric conductor) which may deteriorate the barrier, and hence the durability of the reactor. To prevent these problems, coke deposit can easily be removed by cleaning the inner walls of the reactor and polishing them with sandpaper. Another convenient way is to apply a pure CO<sub>2</sub> or pure O<sub>2</sub> plasma to remove the coke deposit. Finally, the central electrode may be covered by a dielectric barrier, as achieved for the 6 high-voltage tubular electrodes where no coke deposit has been evidenced.

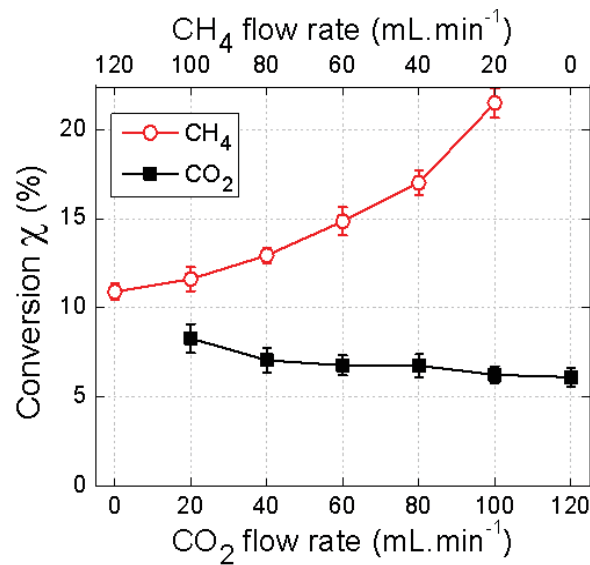


Figure 72 : CO<sub>2</sub> and CH<sub>4</sub> conversions as a function of the CO<sub>2</sub> and CH<sub>4</sub> flow rates with  $\Phi_{\text{Tot}} = 1920 \text{ mL}\cdot\text{min}^{-1}$ ,  $\Phi_{\text{Ar}} = 1800 \text{ mL}\cdot\text{min}^{-1}$ ,  $\Phi_{\text{CO}_2} + \Phi_{\text{CH}_4} = 120 \text{ mL}\cdot\text{min}^{-1}$ , plasma power = 45 W,  $f = 19.5 \text{ kHz}$ .

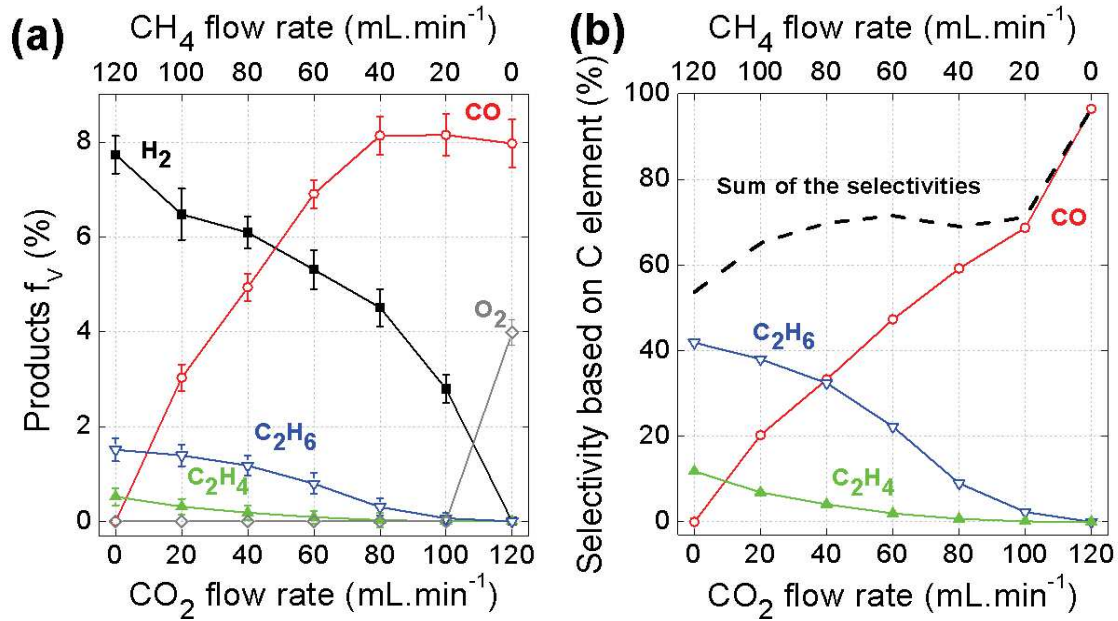


Figure 73 : (a) Volumetric fractions of H<sub>2</sub>, CO, O<sub>2</sub>, C<sub>2</sub>H<sub>4</sub> and C<sub>2</sub>H<sub>6</sub> (using the TCD) and (b) C-based selectivity of the quantified gaseous products as a function of the CO<sub>2</sub> and CH<sub>4</sub> flow rates with  $\Phi_{\text{Tot}} = 1920 \text{ mL}\cdot\text{min}^{-1}$ ,  $\Phi_{\text{Ar}} = 1800 \text{ mL}\cdot\text{min}^{-1}$ ,  $\Phi_{\text{CO}_2} + \Phi_{\text{CH}_4} = 120 \text{ mL}\cdot\text{min}^{-1}$ , plasma power = 45 W,  $f = 19.5 \text{ kHz}$ .

### 2.1.1. Overview of the important reactions

Plasmas are complex media where several hundred reactions of production and consumption can occur [152, 295]. The most plausible mechanisms for the formation and consumption of intermediate and value added products in the CO<sub>2</sub>/CH<sub>4</sub> gas mixture are listed in Table 15. In the following sections, we explain how the most important reaction products are formed.

All the statements presented below should be considered with caution, as they are only based on the reactions listed in Table 15, but not on a real model. Therefore, we do not take into account, for example, the calculated densities of the reactants. The use of model calculations, which can simulate and describe much more complicated chemistry, could be indeed really useful.

Table 15 : Reactions for the formation and consumption of intermediate and value added products of CH<sub>4</sub> and CO<sub>2</sub> conversion.

	Reaction	Rate constant	Ref.
R1	$\text{CH}_4 + e \rightarrow \text{CH}_3 \cdot + \text{H} \cdot + e$	$\sigma_1^*$	[296]
R2	$\text{CH}_2 \cdot + \text{O} \cdot \rightarrow \text{CO} + \text{H}_2$	$5.53 \cdot 10^{-11} \text{ cm}^3 \cdot \text{s}^{-1}$	[297]
R3	$\text{CH}_3 \cdot \rightarrow \text{CH}_2 \cdot + \text{H} \cdot$	$1.69 \cdot 10^{-08} \text{ cm}^3 \cdot \text{s}^{-1}$	[298]
R4	$\text{CH}_3^+ + e \rightarrow \text{CH}_2 \cdot + \text{H} \cdot$	$2.25 \cdot 10^{-08} \text{ cm}^3 \cdot \text{s}^{-1}$	[296, 299]
R5	$\text{CH}_3^+ + e \rightarrow \text{CH} \cdot + \text{H}_2$	$7.88 \cdot 10^{-09} \text{ cm}^3 \cdot \text{s}^{-1}$	[296, 299]
R6	$\text{CH}_3 \cdot + \text{H} \cdot \rightarrow \text{CH}_2 \cdot + \text{H}_2$	$1.00 \cdot 10^{-10} \text{ cm}^3 \cdot \text{s}^{-1}$	[298]
R7	$\text{CH}_4 + \text{H} \cdot \rightarrow \text{CH}_3 \cdot + \text{H}_2$	$5.83 \cdot 10^{-13} \text{ cm}^3 \cdot \text{s}^{-1}$	[298]
R8	$\text{CH}_4^+ + \text{H} \cdot \rightarrow \text{CH}_3^+ + \text{H}_2$	$1.00 \cdot 10^{-11} \text{ cm}^3 \cdot \text{s}^{-1}$	[300]
R9	$\text{H} \cdot + \text{H} \cdot \rightarrow \text{H}_2$	$1.44 \cdot 10^{-14} \text{ cm}^3 \cdot \text{s}^{-1}$	[301]
R10	$\text{CO}_2 + \text{H} \cdot \rightarrow \text{CO} + \text{OH} \cdot$	$1.40 \cdot 10^{-29} \text{ cm}^3 \cdot \text{s}^{-1}$	[302]
R11	$\text{CH} \cdot + \text{O} \cdot \rightarrow \text{CO} + \text{H} \cdot$	$6.90 \cdot 10^{-11} \text{ cm}^3 \cdot \text{s}^{-1}$	[298]
R12	$\text{CO}_2 + \text{CH} \cdot \rightarrow 2\text{CO} + \text{H} \cdot$	$9.68 \cdot 10^{-13} \text{ cm}^3 \cdot \text{s}^{-1}$	[297]
R13	$\text{CH}_3 \cdot + \text{CH}_3 \cdot \rightarrow \text{C}_2\text{H}_6$	$4.20 \cdot 10^{-11} \text{ cm}^3 \cdot \text{s}^{-1}$	[303]
R14	$\text{C}_2\text{H}_5 \cdot + \text{H} \cdot \rightarrow \text{C}_2\text{H}_6$	$2.25 \cdot 10^{-10} \text{ cm}^3 \cdot \text{s}^{-1}$	[304]
R15	$\text{C}_2\text{H}_5 \cdot + \text{CH}_4 \rightarrow \text{C}_2\text{H}_6 + \text{CH}_3 \cdot$	$1.83 \cdot 10^{-24} \text{ cm}^3 \cdot \text{s}^{-1}$	[302]
R16	$\text{C}_2\text{H}_6 + e \rightarrow \text{C}_2\text{H}_5 \cdot + \text{H} \cdot + e$	$\sigma_{16}^*$	[305]
R17	$\text{C}_2\text{H}_5 \cdot + e \rightarrow \text{C}_2\text{H}_4 + \text{H} \cdot + e$	$\sigma_{17}^*$	[305]
R18	$\text{CH}_4 + \text{CH} \cdot \rightarrow \text{C}_2\text{H}_4 + \text{H} \cdot$	$9.74 \cdot 10^{-11} \text{ cm}^3 \cdot \text{s}^{-1}$	[298]
R19	$\text{CH}_3 \cdot + \text{CH}_2 \cdot \rightarrow \text{C}_2\text{H}_4 + \text{H} \cdot$	$7.01 \cdot 10^{-11} \text{ cm}^3 \cdot \text{s}^{-1}$	[298]
R20	$\text{C}_2\text{H}_5 \cdot + \text{O} \cdot \rightarrow \text{C}_2\text{H}_4 + \text{OH} \cdot$	$4.40 \cdot 10^{-11} \text{ cm}^3 \cdot \text{s}^{-1}$	[297]
R21	$\text{CO}_2 + e \rightarrow \text{CO} + \text{O} \cdot + e$	$\sigma_{21}^*$	[7]
R22	$\text{CO}_2 + e^- \xrightarrow{\text{CH}_4} \text{CO} + \text{O} \cdot + e^-$	$\sigma_{22}^*$	[7]
R23	$\text{CO}_2 + \text{O} \cdot \rightarrow \text{CO} + \text{O}_2$	$2.01 \cdot 10^{-10} \text{ cm}^3 \cdot \text{s}^{-1}$	[306]
R24	$\text{CO}_2^+ + e \rightarrow \text{CO} + \text{O} \cdot$	$2.71 \cdot 10^{-07} \text{ cm}^3 \cdot \text{s}^{-1}$	[299]
R25	$\text{CH}_3 \cdot + \text{O} \cdot \rightarrow \text{H}_2\text{CO} + \text{H} \cdot$	$1.12 \cdot 10^{-10} \text{ cm}^3 \cdot \text{s}^{-1}$	[307]
R26	$\text{CH}_2 \cdot + \text{O}_2 \rightarrow \text{H}_2\text{CO} + \text{O} \cdot$	$5.39 \cdot 10^{-13} \text{ cm}^3 \cdot \text{s}^{-1}$	[298, 308]

\*: this reaction is described with a cross section.

### 2.1.2. Production of hydrogen

Several chemical reactions give rise to the production of molecular hydrogen through the dissociation of hydrocarbon species upon collision with an atom (R2), an electron (R5) or a H radical (R6, R7 and R8). The rate constants of these reactions are in the order of  $10^{-13}$ - $10^{-10}$  cm<sup>3</sup>.s<sup>-1</sup>, except for R5 which is somewhat higher ( $7.88 \cdot 10^{-9}$  cm<sup>3</sup>.s<sup>-1</sup>) as the collision occurs between an energetic electron and an ion. Although the rate constant of R9 is a bit lower than the other ones ( $1.44 \cdot 10^{-14}$  cm<sup>3</sup>.s<sup>-1</sup>), the recombination of two H radicals (also possible in a three-body recombination) may be considered as one possible pathway since  $v = k_{11}[\text{H}]^2$  and H is produced in many other reactions such as R3, R4, R11, R12, R16, R17, R18, R19 and R25. Electron impact reactions R16 and R17 are not described with a rate constant but with a cross section  $\sigma$  which depends on the electron temperature.

### 2.1.3. Production of CO

The formation of CO is directly correlated with the dissociation of CO<sub>2</sub>. The reactions responsible for the production of CO are given by R2, R10, R11, R12, R21, R22, R23 [309].

(R21) is electron impact dissociation of CO<sub>2</sub> into CO and O, which is the most important process in CO<sub>2</sub> splitting. When CH<sub>4</sub> is present, the O atoms will be further consumed by R2, R11, R20, R23 and R25 and this explains the higher CO<sub>2</sub> conversion when more CH<sub>4</sub> is present in the gas mixture. Indeed, as stated by the Le Chatelier's principle, the dissociation is more favorable as one (or both) of the reaction products is constantly consumed. This effect has been demonstrated in the literature: Tagawa et al. have observed an increasing CO<sub>2</sub> conversion by placing an O<sub>2</sub> trapper membrane into a CO<sub>2</sub>/CH<sub>4</sub> discharge in order to separate O<sub>2</sub> from the gas stream. As a consequence, the CO/CO<sub>2</sub> equilibrium is more shifted to CO [310].

### 2.1.4. Production of ethane

The recombination of two CH<sub>3</sub>· radicals can lead to the production of ethane according to reaction (R13). R14 and R15 could also lead to the production of ethane but are less probable. Indeed, as computed by Snoeckx et al. in the case of a similar atmospheric DBD source supplied in CH<sub>4</sub>-CO<sub>2</sub>, the density of CH<sub>3</sub> is always higher than the one of C<sub>2</sub>H<sub>5</sub> [152].

### 2.1.5. Production of ethylene

The formation of ethylene may result from a two-step collisional mechanism, where first an electron collision leads to the dissociation of C<sub>2</sub>H<sub>6</sub> into C<sub>2</sub>H<sub>5</sub>· and H radicals (R16), followed by a second electron collision with C<sub>2</sub>H<sub>5</sub>· resulting in the abstraction of a H radical to produce ethylene (R17). This simple mechanism can explain why  $f_{V,C_2H_4}$  is always lower than  $f_{V,C_2H_6}$ .

### 2.1.6. Other reaction products

Formaldehyde traces have also been detected. Their formation can result from CH<sub>3</sub> radicals (R25) or to a lower extent from CH<sub>2</sub> radicals (R26). Other oxygenated products have not been detected at the conditions under study, probably because their amounts are under the limit of detection of the gas chromatography detectors. According to the literature, the formation of other oxygenated organic molecules such as acetic acid or methanol may also occur in a plasma [48, 311, 312].

The higher volumetric fraction of H<sub>2</sub>, compared to ethane and ethylene, can be explained according to several chemical reactions (R2, R5, R6, R7, R8 and R9). Indeed, there are more reactions for H<sub>2</sub> and H· formation compared to reactions for C<sub>2</sub>H<sub>6</sub> and C<sub>2</sub>H<sub>4</sub> formation. Moreover, there are more reactions consuming C<sub>2</sub>H<sub>6</sub> or C<sub>2</sub>H<sub>4</sub> than consuming H<sub>2</sub>. C<sub>2</sub>H<sub>6</sub> or C<sub>2</sub>H<sub>4</sub> is indeed very easily consumed once it is produced. That is why the H<sub>2</sub> amount is always higher than the amounts of C<sub>2</sub>H<sub>6</sub> and C<sub>2</sub>H<sub>4</sub>.

## 2.2. Effect of the power

Figure 74 shows the CH<sub>4</sub> and CO<sub>2</sub> conversions versus the power applied to the DBD in the range between 30W and 80W for  $\Phi_{Ar} = 1680 \text{ mL}\cdot\text{min}^{-1}$ ,  $\Phi_{CO_2} = \Phi_{CH_4} = 120 \text{ mL}\cdot\text{min}^{-1}$  and an AC frequency of 19.5 kHz. The CO<sub>2</sub> conversion increases from 2.0% to 7.5% upon rising power, while the CH<sub>4</sub> conversion increases from 6.7% to 14.8% in the same power range. The two conversions can be considered as linearly increasing with the power since their correlation coefficients are  $r^2(\text{CO}_2)=0.976$  and  $r^2(\text{CH}_4)=0.899$ . The slopes of both curves are almost the same, consistently with the results of Zheng et al performed in a 2-electrode DBD reactor [313]. It is also clear that the methane conversion is always higher than  $\chi_{CO_2}$  (difference of at least 5%) thanks to its lower bond energy. The volumetric fractions of H<sub>2</sub>,

CO, C<sub>2</sub>H<sub>4</sub>, C<sub>2</sub>H<sub>6</sub> plotted in Figure 75 versus the power indicate that the production of syngas (hydrogen and carbon monoxide) also increases linearly with the power, and both products are formed nearly equally, yielding a syngas ratio close to 1. A linear increase is also observed in the case of C<sub>2</sub>H<sub>4</sub> and C<sub>2</sub>H<sub>6</sub>, although the slopes are less significant.

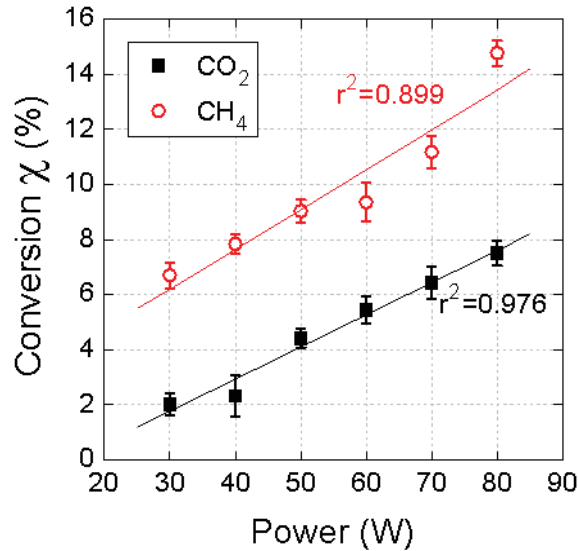


Figure 74 : Conversions of CO<sub>2</sub> and CH<sub>4</sub> versus the power ( $\Phi_{\text{Ar}} = 1680 \text{ mL}\cdot\text{min}^{-1}$ ;  $\Phi_{\text{CO}_2} = \Phi_{\text{CH}_4} = 120 \text{ mL}\cdot\text{min}^{-1}$ ;  $f = 19.5 \text{ kHz}$ ).

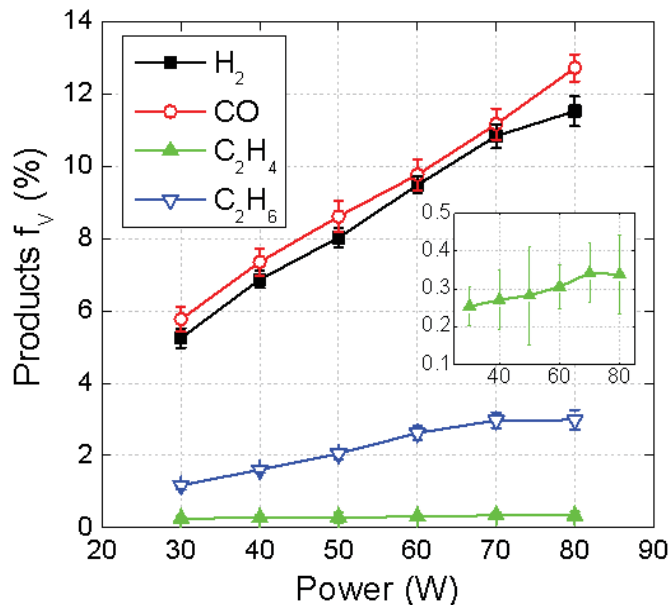


Figure 75 : Volumetric fractions of H<sub>2</sub>, CO, C<sub>2</sub>H<sub>4</sub> and C<sub>2</sub>H<sub>6</sub> (using the TCD) versus the power ( $\Phi_{\text{Ar}} = 1680 \text{ mL}\cdot\text{min}^{-1}$ ;  $\Phi_{\text{CO}_2} = \Phi_{\text{CH}_4} = 120 \text{ mL}\cdot\text{min}^{-1}$ ;  $f = 19.5 \text{ kHz}$ ).

The linear increase of the CO<sub>2</sub> and CH<sub>4</sub> conversions as a function of the power results from a linear increase in the electron density (Figure 74). Indeed, the dissociation of C-H and C=O bonds requires energies of a few eV that may be mostly transferred from the electrons. An increase in the plasma power can induce higher electron temperatures and higher electron densities. In our case, the increase in electron temperature may be assumed as negligible since in a classical DBD, it would induce a stronger filamentary regime that has not been observed here. Increasing the plasma power can also induce higher electron densities that can be assumed as linearly depending on the power if the electron permeability and the electric field profile are considered as weakly dependent on the applied power.

For the production of C<sub>2</sub>H<sub>4</sub> and C<sub>2</sub>H<sub>6</sub>, a linear increase upon increasing power is also observed, but the slopes are less pronounced than for CO and H<sub>2</sub>. This is probably due to the fact that the production of these molecules is not simply based on one electron impact reaction, like the formation of H<sub>2</sub> from CH<sub>4</sub> and the splitting of CO<sub>2</sub> into CO. Indeed, in order to obtain C<sub>2</sub>H<sub>6</sub>, two CH<sub>3</sub>· radicals are necessary (R13) while to obtain C<sub>2</sub>H<sub>4</sub>, two electronic collisions with C<sub>2</sub>H<sub>6</sub> are required (R16 and R17).

### 2.3. Effect of the carrier gas

The influence of the carrier gas (argon or helium) is investigated for the same flow rate set to 1800 mL.min<sup>-1</sup> and the reactive gas flow rates set to  $\Phi_{\text{CO}_2} = \Phi_{\text{CH}_4} = 60 \text{ mL.min}^{-1}$ . The nature of the carrier gas seems to have an important impact on the conversion of CO<sub>2</sub> and CH<sub>4</sub>; see Figure 76a. The conversion of CH<sub>4</sub> is indeed higher in the presence of helium than with argon (respectively 21.4% and 16.4%) while the opposite effect is observed for the conversion of CO<sub>2</sub> since  $\chi_{\text{CO}_2}=6.8\%$  with helium and  $\chi_{\text{CH}_4}=11.5\%$  with argon. It is also worth mentioning that for the same plasma power (60W) and frequency (17.1 kHz), a filamentary discharge and a glow discharge are obtained with argon and helium, respectively, as shown in Figure 76b and Figure 76c.

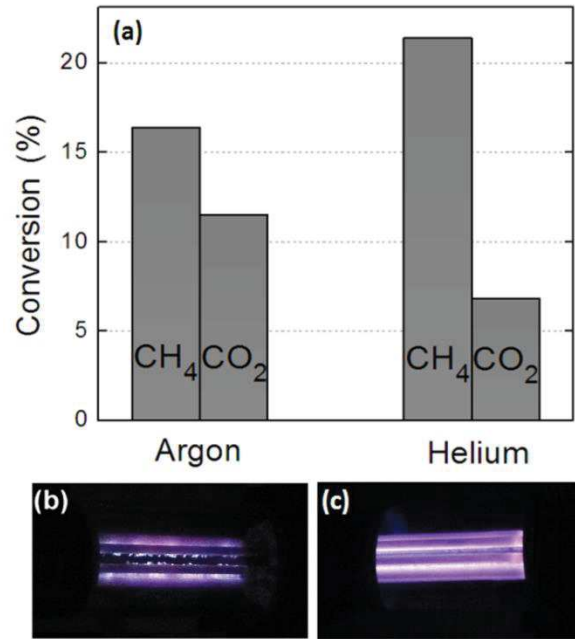


Figure 76 : (a) Conversions of CH<sub>4</sub> and CO<sub>2</sub> in Ar/CO<sub>2</sub>/CH<sub>4</sub> and He/CO<sub>2</sub>/CH<sub>4</sub> plasmas with  $\Phi_{\text{Tot}} = 1920 \text{ mL}\cdot\text{min}^{-1}$ ,  $\Phi_{\text{Ar}}$  or  $\Phi_{\text{He}} = 1800 \text{ mL}\cdot\text{min}^{-1}$ ,  $\Phi_{\text{CO}_2} = \Phi_{\text{CH}_4} = 60 \text{ mL}\cdot\text{min}^{-1}$ , plasma power = 60 W and  $f = 17.1 \text{ kHz}$ ; (b) Picture of the Ar/CO<sub>2</sub>/CH<sub>4</sub> discharge, illustrating the filamentary behavior; (c) Picture of the He/CO<sub>2</sub>/CH<sub>4</sub> discharge, illustrating the glow mode.

According to Figure 76,  $\chi_{\text{CH}_4}$  is always higher than  $\chi_{\text{CO}_2}$  whatever the nature of the carrier gas. Indeed, in a plasma, the dissociation of CH<sub>4</sub> is easier than for CO<sub>2</sub> since the bond dissociation energy of C-H (4.48 eV) is lower than the bond dissociation energy of C=O (5.52 eV) [314]. However, the fact that CH<sub>4</sub> is more efficiently dissociated in He than in Ar, whereas CO<sub>2</sub> is more efficiently dissociated in Ar than in He, is less straightforward. The reason is that the shape of the electron energy distribution function (EEDF) is different when the plasma is in the filamentary regime (Ar) or in the glow regime (He). The EEDF of these two regimes are sketched in Figure 77, based on data from the literature [241]. The bond dissociation energies of C-H and C=O are also reported in Figure 77. In the filamentary regime, the EEDF is characterized by (i) a number of warm electrons much lower than in a glow discharge but also by (ii) a tail extending towards higher energies, meaning that the hot electrons (even if not in a large number) can be involved into new collisional processes, which require a stronger activation energy [315]. In the case of the CH<sub>4</sub> dissociation, all the electrons that contribute to breaking of the C-H bonds, must be located at the right side of BDE(C-H) and under the EEDF curves: this corresponds to the area A<sub>1</sub> in the glow regime (He) and A<sub>3</sub> in the filamentary regime (Ar) (see insert in Figure 77). As A<sub>1</sub> is larger than A<sub>3</sub>, more electrons can participate to the dissociation of CH<sub>4</sub> in the case of He, hence this explains

why  $(\chi_{\text{CH}_4})_{\text{He}} > (\chi_{\text{CH}_4})_{\text{Ar}}$ . On the other hand, a higher electron energy is needed for breaking the C=O bonds of CO<sub>2</sub>: all electrons that contribute to this bond breaking, must be located at the right side of BDE(C=O), and under the EEDF curves: this corresponds to area A<sub>2</sub> in the glow regime (He) and to area A<sub>4</sub> in the filamentary regime (Ar). As A<sub>4</sub> is larger than A<sub>2</sub>, more electrons can participate to the dissociation of CO<sub>2</sub> in Ar than in He, and this explains why  $(\chi_{\text{CO}_2})_{\text{Ar}} > (\chi_{\text{CO}_2})_{\text{He}}$ . Finally, if we consider the areas which correspond to the electrons that can contribute to the dissociation of C-H and C=O bonds for both the glow and filamentary regimes, it appears that  $A_1 > A_3 > A_4 > A_2$ . Hence, this corresponds to  $(\chi_{\text{CH}_4})_{\text{He}} > (\chi_{\text{CH}_4})_{\text{Ar}} > (\chi_{\text{CO}_2})_{\text{Ar}} > (\chi_{\text{CO}_2})_{\text{He}}$ , which is indeed observed in Figure 76. In summary, the nature of the carrier gas – and consequently the regime (glow or filamentary) of the DBD – directly impacts the shape of the EEDF and therefore the electron collision processes that may occur.

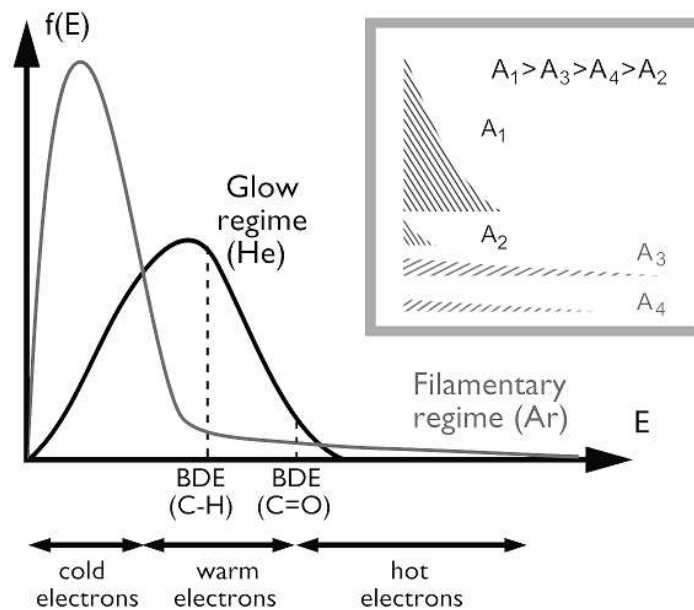


Figure 77 : Schematic sketch of the EEDFs in the case of a glow discharge (He) and a filamentary discharge (Ar) at thermodynamic equilibrium. Also indicated are the bond dissociation energies (BDE) for C-H and C=O bonds. The insert shows the fractions of electrons that can contribute to dissociation of C-H and C=O bonds in both regimes (see text for more explanation).

### 3. Conversion, specific energy input and energy efficiency: comparison with literature

The specific energy input (SEI) corresponds to the energy density ( $E_d$ ) in  $\text{J}\cdot\text{cm}^{-3}$ , and can also be expressed in  $\text{eV}\cdot\text{molecule}^{-1}$  as defined by the following equations:

$$E_d (\text{J}\cdot\text{cm}^{-3}) = \frac{\text{Power (J}\cdot\text{s}^{-1})}{\text{Gas flow rate (cm}^3\cdot\text{s}^{-1})} \quad \text{Eq. 6.3}$$

$$\begin{aligned} \text{SEI (eV}\cdot\text{molecule}^{-1}) \\ = \frac{E_d (\text{J}\cdot\text{cm}^{-3}) \times 6.24 \times 10^{18} (\text{eV}\cdot\text{J}^{-1}) \times 24500 (\text{cm}^3\cdot\text{mol}^{-1})}{6.022 \times 10^{23} (\text{molecule}\cdot\text{mol}^{-1})} \end{aligned} \quad \text{Eq. 6.4}$$

The energy efficiency of the CO<sub>2</sub> conversion ( $\eta_{\text{CO}_2}$ ) has been calculated (in %) from the conversion  $\chi_{\text{CO}_2}$ , the enthalpy of the dry reforming reaction ( $\text{CO}_2 + \text{CH}_4 \rightarrow 2\text{H}_2 + 2\text{CO}$ ) namely  $\Delta H_{298\text{K}}^0 = 247.3 \text{ kJ}\cdot\text{mol}^{-1} = 2.56 \text{ eV}\cdot\text{molecule}^{-1}$  and the SEI value, according to the following equation:

$$\eta_{\text{CO}_2} (\%) = \frac{\chi_{\text{CO}_2} (\%) \times \Delta H_{298\text{K}}^0 (\text{eV}\cdot\text{molecule}^{-1})}{\text{SEI (eV}\cdot\text{molecule}^{-1})} \quad \text{Eq. 6.5}$$

The same equation can be written for the energy efficiency of the CH<sub>4</sub> conversion ( $\eta_{\text{CH}_4}$ ). Hence, the energy efficiency is separately defined for CO<sub>2</sub> and CH<sub>4</sub> in this chapter.

Equation 6.5 indicates that an increase in the SEI systematically induces a decrease in  $\eta$ , at least when the conversion stays constant, and this means that we should have a SEI value as low as possible to obtain a more energy efficient process. This is indeed clear from Figure 78, where the energy efficiencies of both CH<sub>4</sub> and CO<sub>2</sub> clearly drop upon higher SEI. For a SEI as low as  $5.7 \text{ eV}\cdot\text{molecule}^{-1}$ ,  $\eta_{\text{CO}_2}^{\text{max}} = 3.3\%$  while  $\eta_{\text{CH}_4}^{\text{max}} = 4.9\%$ .

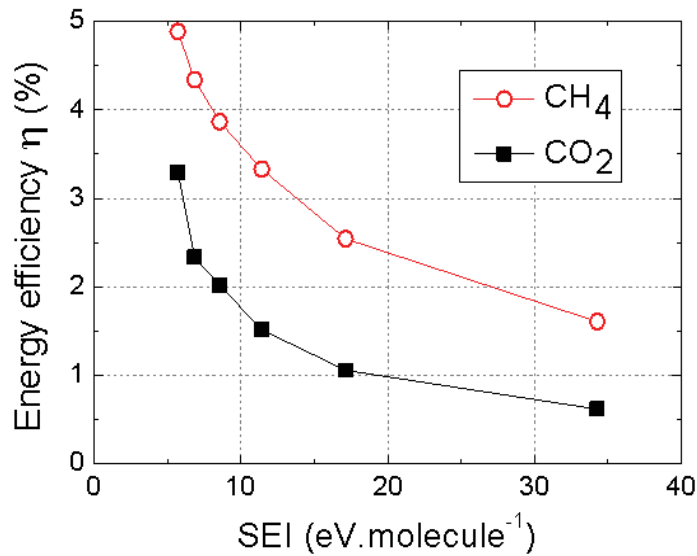


Figure 78 : Energy efficiency as a function of specific energy input in our experimental set-up with  $\Phi_{\text{Tot}} = 1920 \text{ mL}\cdot\text{min}^{-1}$ ,  $\Phi_{\text{Ar}} = 1800 \text{ mL}\cdot\text{min}^{-1}$ ,  $\Phi_{\text{CO}_2} + \Phi_{\text{CH}_4} = 120 \text{ mL}\cdot\text{min}^{-1}$ , plasma power = 45 W, frequency = 19.5 kHz.

A comparison of our multiple electrode DBD reactor with other atmospheric plasma sources is presented in Table 16. This table reports various plasma sources: DBD, AC glow discharges, pulsed corona and gliding arcs with different geometries and specific operating parameters, namely: frequency, plasma power, nature of the carrier gas or reactive gas, and CO<sub>2</sub> flow rate. Note that some of these experiments apply to pure CO<sub>2</sub> splitting, while others refer to dry reforming (i.e., conversion of both CO<sub>2</sub> and CH<sub>4</sub>). However, we focus here only on the CO<sub>2</sub> conversion. Also, it should be noted that some experiments were carried out for the pure greenhouse gases, while others made use of a carrier gas. The conversion and energy efficiency is in general higher in a carrier gas but it is obviously less interesting for applications. The optimal CO<sub>2</sub> conversions for all these cases are plotted in Figure 79 as a function of the corresponding SEI while their energy efficiencies are plotted in Figure 80 as a function of the CO<sub>2</sub> flow rates. In these figures, each squared number refers to one of the plasma sources listed in Table 16.

A first remark is that no atmospheric plasma source can reach a  $\chi_{\text{CO}_2}$  higher than 25%. Moreover, no general trend can be deduced: the cloud of points indicates that some plasma sources are very energy-consuming with high  $\chi_{\text{CO}_2}$  (#8, #14 and #15) while some others are much more dedicated to CO<sub>2</sub> reforming at a lower energy cost (#1, #4, #7, #17, #18 and #19) since they are located close to the vertical line at 2.56 eV/molecule, standing for the enthalpy

of reaction (2). The plasma source #7 shows a good energy efficiency, but is not suitable as it can handle CO<sub>2</sub> flow rates of only 0.8 mL.min<sup>-1</sup>. The plasma sources #17 and #19 present interesting conversions for SEI as low as ours, but with the disadvantage of their geometry, which is a pulsed corona and a gliding arc, respectively. Indeed, the advantage of using a tubular DBD lies in the ability to place it at the nozzle exit of a combustion process to treat the entire gas flow since all the gas passes through the discharge zone. On the contrary, a pulsed corona and a gliding arc can exhibit “dead volumes” where the gas passes through the reactor without being treated in the plasma zone. Furthermore, the corona source is not adapted for high flow rates treatment as its discharge volume is not that important, which makes it a good candidate only to handle low flow rates. The plasma source #4 is an interesting alternative to our plasma process. In our case, the CO<sub>2</sub> conversion is not so high but the SEI is quite low, so this yields a good energy efficiency, as shown in Figure 80 (#1). Our plasma source shows a good compromise between a high energy efficiency and the treatment of a significant CO<sub>2</sub> flow rate, probably thanks to the multielectrode configuration.

Table 16 : Comparison of various plasma sources dedicated to the conversion of CO<sub>2</sub> at atmospheric pressure. The CO<sub>2</sub> conversions vs SEI and the energy efficiency as a function of CO<sub>2</sub> flow rate for all these cases are reported in Figure 79 and Figure 80, respectively.

#	Plasma source		Frequency (kHz)	Power (W)	Carrier or reactive gas	CO <sub>2</sub> flow rate (mL.min <sup>-1</sup> )	Ref.
	Type	Geometry					
1	DBD	Tube multi-electrodes	19.5	45	Ar	120	Our reactor
2	DBD	Tube	30	100	/	50	[117]
3	DBD	Plane	30	500	CH <sub>4</sub>	500	[312]
4	DBD	Tube	2.2	45	Ar	80	[313]
5	DBD	Plane	25	15	He/CH <sub>4</sub>	5	[51]
6	DBD	Tube	25	100	CH <sub>4</sub>	60	[153]
7	DBD	Tube	8.1	0.11	/	0.8	[309]
8	DBD	Tube	20	74	CH <sub>4</sub>	15	[261]
9	AC glow discharge	Tube	8.1	2.78	He	2.5	[316]
10			8.1	3.64	Ar	2.5	
11			8.1	5.25	N <sub>2</sub>	2.5	
12			8.1	2.78	He	1.5	
13			8.1	3.64	Ar	1.5	
14			8.1	5.25	N <sub>2</sub>	1.5	
15			8.1	3.64	Ar	0.75	
16			8.1	5.25	N <sub>2</sub>	0.75	
17	Pulsed corona	Electrode tip	20-200	9	/	47.5	[317]
18	DBD	Tube	30	60	Ar/CH <sub>4</sub>	60	[318]
19	Gliding arc	“V” shaped electrode	20	225	/	2000	[136]

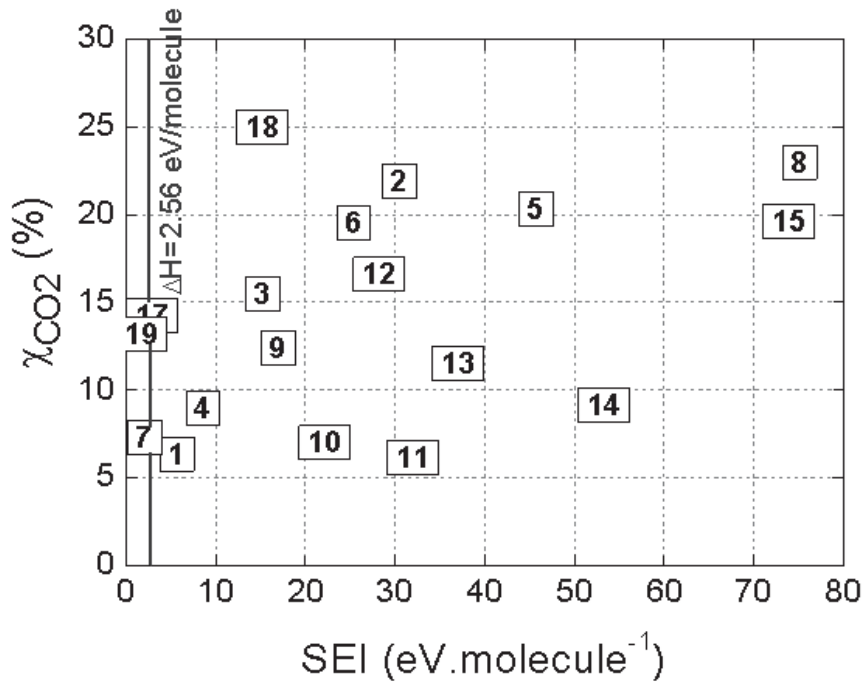


Figure 79 : CO<sub>2</sub> conversions vs SEI for the various plasma sources listed in Table 16.

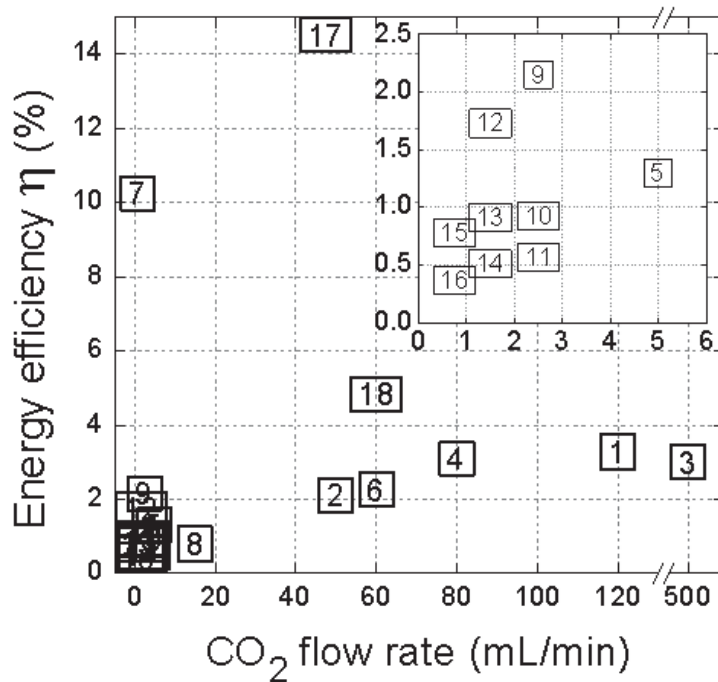


Figure 80 : Energy efficiency (%) of the various atmospheric plasma sources listed in Table 16, as a function of the CO<sub>2</sub> flow rates. The area in the left bottom is enlarged as an insert, placed in the right top of the figure.

## 4. Conclusion

The production of syngas (CO and H<sub>2</sub>), C<sub>2</sub>H<sub>4</sub> and C<sub>2</sub>H<sub>6</sub> has been achieved at atmospheric pressure in a dielectric barrier discharge operating in CO<sub>2</sub> and CH<sub>4</sub>, with Ar or He as carrier gases. The main mechanisms responsible for the production of these compounds have been discussed. In this study, the effect of the concentration of CO<sub>2</sub>/CH<sub>4</sub> in the mixture on the conversion has been demonstrated.

Furthermore, the effect of power has also been reported, showing a linear increase in the CO<sub>2</sub> and CH<sub>4</sub> conversions but also in the production of syngas as a function of the applied power.

Finally, the energy efficiency of the CO<sub>2</sub> conversion has been calculated and compared with those of other atmospheric plasma sources. Our DBD reactor offers very encouraging results as it offers one of the best compromises between a high energy efficiency and the treatment of a large CO<sub>2</sub> flow rate.

# **Chapter VII - Conclusions and perspectives**

## 1. Conclusions

The increasing interest on the conversion of CO<sub>2</sub> by means of plasma technology has clearly been pointed in the literature in recent decades. Indeed, the utilization of this waste (CO<sub>2</sub>) and converting it into a new feedstock (raw materials for the chemical industry and fuels) fulfills sustainable/green chemistry and “cradle-to-cradle” concept. Therefore, the plasma scientific community is nowadays trying to carry out systematic studies, by means of both experiments and theoretical simulations, in order to improve the knowledge and also the performance concerning the CO<sub>2</sub> splitting and see how to maximize the efficiency of this process. The CO<sub>2</sub> splitting reaction is highly endothermic, so the energy efficiency of the process is a critical issue. Systematic investigations for the optimum operating conditions are highly needed in order to use plasma technology for practical applications.

In this PhD project, the CO<sub>2</sub> splitting towards O<sub>2</sub> and CO was investigated in a flowing cylindrical dielectric barrier discharge (DBD) operating at atmospheric pressure. Several experimental diagnostics, like MS/GC, OES and an oscilloscope, were used. MS/GC permits to determine the conversions and the yields of various products. OES allows us to determine some specific species present in the plasma and the gas temperature  $T_{\text{gas}}$  (by assuming that  $T_{\text{gas}} \approx T_{\text{rot}}$ ). Moreover, analysis by an oscilloscope was carried out to make a detailed electrical characterization and to determine the power absorbed by the plasma. The work was divided in three parts. The first one was dedicated to a pure CO<sub>2</sub> plasma, whereas the second and the third were dedicated to a CO<sub>2</sub> discharge with H<sub>2</sub>O or CH<sub>4</sub> addition, respectively. All three chapters have their own conclusion but we make a general conclusion in this section again.

In *Chapter IV*, the pure CO<sub>2</sub> splitting process was discussed in detail. Experiments were carried out through studying the basic plasma parameters, i.e. varying the gas flow rate, applied frequency, power, pulsation of the high AC voltage, dielectric thickness and dielectric material, focusing on the CO<sub>2</sub> conversion and energy efficiency. The aim of this part was to have a better insight of the physical parameters of the discharge by looking for the key parameters in a systematic way for an efficient decomposition of CO<sub>2</sub>. In literature, not many electrical studies of a DBD operating in filamentary regime are found, especially on the topic of CO<sub>2</sub> plasma treatment. Therefore, we built a new methodology/approach for characterizing electrically the discharge in detail. The CO<sub>2</sub> discharge operates in filamentary mode and we were able to show that such in-depth study was quite valuable for understanding the link between electrical parameters and the conversion trends. We were also able to figure out a

reach of the steady state regime in a DBD after a certain amount of time of plasma ignition (evidenced by OES and oscilloscope). Indeed, this transition is often neglected by the plasma community.

The combined CO<sub>2</sub>-H<sub>2</sub>O discharge was investigated in *Chapter V*. The fact to add a source of hydrogen into CO<sub>2</sub> discharge is a very interesting idea from the point of view of targeting value-added products, here for instance syngas (CO + H<sub>2</sub>). Literature dealing with such mixture of plasma is very limited, especially in the understanding of the chemistry related to CO<sub>2</sub>-H<sub>2</sub>O plasmas. We showed that it is possible to target syngas but also hydrogen peroxide. Moreover, our experimental data were compared by computer simulations performed by Snoeckx, in order to elucidate the underlying mechanisms of the CO<sub>2</sub> splitting process in the presence of water. The model gave conversions and product formations quite close to the experimental results (the trends in conversion and selectivity are very similar). Throughout this study, we clearly identified the influence of the water content and the SEI on the conversion and product formation.

Finally, the CO<sub>2</sub> discharge in the presence of CH<sub>4</sub> was investigated in *Chapter VI*. In this case, in addition to syngas, other value-added target molecules were formed such as ethane, ethylene, acetylene and formaldehyde. CO<sub>2</sub> and CH<sub>4</sub> conversion as well as the selectivities of different products were discussed. The influence of the plasmagen gas was also investigated. Argon, giving place to more filamentary discharges, leads to a better CO<sub>2</sub> conversion compared to discharges containing helium. On the other hand, the latter leads to more glow (homogeneous) discharges where the CH<sub>4</sub> conversion becomes higher compared to the discharges containing argon.

Overall, throughout all these studies, we can figure out the most important parameters dictating the CO<sub>2</sub> splitting process. In a CO<sub>2</sub> discharge, the main products are CO and O<sub>2</sub> and they are formed mainly from electron impact dissociation. This is also evidenced by simulations. Therefore, the amount of electrons and their energy play a crucial role on the dissociation process. The electrons do not have a fixed energy but their energy is expressed in terms of a distribution. Therefore, in collisions involving electron impact processes, the reaction rate coefficients are described by means of the electron energy distribution function (EEDF). Experimentally, it is very difficult to determine this distribution accurately. However, it is known that the shape of the distribution depends on parameters like the electron density  $n_e$  and electron temperature  $T_e$ , which is, on its own, dependent on the

electric field in the gap. This field results from the voltage applied over the plasma. In a filamentary mode such as in a CO<sub>2</sub> discharge, the plasma voltage is considered as an effective voltage, since the filamentary mode is responsible for an inhomogeneous electric field in the whole electrode-barrier gap, which is different from the case of a diffuse and homogeneous glow discharge. Therefore, the plasma voltage is considered as an average value. As a result, by increasing the plasma voltage, the reduced electric field  $E/n$  will rise, and this will affect the EEDF, which will in turn affect the electron impact reaction rates, and thus the CO<sub>2</sub> conversion. A higher plasma voltage leads to more accelerated electrons, and can thus enhance the rates of electron impact excitation, ionization and dissociation of CO<sub>2</sub> and improve the conversion and energy efficiency of the CO<sub>2</sub> splitting process. The other critical parameter for the efficiency of the process is the electron density  $n_e$ . Via our electrical characterization, we showed how to determine the charge accumulation in the plasma zone. The plasma charge  $Q_{pl}$ , being related to the plasma current  $i_{pl}$ , gives an idea about the order of magnitude of the electron density and how it varies. Note that the total number of electrons is not the most important parameter for an efficient process, but the number of electrons which have enough energy to split CO<sub>2</sub> (depending on the shape of the EEDF and thus, defining the energy efficiency of the splitting process as already mentioned). These two are the main electrical parameters which dictate the efficiency of CO<sub>2</sub> conversion, apart of the residence time, which is of course also crucial. The higher the residence time, the more CO<sub>2</sub> will spend time in the discharge zone and can be treated. Indeed if the gas remains in the discharge longer, the probability that the gas interacts with microdischarges becomes more important and this enhances the treatment of CO<sub>2</sub>.

Besides, other minor parameters are also noteworthy for the efficiency of the process. Among them, we can quote the number of microdischarges  $N_{md}$  (present throughout the discharge zone) which occurs for a certain given residence time. The repartition and the number of microdischarges are of course important since the flowing CO<sub>2</sub> passes through the plasma by interacting with these microdischarges. In fact, these microdischarges are the real source of reactivity in the plasma, where quasi all the initiation of chemical reactions (excitation, dissociation, ionization) occurs. This is also the reason why in computer models electric pulses (representing microdischarges) are simulated. If there is a better repartition of the microdischarge (higher  $N_{md}$ ), the CO<sub>2</sub> gas flowing through the reactor will have a larger chance to pass through and interact with at least one microdischarge, leading to a higher conversion.

We also show that there are also other fundamental parameters that contribute to a non-efficient CO<sub>2</sub> dissociation, like the temperature. Indeed, a high gas or wall reactor temperature leads to a loss of energy. Instead of contributing to the splitting, the power is spent more for heating the gas or the walls, so that a lower fraction can be dedicated to the CO<sub>2</sub> dissociation.

From all these correlations, the trends in CO<sub>2</sub> conversion (and energy efficiency) can clearly be explained. The effect of all the physical aspects is studied in the three chapters (*Chapters IV-VI*) but in addition, a chemical aspect is also studied in the last two chapters (CO<sub>2</sub>-H<sub>2</sub>O and CO<sub>2</sub>-CH<sub>4</sub> discharges). In good conditions, CO<sub>2</sub> conversion values as high as 20% were reached. The conversion has to be related to the energy efficiency of the process as it is the combination of these two which is important to describe a chemical process. In terms of energy efficiency of the CO<sub>2</sub> dissociation process, we can say that the values obtained during this PhD are quite good, when comparing to the literature dealing with CO<sub>2</sub> splitting in DBD at atmospheric pressure. In good conditions, values as high as 15% (in energy efficiency) could be obtained whereas the average values found in literature were generally close to 10%.

## 2. Perspectives and future works

As mentioned before, the efficiency of the CO<sub>2</sub> dissociation process can be improved when using a packed-bed DBD configuration (i.e., when the gap between the two electrodes is packed with dielectric pellets or full/porous beads). This typically yields a higher conversion and energy efficiency. These improvements are attributed to the polarization of the dielectric beads, enhancing the local electric field, particularly at the contact points between the beads. In this sense, the material of the dielectric barrier is also of great importance, as highlighted in one of our studies. This configuration becomes even more interesting when a catalyst is added into the discharge or in the post-discharge, in order to target some specific molecules. In such a case, it could allow the selective production of value-added chemicals but also improve the energy efficiency of CO<sub>2</sub> splitting. Meanwhile, the chemistry and physics in such a DBD system is not very well known. It would be of great interest to apply the new methodology of electrical characterization for a CO<sub>2</sub> discharge presented in this work, to a packed-bed DBD, in the absence and presence of catalysts. This would lead to a better insight of the consequences of all the microdischarges spread out in the packed-bed DBD reactor, and hence of the role on the conversion and efficiency of the CO<sub>2</sub> splitting process. When the catalyst

added in the discharge would be metallic, i.e. conducting, it would affect the electrical behavior of the discharge. Indeed, the combination of conducting material (catalysts) and insulator material (dielectric beads and dielectric barrier) could be very interesting to study. This work would not only be interesting for a pure CO<sub>2</sub> discharge, but also for combined CO<sub>2</sub>/CH<sub>4</sub> or CO<sub>2</sub>/H<sub>2</sub>O discharges. By adding catalysts made of various metals in the discharge, different extra studies would thus be necessary, such as catalyst characterization by XPS, EDX, BET. Plasma catalysis is a new field, which requires a lot of scientific research in order to better understand the mechanisms of the interactions between the plasma and the catalysts, and particularly the synergistic effect between plasma and catalyst surface.

Finally, in order to complete the electrical characterization and the study of the physical aspects of the plasma, information concerning the electron density and the energy of the electrons (i.e. the EEDF) should be obtained in the near future, for instance via further simulations and a Langmuir probe.

## List of publications and conference contributions

### 1. Publications related to this PhD dissertation

- A. Ozkan, T. Dufour, T. Silva, N. Britun, R. Snyders, F. Reniers and A. Bogaerts, DBD in burst mode: solution for more efficient CO<sub>2</sub> conversion?, *Plasma Sources Science and Technology*, 25 (2016) 055005  
DOI: 10.1088/0963-0252/25/5/055005
- A. Ozkan, T. Dufour, A. Bogaerts and F. Reniers, How do the barrier thickness and dielectric material influence the filamentary mode and CO<sub>2</sub> conversion in a flowing DBD?, *Plasma Sources Science and Technology*, 25(4) (2016) 045016  
DOI: 10.1088/0963-0252/25/4/045016
- A. Ozkan, T. Dufour, T. Silva, N. Britun, R. Snyders, A. Bogaerts and F. Reniers, The influence of power and frequency on the filamentary behavior of a flowing DBD—application to the splitting of CO<sub>2</sub>, *Plasma Sources Science and Technology*, 25(2) (2016) 025013  
DOI: 10.1088/0963-0252/25/2/025013
- A. Ozkan, T. Dufour, G. Arnoult, P. De Keyzer, A. Bogaerts and F. Reniers, CO<sub>2</sub>–CH<sub>4</sub> conversion and syngas formation at atmospheric pressure using a multi-electrode dielectric barrier discharge, *Journal of CO<sub>2</sub> utilization*, 9 (2015) 74-81  
DOI: 10.1016/j.jcou.2015.01.002
- R. Snoeckx, A. Ozkan, F. Reniers and A. Bogaerts, The quest for value-added products from CO<sub>2</sub> and H<sub>2</sub>O in a dielectric barrier discharge: a chemical kinetics study, *accepted in ChemSusChem*, (2016)

### 2. Publications not related to this PhD dissertation

- J. Hubert, C. Poleunis, A. Delcorte, P. Laha, J. Bossert, S. Lambeets, A. Ozkan, P. Bertrand, H. Terryn and F. Reniers, Plasma polymerization of C<sub>4</sub>Cl<sub>6</sub> and C<sub>2</sub>H<sub>2</sub>Cl<sub>4</sub> at atmospheric pressure, *Polymer* 54 (2013) 4085-4092  
DOI: 10.1016/j.polymer.2013.05.068

### 3. Conference contributions

- Ozkan, T. Dufour, T. Silva, N. Britun, R. Snyders, A. Bogaerts and F. Reniers, "The influence of power and frequency on the filamentary behavior of a flowing DBD – Application to the splitting of CO<sub>2</sub>", Poster presentation on "SRC 2015 Société Royale de Chimie", ULB, Brussels, BE, 10 October 2015
- R. Snoeckx, A. Ozkan, R. Aerts, T. Dufour, F. Reniers and A. Bogaerts, "A combined study for turning CO<sub>2</sub> and H<sub>2</sub>O into value-added products in a dielectric barrier discharge", Passive contribution - poster on "22<sup>nd</sup> International Symposium on Plasma Chemistry", UAntwerpen, Antwerpen, BE, 06-10 July 2015
- Ozkan, T. Dufour, T. Silva, N. Britun, R. Snyders, A. Bogaerts and F. Reniers, "CO<sub>2</sub> splitting by DBD: understanding the influence of electrical parameters and regimes", Poster presentation on "22<sup>nd</sup> International Symposium on Plasma Chemistry", UAntwerpen, Antwerpen, BE, 06-10 July 2015
- Ozkan, T. Dufour, R. Snoeckx, A. Bogaerts and F. Reniers, "Study of the reactivity of atmospheric pressure CO<sub>2</sub>/H<sub>2</sub>O plasmas", Poster presentation on "Plasma Workshop IAP - Plasma diagnostics & Glow discharge", Reims, FR, 10-12 June 2014
- Ozkan, R. Snoeckx, A. Bogaerts and F. Reniers, "Study of the reactivity of atmospheric pressure CO<sub>2</sub>/H<sub>2</sub>O plasmas", Poster presentation on "Solvay Workshop - Plasmas for Environmental Applications", ULB, Brussels, BE, 31 March - 02 April 2014
- Ozkan, R. Snoeckx, G. Arnoult, T. Bieber, P. De Keyzer, A. Bogaerts and F. Reniers, "Study of the reactivity of atmospheric pressure CO<sub>2</sub>/H<sub>2</sub>O plasmas", Poster presentation on "Fundamentals of plasma-surface interactions Congress", UAntwerpen, Antwerpen, BE, 31 November 2013
- Ozkan, G. Arnoult, T. Bieber, P. De Keyser and F. Reniers, "Synthesis of small organic molecules from a CO<sub>2</sub>/CH<sub>4</sub> mixture by dielectric barrier discharge (DBD): gas composition and power effect", Passive contribution - poster on "AVS 60th International Symposium & Exhibition", Long Beach California, US, October 2013
- Ozkan, G. Arnoult, T. Bieber, P. De Keyser and F. Reniers, "Conversion du CO<sub>2</sub> par décharge à barrière diélectrique à pression atmosphérique : Effet de la composition du gaz, de la puissance et de la nature du gaz plasmagène", Poster presentation on "SRC 2013 Société Royale de Chimie", UMons, Mons, BE, 10 October 2013

- Ozkan, G. Arnoult, P. De Keyzer and F. Reniers, "Conversion of CO<sub>2</sub> and CH<sub>4</sub> mixtures using a dielectric barrier discharge: gas composition and power effect", Poster presentation on "19<sup>th</sup> International Vacuum Congress - IVC-19 ", Paris, FR, 9-13 September 2013

## Bibliography

- [1] M. Meinshausen, S.J. Smith, K. Calvin, J.S. Daniel, M. Kainuma, J. Lamarque, K. Matsumoto, S. Montzka, S. Raper and K. Riahi, The RCP greenhouse gas concentrations and their extensions from 1765 to 2300, *Climatic change*, **109**(1-2) (2011) 213-241
- [2] A. Zecchina, Energy sources and carbon dioxide waste, *Rendiconti Lincei*, **25**(1) (2014) 113-117
- [3] J.H. Seinfeld and S.N. Pandis, *Atmospheric chemistry and physics: from air pollution to climate change*: (John Wiley & Sons; 2012).
- [4] S. Solomon, G.-K. Plattner, R. Knutti and P. Friedlingstein, Irreversible climate change due to carbon dioxide emissions, *Proceedings of the national academy of sciences*, **106**(6) (2009) 1704-1709
- [5] G.A. Schmidt, R.A. Ruedy, R.L. Miller and A.A. Lacis, Attribution of the present-day total greenhouse effect, *Journal of Geophysical Research: Atmospheres (1984–2012)*, **115**(D20) (2010)
- [6] P.W. Atkins and R.S. Friedman, *Molecular quantum mechanics*: (Oxford university press; 2011).
- [7] Y. Itikawa, Cross sections for electron collisions with carbon dioxide, *Journal of Physical and Chemical Reference Data*, **31**(3) (2002) 749-768
- [8] H. Fischer, J. Schmitt, S. Eggleston, R. Schneider, J. Elsig, F. Joos, M. Leuenberger, T. Stocker, P. Köhler and V. Brovkin, ice core-based isotopic constraints on past carbon cycle changes, *PAGES Magazine*, **23**(1) (2015) 12-13
- [9] K.R. Gurney, D.L. Mendoza, Y. Zhou, M.L. Fischer, C.C. Miller, S. Geethakumar and S. de la Rue du Can, High resolution fossil fuel combustion CO<sub>2</sub> emission fluxes for the United States, *Environmental Science & Technology*, **43**(14) (2009) 5535-5541
- [10] M.R. Allen, D.J. Frame, C. Huntingford, C.D. Jones, J.A. Lowe, M. Meinshausen and N. Meinshausen, Warming caused by cumulative carbon emissions towards the trillionth tonne, *Nature*, **458**(7242) (2009) 1163-1166
- [11] D.P. Van Vuuren, J. Edmonds, M. Kainuma, K. Riahi, A. Thomson, K. Hibbard, G.C. Hurtt, T. Kram, V. Krey and J.-F. Lamarque, The representative concentration pathways: an overview, *Climatic change*, **109** (2011) 5-31
- [12] M. Aresta, *Carbon dioxide as chemical feedstock*: (John Wiley & Sons; 2010).
- [13] R.A. Feely, S.C. Doney and S.R. Cooley, Ocean acidification: present conditions and future changes in a high-CO<sub>2</sub> world, *Oceanography* **22**(4) (2009) 36-47
- [14] N.L. Bindoff, J. Willebrand, V. Artale, A. Cazenave, J.M. Gregory, S. Gulev, K. Hanawa, C. Le Quéré, S. Levitus, Y. Nojiri, C. Shum, L. Talley and A. Unnikrishnan, *Observations: oceanic climate change and sea level*: (Cambridge University Press; 2007).
- [15] S. Rahmstorf, A semi-empirical approach to projecting future sea-level rise, *Science*, **315**(5810) (2007) 368-370
- [16] P. Jones, K. Trenberth, P. Ambenje, R. Bojariu, D. Easterling, T. Klein, D. Parker, J. Renwick, M. Rusticucci and B. Soden, Observations: surface and atmospheric climate change, *In Climate Change 2007: The Physical Science Basis Contribution of Working Group I to the Fourth Assessment Report of the Intergovernmental Panel on Climate Change*, (2007) 235-336
- [17] A. Grinsted, J.C. Moore and S. Jevrejeva, Reconstructing sea level from paleo and projected temperatures 200 to 2100 AD, *Climate Dynamics*, **34**(4) (2010) 461-472

- [18] J.A. Church and N.J. White, A 20th century acceleration in global sea-level rise, *Geophysical research letters*, **33**(1) (2006)
- [19] J.G. Canadell, C. Le Quéré, M.R. Raupach, C.B. Field, E.T. Buitenhuis, P. Ciais, T.J. Conway, N.P. Gillett, R. Houghton and G. Marland, Contributions to accelerating atmospheric CO<sub>2</sub> growth from economic activity, carbon intensity, and efficiency of natural sinks, *Proceedings of the national academy of sciences*, **104**(47) (2007) 18866-18870
- [20] J.T. Houghton, G.J. Jenkins and J. Ephraums, Climate change: the IPCC scientific assessment, *American Scientist;(United States)*, **80**(6) (1990)
- [21] S. Solomon, D. Qin, M. Manning, M. Marquis, K. Averyt, M. Tignor, H. Miller and Z. Chen. Climate change. The physical science basis: working group 1 to the Fourth Assessment Report of the Intergovernmental Panel on Climate Change. Cambridge University Press, Cambridge; 2007.
- [22] J. Gibbins and H. Chalmers, Carbon capture and storage, *Energy Policy*, **36**(12) (2008) 4317-4322
- [23] D.C. Thomas and S.M. Benson, *Carbon Dioxide Capture for Storage in Deep Geologic Formations-Results from the CO<sub>2</sub> Capture Project: Vol 2-Geologic Storage of Carbon Dioxide with Monitoring and Verification*: (Elsevier; 2015).
- [24] R.S. Haszeldine, Carbon capture and storage: how green can black be?, *Science*, **325**(5948) (2009) 1647-1652
- [25] P. Feron and C. Hendriks, CO<sub>2</sub> capture process principles and costs, *Oil & Gas Science And Technology*, **60**(3) (2005) 451-459
- [26] W. McDonough and M. Braungart, *Cradle to cradle: Remaking the way we make things*: (MacMillan; 2010).
- [27] J. Christophe, T. Doneux and C. Buess-Herman, Electroreduction of carbon dioxide on copper-based electrodes: activity of copper single crystals and copper–gold alloys, *Electrocatalysis*, **3**(2) (2012) 139-146
- [28] T. Sakakura, J.-C. Choi and H. Yasuda, Transformation of carbon dioxide, *Chemical Reviews*, **107**(6) (2007) 2365-2387
- [29] J.H. Jones, The Cativa™ process for the manufacture of acetic acid, *Platinum Metals Review*, **44**(3) (2000) 94-105
- [30] G.J. Sunley and D.J. Watson, High productivity methanol carbonylation catalysis using iridium: The Cativa™ process for the manufacture of acetic acid, *Catalysis Today*, **58**(4) (2000) 293-307
- [31] M.E. Dry, The Fischer–Tropsch process: 1950–2000, *Catalysis today*, **71**(3) (2002) 227-241
- [32] J.M. Thomas and W.J. Thomas, *Principles and practice of heterogeneous catalysis*: (John Wiley & Sons; 2014).
- [33] J. Amouroux, S. Cavadias and A. Doubla, editors. Carbon Dioxide reduction by non-equilibrium electrocatalysis plasma reactor. IOP Conference Series: Materials Science and Engineering; 2011: IOP Publishing.
- [34] L.F. Spencer and A.D. Gallimore, Efficiency of CO<sub>2</sub> dissociation in a radio-frequency discharge, *Plasma Chemistry and Plasma Processing*, **31**(1) (2011) 79-89
- [35] M.S. Fan, A.Z. Abdullah and S. Bhatia, Catalytic technology for carbon dioxide reforming of methane to synthesis gas, *ChemCatChem*, **1**(2) (2009) 192-208
- [36] M. Scapinello, L.M. Martini and P. Tosi, CO<sub>2</sub> Hydrogenation by CH<sub>4</sub> in a Dielectric Barrier Discharge: Catalytic Effects of Nickel and Copper, *Plasma Processes and Polymers*, **11**(7) (2014) 624-628

- [37] X. Tu, H.J. Gallon, M.V. Twigg, P.A. Gorry and J.C. Whitehead, Dry reforming of methane over a Ni/Al<sub>2</sub>O<sub>3</sub> catalyst in a coaxial dielectric barrier discharge reactor, *Journal of Physics D: Applied Physics*, **44**(27) (2011) 274007
- [38] X. Tu and J. Whitehead, Plasma-catalytic dry reforming of methane in an atmospheric dielectric barrier discharge: Understanding the synergistic effect at low temperature, *Applied Catalysis B: Environmental*, **125** (2012) 439-448
- [39] A. Goeppert, M. Czaun, J.-P. Jones, G.S. Prakash and G.A. Olah, Recycling of carbon dioxide to methanol and derived products—closing the loop, *Chemical Society Reviews*, **43**(23) (2014) 7995-8048
- [40] M. Aresta, A. Dibenedetto and A. Angelini, Catalysis for the valorization of exhaust carbon: From CO<sub>2</sub> to chemicals, materials, and fuels. Technological use of CO<sub>2</sub>, *Chemical reviews*, **114**(3) (2013) 1709-1742
- [41] E. Linley, S.P. Denyer, G. McDonnell, C. Simons and J.-Y. Maillard, Use of hydrogen peroxide as a biocide: new consideration of its mechanisms of biocidal action, *Journal of antimicrobial chemotherapy*, **67**(7) (2012) 1589-1596
- [42] G.E. McDonnell, *Antisepsis, disinfection, and sterilization: (American Society of Microbiology; 2007).*
- [43] M. Finnegan, E. Linley, S.P. Denyer, G. McDonnell, C. Simons and J.-Y. Maillard, Mode of action of hydrogen peroxide and other oxidizing agents: differences between liquid and gas forms, *Journal of Antimicrobial Chemotherapy*, (2010) dkq308
- [44] G. Centi, E.A. Quadrelli and S. Perathoner, Catalysis for CO<sub>2</sub> conversion: a key technology for rapid introduction of renewable energy in the value chain of chemical industries, *Energy & Environmental Science*, **6**(6) (2013) 1711-1731
- [45] P.L. Spath and D.C. Dayton, Preliminary screening-technical and economic assessment of synthesis gas to fuels and chemicals with emphasis on the potential for biomass-derived syngas, (2003)
- [46] M.K. Nikoo and N. Amin, Thermodynamic analysis of carbon dioxide reforming of methane in view of solid carbon formation, *Fuel Processing Technology*, **92**(3) (2011) 678-691
- [47] Y. Li, Y. Wang, X. Zhang and Z. Mi, Thermodynamic analysis of autothermal steam and CO<sub>2</sub> reforming of methane, *International Journal of Hydrogen Energy*, **33**(10) (2008) 2507-2514
- [48] L. Zhou, B. Xue, U. Kogelschatz and B. Eliasson, Nonequilibrium plasma reforming of greenhouse gases to synthesis gas, *Energy & fuels*, **12**(6) (1998) 1191-1199
- [49] J. Zhu, D. Zhang and K. King, Reforming of CH<sub>4</sub> by partial oxidation: thermodynamic and kinetic analyses, *Fuel*, **80**(7) (2001) 899-905
- [50] J. Luque, M. Kraus, A. Wokaun, K. Haffner, U. Kogelschatz and B. Eliasson, Gas temperature measurement in CH<sub>4</sub>/CO<sub>2</sub> dielectric-barrier discharges by optical emission spectroscopy, *Journal of applied physics*, **93**(8) (2003) 4432-4438
- [51] Y. Li, G.-h. Xu, C.-j. Liu, B. Eliasson and B.-z. Xue, Co-generation of syngas and higher hydrocarbons from CO<sub>2</sub> and CH<sub>4</sub> using dielectric-barrier discharge: effect of electrode materials, *Energy & fuels*, **15**(2) (2001) 299-302
- [52] M.M. Halman, *Chemical Fixation of Carbon Dioxide Methods for Recycling CO<sub>2</sub> into Useful Products: (CRC press; 1993).*
- [53] Q. Song, R. Xiao, Y. Li and L. Shen, Catalytic carbon dioxide reforming of methane to synthesis gas over activated carbon catalyst, *Industrial & Engineering Chemistry Research*, **47**(13) (2008) 4349-4357
- [54] G. Zhang, L. Hao, Y. Jia and Y. Zhang, CO<sub>2</sub> reforming of CH<sub>4</sub> over efficient bimetallic Co-Zr/AC catalyst for H<sub>2</sub> production, *International Journal of Hydrogen Energy*, **40**(37) (2015) 12868-12879

- [55] G. Zhang, Y. Du, Y. Xu and Y. Zhang, Effects of preparation methods on the properties of cobalt/carbon catalyst for methane reforming with carbon dioxide to syngas, *Journal of Industrial and Engineering Chemistry*, **20**(4) (2014) 1677-1683
- [56] G. Zhang, J. Qu, A. Su, Y. Zhang and Y. Xu, Towards understanding the carbon catalyzed CO<sub>2</sub> reforming of methane to syngas, *Journal of Industrial and Engineering Chemistry*, **21** (2015) 311-317
- [57] G. Zhang, A. Su, Y. Du, J. Qu and Y. Xu, Catalytic performance of activated carbon supported cobalt catalyst for CO<sub>2</sub> reforming of CH<sub>4</sub>, *Journal of colloid and interface science*, **433** (2014) 149-155
- [58] S. Wang and G. Lu, Thermogravimetric Analysis of Carbon Deposition over Ni/ $\gamma$ -Al<sub>2</sub>O<sub>3</sub> Catalysts in Carbon Dioxide Reforming of Methane, *Energy & fuels*, **12**(6) (1998) 1235-1240
- [59] K. Tomishige, Y.-g. Chen and K. Fujimoto, Studies on carbon deposition in CO<sub>2</sub> reforming of CH<sub>4</sub> over nickel–magnesia solid solution catalysts, *Journal of Catalysis*, **181**(1) (1999) 91-103
- [60] K. Denbigh, The principles of chemical equilibrium, *Cambridge University Press, Cambridge*, (1966) 287
- [61] J. Rowlinson. The Principles of Chemical Equilibrium.: Kenneth Denbigh: 3rd Edn. University Press, Cambridge, 1971. 494 pp.,£ 4.40 (cloth);£ 1.50 (paper). Pergamon; 1972.
- [62] M.A. Lieberman and A.J. Lichtenberg, *Principles of plasma discharges and materials processing*: (John Wiley & Sons, Inc. Publication; 1994).
- [63] H.V. Boenig, *Fundamentals of plasma chemistry and technology*: (CRC; 1988).
- [64] A. Fridman, *Plasma chemistry*: (Cambridge university press; 2008).
- [65] K.F. Jensen and W. Kern, Thermal chemical vapor deposition, *Thin Film Processes II*, (1991)
- [66] U. Kogelschatz, Dielectric-barrier discharges: their history, discharge physics, and industrial applications, *Plasma chemistry and plasma processing*, **23**(1) (2003) 1-46
- [67] Y.P. Raizer and J.E. Allen, *Gas discharge physics*: (Springer Berlin; 1997).
- [68] Y. Wang and D. Wang, Influence of impurities on the uniform atmospheric-pressure discharge in helium, *Physics of Plasmas (1994-present)*, **12**(2) (2005) 023503
- [69] A. Sublet, C. Ding, J. Dorier, C. Hollenstein, P. Fayet and F. Coursimault, Atmospheric and sub-atmospheric dielectric barrier discharges in helium and nitrogen, *Plasma Sources Science and Technology*, **15**(4) (2006) 627
- [70] F. Massines, N. Gherardi, N. Naudé and P. Ségur, Glow and Townsend dielectric barrier discharge in various atmosphere, *Plasma Physics and Controlled Fusion*, **47**(12B) (2005) B577
- [71] T. Yokoyama, M. Kogoma, T. Moriwaki and S. Okazaki, The mechanism of the stabilisation of glow plasma at atmospheric pressure, *Journal of Physics D: Applied Physics*, **23**(8) (1990) 1125
- [72] H.-E. Wagner, R. Brandenburg, K. Kozlov, A. Sonnenfeld, P. Michel and J. Behnke, The barrier discharge: basic properties and applications to surface treatment, *Vacuum*, **71**(3) (2003) 417-436
- [73] D. Merche, N. Vandencastele and F. Reniers, Atmospheric plasmas for thin film deposition: A critical review, *Thin Solid Films*, **520**(13) (2012) 4219-4236
- [74] V.G. Samoilovič, V.I. Gibalov and K.V. Kozlov, *Physical chemistry of the barrier discharge*: (Deutscher Verlag für Schweisstechnik; 1997).
- [75] U. Kogelschatz, Filamentary, patterned, and diffuse barrier discharges, *Plasma Science, IEEE Transactions on*, **30**(4) (2002) 1400-1408

- [76] A. Kulikovskiy, Positive streamer in a weak field in air: A moving avalanche-to-streamer transition, *Physical Review E*, **57**(6) (1998) 7066
- [77] L. Dong, Z. Yin, X. Li and L. Wang, Spatio-temporal dynamics of discharge domains in a dielectric barrier discharge device, *Plasma Sources Science and Technology*, **12**(3) (2003) 380
- [78] F. Peeters. The electrical dynamics of dielectric barrier discharges: Technische Universiteit Eindhoven; 2015.
- [79] G. Nersisyan and W. Graham, Characterization of a dielectric barrier discharge operating in an open reactor with flowing helium, *Plasma Sources Science and Technology*, **13**(4) (2004) 582
- [80] A. Chiper, V. Anita, C. Agheorghiesei, V. Pohoata, A. Anita and G. Popa, editors. Spectral diagnostic for a DBD plasma in air and He/N<sub>2</sub> gas mixture. Proc 16th Int Symp on Plasma Chemistry (Taormina, Italy); 2003.
- [81] F. Massines, P. Segur, N. Gherardi, C. Khamphan and A. Ricard, Physics and chemistry in a glow dielectric barrier discharge at atmospheric pressure: diagnostics and modelling, *Surface and Coatings Technology*, **174** (2003) 8-14
- [82] N. Naudé, J. Cambreonne, N. Gherardi and G. Massines, editors. Electrotechnical approach of a process based on glow dielectric barrier discharge. Proc 16th Int Symp Plasma Chemistry (Taormina, Italy); 2003.
- [83] R. Valdivia-Barrientos, J. Pacheco-Sotelo, M. Pacheco-Pacheco, J. Benítez-Read and R. López-Callejas, Analysis and electrical modelling of a cylindrical DBD configuration at different operating frequencies, *Plasma sources science and technology*, **15**(2) (2006) 237
- [84] J.M. Williamson, D.D. Trump, P. Bletzinger and B.N. Ganguly, Comparison of high-voltage ac and pulsed operation of a surface dielectric barrier discharge, *Journal of Physics D: Applied Physics*, **39**(20) (2006) 4400
- [85] R. Brandenburg, V. Maiorov, Y.B. Golubovskii, H. Wagner, J. Behnke and J. Behnke, Diffuse barrier discharges in nitrogen with small admixtures of oxygen: discharge mechanism and transition to the filamentary regime, *Journal of Physics D: Applied Physics*, **38**(13) (2005) 2187
- [86] U. Pal, M. Kumar, M. Tyagi, B. Meena, H. Khatun and A. Sharma, editors. Discharge analysis and electrical modeling for the development of efficient dielectric barrier discharge. Journal of physics: Conference series; 2010: IOP Publishing.
- [87] S. Liu and M. Neiger, Electrical modelling of homogeneous dielectric barrier discharges under an arbitrary excitation voltage, *Journal of Physics D: Applied Physics*, **36**(24) (2003) 3144
- [88] B. Eliasson and U. Kogelschatz, Modeling and applications of silent discharge plasmas, *Plasma Science, IEEE Transactions on*, **19**(2) (1991) 309-323
- [89] J. Yao, Z. Zhang, Z. Yu, S. Xu, Q. Yu and J. Zhao, editors. A study on the equivalent electric circuit simulation model of DBD streamer and glow alternate discharge. Journal of Physics: Conference Series; 2013: IOP Publishing.
- [90] R. Siliprandi, H. Roman, R. Barni and C. Riccardi, Characterization of the streamer regime in dielectric barrier discharges, *Journal of applied physics*, **104**(6) (2008) 063309
- [91] A. Chirokov, A. Gutsol, A. Fridman, K. Sieber, J. Grace and K. Robinson, Analysis of two-dimensional microdischarge distribution in dielectric-barrier discharges, *Plasma Sources Science and Technology*, **13**(4) (2004) 623
- [92] Y. Akishev, G. Aponin, A. Balakirev, M. Grushin, V. Karalnik, A. Petryakov and N. Trushkin, Role of the volume and surface breakdown in a formation of microdischarges in a steady-state DBD, *The European Physical Journal D*, **61**(2) (2011) 421-429

- [93] S. Pal, S. Prakash and S. Kumar, Dissociative ionisation of methane by electron impact, *International journal of mass spectrometry and ion processes*, **153**(2) (1996) 79-86
- [94] A. Ozkan, T. Dufour, G. Arnoult, P. De Keyzer, A. Bogaerts and F. Reniers, CO<sub>2</sub>-CH<sub>4</sub> conversion and syngas formation at atmospheric pressure using a multi-electrode dielectric barrier discharge, *Journal of CO<sub>2</sub> utilization*, **9** (2015) 74-81
- [95] N. Pinhao, A. Janeco and J. Branco, Influence of Helium on the Conversion of Methane and Carbon dioxide in a Dielectric Barrier Discharge, *Plasma Chemistry and Plasma Processing*, **31**(3) (2011) 427-439
- [96] V. Goujard, J.-M. Tatibouët and C. Batiot-Dupeyrat, Carbon dioxide reforming of methane using a dielectric barrier discharge reactor: effect of helium dilution and kinetic model, *Plasma Chemistry and Plasma Processing*, **31**(2) (2011) 315-325
- [97] M. Ramakers, I. Michielsen, R. Aerts, V. Meynen and A. Bogaerts, Effect of argon or helium on the CO<sub>2</sub> conversion in a dielectric barrier discharge, *Plasma Processes and Polymers*, **12** (2015) 755-763
- [98] S. Heijkers, R. Snoeckx, T.s. Kozák, T. Silva, T. Godfroid, N. Britun, R. Snyders and A. Bogaerts, CO<sub>2</sub> Conversion in a Microwave Plasma Reactor in the Presence of N<sub>2</sub>: Elucidating the Role of Vibrational Levels, *The Journal of Physical Chemistry C*, **119**(23) (2015) 12815-12828
- [99] R. Snoeckx, S. Heijkers, K. Van Wesenbeeck, S. Lenaerts and A. Bogaerts, CO<sub>2</sub> conversion in a dielectric barrier discharge plasma: N<sub>2</sub> in the mix as a helping hand or problematic impurity?, *Energy & Environmental Science*, (2016)
- [100] J.B. Boffard, R. Jung, C.C. Lin and A. Wendt, Optical emission measurements of electron energy distributions in low-pressure argon inductively coupled plasmas, *Plasma Sources Science and Technology*, **19**(6) (2010) 065001
- [101] G. Hagelaar and L. Pitchford, Solving the Boltzmann equation to obtain electron transport coefficients and rate coefficients for fluid models, *Plasma Sources Science and Technology*, **14**(4) (2005) 722
- [102] T. Kozák and A. Bogaerts, Evaluation of the energy efficiency of CO<sub>2</sub> conversion in microwave discharges using a reaction kinetics model, *Plasma Sources Science and Technology*, **24**(1) (2015) 015024
- [103] T. Kozák and A. Bogaerts, Splitting of CO<sub>2</sub> by vibrational excitation in non-equilibrium plasmas: A reaction kinetics model, *Plasma Sources Science and Technology*, **23**(4) (2014) 045004
- [104] B. Eliasson and U. Kogelschatz, Nonequilibrium volume plasma chemical processing, *Plasma Science, IEEE Transactions on*, **19**(6) (1991) 1063-1077
- [105] R. McAdams, Prospects for non-thermal atmospheric plasmas for pollution abatement, *Journal of Physics D: Applied Physics*, **34**(18) (2001) 2810
- [106] M. Kraus, B. Eliasson, U. Kogelschatz and A. Wokaun, CO<sub>2</sub> reforming of methane by the combination of dielectric-barrier discharges and catalysis, *Physical Chemistry Chemical Physics*, **3**(3) (2001) 294-300
- [107] F. Massines, N. Gherardi, N. Naude and P. Segur, Glow and Townsend dielectric barrier discharge in various atmosphere, *Plasma physics and controlled fusion*, **47**(12B) (2005) B577
- [108] J.L. Walsh and M.G. Kong, 10 ns pulsed atmospheric air plasma for uniform treatment of polymeric surfaces, (2007)
- [109] S.O. Macheret, M.N. Shneider and R.B. Miles, Modeling of air plasma generation by repetitive high-voltage nanosecond pulses, *Plasma Science, IEEE Transactions on*, **30**(3) (2002) 1301-1314

- [110] R. Snoeckx, S. Heijckers, K. Van Wesenbeeck, S. Lenaerts and A. Bogaerts, CO<sub>2</sub> conversion in a dielectric barrier discharge plasma: N<sub>2</sub> in the mix as a helping hand or problematic impurity?, *Energy & Environmental Science*, **9** (2016) 999-1011
- [111] R. Snoeckx, M. Setareh, R. Aerts, P. Simon, A. Maghari and A. Bogaerts, Influence of N<sub>2</sub> concentration in a CH<sub>4</sub>/N<sub>2</sub> dielectric barrier discharge used for CH<sub>4</sub> conversion into H<sub>2</sub>, *International Journal of Hydrogen Energy*, **38**(36) (2013) 16098-16120
- [112] F. Brehmer, S. Welzel, M. van de Sanden and R. Engeln, CO and byproduct formation during CO<sub>2</sub> reduction in dielectric barrier discharges, *Journal of Applied Physics*, **116**(12) (2014) 123303
- [113] X. Duan, Y. Li, W. Ge and B. Wang, Degradation of CO<sub>2</sub> through dielectric barrier discharge microplasma, *Greenhouse Gases: Science and Technology*, **5**(2) (2015) 131-140
- [114] D. Mei, X. Zhu, Y.-L. He, J.D. Yan and X. Tu, Plasma-assisted conversion of CO<sub>2</sub> in a dielectric barrier discharge reactor: understanding the effect of packing materials, *Plasma Sources Science and Technology*, **24**(1) (2015) 015011
- [115] Q. Yu, M. Kong, T. Liu, J. Fei and X. Zheng, Characteristics of the decomposition of CO<sub>2</sub> in a dielectric packed-bed plasma reactor, *Plasma Chemistry and Plasma Processing*, **32**(1) (2012) 153-163
- [116] S. Wang, Y. Zhang, X. Liu and X. Wang, Enhancement of CO<sub>2</sub> Conversion Rate and Conversion Efficiency by Homogeneous Discharges, *Plasma Chemistry and Plasma Processing*, **32**(5) (2012) 979-989
- [117] S. Paulussen, B. Verheyde, X. Tu, C. De Bie, T. Martens, D. Petrovic, A. Bogaerts and B. Sels, Conversion of carbon dioxide to value-added chemicals in atmospheric pressure dielectric barrier discharges, *Plasma Sources Science and Technology*, **19**(3) (2010) 034015
- [118] A. Ozkan, T. Dufour, T. Silva, N. Britun, R. Snyders, A. Bogaerts and F. Reniers, The influence of power and frequency on the filamentary behavior of a flowing DBD—application to the splitting of CO<sub>2</sub>, *Plasma Sources Science and Technology*, **25**(2) (2016) 025013
- [119] B. Eliasson, M. Hirth and U. Kogelschatz, Ozone synthesis from oxygen in dielectric barrier discharges, *Journal of Physics D: Applied Physics*, **20**(11) (1987) 1421
- [120] U. Kogelschatz, B. Eliasson and W. Egli, From ozone generators to flat television screens: history and future potential of dielectric-barrier discharges, *Pure and Applied Chemistry*, **71**(10) (1999) 1819-1828
- [121] G. Vezzu, J.L. Lopez, A. Freilich and K.H. Becker, Optimization of large-scale ozone generators, *Plasma Science, IEEE Transactions on*, **37**(6) (2009) 890-896
- [122] R. Aerts, W. Somers and A. Bogaerts, Carbon Dioxide Splitting in a Dielectric Barrier Discharge Plasma: A Combined Experimental and Computational Study, *ChemSusChem*, **8**(4) (2015) 702-716
- [123] R. Snoeckx, Y. Zeng, X. Tu and A. Bogaerts, Plasma-based dry reforming: improving the conversion and energy efficiency in a dielectric barrier discharge, *RSC Advances*, **5**(38) (2015) 29799-29808
- [124] X. Tu, H.J. Gallon and J.C. Whitehead, Transition behavior of packed-bed dielectric barrier discharge in argon, *Plasma Science, IEEE Transactions on*, **39**(11) (2011) 2172-2173
- [125] K. Van Laer and A. Bogaerts, Improving the Conversion and Energy Efficiency of Carbon Dioxide Splitting in a Zirconia-Packed Dielectric Barrier Discharge Reactor, *Energy Technology*, **3**(10) (2015) 1038-1044

- [126] Y. Zhang, H.-y. Wang, W. Jiang and A. Bogaerts, Two-dimensional particle-in-cell/Monte Carlo simulations of a packed-bed dielectric barrier discharge in air at atmospheric pressure, *New Journal of Physics*, **17**(8) (2015) 083056
- [127] R. Aerts, T. Martens and A. Bogaerts, Influence of vibrational states on CO<sub>2</sub> splitting by dielectric barrier discharges, *The Journal of Physical Chemistry C*, **116**(44) (2012) 23257-23273
- [128] Z. Xie, K. Jogan and J.-S. Chang, editors. The effect of residential time on the reduction of CO<sub>2</sub> from combustion flue gases by a corona torch reactor. Industry Applications Society Annual Meeting, 1990, Conference Record of the 1990 IEEE; 1990: IEEE.
- [129] M. Janda and Z. Machala, Transient-Spark Discharge in Mixtures at Atmospheric Pressure, *Plasma Science, IEEE Transactions on*, **36**(4) (2008) 916-917
- [130] Z. Bo, J. Yan, X. Li, Y. Chi, K. Cen and B. Cheron, Effects of oxygen and water vapor on volatile organic compounds decomposition using gliding arc gas discharge, *Plasma Chemistry and Plasma Processing*, **27**(5) (2007) 546-558
- [131] A. Czernichowski, Gliding arc: applications to engineering and environment control, *Pure and Applied Chemistry*, **66**(6) (1994) 1301-1310
- [132] Z. Bo, J. Yan, X. Li, Y. Chi and K. Cen, Scale-up analysis and development of gliding arc discharge facility for volatile organic compounds decomposition, *Journal of hazardous materials*, **155**(3) (2008) 494-501
- [133] A. Fridman, S. Nester, L.A. Kennedy, A. Saveliev and O. Mutaf-Yardimci, Gliding arc gas discharge, *Progress in Energy and Combustion Science*, **25**(2) (1999) 211-231
- [134] T. Nunnally, K. Gutsol, A. Rabinovich, A. Fridman, A. Gutsol and A. Kemoun, Dissociation of CO<sub>2</sub> in a low current gliding arc plasmatron, *Journal of Physics D: Applied Physics*, **44**(27) (2011) 274009
- [135] A. Indarto, J.-W. Choi, H. Lee and H.K. Song, Conversion of CO<sub>2</sub> by gliding arc plasma, *Environmental engineering science*, **23**(6) (2006) 1033-1043
- [136] A. Indarto, D.R. Yang, J.-W. Choi, H. Lee and H.K. Song, Gliding arc plasma processing of CO<sub>2</sub> conversion, *Journal of hazardous materials*, **146**(1) (2007) 309-315
- [137] A. Grill, *Cold plasma in materials fabrication*: (IEEE Press, New York; 1994).
- [138] L. Spencer and A. Gallimore, CO<sub>2</sub> dissociation in an atmospheric pressure plasma/catalyst system: a study of efficiency, *Plasma Sources Science and Technology*, **22**(1) (2013) 015019
- [139] A. Vesel, M. Mozetic, A. Drenik and M. Balat-Pichelin, Dissociation of CO<sub>2</sub> molecules in microwave plasma, *Chemical Physics*, **382**(1) (2011) 127-131
- [140] T. Silva, N. Britun, T. Godfroid and R. Snyders, Optical characterization of a microwave pulsed discharge used for dissociation of CO<sub>2</sub>, *Plasma Sources Science and Technology*, **23**(2) (2014) 025009
- [141] J. Rifkin, The hydrogen economy: the creation of the worldwide energy web and the redistribution of power on earth Tarcher, *Putnam, New York*, (2002)
- [142] U. Bossel, Does a hydrogen economy make sense?, *Proceedings of the IEEE*, **94**(10) (2006) 1826-1837
- [143] Z. Jiang, T. Xiao, V.á. Kuznetsov and P.á. Edwards, Turning carbon dioxide into fuel, *Philosophical Transactions of the Royal Society of London A: Mathematical, Physical and Engineering Sciences*, **368**(1923) (2010) 3343-3364
- [144] M. Mikkelsen, M. Jørgensen and F.C. Krebs, The teraton challenge. A review of fixation and transformation of carbon dioxide, *Energy & Environmental Science*, **3**(1) (2010) 43-81
- [145] L.F. Khilyuk, J.O. Robertson Jr, B. Endres and G. Chilingarian, *Gas migration: events preceding earthquakes*: (Gulf Professional Publishing; 2000).

- [146] G. Karavalakis, M. Hajbabaei, T.D. Durbin, K.C. Johnson, Z. Zheng and W.J. Miller, The effect of natural gas composition on the regulated emissions, gaseous toxic pollutants, and ultrafine particle number emissions from a refuse hauler vehicle, *Energy*, **50** (2013) 280-291
- [147] R.K. Pachauri, M. Allen, V. Barros, J. Broome, W. Cramer, R. Christ, J. Church, L. Clarke, Q. Dahe and P. Dasgupta, Climate Change 2014: Synthesis Report. Contribution of Working Groups I, II and III to the Fifth Assessment Report of the Intergovernmental Panel on Climate Change, (2014)
- [148] C.-j. Liu, G.-h. Xu and T. Wang, Non-thermal plasma approaches in CO<sub>2</sub> utilization, *Fuel Processing Technology*, **58**(2) (1999) 119-134
- [149] A. Gutsol, A. Rabinovich and A. Fridman, Combustion-assisted plasma in fuel conversion, *Journal of Physics D: Applied Physics*, **44**(27) (2011) 274001
- [150] X. Tao, M. Bai, X. Li, H. Long, S. Shang, Y. Yin and X. Dai, CH<sub>4</sub>-CO<sub>2</sub> reforming by plasma—challenges and opportunities, *Progress in Energy and Combustion Science*, **37**(2) (2011) 113-124
- [151] G. Petitpas, J.-D. Rollier, A. Darmon, J. Gonzalez-Aguilar, R. Metkemeijer and L. Fulcheri, A comparative study of non-thermal plasma assisted reforming technologies, *International Journal of Hydrogen Energy*, **32**(14) (2007) 2848-2867
- [152] R. Snoeckx, R. Aerts, X. Tu and A. Bogaerts, Plasma-based dry reforming: a computational study ranging from the nanoseconds to seconds time scale, *The Journal of Physical Chemistry C*, **117**(10) (2013) 4957-4970
- [153] Y.-p. Zhang, Y. Li, Y. Wang, C.-j. Liu and B. Eliasson, Plasma methane conversion in the presence of carbon dioxide using dielectric-barrier discharges, *Fuel Processing Technology*, **83**(1) (2003) 101-109
- [154] T. Nozaki, V. Goujard, S. Yuzawa, S. Moriyama, A. Ağırıl and K. Okazaki, Selective conversion of methane to synthetic fuels using dielectric barrier discharge contacting liquid film, *Journal of Physics D: Applied Physics*, **44**(27) (2011) 274010
- [155] G. Scarduelli, G. Guella, D. Ascenzi and P. Tosi, Synthesis of liquid organic compounds from CH<sub>4</sub> and CO<sub>2</sub> in a dielectric barrier discharge operating at atmospheric pressure, *Plasma Processes and Polymers*, **8**(1) (2011) 25-31
- [156] Y. Li, C.-J. Liu, B. Eliasson and Y. Wang, Synthesis of oxygenates and higher hydrocarbons directly from methane and carbon dioxide using dielectric-barrier discharges: product distribution, *Energy & fuels*, **16**(4) (2002) 864-870
- [157] J.-J. Zou, Y.-p. Zhang, C.-J. Liu, Y. Li and B. Eliasson, Starch-enhanced synthesis of oxygenates from methane and carbon dioxide using dielectric-barrier discharges, *Plasma Chemistry and Plasma Processing*, **23**(1) (2003) 69-82
- [158] V. Goujard, J.-M. Tatibouët and C. Batiot-Dupeyrat, Use of a non-thermal plasma for the production of synthesis gas from biogas, *Applied Catalysis A: General*, **353**(2) (2009) 228-235
- [159] T. Kolb, J.H. Voigt and K.-H. Gericke, Conversion of methane and carbon dioxide in a DBD reactor: influence of oxygen, *Plasma Chemistry and Plasma Processing*, **33**(4) (2013) 631-646
- [160] B. Fidalgo, A. Domínguez, J. Pis and J. Menéndez, Microwave-assisted dry reforming of methane, *International Journal of Hydrogen Energy*, **33**(16) (2008) 4337-4344
- [161] T.-S. Kim, S. Song, K.-M. Chun and S.H. Lee, An experimental study of syn-gas production via microwave plasma reforming of methane, iso-octane and gasoline, *Energy*, **35**(6) (2010) 2734-2743
- [162] W. Cho, W.-S. Ju, S.-H. Lee, Y.-S. Baek and Y.C. Kim, Investigation of Synthesis Gas Production from Natural Gas and CO<sub>2</sub> by Microwave Plasma Technology, *Studies in Surface Science and Catalysis*, **153** (2004) 205-208

- [163] D. Li, X. Li, M. Bai, X. Tao, S. Shang, X. Dai and Y. Yin, CO<sub>2</sub> reforming of CH<sub>4</sub> by atmospheric pressure glow discharge plasma: a high conversion ability, *International Journal of Hydrogen Energy*, **34**(1) (2009) 308-313
- [164] Y. Yang, Methane conversion and reforming by nonthermal plasma on pins, *Industrial & engineering chemistry research*, **41**(24) (2002) 5918-5926
- [165] A. Huang, G. Xia, J. Wang, S.L. Suib, Y. Hayashi and H. Matsumoto, CO<sub>2</sub> reforming of CH<sub>4</sub> by atmospheric pressure ac discharge plasmas, *Journal of Catalysis*, **189**(2) (2000) 349-359
- [166] A.B. Redondo, E. Troussard and J. Van Bokhoven, Non-oxidative methane conversion assisted by corona discharge, *Fuel Processing Technology*, **104** (2012) 265-270
- [167] A. Ghorbanzadeh, R. Lotfalipour and S. Rezaei, Carbon dioxide reforming of methane at near room temperature in low energy pulsed plasma, *international journal of hydrogen energy*, **34**(1) (2009) 293-298
- [168] G. Ni, Y. Lan, C. Cheng, Y. Meng and X. Wang, Reforming of methane and carbon dioxide by DC water plasma at atmospheric pressure, *international journal of hydrogen energy*, **36**(20) (2011) 12869-12876
- [169] L. Xiang, M.-g. BAI, X.-m. TAO, S.-y. SHANG, Y.-x. YIN and X.-y. DAI, Carbon dioxide reforming of methane to synthesis gas by an atmospheric pressure plasma jet, *Journal of Fuel Chemistry and Technology*, **38**(2) (2010) 195-200
- [170] S. Yao, E. Suzuki, N. Meng and A. Nakayama, A high-efficiency reactor for the pulsed plasma conversion of methane, *Plasma Chemistry and Plasma Processing*, **22**(2) (2002) 225-237
- [171] H. Lee and H. Sekiguchi, Plasma-catalytic hybrid system using spouted bed with a gliding arc discharge: CH<sub>4</sub> reforming as a model reaction, *Journal of Physics D: Applied Physics*, **44**(27) (2011) 274008
- [172] A. Indarto, J.-W. Choi, H. Lee and H.K. Song, Effect of additive gases on methane conversion using gliding arc discharge, *Energy*, **31**(14) (2006) 2986-2995
- [173] M.J. Gallagher, R. Geiger, A. Polevich, A. Rabinovich, A. Gutsol and A. Fridman, On-board plasma-assisted conversion of heavy hydrocarbons into synthesis gas, *Fuel*, **89**(6) (2010) 1187-1192
- [174] Z. Bo, J. Yan, X. Li, Y. Chi and K. Cen, Plasma assisted dry methane reforming using gliding arc gas discharge: effect of feed gases proportion, *International Journal of Hydrogen Energy*, **33**(20) (2008) 5545-5553
- [175] K. Pornmai, A. Jindanin, H. Sekiguchi and S. Chavadej, Synthesis gas production from CO<sub>2</sub>-containing natural gas by combined steam reforming and partial oxidation in an AC gliding arc discharge, *Plasma Chemistry and Plasma Processing*, **32**(4) (2012) 723-742
- [176] X. Tu and J.C. Whitehead, Plasma dry reforming of methane in an atmospheric pressure AC gliding arc discharge: Co-generation of syngas and carbon nanomaterials, *International Journal of Hydrogen Energy*, **39**(18) (2014) 9658-9669
- [177] N. Rueangjitt, T. Sreethawong and S. Chavadej, Reforming of CO<sub>2</sub>-containing natural gas using an AC gliding arc system: effects of operational parameters and oxygen addition in feed, *Plasma Chemistry and Plasma Processing*, **28**(1) (2008) 49-67
- [178] A.E.E. Putra, S. Nomura, S. Mukasa and H. Toyota, Hydrogen production by radio frequency plasma stimulation in methane hydrate at atmospheric pressure, *international journal of hydrogen energy*, **37**(21) (2012) 16000-16005
- [179] J. Yuan, X. Zhong and S. Tan, Methane conversion in the presence of oxygen under low-temperature radio frequency plasma, *Journal of Natural Gas Chemistry*, **19**(6) (2010) 605-610

- [180] B. Gaudernack and S. Lynum, Hydrogen from natural gas without release of CO<sub>2</sub> to the atmosphere, *International journal of hydrogen energy*, **23**(12) (1998) 1087-1093
- [181] J. Albo, M. Alvarez-Guerra, P. Castaño and A. Irabien, Towards the electrochemical conversion of carbon dioxide into methanol, *Green Chemistry*, **17**(4) (2015) 2304-2324
- [182] E.E. Benson, C.P. Kubiak, A.J. Sathrum and J.M. Smieja, Electrocatalytic and homogeneous approaches to conversion of CO<sub>2</sub> to liquid fuels, *Chemical Society Reviews*, **38**(1) (2009) 89-99
- [183] J.R. Scheffe and A. Steinfeld, Oxygen exchange materials for solar thermochemical splitting of H<sub>2</sub>O and CO<sub>2</sub>: a review, *Materials Today*, **17**(7) (2014) 341-348
- [184] E.V. Kondratenko, G. Mul, J. Baltrusaitis, G.O. Larrazábal and J. Pérez-Ramírez, Status and perspectives of CO<sub>2</sub> conversion into fuels and chemicals by catalytic, photocatalytic and electrocatalytic processes, *Energy & environmental science*, **6**(11) (2013) 3112-3135
- [185] A.H. McDaniel, E.C. Miller, D. Arifin, A. Ambrosini, E.N. Coker, R. O'Hayre, W.C. Chueh and J. Tong, Sr-and Mn-doped LaAlO<sub>3</sub>- $\delta$  for solar thermochemical H<sub>2</sub> and CO production, *Energy & Environmental Science*, **6**(8) (2013) 2424-2428
- [186] S. Samukawa, M. Hori, S. Rauf, K. Tachibana, P. Bruggeman, G. Kroesen, J.C. Whitehead, A.B. Murphy, A.F. Gutsol and S. Starikovskaia, The 2012 plasma roadmap, *Journal of Physics D: Applied Physics*, **45**(25) (2012) 253001
- [187] A. Bogaerts, T. Kozák, K. Van Laer and R. Snoeckx, Plasma-based conversion of CO<sub>2</sub>: current status and future challenges, *Faraday discussions*, **183** (2015) 217-232
- [188] P. Bruggeman and C. Leys, Non-thermal plasmas in and in contact with liquids, *Journal of Physics D: Applied Physics*, **42**(5) (2009) 053001
- [189] B.R. Locke and K.-Y. Shih, Review of the methods to form hydrogen peroxide in electrical discharge plasma with liquid water, *Plasma Sources Science and Technology*, **20**(3) (2011) 034006
- [190] M.A. Malik, A. Ghaffar and S.A. Malik, Water purification by electrical discharges, *Plasma Sources Science and Technology*, **10**(1) (2001) 82
- [191] P. Sunka, V. Babický, M. Clupek, P. Lukes, M. Simek, J. Schmidt and M. Cernak, Generation of chemically active species by electrical discharges in water, *Plasma Sources Science and Technology*, **8**(2) (1999) 258
- [192] B.R. Locke and S.M. Thagard, Analysis and review of chemical reactions and transport processes in pulsed electrical discharge plasma formed directly in liquid water, *Plasma Chemistry and Plasma Processing*, **32**(5) (2012) 875-917
- [193] T. Ihara, M. Kiboku and Y. Iriyama, Plasma Reduction of CO<sub>2</sub> with H<sub>2</sub>O for the Formation of Organic Compounds, *Bulletin of the Chemical Society of Japan*, **67**(1) (1994) 312-314
- [194] T. Ihara, T. Ouro, T. Ochiai, M. Kiboku and Y. Iriyama, Formation of Methanol by Microwave-Plasma Reduction of CO<sub>2</sub> with H<sub>2</sub>O, *Bulletin of the Chemical Society of Japan*, **69**(1) (1996) 241-244
- [195] G. Chen, T. Silva, V. Georgieva, T. Godfroid, N. Britun, R. Snyders and M.P. Delplancke-Ogletree, Simultaneous dissociation of CO<sub>2</sub> and H<sub>2</sub>O to syngas in a surface-wave microwave discharge, *International journal of hydrogen energy*, **40**(9) (2015) 3789-3796
- [196] S. Futamura and H. Kabashima, Synthesis Gas Production from CO<sub>2</sub> and H<sub>2</sub>O with Nonthermal Plasma, *Studies in Surface Science and Catalysis*, **153** (2004) 119-124
- [197] S. Futamura, H. Kabashima and G. Annadurai, Roles of CO<sub>2</sub> and H<sub>2</sub>O as oxidants in the plasma reforming of aliphatic hydrocarbons, *Catalysis today*, **115**(1) (2006) 211-216

- [198] N. Hayashi, T. Yamakawa and S. Baba, Effect of additive gases on synthesis of organic compounds from carbon dioxide using non-thermal plasma produced by atmospheric surface discharges, *Vacuum*, **80**(11) (2006) 1299-1304
- [199] S. Mahammadunnisa, E.L. Reddy, D. Ray, C. Subrahmanyam and J.C. Whitehead, CO<sub>2</sub> reduction to syngas and carbon nanofibres by plasma-assisted in situ decomposition of water, *International Journal of Greenhouse Gas Control*, **16** (2013) 361-363
- [200] L. Guo, X. Ma, Y. Xia, X. Xiang and X. Wu, A novel method of production of ethanol by carbon dioxide with steam, *Fuel*, **158** (2015) 843-847
- [201] A. Sarani, N. De Geyter, A.Y. Nikiforov, R. Morent, C. Leys, J. Hubert and F. Reniers, Surface modification of PTFE using an atmospheric pressure plasma jet in argon and argon+ CO<sub>2</sub>, *Surface and Coatings Technology*, **206**(8) (2012) 2226-2232
- [202] Y. Chen-Yang, J. Liao, J. Kau, J. Huang, W. Chang and C. Chen, Surface modifications of expanded poly (tetrafluoroethylene) sheets assisted by CO<sub>2</sub> antenna coupling microwave plasma, *Macromolecules*, **33**(15) (2000) 5638-5643
- [203] N. Médard, J.-C. Soutif and F. Poncin-Epaillard, CO<sub>2</sub>, H<sub>2</sub>O, and CO<sub>2</sub>/H<sub>2</sub>O plasma chemistry for polyethylene surface modification, *Langmuir*, **18**(6) (2002) 2246-2253
- [204] H.-Y. Yu, Y.-J. Xie, M.-X. Hu, J.-L. Wang, S.-Y. Wang and Z.-K. Xu, Surface modification of polypropylene microporous membrane to improve its antifouling property in MBR: CO<sub>2</sub> plasma treatment, *Journal of Membrane Science*, **254**(1) (2005) 219-227
- [205] M. Aouinti, P. Bertrand and F. Poncin-Epaillard, Characterization of polypropylene surface treated in a CO<sub>2</sub> plasma, *Plasmas and polymers*, **8**(4) (2003) 225-236
- [206] F. Poncin-Epaillard and M. Aouinti, Characterization of CO<sub>2</sub> plasma and interactions with polypropylene film, *Plasmas and polymers*, **7**(1) (2002) 1-17
- [207] Q.T. Le, J. Pireaux and R. Caudano, XPS study of the PET film surface modified by CO<sub>2</sub> plasma: effects of the plasma parameters and ageing, *Journal of adhesion science and technology*, **11**(5) (1997) 735-751
- [208] D.S. Wavhal and E.R. Fisher, Modification of porous poly (ether sulfone) membranes by low-temperature CO<sub>2</sub>-plasma treatment, *Journal of Polymer Science Part B: Polymer Physics*, **40**(21) (2002) 2473-2488
- [209] D.S. Wavhal and E.R. Fisher, Modification of polysulfone ultrafiltration membranes by CO<sub>2</sub> plasma treatment, *Desalination*, **172**(2) (2005) 189-205
- [210] R.E. Allred and W.C. Schimpf, CO<sub>2</sub> plasma modification of high-modulus carbon fibers and their adhesion to epoxy resins, *Journal of adhesion science and technology*, **8**(4) (1994) 383-394
- [211] E. Mathieu, Mémoire sur le mouvement vibratoire d'une membrane de forme elliptique, *Journal de mathématiques pures et appliquées*, (1868) 137-203
- [212] R.E. March, An introduction to quadrupole ion trap mass spectrometry, *Journal of mass spectrometry*, **32**(4) (1997) 351-369
- [213] D.A. Skoog, D.M. West, F.J. Holler and S. Crouch, Fundamentals of Analytical Chemistry, Thomson Learning, Inc, USA, (1996)
- [214] R.W.B. Pearse, A.G. Gaydon, R.W.B. Pearse and A.G. Gaydon. The identification of molecular spectra. 297: Chapman and Hall London; 1976.
- [215] U. Fantz, Emission spectroscopy of molecular low pressure plasmas, *Contributions to Plasma Physics*, **44** (2004) 508-515
- [216] N. Masoud, K. Martus, M. Figus and K. Becker, Rotational and Vibrational Temperature Measurements in a High-Pressure Cylindrical Dielectric Barrier Discharge (C-DBD), *Contributions to Plasma Physics*, **45**(1) (2005) 32-39

- [217] M. Shimada, G.R. Tynan and R. Cattolica, Rotational and translational temperature equilibrium in an inductively coupled plasma, *Journal of Vacuum Science & Technology A*, **24**(5) (2006) 1878-1883
- [218] A. Fridman and L.A. Kennedy, *Plasma physics and engineering*: (CRC press; 2004).
- [219] V.N. Ochkin, *Spectroscopy of low temperature plasma*: (John Wiley & Sons; 2009).
- [220] N. Britun, T. Godfroid, S. Konstantinidis and R. Snyders, Time-resolved gas temperature evolution in pulsed Ar-N<sub>2</sub> microwave discharge, *Applied Physics Letters*, **98**(14) (2011) 141502
- [221] N. Britun, T. Godfroid and R. Snyders, Time-resolved study of pulsed Ar-N<sub>2</sub> and Ar-N<sub>2</sub>-H<sub>2</sub> microwave surfaguide discharges using optical emission spectroscopy, *Plasma Sources Science and Technology*, **21**(3) (2012) 035007
- [222] R. Feng, G. Castle and S. Jayaram, Automated system for power measurement in the silent discharge, *Industry Applications, IEEE Transactions on*, **34**(3) (1998) 563-570
- [223] T. Manley, The electric characteristics of the ozonator discharge, *Transactions of the electrochemical society*, **84**(1) (1943) 83-96
- [224] S. Liu and M. Neiger, Excitation of dielectric barrier discharges by unipolar submicrosecond square pulses, *Journal of Physics D: Applied Physics*, **34**(11) (2001) 1632
- [225] S. Tao, L. Kaihua, Z. Cheng, Y. Ping, Z. Shichang and P. Ruzheng, Experimental study on repetitive unipolar nanosecond-pulse dielectric barrier discharge in air at atmospheric pressure, *Journal of Physics D: Applied Physics*, **41**(21) (2008) 215203
- [226] H. Jiang, T. Shao, C. Zhang, W. Li, P. Yan and E. Schamiloglu, editors. Study on QV Lissajous figures in nanosecond-pulsed surface discharge. Power Modulator and High Voltage Conference (IPMHVC), 2012 IEEE International; 2012: IEEE.
- [227] H. Jiang, T. Shao, C. Zhang, W. Li, P. Yan, X. Che and E. Schamiloglu, Experimental study of QV Lissajous figures in nanosecond-pulse surface discharges, *Dielectrics and Electrical Insulation, IEEE Transactions on*, **20**(4) (2013) 1101-1111
- [228] T. Shao, H. Jiang, C. Zhang, P. Yan, M.I. Lomaev and V.F. Tarasenko, Time behaviour of discharge current in case of nanosecond-pulse surface dielectric barrier discharge, *EPL (Europhysics Letters)*, **101**(4) (2013) 45002
- [229] R. Valdivia-Barrientos, J. Pacheco-Sotelo, M. Pacheco-Pacheco, J. Benitez-Read and R. López-Callejas, Analysis and electrical modelling of a cylindrical DBD configuration at different operating frequencies, *Plasma sources science and technology*, **15**(2) (2006) 237
- [230] R. Dorai and M.J. Kushner, Consequences of unburned hydrocarbons on microstreamer dynamics and chemistry during plasma remediation of NO<sub>x</sub> using dielectric barrier discharges, *Journal of Physics D: Applied Physics*, **36**(9) (2003) 1075
- [231] D.S. Stafford and M.J. Kushner, O<sub>2</sub> (1) production in He/O<sub>2</sub> mixtures in flowing low pressure plasmas, *J Appl Phys*, **96**(5) (2004) 2451-2465
- [232] W. Van Gaens and A. Bogaerts, Kinetic modelling for an atmospheric pressure argon plasma jet in humid air, *Journal of Physics D: Applied Physics*, **46**(27) (2013) 275201
- [233] R. Snoeckx, A. Ozkan, F. Reniers and A. Bogaerts, The quest for value-added products from CO<sub>2</sub> and H<sub>2</sub>O in a dielectric barrier discharge: a chemical kinetics study, *accepted in ChemSusChem*, (2016)
- [234] R. Aerts, R. Snoeckx and A. Bogaerts, In-Situ Chemical Trapping of Oxygen in the Splitting of Carbon Dioxide by Plasma, *Plasma Processes and Polymers*, **11**(10) (2014) 985-992
- [235] T. Kozák and A. Bogaerts, Evaluation of the energy efficiency of CO<sub>2</sub> conversion in microwave discharges using a reaction kinetics model, *Plasma Sources Science and Technology*, **24**(1) (2014) 015024

- [236] R. Aerts, X. Tu, W. Van Gaens, J. Whitehead and A. Bogaerts, Gas purification by nonthermal plasma: a case study of ethylene, *Environmental science & technology*, **47**(12) (2013) 6478-6485
- [237] A. Ozkan, T. Dufour, T. Silva, N. Britun, R. Snyders, F. Reniers and A. Bogaerts, DBD in burst mode: solution for more efficient CO<sub>2</sub> conversion?, *submitted to Plasma Sources Science and Technology*, (2016)
- [238] A. Ozkan, T. Dufour, A. Bogaerts and F. Reniers, How do the barrier thickness and dielectric material influence the filamentary mode and CO<sub>2</sub> conversion in a flowing DBD?, *Plasma Sources Science and Technology (in progress)*, (2016)
- [239] O. Motret, C. Hibert, S. Pellerin and J. Pouvesle, Rotational temperature measurements in atmospheric pulsed dielectric barrier discharge-gas temperature and molecular fraction effects, *Journal of Physics D: Applied Physics*, **33**(12) (2000) 1493
- [240] A. Ozkan, T. Dufour, T. Silva, N. Britun, R. Snyders, A. Bogaerts and F. Reniers, The influence of power and frequency on the filamentary behavior of a flowing DBD – Application to the splitting of CO<sub>2</sub>, *Plasma Sources Science and Technology*, **25**(2) (2016) 025013
- [241] V.A. Godyak, Nonequilibrium EEDF in gas discharge plasmas, *IEEE transactions on plasma science*, **34**(3) (2006) 755
- [242] I. Belov, S. Paulussen and A. Bogaerts, The influence of reactor walls surface conductivity on the electrical properties and conversion efficiency in a Dielectric Barrier Discharge in CO<sub>2</sub>, *submitted to Plasma Sources Science and Technology*,
- [243] P. Bruggeman, N. Sadeghi, D. Schram and V. Linss, Gas temperature determination from rotational lines in non-equilibrium plasmas: a review, *Plasma Sources Science and Technology*, **23**(2) (2014) 023001
- [244] F. Brehmer, S. Welzel, B. Klarenaar, H. van der Meiden, M. van de Sanden and R. Engeln, Gas temperature in transient CO<sub>2</sub> plasma measured by Raman scattering, *Journal of Physics D: Applied Physics*, **48**(15) (2015) 155201
- [245] R.O.J. J. B. Boffard, C.C. Lin, L. E. Aneskavich and A. E. Wendt. Argon 420.1–419.8 nm emission line ratio for measuring plasma effective electron temperatures. *J Phys D: Appl Phys*. 2012.
- [246] R. Shrestha, R. Tyata and D. Subedi, Effect of applied voltage in electron density of homogeneous dielectric barrier discharge at atmospheric pressure, *Himalayan Physics*, **4** (2013) 10-13
- [247] A.J. Wu, H. Zhang, X.D. Li, S.Y. Lu, C.M. Du and J.H. Yan, Determination of Spectroscopic Temperatures and Electron Density in Rotating Gliding Arc Discharge, *Plasma Science, IEEE Transactions on*, **43**(3) (2015) 836-845
- [248] D. Mei, Y.L. He, S. Liu, J. Yan and X. Tu, Optimization of CO<sub>2</sub> Conversion in a Cylindrical Dielectric Barrier Discharge Reactor Using Design of Experiments, *Plasma Processes and Polymers*, (2015)
- [249] H. Jiang, T. Shao, C. Zhang, Z. Niu, Y. Yu, P. Yan and Y. Zhou, Comparison of AC and nanosecond-pulsed DBDs in atmospheric air, *Plasma Science, IEEE Transactions on*, **39**(11) (2011) 2076-2077
- [250] T. Shao, Y. Yu, C. Zhang, D. Zhang, Z. Niu, J. Wang, P. Yan and Y. Zhou, Excitation of atmospheric pressure uniform dielectric barrier discharge using repetitive unipolar nanosecond-pulse generator, *Dielectrics and Electrical Insulation, IEEE Transactions on*, **17**(6) (2010) 1830-1837
- [251] C. Zhang, T. Shao, H. Ma, C. Ren, P. Yan and Y. Zhou, Comparison of s-and ns-Pulse Gliding Discharges in Air Flow, *Plasma Science, IEEE Transactions on*, **42**(10) (2014) 2354-2355

- [252] T. Shao, C. Zhang, Y. Zhou, Q. Xie, Z. Zhou and P. Yan, Diffuse Discharges in Open Air Sustained by Microsecond and Nanosecond Pulses, *Plasma Science, IEEE Transactions on*, **42**(10) (2014) 2408-2409
- [253] C. Zhang, T. Shao, R. Wang, Z. Zhou, Y. Zhou and P. Yan, A comparison between characteristics of atmospheric-pressure plasma jets sustained by nanosecond-and microsecond-pulse generators in helium, *Physics of Plasmas (1994-present)*, **21**(10) (2014) 103505
- [254] T. Jiang, Y. Li, C.-j. Liu, G.-h. Xu, B. Eliasson and B. Xue, Plasma methane conversion using dielectric-barrier discharges with zeolite A, *Catalysis Today*, **72**(3) (2002) 229-235
- [255] A. Ghorbanzadeh and H. Modarresi, Carbon dioxide reforming of methane by pulsed glow discharge at atmospheric pressure: The effect of pulse compression, *Journal of applied physics*, **101**(12) (2007)
- [256] S. Yao, M. Okumoto, A. Nakayama and E. Suzuki, Plasma reforming and coupling of methane with carbon dioxide, *Energy & fuels*, **15**(5) (2001) 1295-1299
- [257] T. Shao, C. Zhang, Z. Fang, Y. Yu, D. Zhang, P. Yan, Y. Zhou and E. Schamiloglu, A comparative study of water electrodes versus metal electrodes for excitation of nanosecond-pulse homogeneous dielectric barrier discharge in open air, *Plasma Science, IEEE Transactions on*, **41**(10) (2013) 3069-3078
- [258] Z. Jiang and Z.-j. Jiang, Synthesis and optimization of proton exchange membranes by a pulsed plasma enhanced chemical vapor deposition technique, *International Journal of Hydrogen Energy*, **37**(15) (2012) 11276-11289
- [259] A.A.a. Ndong, N. Zouzou, N. Benard and E. Moreau, Geometrical optimization of a surface DBD powered by a nanosecond pulsed high voltage, *Journal of Electrostatics*, **71**(3) (2013) 246-253
- [260] T. Shao, W. Yang, C. Zhang, Z. Fang, Y. Zhou and E. Schamiloglu, Temporal evolution of atmosphere pressure plasma jets driven by microsecond pulses with positive and negative polarities, *EPL (Europhysics Letters)*, **107**(6) (2014) 65004
- [261] H.K. Song, H. Lee, J.-W. Choi and B.-k. Na, Effect of electrical pulse forms on the CO<sub>2</sub> reforming of methane using atmospheric dielectric barrier discharge, *Plasma chemistry and plasma processing*, **24**(1) (2004) 57-72
- [262] H. Lee, C.-H. Lee, J.-W. Choi and H.K. Song, The effect of the electric pulse polarity on CO<sub>2</sub> reforming of CH<sub>4</sub> using dielectric barrier discharge, *Energy & fuels*, **21**(1) (2007) 23-29
- [263] A. Khacef and J.M. Cormier, Pulsed sub-microsecond dielectric barrier discharge treatment of simulated glass manufacturing industry flue gas: removal of SO<sub>2</sub> and NO<sub>x</sub>, *Journal of Physics D: Applied Physics*, **39**(6) (2006) 1078
- [264] A. Ghorbanzadeh, S. Norouzi and T. Mohammadi, High energy efficiency in syngas and hydrocarbon production from dissociation of CH<sub>4</sub>-CO<sub>2</sub> mixture in a non-equilibrium pulsed plasma, *Journal of Physics D: Applied Physics*, **38**(20) (2005) 3804
- [265] N. Benard and E. Moreau, Capabilities of the dielectric barrier discharge plasma actuator for multi-frequency excitations, *Journal of Physics D: Applied Physics*, **43**(14) (2010) 145201
- [266] H. Gejima, R. Takinami, K. Fukagata, T. Mitsumoji, T. Sueki and M. Ikeda, Suppression of vortex shedding from a pantograph head using vortex generator-type plasma actuators, *Journal of Fluid Science and Technology*, **10**(1) (2015) JFST0006-JFST0006
- [267] N. Benard, P. Sujar-Garrido, K.D. Bayoda, J.-P. Bonnet and E. Moreau, editors. Pulsed dielectric barrier discharge for manipulation of turbulent flow downstream a backward-

- facing-step. 52nd AIAA Aerospace Sciences Meeting, National Harbor, MD, USA, January; 2014.
- [268] N. Benard, J.-P. Bonnet, G. Touchard and E. Moreau, Flow control by dielectric barrier discharge actuators: jet mixing enhancement, *AIAA journal*, **46**(9) (2008) 2293-2305
- [269] D. Roupasov, A. Nikipelov, M. Nudnova and A.Y. Starikovskii, Flow separation control by plasma actuator with nanosecond pulsed-periodic discharge, *AIAA journal*, **47**(1) (2009) 168-185
- [270] J. Little, M. Nishihara, I. Adamovich and M. Samimy, High-lift airfoil trailing edge separation control using a single dielectric barrier discharge plasma actuator, *Experiments in fluids*, **48**(3) (2010) 521-537
- [271] N. Benard and E. Moreau, Electrical and mechanical characteristics of surface AC dielectric barrier discharge plasma actuators applied to airflow control, *Experiments in Fluids*, **55**(11) (2014) 1-43
- [272] J.-h. Choi, D.-y. Huh and Y.-s. Kim, editors. The improved burst mode in the stand-by operation of power supply. Applied Power Electronics Conference and Exposition, 2004 APEC'04 Nineteenth Annual IEEE; 2004: IEEE.
- [273] T. Andersen, M.S. Rødgaard, M.A. Andersen, O.C. Thomsen, K. Lorenzen, C. Mangeot and A. Steenstrup, editors. Integrated high voltage power supply utilizing burst mode control and its performance impact on dielectric electro active polymer actuators. 13th International Conference on New Actuators and 7th International Exhibition on Smart Actuators and Drive Systems; 2012.
- [274] L. Martini, G. Dilecce, G. Guella, A. Maranzana, G. Tonachini and P. Tosi, Oxidation of CH<sub>4</sub> by CO<sub>2</sub> in a dielectric barrier discharge, *Chemical Physics Letters*, **593** (2014) 55-60
- [275] N. Masoud, K. Martus, M. Figus and K. Becker, Rotational and vibrational temperature measurements in a high-pressure cylindrical dielectric barrier discharge (C-DBD), *Contributions to Plasma Physics*, **45**(1) (2005) 32-39
- [276] P. Reginald William Blake and G. Alfred Gordon, *The identification of molecular spectra*. 4th edition ed. London/New York: (Chapman and Hall/Wiley; 1976).
- [277] J.-P. Manceau. Etude du phénomène de relaxation diélectrique dans les capacités Métal-Isolant-Métal: Université Joseph-Fourier-Grenoble I; 2008.
- [278] M. Forte, J. Jolibois, J. Pons, E. Moreau, G. Touchard and M. Cazalens, Optimization of a dielectric barrier discharge actuator by stationary and non-stationary measurements of the induced flow velocity: application to airflow control, *Experiments in Fluids*, **43**(6) (2007) 917-928
- [279] T. Opalińska and A. Szymański, A Barrier Discharge Reactor with Ferroelectric Electrodes I. Influence of thickness and surface area of electrodes, *Contributions to Plasma Physics*, **36**(1) (1996) 63-73
- [280] V.I. Gibalov and G.J. Pietsch, Properties of dielectric barrier discharges in extended coplanar electrode systems, *Journal of Physics D: Applied Physics*, **37**(15) (2004) 2093
- [281] J. Pons, E. Moreau and G. Touchard, Asymmetric surface dielectric barrier discharge in air at atmospheric pressure: electrical properties and induced airflow characteristics, *Journal of physics D: applied physics*, **38**(19) (2005) 3635
- [282] T.C. Corke, C.L. Enloe and S.P. Wilkinson, Dielectric barrier discharge plasma actuators for flow control\*, *Annual Review of Fluid Mechanics*, **42** (2010) 505-529
- [283] D. Opaits, Dielectric barrier discharge plasma actuator for flow control, *NASA/CR—2012-217655*, (2012)
- [284] J.-Y. Wang, G.-G. Xia, A. Huang, S.L. Suib, Y. Hayashi and H. Matsumoto, CO<sub>2</sub> decomposition using glow discharge plasmas, *Journal of Catalysis*, **185**(1) (1999) 152-159

- [285] R. Li, Y. Yamaguchi, S. Yin, Q. Tang and T. Sato, Influence of dielectric barrier materials to the behavior of dielectric barrier discharge plasma for CO<sub>2</sub> decomposition, *Solid State Ionics*, **172**(1) (2004) 235-238
- [286] R. Li, Q. Tang, S. Yin and T. Sato, Plasma catalysis for CO<sub>2</sub> decomposition by using different dielectric materials, *Fuel processing technology*, **87**(7) (2006) 617-622
- [287] R. Li, Q. Tang, S. Yin and T. Sato, Investigation of dielectric barrier discharge dependence on permittivity of barrier materials, *Applied physics letters*, **90**(13) (2007) 131502
- [288] M.R. Stuart, Dielectric constant of quartz as a function of frequency and temperature, *Journal of Applied Physics*, **26**(12) (1955) 1399-1404
- [289] L.-Y. Chen and G.W. Hunter, editors. Temperature Dependent Dielectric Properties of Polycrystalline 96% Al<sub>2</sub>O<sub>3</sub>. MRS Proceedings; 2004: Cambridge Univ Press.
- [290] S. Kobayashi and Y. Saito. Secondary Electron Emission (SEE) Measurements on Materials Under Stress (Preliminary Measurements of SEE Under High Temperature Condition). DTIC Document, 2003.
- [291] Y. Yamano, S. Kobayashi, S. Michizono and Y. Saito, Secondary electron emission and surface charging evaluation of alumina ceramics and sapphire, *Dielectrics and Electrical Insulation, IEEE Transactions on*, **13**(1) (2006) 72-78
- [292] C. Mueller, The secondary electron emission of pyrex glass, *Journal of Applied Physics*, **16**(8) (1945) 453-458
- [293] J.E. Harry, *Introduction to Plasma Technology: Science, Engineering, and Applications*: (John Wiley & Sons; 2013).
- [294] M. Hernández-Hernández, M. Tapia-Gaspar, E. Basurto, C. Vargas and J. Hernández-Ávila, Current-Voltage and the Paschen-like's law for dc discharges in ternary mixtures of N<sub>2</sub>, O<sub>2</sub>, CO<sub>2</sub> and H<sub>2</sub>O at low pressures, *proceedings of the 20th ICPIG conference*, (2009)
- [295] C. De Bie, T. Martens, J. van Dijk, S. Paulussen, B. Verheyde, S. Corthals and A. Bogaerts, Dielectric barrier discharges used for the conversion of greenhouse gases: modeling the plasma chemistry by fluid simulations, *Plasma Sources Science and Technology*, **20**(2) (2011) 024008
- [296] R. Janev and D. Reiter, Collision processes of CH<sub>y</sub> and CH<sub>y</sub><sup>+</sup> hydrocarbons with plasma electrons and protons, *Physics of Plasmas (1994-present)*, **9**(9) (2002) 4071-4081
- [297] D. Baulch, C. Bowman, C. Cobos, R. Cox, T. Just, J. Kerr, M. Pilling, D. Stocker, J. Troe and W. Tsang, Evaluated kinetic data for combustion modeling: supplement II, *Journal of physical and chemical reference data*, **34**(3) (2005) 757-1397
- [298] D. Baulch, C. Cobos, R. Cox, C. Esser, P. Frank, T. Just, J. Kerr, M. Pilling, J. Troe and R. Walker, Evaluated kinetic data for combustion modelling, *Journal of Physical and Chemical Reference Data*, **21**(3) (1992) 411-734
- [299] A. Florescu-Mitchell and J. Mitchell, Dissociative recombination, *Physics Reports*, **430**(5) (2006) 277-374
- [300] J. Woodall, M. Agúndez, A. Markwick-Kemper and T. Millar, The UMIST database for astrochemistry 2006, *Astronomy & Astrophysics*, **466**(3) (2007) 1197-1204
- [301] J. Dingle and D. Le Roy, Kinetics of the reaction of atomic hydrogen with acetylene, *The Journal of Chemical Physics*, **18**(12) (1950) 1632-1637
- [302] W. Tsang and R. Hampson, Chemical kinetic data base for combustion chemistry. Part I. Methane and related compounds, *Journal of Physical and Chemical Reference Data*, **15**(3) (1986) 1087-1279
- [303] G. Hancock, V. Haverd and M. Morrison, Infrared emission accompanying the gas phase recombination of alkyl radicals, *Physical Chemistry Chemical Physics*, **5**(14) (2003) 2981-2987

- [304] L.B. Harding, Y. Georgievskii and S.J. Klippenstein, Predictive theory for hydrogen atom-Hydrocarbon radical association kinetics, *The Journal of Physical Chemistry A*, **109**(21) (2005) 4646-4656
- [305] R. Janev and D. Reiter, Collision Processes of  $C_2$ ,  $3H_y$  and  $C_2$ ,  $3H_y^+$  hydrocarbons with Electrons and Protons, *Physics of Plasmas (1994-present)*, **11**(2) (2004) 780-829
- [306] M.J. Gauthier and D.R. Snelling, La Photolyse de l'Ozone a 253.7 nm: Desactivation de O ( $^1D$ ) et de O<sub>2</sub> ( $^1\Sigma$ ) par les Gaz de l'Atmosphere, *Journal of Photochemistry*, **4**(1) (1975) 27-50
- [307] S. Hadj-Ziane, B. Held, P. Pignolet, R. Peyrous and C. Coste, Ozone generation in an oxygen-fed wire-to-cylinder ozonizer at atmospheric pressure, *Journal of Physics D: Applied Physics*, **25**(4) (1992) 677
- [308] D.-C. Fang and X.-Y. Fu, CASSCF and CAS+ 1+ 2 Studies on the Potential Energy Surface and the Rate Constants for the Reactions between CH<sub>2</sub> and O<sub>2</sub>, *The Journal of Physical Chemistry A*, **106**(12) (2002) 2988-2993
- [309] J.-Y. Wang, G.-G. Xia, A. Huang, S.L. Suib, Y. Hayashi and H. Matsumoto, CO<sub>2</sub> decomposition using glow discharge plasmas, *Journal of Catalysis*, **185**(1) (1999) 152-159
- [310] Y. Tagawa, S. Mori, M. Suzuki, I. Yamanaka, T. Obara, J. Ryu and Y. Kato, Synergistic Decomposition of CO<sub>2</sub> by Hybridization of a Dielectric Barrier Discharge Reactor and a Solid Oxide Electrolyser Cell, *Kagaku Kogaku Ronbunshu*, **37**(2) (2011) 114-119
- [311] M. Pham, V. Goujard, J. Tatibouet and C. Batiot-Dupeyrat, Activation of methane and carbon dioxide in a dielectric-barrier discharge-plasma reactor to produce hydrocarbons—Influence of La<sub>2</sub>O<sub>3</sub>/γ-Al<sub>2</sub>O<sub>3</sub> catalyst, *Catalysis Today*, **171**(1) (2011) 67-71
- [312] B. Eliasson, U. Kogelschatz, B. Xue and L.-M. Zhou, Hydrogenation of carbon dioxide to methanol with a discharge-activated catalyst, *Industrial & engineering chemistry research*, **37**(8) (1998) 3350-3357
- [313] G. Zheng, J. Jiang, Y. Wu, R. Zhang and H. Hou, The mutual conversion of CO<sub>2</sub> and CO in dielectric barrier discharge (DBD), *Plasma chemistry and plasma processing*, **23**(1) (2003) 59-68
- [314] M.H. Stans, Bond dissociation energies in simple molecules, *NIST Special Publication*, **1** (1970) 58
- [315] M.A. Lieberman and A.J. Lichtenberg, Principles of plasma discharges and materials processing, *MRS Bulletin*, **30** (1994) 899-901
- [316] S.L. Brock, M. Marquez, S.L. Suib, Y. Hayashi and H. Matsumoto, Plasma decomposition of CO<sub>2</sub> in the presence of metal catalysts, *Journal of Catalysis*, **180**(2) (1998) 225-233
- [317] Y. Wen and X. Jiang, Decomposition of CO<sub>2</sub> using pulsed corona discharges combined with catalyst, *Plasma Chemistry and Plasma Processing*, **21**(4) (2001) 665-678
- [318] A.-J. Zhang, A.-M. Zhu, J. Guo, Y. Xu and C. Shi, Conversion of greenhouse gases into syngas via combined effects of discharge activation and catalysis, *Chemical Engineering Journal*, **156**(3) (2010) 601-606

